Mechanical Behavior and Radiation Effects

2026 Principal Investigators' Meeting

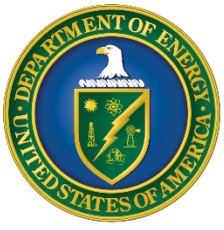

U.S. DEPARTMENT of ENERGY | Office of Science

Foreword

This volume comprises the scientific content of the 2026 Mechanical Behavior and Radiation Effects Principal Investigators' (PI) Meeting sponsored by the Division of Materials Science and Engineering (DMSE) in the Office of Basic Energy Sciences (BES) of the U. S. Department of Energy (DOE). The meeting, held on September 15-17, is the tenth such meeting on this topic and is one among a series of research theme-based PI Meetings being held by DMSE. The meeting's focus is on research in mechanical behavior and radiation effects of materials.

The studies of mechanical behavior and radiation effects have a long and important history with respect to the generation, transmission, utilization and conservation of energy. It is a tribute to the researchers that they have continued to move the field forward into a number of important areas, as can be seen by the diversity of projects being presented at this meeting. Some of the projects represent newer directions in this program, such as work in polymer systems and functional materials. Attendees will note a number of new projects and research directions since the previous meeting including several recipients of Early Career Research Program awards. These new projects add to the exciting areas of research and cutting-edge techniques that are a hallmark of this program.

The purpose of the Mechanical Behavior and Radiation Effects PI Meeting is to bring together researchers funded by DMS&E in this important area of research on a periodic basis (approximately every two years) in order to facilitate the exchange of new results and research highlights, to nucleate new ideas and collaborations among the participants, and to identify needs of the research community. The meeting will also help DMSE staff in assessing the state of the program, identifying new research directions and recognizing programmatic needs.

I would like to express my sincere thanks to all the attendees for their active participation and for sharing their ideas and new research results. I greatly appreciated the help of Dr. Mark DiTusa, a AAAS Fellow in the Office of Nuclear Energy, who helped with setting up this meeting and presented a dynamic talk on science communication. I would also like to express my sincere gratitude to Ms. Kerry Hochberger in DMSE, and Paul Hudson, April Ward and Kutter Craig at the Oak Ridge Institute of Science and Education (ORISE) for their dedicated and outstanding work in taking care of all the logistical aspects of the meeting

John Vetrano
Program Manager
Mechanical Behavior and Radiation Effects
Division of Materials Sciences and Engineering
Office of Basic Energy Sciences
U.S. Department of Energy

Table of Contents

Agenda **8**

Poster Listing **11**

Abstracts **15**

Center for PRredictive Integrated Structural Materials Science – PRISMS Center
J. Allison, A. Misra, A. Bucsek, V. Gavini, E. Holm, B. Puchala, L. Qi, V. Sundararaghavan, K. Thornton, and A. Van der Ven *16*

Driven defect-phases in irradiated alloys: A novel paradigm to enhance radiation resistance and resilience
Pascal Bellon, Robert S. Averback, and Marie A. Charpagne *21*

Role of Subgrain Heterogeneous Processes in Slip Localization in Polycrystalline Metals During Cyclic Plasticity
I. J. Beyerlein, T. M. Pollock, M. P. Miller, and K. E. Nygren *25*

Nanomechanics and Nanometallurgy of Boundaries
Brad L. Boyce, Remi Dingreville, Doug Medlin, and Stephen House *30*

Effect of Gradient Architectures on the Strength, Deformation, and Failure of Nanoglasses
Paulo S. Branicio *35*

Beyond Shear: Improving the Prediction of Plastic Deformation Activation in HCP Materials
Ashley Bucsek and Huseyin Sehitoglu *40*

AI-enabled real-time reconstructions and interpretation for rapid 3D Xray diffraction and imaging of materials under stress and extreme environments
Ashley Bucsek, Reeju Pokharel, and Peter Kenesei *45*

Elucidating the influence of bulk slip morphology on hydrogen environment-assisted cracking behavior in precipitation-hardened alloys
James T. Burns *48*

The Role of Local Chemical Order on Defect Kinetics in Alloys under Irradiation
Penghui Cao *52*

Deformation Twinning Networks in Metals with Hexagonal Close-Packed Crystal Symmetry
Laurent Capolungo, Hi Vo, Khanh Dang, and Rodney McCabe *57*

Dynamic Grain Boundary Chemistry for Efficient Defect Sinks in Irradiated Nanoceramics
Ricardo H. R. Castro *62*

Radiation-induced heterostructure formation
Marie A. Charpagne *66*

Role of nanoscale heterogeneities on charged species transport in oxide and oxide growth
Adrien Couet, Yongfeng Zhang, and Jennifer T. Choy *68*

Understanding the effect of stress on complexion transitions and the interplay with creep in thermally stabilized nanocrystalline materials
Maarten P. de Boer, Gregory S. Rohrer, and Elizabeth C. Dickey *73*

No effect of curvature on the radiation response of Cu-Nb phase boundaries
M. J. Demkowicz, and K. Y. Xie *78*

Fundamental Insights into Defect Generation and Transport at Extended Defects for Resilient Energy Materials
S. Dillon, W. Neilson, J. White , M. Cooper, D. Andersson, Y. Wang, B. Uberuaga, K. Burke, and S. Finkeldei *81*

Understanding the Mechanics of Reverse Phase Transformation and Detwinning in BCC Metal Microstructures
Avinash M. Dongare *87*

The Origins of Strain Localization and Crack Nucleation in Complex Alloys Under Cyclic Loading
J. A. El-Awady and S. I. Rao *92*

Computational and Experimental Study of Slip Transfer in a BCC-B2 alloy
Maryam Ghazisaeidi and Michael Mills *97*

Electro-Chemo-Mechanical Fatigue in Lithium
Wendy Gu and William Chueh *102*

Understanding the role of temperature on grain boundary migration
Eric R. Homer, Gregory B. Thompson and Oliver K. Johnson *104*

Understanding the Role of Surface Energy in the Deformation of Metal Nanoparticles
Tevis D.B. Jacobs and Ashlie Martini *108*

Understanding the Interplay between Hydrogen and Chemical Short-Range Order in Multi-Principal Element Alloys
Miaomiao Jin and Yang Yang..... *113*

Elucidating Grain Growth in Thermo-Magnetic Processed Materials by Transfer Learning and Reinforcement Learning
Amanda R. Krause, Michael R. Tonks, Joel B. Harley, and Michael S. Kesler *118*

Mechanical Behavior of Materials at the Micrometer Scale under Different Environments
Seok-Woo Lee..... *123*

Understanding The Influence of Ca and Zn on Twinning-Detwinning Behavior in Mg Alloys During In-SEM Cyclic Loading
Aeriel Leonard *127*

Discovering the Mechanisms of Photoplasticity in Semiconductors
Lin Li..... *131*

Influence of 3D heterophase interface structure on deformation physics
Nathan A. Mara and Irene J. Beyerlein..... *136*

Interplay between radiation-induced segregation and irradiation-induced grain boundary migration
Emmanuelle Marquis, Fadi Abdeljawad, Enrique Martinez, and Suveen Mathaudhu *141*

Metal-ceramic interfaces at high temperatures
Yuri Mishin..... *145*

Plasticity of High-Strength Multiphase Metallic Composites
Amit Misra *150*

Mechanistic, Quantitative Understanding of the Dynamics of Many, Interacting Defect Clusters for Tailoring Irradiation Responses
Dane Morgan, Paul M. Voyles, and Kevin G. Field..... *156*

Modeling the Molecular Mechanisms of Interfacial Welding in Self-Healing Polymers
Thomas C. O'Connor..... *161*

Understanding Irradiation-Assisted Plasticity in Complex Concentrated Alloys: Aging-Enhanced Ductility in Ti-Zr-Nb-O
Hyunseok Oh *166*

Assessing energetic contributions to slip/twinning selection in low symmetry ceramics
Corinne E. Packard and Garrit J. Tucker *171*

Fundamental Studies of the Mechanical Behavior of Charged Hetero-Interfaces
Nitin P. Padture and Yue Qi *175*

Determining rate-controlling, grain-boundary-mediated mechanisms in nanocrystalline and ultrafine grained metallic films
Olivier Pierron, Josh Kacher, and Ting Zhu *180*

Closing the Loop: AI-Accelerated Interstitial Engineering of Complex Concentrated Alloys
Stephanie Ribet, Andrew Minor, Brandon Bocklund, Aurelien Perron, and Mingwei Zhang *185*

Damage-Tolerance in Structural Materials
Robert O. Ritchie, Mark Asta, and Andrew M. Minor *186*

Structural Short-Range Order and the Damage Tolerance of Amorphous Grain Boundary Complexions
Timothy J. Rupert *191*

Ion-irradiation-assisted strain relaxation in epitaxial high entropy oxide films
Ritesh Sachan *196*

Interplay of plasticity events, fracture, and local microstructure on 3D growth of small fatigue cracks
Michael D. Sangid *200*

Crack-Tip Mechanisms Driving Environmental Degradation
D.K. Schreiber, A. Devaraj, K. Kruska, K.M. Rosso, M.L. Sushko, and C. Wang *202*

Low-Pressure, Extreme Strain-Rate Mechanics from Microparticle Impact
Christopher A. Schuh *207*

Towards High-Throughput Computation of Phase-and Defect Diagrams
Christopher A. Schuh *212*

Toughening mechanisms in ceramic nanocomposites
Brian W. Sheldon, Jun Lou, and Nitin P. Padture *217*

Micromechanics of Migrating Interfaces
Ryan Sills *221*

Origins of elastomeric nanocomposite reinforcement: internal volume and stress competitions between coexisting hard and soft solids
David S. Simmons *226*

Closed-loop, Feedback-driven Design of Metastable Alloys with Predictable Strength-toughness via a Scalable, Agentic Multimodal Diffraction-Chemistry Framework
Douglas Spearot, Ravit Silverstein, Yijia Gu, Daniel Gianola, Arda Genc, and Austin Wade *228*

Radiation Effects in High-Entropy Carbides
Izabela Szlufarska *229*

Mapping the Damage Evolution Hierarchy in Compositionally Complex Alloys
Mitra L. Taheri, Michael L. Falk, and Jaime Marian *233*

Mechanisms of Irradiation-Induced Grain Subdivision
Michael Tonks, Assel Aitkaliyeva, and Simon Phillpot *239*

Irradiation Defect Formation and Evolution in Doped Metallic Interfaces
Jason R. Trelewicz and Andrea M. Hodge *244*

Disorder & Diffusion in Complex Oxides: Towards Prediction & Control
Blas Pedro Uberuaga, Caitlin Kohnert, Cortney Kreller, Brianna Musico, Yongqiang Wang, and Arjen van Veelen *249*

Understanding the Competition between Plastic Flow and Fracture in BCC Transition Metals
Christopher R. Weinberger and Gregory B. Thompson *253*

Understanding Mechanisms of Irradiation-Induced Crystallization
Janelle P. Wharry *258*

Integration of High-Throughput Experiments and Physics-Informed Machine Learning to Understand Irradiation-Induced Swelling in Metallic Glass
Yang Yang *261*

Understanding Elevated-Temperature Plasticity in Refractory Complex Concentrated Alloys
Mingwei Zhang *265*

Author Index 270

Agenda

MBRE PI Meeting, September 15, 2026

Start Time	End Time	Speaker	Project Title
8:00	8:10	John Vetrano	Welcome
8:10	8:30	Bindu Nair, Office of Basic Energy Sciences	Welcome and BES Q&A
Session chair		Jaafar El-Awady	
8:30	8:50	Nitin Padture, Brown	Fundamental Studies of the Mechanical Behavior of Charged Hetero-Interfaces
8:50	9:10	Tevis Jacobs, Pitt	Understanding the Role of Surface Energy in the Deformation of Metal Nanoparticles
9:10	9:30	Yongfeng Zhang (Couet), Wisconsin	Role of nanoscale heterogeneities on charged species transport in oxide
9:30	9:50	Amit Misra, Michigan	Plasticity of High-Strength Multiphase Metallic Composites
9:50	10:10	Break	
Session chair		Yuri Mishin	
10:10	10:30	Paulo Branicio, USC	Effect of Gradient Architectures on the Strength, Deformation and Failure of Nanoglasses
10:30	10:50	Dane Morgan, Wisconsin	Mechanistic, Quantitative Understanding of the Dynamics of Many, Interacting Defect Clusters for Tailoring Irradiation Responses
10:50	11:10	Ashley Bucsek, Michigan	Beyond Shear: Improving the Prediction of Plastic Deformation Activation in HCP Materials
11:10	11:30	Joel Harley (Krause), Florida	Elucidating Grain Growth in Thermo-Magnetic Processed Materials by Transfer Learning and Reinforcement Learning
11:30	11:50	Sarah Finkeldei, UC-Irvine	Fundamental Insights into Defect Generation and Transport at Extended Defects for Resilient Energy Materials
11:50	13:30	Lunch - Poster lightning talks	
13:30	15:30	Posters	
Session chair		Ryan Sills	
15:30	15:50	Ritesh Sachan, Oklahoma State	Atomic-scale Understanding of Irradiation-Induced Order/Disorder Transformations in High-Entropy Oxides
15:50	16:10	Rob Ritchie, LBNL	Damage-Tolerance of Structural Materials
16:10	16:30	Mia Jin, Penn State	Understanding the interplay between hydrogen and chemical short-range order in multiple principal element alloys
16:30	16:50	Mitra Taheri, Johns Hopkins	Mapping the Damage Evolution Hierarchy in Compositionally Complex Alloys
16:50	17:10	Corinne Packard, USC	Elucidating the Role of Pressure and Shear in Controlling Twinning in Low-Symmetry Ceramics
17:10	17:30	Hi Vo (Capolungo), LANL	Multi-Scale Study of the Role of Microstructure in the Deformation Behavior of Hexagonal Materials
17:30	19:00	Dinner on your own	
19:00	21:00	Open Poster Session	

MBRE PI Meeting, September 16, 2026

Start Time	End Time	Speaker	Project Title
8:20	8:30	John Vetrano	Intro to Day 2
Session chair		Maryam Ghazisaeidi	
8:30	8:50	John Allison, Michigan	Center for PRedictive Integrated Structural Materials Science PRISMS Center
8:50	9:10	Nathan Mara, Minnesota	Influence of 3D Heterophase Interface Structure on Deformation Physics
9:10	9:30	Michael Tonks, Florida	Mechanisms of Irradiation-Induced Grain Subdivision
9:30	9:50	Jason Trelewicz, Stony Brook	Irradiation Defect Formation and Evolution in Doped Metallic Interfaces
9:50	10:10	Break	
Session chair		Seok-Woo Lee	
10:10	10:30	John Vetrano, BES	Programmatic Updates
10:30	10:50	Blas Uberuaga, LANL	Disorder and Diffusion in Complex Oxides: Towards Prediction and Control
10:50	11:10	Eric Homer, BYU	Computational and Experimental Investigation of Cryogenic Grain Boundary Motion for Enhanced Mechanical Properties
11:10	11:30	Lin Li, Arizona State	Discovering the Mechanisms of Photoplasticity in Semiconductors
11:30	12:00	Mark Feuer DiTusa - AAAS Fellow	Science Communication/Discussion/Q&A
12:00	13:30	Lunch - Dr. Aaron Stone (International Engagement) and poster lightning talks	
13:30	15:40	Poster Session	
Session chair		Wendy Gu	
15:40	16:00	Penghui Cao, UCSD	The Role of Local Chemical Order on Defect Kinetics in Alloys under Irradiation
16:00	16:20	Thomas O'Connor, Carnegie Mellon	Modeling the Molecular Mechanisms of Interfacial Welding in Self-Healing Polymers
16:20	16:40	Aeriel Leonard, Ohio State	The Role of Strain Localization at Interfaces on Fatigue Crack Initiation in Highly Textured Magnesium Alloy
16:40	17:00	Hyunseok Oh, Wisconsin	Understanding Irradiation-Assisted Plasticity in Complex Concentrated Alloys
17:00	17:20	Mingwei Zhang, UC-Davis	Understanding Elevated-Temperature Plasticity in Refractory Complex Concentrated Alloys
17:20	19:00	Dinner on your own	
19:00	21:00	Open Poster Session	

MBRE PI Meeting, September 17, 2026

Start Time	End Time	Speaker	Project Title
8:20	8:30	John Vetrano	Intro to Day 3
Session chair		Greg Thompson	
8:30	8:50	David Simmons, USF	Establishing Mechanistic Relationships between Polymer-Particle Coupling, Fatigue, and Failure for Ultra-Tough Elastomeric Nanocomposites
8:50	9:10	Michael Demkowicz, Texas A&M	Improving radiation response of solid-state interfaces via control of curvature
9:10	9:30	Olivier Pierron, Georgia Tech	Fundamental investigation of grain boundary mediated mechanisms in ultrafine grained metallic films
9:30	9:50	Emmanuelle Marquis, Michigan	Interplay between Radiation-Induced Segregation and Irradiation-Induced Grain Boundary Migration
9:50	10:10	Break	
Session chair		Marie Charpagne	
10:10	10:30	Izabela Szlufarska, Wisconsin	Radiation effects in high entropy carbides
10:30	10:50	Irene Beyerlein, UCSB	The Role of Subgrain Heterogeneous Processes in Slip Localization in Polycrystalline Metals During Cyclic Plasticity
10:50	11:10	Brad Boyce, SNL/NM	Nanomechanics and Nanometallurgy of Boundaries
11:10	11:30	Dan Schreiber, PNNL	Crack-Tip Mechanisms Driving Environmental Degradation
11:30	11:50	Chris Schuh, Northwestern	Microparticle Impacts for Extreme Mechanics
11:50		Final Wrap-up - Vetrano	

Poster session I
Tuesday, September 15, 2026

Lead PI: John Allison, Michigan
Presenter: Liang Qi
Center for PRedictive Integrated Structural Materials Science PRISMS Center

Lead PI: Pascal Bellon, UIUC
Presenter: Pascal Bellon
Driven defect-phases in irradiated alloys: A novel paradigm to enhance radiation resistance and resilience

Lead PI: Ricardo Castro, Lehigh
Presenter: Ricardo Castro
Dynamic Grain Boundary for Effective Defect Sinks in Irradiated Nanoceramics

Lead PI: Maarten de Boer, Carnegie Mellon
Presenter: Maarten de Boer
Understanding the effect of stress on complexion transitions and the interplay with creep in thermally stabilized nanocrystalline materials

Lead PI: Jaafar El-Awady, Johns Hopkins
Presenter: Jaafar El-Awady
The Origins of Strain Localization and Crack Nucleation in Complex Alloys Under Cyclic Loading

Lead PI: Mayram Ghazisaeidi, Ohio State
Presenter: Maryam Ghazisaeidi
Mechanisms of Deformation and Slip Transmission in Two Phase BCC/B2 Refractory High Entropy Alloys

Lead PI: Wendy Gu, Stanford
Presenter: Wendy Gu
Electro-Chemo-Mechanical Fatigue of Lithium and Lithium Alloys

Lead PI: Eric Homer, BYU
Presenter: Greg Thompson
Computational and Experimental Investigation of Cryogenic Grain Boundary Motion for Enhanced Mechanical Properties

Lead PI: Seok-Woo Lee, Connecticut
Presenter: Seok-Woo Lee
Mechanical Properties of Metals at the Micrometer Scale in Different Environments

Lead PI: Emmanuelle Marquis, Michigan
Presenter: Enrique Martinez Saez
Interplay between Radiation-Induced Segregation and Irradiation-Induced Grain Boundary Migration

Lead PI: Stephanie Ribet, LBNL
Presenter: Andy Minor
Genesis - Closing the Loop: AI-Accelerated Interstitial Engineering of Complex Concentrated Alloys

Lead PI: Michael Sangid, UC-Berkeley
Presenter: Michael Sangid
Interplay of Plasticity Events, Fracture, and Local Microstructure on 3D Growth of Small Fatigue Cracks

Poster session I (continued)
Tuesday, September 15, 2026

Lead PI: Doug Spearot, Florida
Presenter: Ravit Silverstein
Genesis - Closed-Loop, Feedback Driven Design of Metastable Alloys with Predictable Strength-Toughness via a Scalable, Agentic Multimodal Diffraction-Chemistry Framework

Lead PI: Michael Tonks, Florida
Presenter: Alhassan Issaka
Mechanisms of Irradiation-Induced Grain Subdivision

Lead PI: Blas Uberuaga, LANL
Presenter: Tinsley DeForest
Disorder and Diffusion in Complex Oxides: Towards Prediction and Control

Lead PI: Janelle Wharry, UIUC
Presenter: Janelle Wharry
Understanding Mechanisms of Irradiation-Induced Crystallization

Lead PI: Yang Yang, Penn State
Presenter: Yang Yang
Integration of High-Throughput Experiments and Physics-Informed Machine Learning to Understand Irradiation-Induced Swelling in Metallic Glass

Poster session II
Wednesday, September 16, 2026

Lead PI: Irene Beyerlein, UCSB
Presenter: Justine Schulte
The Role of Subgrain Heterogeneous Processes in Slip Localization in Polycrystalline Metals During Cyclic Plasticity

Lead PI: Brad Boyce, SNL/NM
Presenter: Heekwon Lee
Nanomechanics and Nanometallurgy of Boundaries

Lead PI: Ashley Bucsek, Michigan
Presenter: Ashley Bucsek
Genesis - AI-enabled real-time reconstructions and interpretation for rapid 3D Xray diffraction and imaging of materials under stress and extreme environments

Lead PI: Jimmy Burns, Virginia
Presenter: Jimmy Burns
Elucidating the influence of bulk slip morphology on hydrogen environment-assisted cracking behavior in precipitation-hardened alloys

Lead PI: Marie Charpagne, UIUC
Presenter: Marie Charpagne
Radiation-Induced Heterostructure Formation

Lead PI: Avinash Dongare, Connecticut
Presenter: Avinash Dongare
Understanding the Mechanics of Reverse Phase Transformation and Detwinning in BCC Metal Microstructures

Lead PI: Sarah Finkeldei, UC-Irvine
Presenter: Will Neilson (LANL)
Advancing clean energy through fundamental insights into defect generation and transport phenomena at grain boundaries in nuclear energy materials

Lead PI: Amanda Krause, Carnegie Mellon
Presenter: Vishal Yadav (Forida)
Elucidating Grain Growth in Thermo-Magnetic Processed Materials by Transfer Learning and Reinforcement Learning

Lead PI: Yuri Mishin, GMU
Presenter: Yuri Mishin
Metal-Ceramic Interfaces at High Temperatures

Lead PI: Olivier Pierron, Georgia Tech
Presenter: Ting Zhu
Fundamental investigation of grain boundary mediated mechanisms in ultrafine grained metallic films

Lead PI: Rob Ritchie, LBNL
Presenter: Andrew Minor
Damage-Tolerance of Structural Materials

Poster session II (continued)
Wednesday, September 16, 2026

Lead PI: Tim Rupert, Johns Hopkins
Presenter: Tim Rupert
Structural Short-Range Order and the Damage Tolerance of Amorphous Grain Boundary Complexions

Lead PI: Dan Schreiber, PNNL
Presenter: Arun Devaraj
Crack-Tip Mechanisms Driving Environmental Degradation

Lead PI: Chris Schuh, Northwestern
Presenter: Thomas Matson
Towards High-Throughput Computation of Phase-and Defect Diagrams

Lead PI: Brian Sheldon, Brown
Presenter: Brian Sheldon
Toughening Mechanisms in Ceramic Nanocomposites

Lead PI: Ryan Sills, Rutgers
Presenter: Ryan Sills
Micromechanics of Migrating Interfaces

Lead PI: Mitra Taheri, Johns Hopkins
Presenter: Jaime Marian
Mapping the Damage Evolution Hierarchy in Compositionally Complex Alloys

Lead PI: Chris Weinberger, Colorado State
Presenter: Chris Weinberger
Understanding the Competition between Plastic Flow and Fracture in BCC Transition Metals

Abstracts

Center for PRredictive Integrated Structural Materials Science – PRISMS Center

PI: J. Allison, University of Michigan (UM) 2012-2026; A. Misra (UM) 2026-2028.
Co-PIs: A. Bucsek (UM), V. Gavini (UM), E. Holm (UM) A. Misra (UM), B. Puchala (UM), L. Qi (UM), V. Sundararaghavan (UM), K. Thornton (UM), A. Van der Ven (UCSB).
Keywords: Software, data repository, magnesium alloys, microstructure, mechanical behavior**.**

Program Scope

The goal of the PRISMS Center is to establish a unique scientific platform that will enable accelerated predictive materials science. The platform has three key thrust areas:

1. **PRISMS Integrated Computational Software:** Develop and establish a suite of integrated, multi-scale, open-source computational tools for predicting the microstructural evolution and mechanical behavior of structural metals.
2. **The Materials Commons:** Develop and deploy "The Materials Commons," a knowledge repository and virtual collaboration space for curating, archiving and disseminating information from experiments and computations.
3. **PRISMS Integrated Science Use Cases:** The use cases demonstrate the application of the integrated PRISMS platform of experiments, theory and simulation for making major advances in the quantitative and predictive understanding of microstructural evolution and mechanical behavior of magnesium alloys.

Recent Progress and Future Plans

In addition to nine faculty members, the PRISMS Center currently has four full time software staff members and over the past two years has supported eighteen graduate students, post-doctoral fellows and part-time staff. We hold an annual workshop to develop our external PRISMS collaborative community and to train external users of PRISMS software tools and Materials Commons and have trained more than 500 users. In addition, a PRISMS Center You-Tube channel has been established with training for PRISMS software. It currently has over 945 subscribers and over 59,000 combined views. Additional information can be found at http://prisms-center.org.

PRISMS Integrated Open-Source Computational Software Four codes make up the PRISMS Open-Source Integrated software: *CASM, PRISMS-PF, PRISMS-Plasticity,* and *DFT-FE*. All are available on GitHub. The codes have major upgrades every year and over 13,000 unique clones (copies) have been downloaded as shown in Figure 1. This is an increase of 5000 over the past two years. Each software package

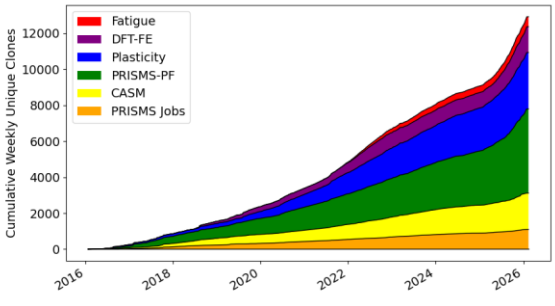

Figure 1. Cumulative clones of PRISMS codes since January 2016.

includes a substantial user manual, formulation notes, commented source code and unit tests.

CASM: CASM, a Clusters Approach to Statistical Mechanics, provides functionality for symmetry identification, enumeration of symmetrically unique supercells and configurations, use of automatically determined or custom reference states for formation energy calculation, and convex hull identification. Updates to CASM include new kinetic Monte Carlo (KMC) features for the analysis of local composition and ordering effects, a new user interface for visualization of enumerated structures and transformation pathways, and the release of `casm-map`, a new CASM-powered tool to map crystal structures and find symmetrically equivalent transformation pathways. CASM was used to develop a new Bayesian framework for propagating uncertainties in first-principles calculations. It is also being used extensively in the Machine-Learned Interatomic Potential project (see below) to automatically enumerate a wide variety of configurations in Mg-Zn-Ca alloys. *https://github.com/prisms-center/CASMCode*

DFT-FE: *DFT-FE* (Density Functional Theory – Finite Element) is a massively parallel code for large-scale real-space DFT calculations using spatially adaptive higher-order finite-element basis. The current development version of DFT-FE has advanced the portability and performance of the code, as well as the code capabilities. The same source code can seamlessly execute on both many-core CPU architectures as well as GPU architectures. DFT-FE is one of the very few DFT codes that can perform DFT calculations at scale on both Perlmutter and Frontier supercomputers. The performance of the code has been enhanced by further algorithmic improvements, including co-design of algorithms with GPU hardware and further building on our mixed precision developments. *https://github.com/dftfeDevelopers/dftfe*

PRISMS-PF: The *PRISMS-PF* phase field code uses the *deal.ii* open-source finite element library and is a massively scalable numerical framework for implementing phase field models for the multiscale materials modeling effort of PRISMS. A major update (PRISMS-PF v3.0) was released in 2025, including code refactoring and new numerical methods for improved performance. The release coincided with release of PRISMS-PF-MC, a suite of scripts for integration with the *Materials Commons*. New PRISMS-PF applications have been released, including crack propagation, fluid flow and implicit time-stepping models.
https://github.com/prisms-center/phaseField

PRISMS-Plasticity: The *PRISMS-Plasticity* code is a massively parallel numerical framework for implementing continuum and crystal plasticity finite element (CPFE) models using the *deal.ii* open source library. A variety of crystal and continuum plasticity material models have been implemented. The PRISMS-Plasticity software includes two frameworks: one for CPFE and one for continuum-scale plasticity. Both frameworks are compatible with subroutines developed as a part of a new PRISMS-Indentation pipeline for virtual indentation experiments. New capabilities were incorporated in the PRISMS-Plasticity framework including ease of post-processing, flexibility in the constitutive formulation and comparison with 3D experimental results. These

include explicit twin incorporation during the deformation, incorporation of additional twin types, and post-processing of the deformation gradient to predict the geometrically necessary dislocations (GND). *https://github.com/prisms-center/plasticity*

PRISMS-MP (Multi-Physics): A new framework has been defined for integrating results from PRISMS-Plasticity and PRISMS-PF to simulate deformation and microstructural evolution. Algorithm and modifications in the existing frameworks necessary for concurrent solution of PRISMS-PF and PRISMS-Plasticity have been completed, and release is scheduled for 3Q 2026. In this coupled approach, the mechanical solver from PRISMS-Plasticity provides PRISMS-PF with the elastic and plastic strain energy distribution during the deformation while PRISMS-PF provides the morphological evolution of twins or recrystallized grains to PRISM-Plasticity.

Materials Commons: The *Materials Commons 2.0* is a publicly available information repository and virtual collaboration space for curating, storing and disseminating materials information from experiments and computations. There are now over 1300 registered users of *Materials Commons* which represents a growth of over 500 over the past two years. Published datasets have been viewed over 50,000 times and downloaded more than 28,000 times. It houses over 9 million files and 70 TB of data in 945 projects, a 30% increase over the past two years. New features added to *Materials Commons* include a new data explorer, ease of use improvements and improvements to citation support. A machine learning workflow was developed for *Materials Commons* involving a computer vision method for segmenting complex microstructures and a graph network capability. A new suite of scripts enables automated capture of phase-field metadata from simulations, streamlining the dataset creation process with complete metadata. *https://materialscommons.org/*

PRISMS Use Cases

The PRISMS Use Cases serve as demonstrations and test beds for the development and demonstration of the PRISMS platform combining experiments, theory and simulation. Highlights from these use cases are summarized below.

Alloying Effects on Deformation Mechanisms Use Case:

In Mg-Y alloys, we experimentally determined that ductility is strongly affected by Y content and is maximized at 2 weight percent (w/o) Y. We hypothesized that this optimum value was due to solute interactions with <c+a> slip rather than the influence Y may have with dislocation core energies as proposed by others. We conducted direct large-scale DFT-FE calculations to accurately compute the core energy difference between Pyr I and II <c+a> screw dislocation and dislocation-solute interaction energies in Mg-Y (and Mg-Zn alloys). We note that these DFT-FE calculations reaching 6,000 atoms are the first of their kind in computing the dislocation energetics. We demonstrated that the relative solute strengthening effects on Pyr I and II <c+a> screw dislocation glide play a decisive role in cross-slip enhancement in Mg-Y, confirming our hypothesis. We account for this by computing a solute concentration dependent critical resolved

shear stress (CRSS) for dislocation glide on pyramidal planes, using the DFT computed dislocation solute interaction energies in a weak pinning model. Molecular dynamics simulations of grain boundary deformation in Mg-Y and Mg-Al alloys identified important new mechanisms for nucleating <c+a> slip.

Using a combination of quantitative *in situ* and *ex situ* experiments coupled with PRISMS-Plasticity we confirmed our hypothesis that with increasing Y content, the resistance to $\{10\bar{1}2\}$ twinning increases relative to dislocation slip modes. Importantly, in these experiments we also observed a new $\{11\bar{2}1\}$ twin mode. We completed analysis of the in-situ DFXM experiment on nucleation and growth of twins in Mg-4w/oAl. The results showed that twins nucleate at triple junctions. DFXM was used to measure local stress fields around twin-twin and twin-grain junctions in situ and in 3D, shedding new light on key mechanisms such as backstresses at grain boundaries. Explicit twin incorporation in PRISMS-Plasticity was utilized to model the 3D deformation characteristics observed in this experiment.

PRISMS Machine Learned Interatomic Potential Framework has been completed providing an infrastructure for validating interatomic potentials against DFT data for accurately determining properties such as dislocation core energies and twin and grain boundary energies. We have systematically constructed a Mg-Zn-Ca system DFT calculation dataset for training a Mg-Zn-Ca potential and begun comparing choices of potentials.

Grain Boundary Effects Use Case:
In situ SEM tensile testing in conjunction with high-resolution electron backscatter diffraction was used to characterize the evolution of GND densities at individual grain boundaries as a function of applied tensile strain in Mg-4Al. The increase in GND density was investigated at four plastic strains. Expressions were developed for the GND density evolution as a function of plastic strain and plastic incompatibility between neighboring grains, from which uniaxial stress-strain response of Mg-4Al were computed and compared with experimental results. This study showed a quantitative correlation between GND density evolution at grain boundaries and the measured strain hardening response of single-phase polycrystalline Mg alloys. These results were used to validate the new GND model incorporated into PRISMS-Plasticity.

Texture Evolution and Recrystallization Use Case:
Sequentially coupled PRISMS-Plasticity and PRISMS-PF models were used to simulate grain level deformation followed by static recrystallization (SRX) and compared to SRX experiments in Mg-Zn-Ca. The simulations quantitatively predict the observed SRX kinetics for a variety of initial deformation and annealing temperatures. The results indicate that the alloying effect leads to a reduction of mobility by a factor of approximately 8 compared to pure Mg. A combination of phenomenological models was used to study co-segregation effects of Ca and Zn at grain boundaries (GBs) in Mg alloys and their influence on texture evolution and recrystallization. The results reveal that Zn co-segregation plays a dominant role in controlling GB mobility, aligning

with experimental observations of slower recrystallization at lower Zn and higher Ca contents.

A comprehensive dynamic recrystallization (DRX) database for Mg-Zn-Ca alloys has been established as a function of deformation temperature, strain rate and strain level for use with DRX simulations using PRISMS-MP. MD simulations were conducted to investigate grain boundary (GB) migration in a large dataset of symmetric tilt GBs in Mg under shear at high temperatures—representing the first systematic study of GB mobility in hexagonal close-packed (HCP) metals. A voxel-wise machine learning (ML) surrogate model was developed for predicting voxel-wise texture evolution and trained using a new PRISMS-Plasticity data set.

2025-2026 Selected PRISMS Center Publications acknowledging DOE-BES support
(out of a total of 25 publications in past two years).

1. S. Lee, M. Pilipchuk, C. Yildirum, D. Greeley, T. Berman, A. Creuziger, E. Rust, C. Detlefts, V. Sundararaghavan, J. Allison, A. Bucsek, "Three-dimensional nucleation and growth of deformation twins in magnesium," 389 (6760) Science (2025)
2. S. Oh, Y. Jin, S. Lee, W. Li, K. Geauvreau, M. Williams, R. Drake, A. Bucsek, "Taking three-dimensional x-ray diffraction (3DXRD) from the synchrotron to the laboratory scale", Nat. Commun. 16 (2025) 3964.
3. S. Das and V. Gavini, "Intrinsic ductility enhancement in Mg alloys elucidated via large-scale ab-initio calculations" Acta Materialia (2026) 122377.
4. Q. Shi, V. Menon, L. Qi, J. Allison, "Experimental characterization and atomistic simulation of grain boundary segregation in Mg-Y alloys" Journal of Magnesium Alloys 13 (2025) 2509-2521.
5. Vaidehi Menon and Liang Qi, "Atomistic simulations and stochastic model of twinning and pyramidal slip nucleation at grain boundaries in Mg alloys," Computational Materials Science 258 (2025) 113975.
6. M. Yaghoobi, T. Berman, J. Allison, "Effects of Zn and Ca on texture evolution and work-hardening of Mg-Zn-Ca alloys at elevated temperature" Journal of Materials Research and Technology, 35 (2025) 37-50.
7. B. Puchala, J. C. Thomas, A. Van der Ven, "CASM Monte Carlo: Calculations of the thermodynamic and kinetic properties of complex multicomponent crystals", Computational Materials Science 260 (2025) 114091.
8. R. Roumina, S. Lee, T. Berman, K. Shanks, J. Allison, A. Bucsek, "Characterization of recrystallized gains during static recrystallization of hot-compressed Mg-Zn-Ca alloys using in-situ far-field high-energy diffraction microscopy", 1-14, Metallurgical and Materials Transactions A (2025)
9. D. Montiel, P. Staublin, S. Chakraborty, T. Berman, C. Patil, M. Pilipchuk, V. Sundararaghavan, J. Allison, and K. Thornton, "Understanding the kinetics of static recrystallization in Mg-Zn-Ca alloys using an integrated PRISMS simulation framework", Computational Materials Science (2026) 114869.
10. M. Pilipchuk, C. Patil, V. Sundararaghavan, "Comparative Analysis of Plasticity based GND Density Estimation Methods for capturing grain size and strain effects", Computational Materials Science 266 (2026) 114567.

Driven defect-phases in irradiated alloys: A novel paradigm to enhance radiation resistance and resilience

Pascal Bellon, Robert S. Averback, Marie A. Charpagne

Department of Materials Science and Engineering, University of Illinois at Urbana-Champaign, Urbana, IL.

Keywords: Irradiation, self-organization, grain boundaries, dislocations, correlative microscopy

Research Scope

Defect-phases refer to quasi-stable chemical phases that form on structural defects such as grain boundaries and dislocations. Controlling the formation of these defect-phases is already showing exceptional promise for designing alloys with tailored mechanical properties. We propose extending this concept to alloy systems driven by irradiation and experiencing defect production, enhanced diffusion (RED), and radiation-induced segregation (RIS). Our recent results have established that these defect-phases can now form stable steady states, thus providing radiation resistance. Furthermore, these driven defect-phases can self-organize at the nanoscale in a wide domain of the irradiation control parameters. Intentional and incidental transients of these control parameters can thus be accommodated locally and reversibly, promoting radiation resilience.

The two main objectives of the project are (i) to elucidate the principles governing the formation and the stability of nonequilibrium defect-phases induced by irradiation in alloys, also referred to as driven defect-phases, and (ii) to assess their potential for enhancing radiation resistance and resilience.

Recent Progress

1. Driven defect-phases along dislocations in phase-separating binary alloy systems

It is well established that the competition between radiation-enhanced diffusion (RED) and ballistic mixing can stabilize self-organized nanoprecipitate patterns [1-4]. We focus here on a different competition, between RED and RIS near dislocations in irradiated alloys, motivated by recent reports on nanoscale segregation and precipitation along dislocations in irradiated alloys. Notably, distinct morphologies have been observed, including continuous or nearly continuous tubular shapes along straight dislocation segments [5-8] and continuous circular shapes around dislocation loops [7,9], as well as quasi-periodic arrangements of nanoprecipitates [7,8,10,11]. It has been recently reported that such structures can impart unprecedented ductility retention in neutron-irradiated ferritic steels [8]. The origin of these quasi-periodic morphologies has been attributed, in some cases, to equilibrium precipitation reactions accelerated by RED [7], and in other cases, to advection, i.e., RIS, followed by precipitation at sinks [12]. The apparent lack of coarsening of these precipitates with irradiation dose has not received much attention, and at

present there is no physical model that explains the stabilization of finite-size precipitates at sinks such as dislocations by the competition between solute advection and solute diffusion.

Our current efforts have focused on examining this new approach to radiation resilience using a generic convective-diffusive model, implemented in a KMC simulation, to capture the competing dynamical processes controlling the evolution of the concentration field near a dislocation in an irradiated alloy. It is found that, in model alloys representing dilute Cu and Fe alloys, a rich morphology of driven defect-phases can be stabilized, including quasi-periodic necklaces of nanoprecipitates, see Figs. 1 and 2 [13]. Motivated by these simulation results, and ideas from past work supported by BES [1,14,15], a novel model is developed showing that the competition between (1) short-range RED thermal diffusion, along and near the dislocation and (2) the evaporation of solute atoms from precipitates and their long-range diffusion by advection (i.e., RIS/solute drag) is sufficient to stabilize quasi-periodic necklaces.

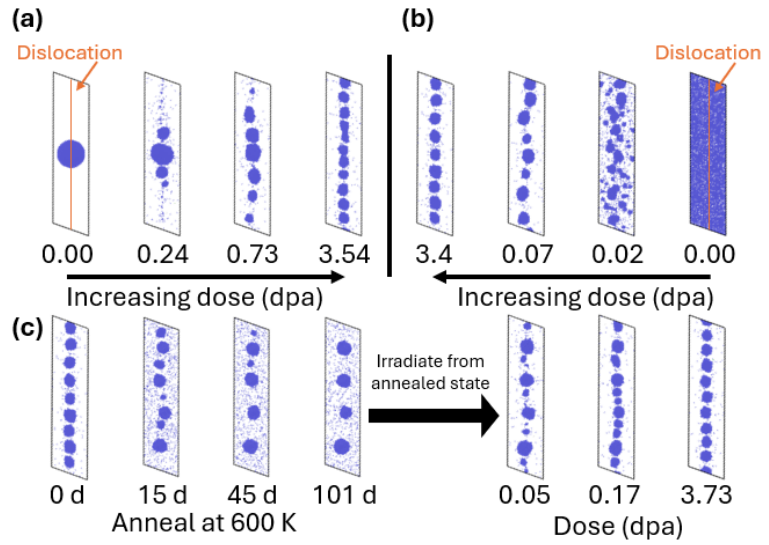

Figure 1. Formation of a steady-state quasi-periodic necklace nanoprecipitate structure for A-3%B alloy irradiated at 600 K at 5×10^{-4} dpa/s. Side views of 3D simulation cells capture solute segregation and precipitation on a dislocation line at the center of the cell (B atoms shown as blue dots). The system length is 49.1 nm. The same steady state is achieved starting (a) from a spherical precipitate or (b) from a random solution. Interruption of irradiation leads to coarsening (c), but the initial steady state is recovered after irradiation is resumed.

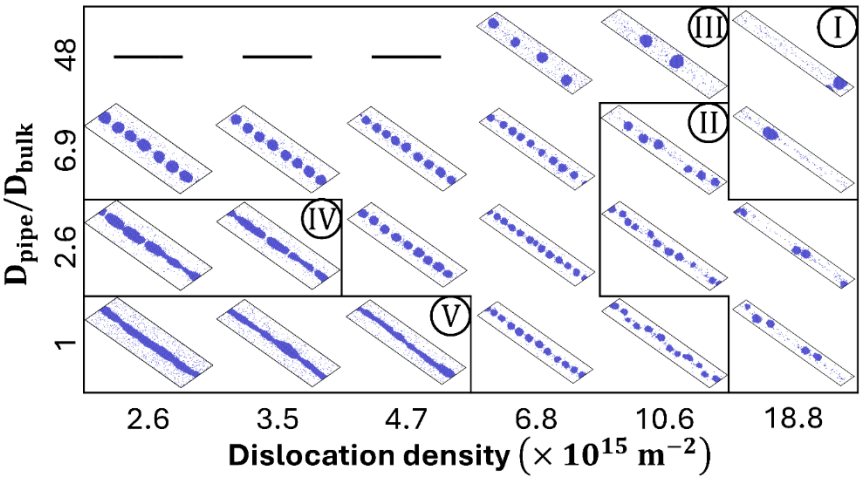

Figure 2. Steady states of A-3%B alloy irradiated at 600 K at 5×10^{-4} dpa/s as a function of dislocation density and pipe diffusion. Five morphologies are observed: (I) a single spherical precipitate, (II) isolated clusters of precipitates, (III) quasi-periodic necklace of spherical precipitates, (IV) piecewise tubular precipitates, and (V) continuous tubular precipitates.

2. Driven defect-phases at GBs in ordering and compound forming binary alloys

Three alloy systems were investigated: Ni-Si, Ni-Ge and Al-Sb [16-18]. These three systems have been chosen because they make it possible to contrast the effects of the type of point defect responsible for solute drag, vacancy for Ni-Ge and Al-Sb, interstitial for Ni-Si, as well as the strength of this coupling at similar homologous irradiation temperatures. The Al-Sb alloy system allows us to investigate whether the dominant factor for promoting GB precipitate self-organization is the solute-defect coupling (strong in Al-Sb) or solute GB diffusivity (slow in Al-Sb). The recent results obtained for Ni-Si and Ni-Ge are summarized below.

Undersaturated nanocrystalline Ni-8.5 at% Si thin films subjected to 2 MeV Ti irradiation at 450˚C to 550˚C were investigated using correlative microscopy combining TEM, STEM and atom probe tomography (APT), and phase field modeling (PFM) [16]. Irradiation at 450˚C was found to produce a stable nanostructure where three phases coexist, namely the FCC matrix, intragranular γ' $L1_2$ ordered precipitates and $Ni_{31}Si_{12}$ precipitates at triple junctions. Analysis of the segregation at GBs and precipitation on TJs suggests that the $Ni_{31}Si_{12}$ precipitates may contribute to pinning off the TJs and thus to the stabilization of this novel nanostructure. In contrast, for thin films with larger initial grain size as well as for bulk samples, no $Ni_{31}Si_{12}$ precipitation was observed. This remarkable effect of grain size is rationalized by noting that the dominant sinks for interstitial elimination shift from the GB network and TJs in nanocrystalline samples with a grain size below $\approx$ 100 nm, to intragranular loops and defect clusters in large-grain samples. This suggests that the initial microstructure, can be employed to guide the stabilization of stable defect-phases in alloys driven far from equilibrium by irradiation. The present results also demonstrate clearly that rationalizing phase selection in these driven defect-phases, leading here to a three-phase coexistence in an undersaturated alloy, requires taking into account the thermodynamic and kinetic coupling between structural defects and the chemical field.

The role of the detailed interactions between chemical phase fields and structural defects, defects created either by processing or by irradiation, was demonstrated in particularly dramatic terms by comparing defect-phases in Ni-10 at% Si with Ni-10 at% Ge [17]. Irradiations were performed using 100 keV He and 2 MeV Ti ions, including both bulk specimens and nanocrystalline thin films. Again, specimen characterization employed TEM, STEM and APT. While the *equilibrium* phase diagrams of these systems are quite similar, and both systems show strong radiation-induced segregation, the evolving defect-phase structures are remarkably different. Ni-Si reveals a high density of Frank loops, while Ni-Ge shows a complex array of dislocations. Moreover, a Ni_3Ge precipitate shell is observed to coat He bubbles, while no segregation of Si is observed at such bubbles. We attribute these differences in behaviors primarily to the fact that solute drag in Ni-Si results from interstitial fluxes whereas in Ni-Ge it derives from vacancy fluxes.

Future Plans

Ongoing and future experiments will consider the Cu-Zr and the Ni-Zr systems, as RIS in these systems appears to the stabilize amorphous precipitates, even at very low Zr concentrations. In addition to representing an additional form of driven defect-phases, it provides new opportunities

as amorphous precipitates may be stable over broad composition range and they may provide insaturable sinks for point defects. PFM modeling, in collaboration with Dr. Remi Dingreville at SNL, and KMC simulations will also be developed to establish stability criteria for driven defect-phases at GBs and along dislocations.

Publications

• S. Das, A. Verma, G. F. Bouobda Moladje, Y. T. Chang, M. A. Charpagne, R. S. Averback, and P. Bellon, "Global self-organization of solute induced by ion irradiation in polycrystalline alloys", Commun. Mater. **6**, 39, 39 (2025).
• S. Das, G. Jawaharram, R. S. Averback, S. J. Dillon, "Electron-irradiation induced creep in amorphous alloys", Phys. Rev. Mat. **10**, 033607 (2026).
• A. Verma, S. Das, Y. T. Chang, N. Saunders, D. Vizoso, R. Dingreville, M. Charpagne, R. S. Averback, and P. Bellon, "Non-equilibrium defect-phase nanostructures stabilized by irradiation in undersaturated Ni-Si nanocrystalline alloy", Acta Mater **314**, 122346, 122346 (2026).
• N. Saunders, R. S. Averback, and P. Bellon, "Self-organized defect-phases along dislocations in irradiated alloys", Physical Review Letters, under review, arxiv.org/abs/2601.11843 (2026).
• A. Verma, Y. T. Chang, M. A. Charpagne, P. Bellon, and R. S. Averback, "The role of radiation-induced segregation in defect-phase formation in Ni-Ge and Ni-Si alloys", Scripta Mater https://doi.org/10.48550/arXiv.2602.12860, in review (2026).

References

[1] R. A. Enrique and P. Bellon, Physical Review Letters **84**, 2885 (2000).
[2] S. W. Chee, B. Stumphy, N. Q. Vo, R. S. Averback, and P. Bellon, Acta Mater **58**, 4088 (2010).
[3] D. Simeone, G. Demange, and L. Luneville, Physical Review E **88**, 032116 (2013).
[4] L. Luneville, P. Garcia, and D. Simeone, Physical Review Letters **124**, 085701, 085701 (2020).
[5] C. A. Williams, J. M. Hyde, G. D. W. Smith, and E. A. Marquis, J Nucl Mater **412**, 100 (2011).
[6] Z. Jiao and G. S. Was, Acta Mater **59**, 1220 (2011).
[7] G. R. Odette, T. Yamamoto, T. J. Williams, R. K. Nanstad, and C. A. English, J Nucl Mater **526**, 151863, 151863 (2019).
[8] A. Chatterjee, S. Mondal, Y. Lu, Y. Wu, and J. P. Wharry, Nat. Comm. **17**, 7667 (2026).
[9] Z. Jiao and G. S. Was, Acta Mater **59**, 4467 (2011).
[10] T. P. Davis, M. A. Auger, N. Almirall, P. Hosemann, G. R. Odette, P. A. J. Bagot, M. P. Moody, and D. E. J. Armstrong, Mater. **14**, 100946 (2020).
[11] G. R. Odette, N. Almirall, P. B. Wells, and T. Yamamoto, Acta Mater **212**, 116922 (2021).
[12] J. H. Ke, H. Ke, G. R. Odette, and D. Morgan, J Nucl Mater **498**, 83 (2018).
[13] N. Saunders, R. S. Averback, and P. Bellon, Physical Review Letters, under review, arxiv.org/abs/2601.11843 (2026).
[14] R. A. Enrique, K. Nordlund, R. S. Averback, and P. Bellon, J Appl Phys **93**, 2917 (2003).
[15] R. S. Averback, P. Bellon, and S. J. Dillon, J Nucl Mater **553**, 153015 (2021).
[16] A. Verma, S. Das, Y. T. Chang, N. Saunders, D. Vizoso, R. Dingreville, M. Charpagne, R. S. Averback, and P. Bellon, Acta Mater **314**, 122346, 122346 (2026).
[17] A. Verma, Y. T. Chang, M. A. Charpagne, P. Bellon, and R. S. Averback, Scripta Mater https://doi.org/10.48550/arXiv.2602.12860, in review (2026).
[18] S. Das, A. Verma, G. F. Bouobda Moladje, Y. T. Chang, M. A. Charpagne, R. S. Averback, and P. Bellon, Commun. Mater. **6**, 39, 39 (2025).

Role of Subgrain Heterogeneous Processes in Slip Localization in Polycrystalline Metals During Cyclic Plasticity

I. J. Beyerlein, T. M. Pollock, University of California at Santa Barbara

M. P. Miller, K. E. Nygren, Cornell University

Keywords: slip localization, lattice rotation, crystal plasticity, triple junction, irreversibility

Research Scope

The overarching goal of this program is to establish a fundamental understanding of the formation and development of rare slip events that precede fatigue fracture of polycrystalline materials made for extreme environments. Fatigue of ductile polycrystalline metals is a microstructure-sensitive localization process, beginning with cyclic plasticity-driven production of substructural inhomogeneities and ending with the eventual development of cracks. While irreversible slip mechanisms under cyclic conditions have been studied extensively, designing a material for extended fatigue life is rarely performed based on knowledge of how rare slip instabilities first form and grow below the scale of the grain. While slip irreversibility has long been suggested as an important aspect of fatigue crack initiation, quantitative information on the localization processes over the large volumes of material, required to capture the relatively rare nucleation events, has been lacking. Thus, a key remaining challenge lies in identifying when, where, why and how cyclic loading leads to the formation and intensification of rare but terminal material instabilities. Such fundamental four-dimensional knowledge would be foundational for physics-based fatigue models and could guide microstructural design of more durable energy-relevant materials for future energy technologies. Our central hypothesis is that a special combination of microstructural and deformation properties of the full 3D mesoscale grain neighborhood makes a rare few slip localizations accumulate irreversibly during cyclic loading. Our project unites a suite of state-of-the-art experiments, High Energy X-ray Diffraction Microscopy (HEDM), Heaviside and High-Resolution Digital Image Correlation (H-DIC, HR-DIC), TriBeam tomography and 3D plasticity modeling techniques.

Recent Progress

The development of exceptionally intense crystallographic slip bands is widely understood to be a microstructural- and material-sensitive process. In prior cycles of this program, using a combination of experimental and computational studies, we identified triple junctions and twin boundaries as sites prone to intense slip band formation, owing to local stress concentration generated by elastic anisotropy. With H-DIC, we recently showed that slip bands are sensitive to grain size, tending to develop more in large grains and with a greater intensity than small grains.

Although this and other studies have shown that slip bands and the associated stress concentrations are sensitive to grain size, further research is needed to propose an explanation for how grain size affects the formation of slip bands.

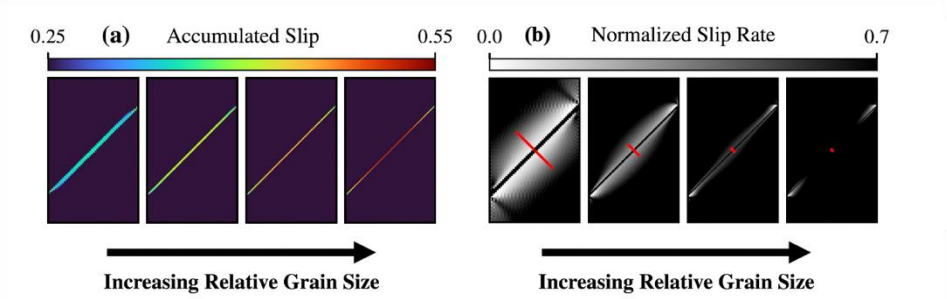

Figure 1. (a) Accumulated slip in the slip localization and (b) spatial distribution of slip rate for different grain sizes (small to four times larger moving from left to right). The smaller the grain, the wider the zone of no slip activity around the slip localization is (marked by the red).

Combining HR-DIC, H-DIC, and a full-field crystal plasticity model that permits the development of discrete, crystallographic slip bands, called SB-FFT, we aimed to identify the effect of grain size on slip band development. With all else being the same and no fitting, SB-FFT predicts that more intense bands form in larger grains (Fig. 1a). We show that both the rate and onset of slip band development correlate with the size of the host grain, with larger grains facilitating earlier and faster slip band development. This grain size effect is linked to the development of a backstress, which is most intense where the slip band intersects the grain boundaries (Fig. 1b). These results can provide insight and guidance for 2D or 3D statistical analyses of grain size effects on slip band intensity in polycrystals.

Nearly all metallic materials, whether weak or strong, pure or alloyed, and in solid solution or precipitate-hardened, deform by slip localizations. Experimental, computational, and theoretical approaches have attempted to link the propensity for slip localizations to intrinsic properties, like elasticity or stacking fault energies, or basic dislocation maneuvers, like cross slip, or microstructure features, like triple junctions. The consequences of strengthening on slip localization formation are not as clear.

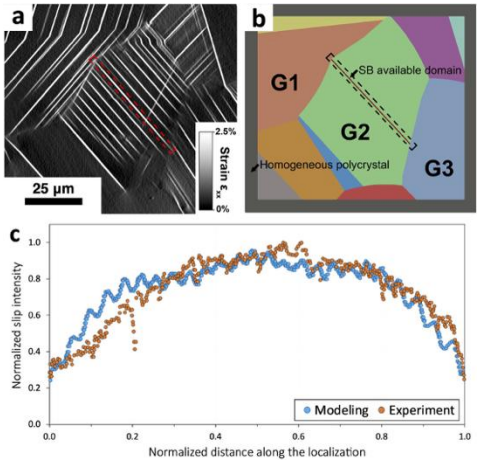

Figure 2. Experimental and modeling results of slip localizations for a Ni-based superalloy subjected to 0.61% plastic strain. (a) Strain map along the loading direction (horizontal) after 0.61% plastic strain. (b) Microstructure model created, and (c) Comparison of the normalized slip intensity between measurement and prediction.

Using a combination of computational and experiment, we aimed to elucidate the role strength plays in slip localization development. A statistical analysis of thousands of slip localizations in 15 fcc and hcp metals deformed at the same two strain levels was performed. To help isolate the process, we employed a CP micromechanical model that can simulate the

growth of a slip localization within a grain as straining proceeds and predict the local stresses and strains associated with the evolution.

For validation, in Fig. 2, we compared the slip accumulated along the slip localization measured by H-DIC and predicted in simulation at 0.61% strain. Both reveal that local slip has accumulated inhomogeneously along the length of the slip localization event. Intensity is reduced where the slip localization meets the grain boundaries and rises with distance from these junctions. The agreement achieved when modeling the evolution of only one slip localization suggests that neighboring slip localizations in the same grain affect each other negligibly.

Figure 3 shows the favorable agreement between the experimental measurements and model predictions for individual slip band intensity and per grain slip band spacing. The shared observation is that stronger metals have more intense bands and fewer bands per grain. The analysis of model predictions reveals that the stronger the metal, the faster and earlier slip localizations intensify. The relationship is attributed to the formation of a zone that surrounds the slip localization where the driving force for slip is absent. We find that the zone size is controlled by the strength of the neighboring grain. Consequently, as strength increases, slip becomes increasingly preferred within the slip localization itself and formation of other slip localizations becomes more likely further away.

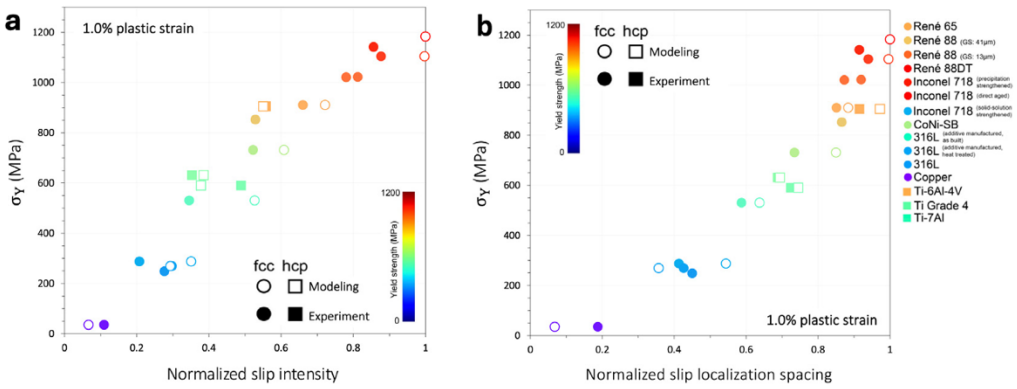

Figure 3. Experimental and modeling results in different alloys and their relationship with material yield strength. (a) for slip localization intensity (b) slip localization spacing at 1.0% plastic strain.

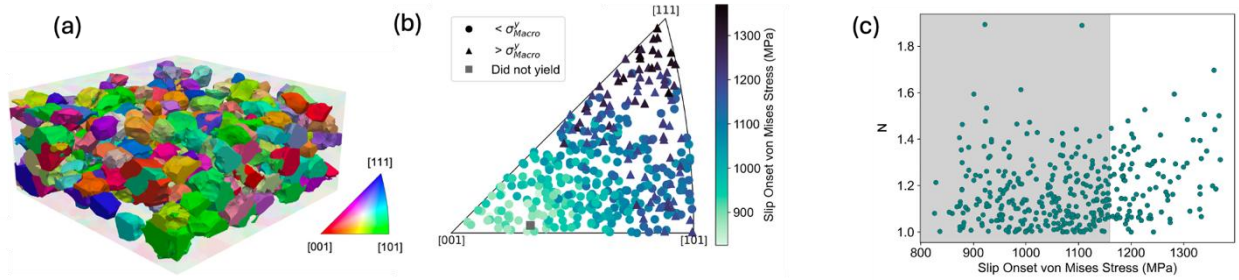

Figure 4. (a) Model polycrystal showing only the grains used in the analysis. (b) IPF colored by the grain yield stress and (c) relationship between number of active slip systems per grain and grain yield stress.

Combining high energy x-ray diffraction microscopy (HEDM) and high-fidelity microstructure CP modeling, we studied the initiation and development of slip in grains within the same polycrystal. The CP model polycrystal is built from the HEDM 3D microstructure, which enables a grain-by-grain comparison of the grain state in situ during loading (Fig. 4a). The one-to-one mapping enables investigations into the early stages of slip evolution and accumulation in hundreds of grains. We found that grain stress at which a grain slips by at least 25% of its volume varies substantially among the grains and nearly 75% of grains yield below the yield stress of the polycrystal (Fig. 4b,c). The substantial variation in grain yield stress ($\pm$ 50% of the polycrystal yield stress) is attributed to the 3D nearest neighborhood, which differ in number of grains, their size distribution, their orientations, grain boundary misorientation, and triple junction character (Fig. 4c). In satisfying compatibility with its neighborhood, a grain develops a heterogeneous stress and strain field. By this same yield criterion, most grains yield "early", at a polycrystal stress that is below the polycrystalline yield stress (Fig. 4c) and neither the grain orientation nor grain volume influences how early a grain yields. The consequence of earlier yielding is greater slip accumulation by the end straining, although the variation in amount accumulated can vary by two orders of magnitude among grains that yield at the same time. These results benefit design of high-performance materials, wherein early slip behavior can shorten fatigue life.

Future Plans

In the upcoming year, we will continue to address the question concerning the relationship between concentrated irreversible slip localization development and lattice rotation distributions in

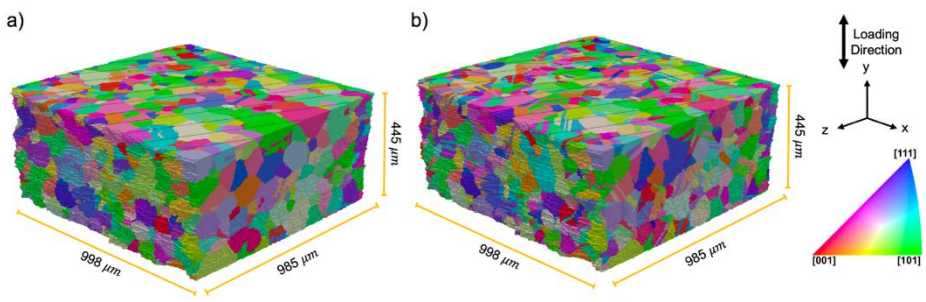

Figure 5. (a) HEDM and (b) TriBeam microstructures of the same polycrystal after fatigue.

individual grains. Analyses to date suggest that the 3D features of the nearest grain neighborhood rather than grain properties largely determine the degree of intragranular orientation spread and irreversibility of slip bands. We plan to couple in-situ fatigue via HEDM, post-fatigue TriBeam, and CP modeling to reveal the links among intragranular orientation distributions, slip activity patterns and features of the local microstructure neighborhood with the aim of gaining insight into which grains develop high levels of orientation spread. Enabling this effort is the first-time merger of the same 3D microstructure after fatigue from HEDM and TriBeam, shown in Fig. 5.

Publications (24 months)

Justine Schulte, *Multimodal Study of the Slip Activity and Intragranular Orientation Evolution in Polycrystalline Ni-based Superalloy IN718*, Ph.D. Dissertation, University of California Santa Barbara, Sept. (2026).

Madeline Vailhe, *Very High Cycle Fatigue Behavior of Alloys*, Ph.D. Dissertation, University of California Santa Barbara, June (2026).

Behnam Ahmadikia, *Modeling the Development and Transmission of Slip Bands in Polycrystalline Materials*, Ph.D. Dissertation, University of California Santa Barbara, Sept. (2024).

Jonathan Hestroffer, *Grain-scale evolution of slip activity and the role of 3D microstructure on slip localization in nickel-based superalloy IN718*, Ph.D. Dissertation, University of California Santa Barbara, Jan. (2025).

W.A. Witzen, J. D. Lamb, M. Arul Kumar, M. P. Echlin, T. M. Pollock, and I. J. Beyerlein, *Resolving crystallographic geometrically necessary dislocations in three dimensions in a hexagonal close packed titanium alloy*, Modelling Simul. Mater. Sci. Eng. **32**, 065035 (2024).

J. M. Hestroffer, J.-C. Stinville, M.-A. Charpagne, M. P. Miller, T. M. Pollock, and I. J. Beyerlein, *Subsurface microstructure effects on surface resolved slip activity*, Journal of the Mechanics and Physics of Solids, **196**, 106023 (2025).

J. M. Hestroffer, J.-C. Stinville, M.-A. Charpagne, M. P. Miller, T. M. Pollock, and I. J. Beyerlein, *Surface—subsurface grain structure relationships*, Acta Materialia, **266**, 119660 (2024).

B. Ahmadikia, D. Shadle, J.-C. Stinville, K. E. Nygren, M. Arul Kumar, T. M. Pollock, M. P. Miller, and I. J. Beyerlein, *Role of microstructure on the development of local orientation gradients in polycrystals*, Journal of Materials Research and Technology, **33**, 168-179 (2024).

J.M. Schulte , D. Shadle, K. Nygren, M.P. Miller, T.M. Pollock, and I.J. Beyerlein, *Nonnegligible influence of bending moments on grain-scale mechanics*, Integrating Materials and Manufacturing Innovation, In press (2026).

B. Ahmadikia, C. Bean, J.-C. Stinville, T. M. Pollock, and I. J. Beyerlein *Modeling the evolution of slip localization: Realization of link to material strength*, Acta Mater., **299**, 121314 (2025).

M. Vailhe, C. Torbet, F. Mignerot, and T. M. Pollock, *Very High Cycle Fatigue Behavior of Refractory Alloy C103*, International Journal of Fatigue, **201**, 109139 (2025).

B. Ahmadikia, A. L. Beyerlein, J. M. Hestroffer, M. Arul Kumar, and I. J. Beyerlein, *Designing Ti-6Al-4V microstructure for strain delocalization using neural networks*, J Mater. Sci. Mater. Theory **8**, 4 (2024).

R. D. White, B. Ahmadikia, and I. J. Beyerlein, *Grain size effects on slip band development*, Int. J. Solids Structures, **322**, 113589 (2025).

R. D. White, Y. Su, J. Kacher, and I. J. Beyerlein, *Predicting slip transmission in polycrystalline Ni*, J. Mech. Phys. Solids, **215**, 106726 (2026).

Nanomechanics and Nanometallurgy of Boundaries

Brad L. Boyce, Remi Dingreville, Doug Medlin, Stephen House

Keywords: Grain boundaries; Ratcheting; Solute; Defects; Mechanical properties

Research Scope

Grain boundaries (GBs) are ubiquitous features in polycrystalline materials, having an outsized influence on material properties in nanocrystalline metals. While it is well understood that elevated temperature stimulates GBs and can thereby destabilize nanocrystalline materials via grain growth, and thereby degrade material properties, other stimuli and microstructure defects can also induce microstructural evolution. To understand how GBs affect the stability and nanomechanics of nanocrystalline metals, this program focuses on the evolutionary nature of GBs. Specifically, we consider GBs as "living" defects whose own internal configuration and defect state evolves with external stimuli. We examine the dynamic changes that occur in GBs by intentionally disrupting their state through mechanical and other stimuli, and we manipulate that response through chemical and microstructural modifications. This effort ranges from fundamental characterization and theory of structural changes in GBs to the role of different GB defects and extended GB networks on various properties in NC metals such as fatigue and radiation tolerance. We emphasize nanocrystalline metals because of the particularly strong interplay between GBs, microstructural stability, and material properties including mechanical behavior, in such systems.

Recent Progress

The central hypothesis of this project is that grain boundaries (GBs) are not static features but "living," dynamic mechanistic entities: mechanically accelerated microstructural evolution occurs when external stimuli such as fatigue introduce additional defects that destabilize boundaries, and this evolution can be moderated by altering the thermodynamic and kinetic properties of the GB itself. Over the past year we advanced this framework along three coupled fronts—the crystallographic and chemical configuration of interfacial defects, the combinatorial synthesis of stabilized nanocrystalline alloys, and the direct in situ observation of boundary dynamics under external stimuli—while adding a new experimental capability for quantifying interfacial defect content directly from atomic-resolution imaging.

At the most fundamental level, our modeling of dislocation content and GB junctions, which serve as exemplar boundary defects, revealed that specific geometric constraints dictate defect motion. For complex faceted structures, motion is often limited because Shockley partial dislocations must change planes, forming $a/2\langle 110\rangle$ unit jogs that require the non-conservative absorption or emission of point defects in order to move [1] (Figure 1). This geometric specificity

was confirmed in boundaries vicinal to Σ33a, where stable dissociated structures exhibiting 9R stacking—characterized by a stacking fault every three {111} planes—are observed only within a narrow angular range of inclination [2]. Turning to the role of chemistry, complementary modeling of the Cu–Ag system demonstrated that chemical modification fundamentally alters the kinetics of GB defects: Ag solute atoms segregate in cluster-like patterns at glissile disconnections and impose a strong pinning effect that causes the disconnection velocity to drop sharply, particularly once the local concentration exceeds a critical value of 7–9 at.% Ag [3], extending an interfacial-defect-diagram framework developed for disconnection–solute interactions [i]. Together these findings establish how local geometric and chemical factors govern the inherent stability and mobility of boundaries and their defects under equilibrium or thermal conditions.

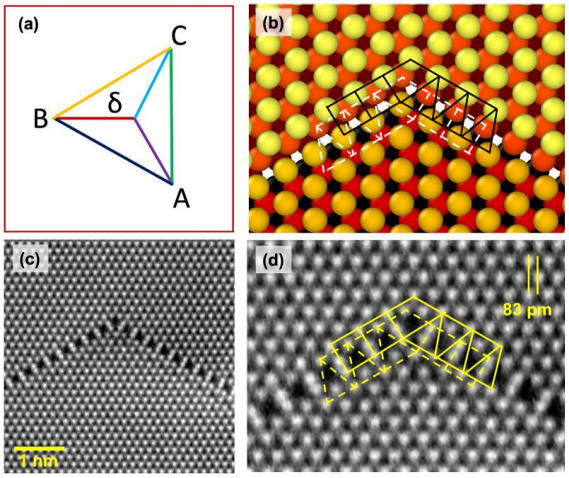

Figure 1. Grain boundary defects such as facet junctions can be described by the sum of an arrangement of dislocations. See [1].

To connect these atomistic predictions to experimental observation, we developed a method that employs the Nye tensor [ii] to quantify the dislocation content of grain-boundary line defects directly from atomic-resolution transmission electron microscopy images [4]. Whereas the Nye tensor is straightforward to apply to bulk crystals, whose natural reference state is simply the perfect lattice, its extension to interfaces requires a bicrystalline reference; we adopt the displacement-shift-complete lattice (DSCL) of the two grains in their ideal orientation for this purpose. Demonstrated on two fundamentally different defects, a disconnection at a Σ3{111} twin boundary and two junctions formed at intersecting Σ3{112} facets in face-centered-cubic Au, the method returns total Burgers-vector content validated against conventional Burgers-circuit analysis, while additionally resolving the local spatial distribution of dislocation content in the immediate neighborhood of the defect cores. Because it can be automated across large interfacial regions now routinely accessible to modern microscopy, this approach overcomes the limitations of manual circuit mapping and provides direct experimental access to the interfacial defects that modeling identifies as rate-controlling.

Building on this understanding of how nanoscale features stabilize boundaries, we drew on high-throughput thin-film libraries to advance the broader goal of understanding stability trends across nanocrystalline microstructures [5]. This effort systematically identified how composition governs the mechanical and electrical behavior of individual boundaries and of the GB network. In Pt–Au, exceptional hardness exceeding 7 GPa was found to arise not solely from grain size or solute strengthening, but crucially from nanoscale composition modulations acting as a distinct and non-negligible strengthening source [6]. In Cu–Ag films, reducing the argon working-gas

pressure from 1.3 to 0.4 Pa raised the kinetic energy of the sputtered atoms and produced denser, harder films, with hardness consistently above 7 GPa for Cu-rich compositions. Structural characterization confirmed complex compositional architectures, including solute segregation to boundaries at high solvent content and periodic intragranular modulations at intermediate compositions, demonstrating that deposition conditions can tune the internal chemical structure needed for stable, high-performance behavior [7].

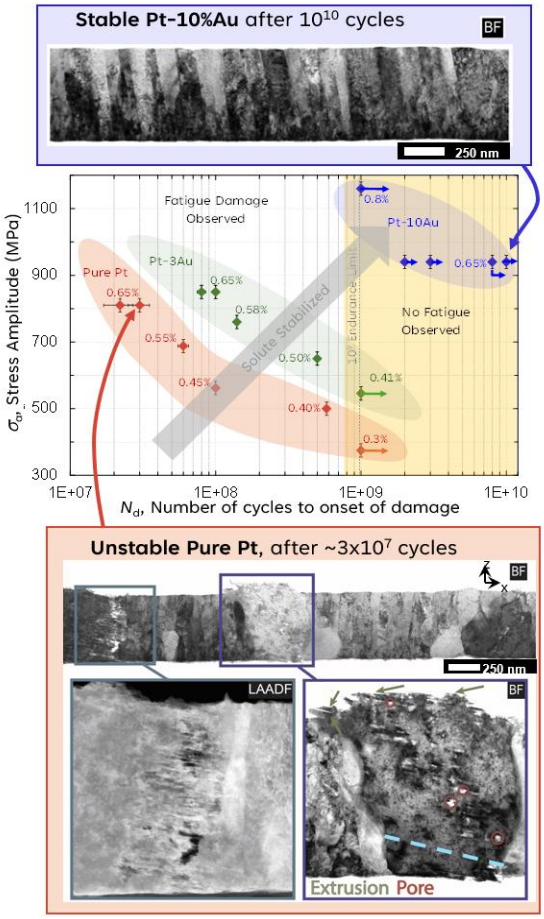

Figure 2. Stabilized binary nanocrystalline alloys exhibit substantial fatigue enhancement attributed to improved grain boundary stability. See [8].

These threads converge in a demonstration that solute-stabilized boundaries can suppress fatigue damage outright [8]. Using a silicon MEMS microresonator to access the gigacycle or very-high-cycle regime, we found that boundary-stabilized nanocrystalline Pt–10 at.% Au sustained no detectable fatigue damage even after 10^{10} cycles at stress amplitudes above 1 GPa, whereas pure Pt and Pt–3Au developed surface extrusions and cracks after roughly 6×10^{7} and 1.2×10^{8} cycles, respectively (Figure 2). Atomistic simulations spanning 1000–1500 fatigue cycles reproduced the underlying mechanism: fatigue drives asymmetric "Brownian ratcheting" of triple junctions and disconnections [iii] that accelerates grain growth, and even modest solute additions slow this migration by more than an order of magnitude. Notably, compositional mapping revealed a nearly uniform Au distribution rather than the anticipated boundary enrichment, yet the several percent of Au retained at the boundaries remained sufficient to pin defects and stabilize the microstructure, indicating that stabilization of interfacial defects, rather than classical solute strengthening, underlies the observed fatigue enhancement.

Finally, in situ observation clarified both the kinetics and the driving forces of boundary evolution under mechanical cycling. In situ SEM/EBSD studies of ⟨111⟩-textured Au films with grain sizes of 90, 120, and 710 nm established that abnormal grain growth precedes extrusion formation [9], consistent with earlier evidence that abnormal grain growth precedes fatigue crack initiation in nanocrystalline metals [iv]. The in-situ SEM observations also identified the low-strain driving force for boundary migration: where cyclic plasticity is limited, coarsening is biased

by anisotropic elastic strain-energy density, preferentially growing in-plane ⟨101⟩ and ⟨112⟩ grain families; at higher amplitudes, or once grains exceed a transition size of ~2–3 μm, plasticity-coupled coarsening dominates and the orientation selectivity is lost [10].

Together these results extend the "living boundary" framework across scales—from the atomic-scale configuration of individual interfacial defects, through the mesoscale driving forces that mobilize them, to the macroscopic demonstration that chemically stabilized boundaries can render a nanostructured metal effectively immune to fatigue.

Future Plans

Our continuing work on "Nanomechanics and Nanometallurgy of Boundaries" treats GBs as "living" defects that evolve under external stimuli. Having established a Nye-tensor framework for quantifying the edge-dislocation content and core structure of line defects, we will now apply it to resolve how defect character, particularly disconnections, governs boundary response under controlled loading. Leveraging in situ TEM tensile bars subjected to prescribed cyclic and thermal histories, we will observe GB ratcheting directly, contrasting the thermal-cycling and stress-cycling response of individual boundaries and testing whether prior thermal treatments that relax GB structure alter the subsequent ratcheting and coarsening behavior under mechanical cycling.

We continue to emphasize GB ratcheting and the abnormal grain growth it accelerates under cyclic loading, using solute strategies to tune disconnection mobility. Building on the demonstrated fatigue immunity of solute-stabilized Pt–Au, we will extend these strategies to Cu–Ag (a eutectic alloy which may elicit further non-equilibrium responses), elucidating the solute-stabilized nanostructures and coarsening-suppressed damage pathways that operate under very-high-cycle fatigue. Insights into stress-induced segregation motivate deeper study of how film stress, controlled via deposition parameters such as Ar pressure, adatom kinetic energy, and incidence angle, can be manipulated to tune segregation architectures, ranging from GB enrichment to intragranular composition modulation, and thereby enhance fatigue performance. Rigorously characterizing these architectures with methods scalable beyond STEM-EDS, including enhanced XRD analysis, remains central to completing the process-structure-property picture. Complementary libraries of new binaries, Pt–Ni (high hardness yet minimal segregation), Cu–Ag, and Cu–Al (tailorable stacking-fault energy and disconnection structure), will test the generality of GB stabilization.

Finally, we will pursue GB response under combined stimuli, addressing emergent and antagonistic mechanisms. Moving beyond chemical stabilization, we will investigate the nanovoids nearly always present in PVD films as controllable sinks that trap cyclic defect content and mitigate mechanically accelerated grain growth. Because void populations can be tuned via Ar pressure, this experimental effort, enabled by high-throughput MEMS fatigue testing, will be complemented by multi-phase-field modeling coupled to cyclic plasticity.

References

[i] C. Hu, S. Berbenni, D. L. Medlin, and R. Dingreville, Discontinuous segregation patterning across disconnections, Acta Materialia 246, 118724 (2023).

[ii] J. F. Nye, Some geometrical relations in dislocated crystals, Acta Metallurgica 1, 153 (1953).

[iii] C. Qiu, M. Punke, Y. Tian, Y. Han, S. Wang, Y. Su, M. Salvalaglio, X. Pan, D. J. Srolovitz, and J. Han, Grain boundaries are Brownian ratchets, Science 385, 980 (2024).

[iv] T. A. Furnish, D. C. Bufford, F. Ren, A. Mehta, K. Hattar, and B. L. Boyce, Evidence that abnormal grain growth precedes fatigue crack initiation in nanocrystalline Ni-Fe, Scripta Materialia 143, 15 (2018).

Publications

1. D. L. Medlin, E. Y. Chen, J. Nathaniel II, R. Dingreville, and C. B. Carter, Atomic-scale arrangement of dislocations at grain-boundary facet junctions, *Acta Materialia* 292, 121068 (2025).
2. A. Hinojos, D. Vizoso, D. Adams, R. Dingreville, and D. L. Medlin, On the distribution of stacking faults at dissociated medium angle grain boundaries: crystallographic geometry and metastability, *Acta Materialia* 300, 121421 (2025).
3. C. Hu, D. L. Medlin, and R. Dingreville, Stability and mobility of disconnections in solute atmospheres: insights from interfacial phase diagrams, *Physical Review Letters* 134, 016202 (2025).
4. I. S. Winter, A. Hinojos, J. E. Nathaniel II, and D. L. Medlin, Quantifying the dislocation content of atomically resolved grain boundary line defects using the Nye tensor, *Journal of Applied Physics* 140, 015304 (2026).
5. S. Desai, M. Jain, S. J. Addamane, D. P. Adams, R. Dingreville, F. W. DelRio, and B. L. Boyce, Navigating high-dimensional process-structure-property relations in nanocrystalline Pt-Au alloys with machine learning, *Materials & Design* 248, 113494 (2024).
6. M. Jain, P. Kotula, K. Dorman, S. Desai, S. Addamane, D. Adams, F. DelRio, R. Dingreville, and B. Boyce, Enhanced strengthening via composition modulation in nanocrystalline Pt-Au, *Scripta Materialia* 271, 116999 (2025).
7. K. R. Dorman, N. Bianco, R. Kothari, C. Sobczak, S. Desai, J. O. Custer, S. Addamane, M. Jain, C. Harris, P. G. Kotula, A. Hinojos, M. A. Rodriguez, B. L. Boyce, R. Dingreville, and D. P. Adams, High-throughput multimodal exploration of a nanocrystalline Cu-Ag library, *Thin Solid Films* 822, 140688 (2025).
8. M. Jain, D. Vizoso, A. Hinojos, A. Barrios, K. Dorman, Y. Yang, D. P. Adams, K. Hattar, D. L. Medlin, O. Pierron, R. Dingreville, and B. Boyce, Putting fatigue to rest via solute-pinned boundaries, *Materials Today* 93, 103187 (2026).
9. A. Baker, K. R. Dorman, K. Hattar, S. D. House, and B. L. Boyce, Controlling fatigue cracking in the transmission electron microscope, *Small Methods* (2025).
10. Y. Yang, A. Barrios, Q. Li, Y. Liu, M. Jain, V. Meyers, T. Zhu, B. L. Boyce, and O. Pierron, Elucidating the origins of grain growth in the high cycle fatigue degradation of Au thin films, *Acta Materialia* 313, 122301 (2026).

Effect of Gradient Architectures on the Strength, Deformation, and Failure of Nanoglasses

Paulo S. Branicio, University of Southern California

Keywords: nanoglasses, gradient architectures, glass-glass interfaces, machine learning, molecular dynamics

Research Scope

Nanoglasses (NGs) are amorphous alloys assembled from glassy nanoparticles (NPs), in which nanometer-sized glassy grains are joined by a percolating network of glass-glass interfaces (GGIs). GGIs delocalize plastic flow that would otherwise collapse into a single catastrophic shear band, giving NGs strength-ductility combinations unreachable by monolithic metallic glasses (MGs). Gradient nanoglasses (GNGs), in which glassy grain size varies continuously through the sample, extend the concept by placing regions of dissimilar deformation resistance in close contact. This program aims to establish an atomistic-to-nanoscale understanding of how gradient architectures control strength, deformation, and failure in NGs, and to convert it into design principles for amorphous alloys with tailored mechanical response.

The working hypothesis is that atomic mobility and stress fields at GGIs couple through two mechanisms. First, the activation energy for atomic rearrangement at a GGI is grain-size dependent, because the free volume and compositional heterogeneity of an interface are inherited from the NPs that formed it, establishing size-dependent thresholds for the onset of plasticity. Second, in a gradient structure this size dependence generates a spatially varying energy landscape for shear transformation zones (STZs), enabling controlled strain delocalization through hierarchical activation of deformation pathways. We further posit that impact-driven consolidation of compositionally tuned NPs produces GGIs with modified barriers and enhanced mobility, yielding deformation mechanisms unavailable to conventionally consolidated NGs.

Four aims are pursued: (1) generation and characterization of relaxed GNG nanostructures across CuZr, NiZr, and NiNb; (2) impact-based synthesis of NG and GNG structures with controllable heterogeneity; (3) AI-driven design using generative models, graph neural networks (GNNs), and Bayesian optimization; and (4) evaluation of mechanical behavior and deformation mechanisms by large-scale molecular dynamics (MD). Recent accomplishments are summarized below.

Recent Progress

Activation-energy landscape of glass-glass interfaces. The mechanical response of an NG is set by the barriers resisting local atomic rearrangement, yet spatially resolved measurements of those barriers at GGIs have been lacking. We combined MD simulations of $Cu_{64}Zr_{36}$ with the activation-relaxation technique (ART) to explicitly sample thermally activated events and map the potential-energy landscape (PEL) of NGs with distinct interfacial geometries [1]. Two archetypes with well-controlled GGIs were built: a 7 nm spherical particle (SP) and a cubic block (CB), each relaxed with free surfaces and then consolidated at 50 K to form SP-GGI and CB-GGI (Fig. 1).

Both precursors develop a Cu-rich surface layer during relaxation; consolidation buries it, and we find the segregated Cu is not erased but persists as a diffuse compositional enrichment at the interface.

Spatially resolved activation-energy distributions reveal that GGIs host a persistent population of low-barrier excitations largely absent from the bulk-like cores: mean barriers fall from about 1.7–1.8 eV in bulk-like cores to roughly 1.3 eV at the interfaces at zero strain. Strain amplifies the low-energy tail, but the onset of plasticity is dictated by the intrinsic energetic softness of the interfaces rather than by strain-induced softening. This preexisting population of soft sites suppresses abrupt shear localization, curtailing the linear elastic regime and distributing deformation. Local von Mises strain maps (Fig. 2) confirm the mechanism: plasticity nucleates and concentrates at GGIs, whereas the reference bulk MG retains a well-defined elastic regime before localizing. The magnitude of the response is governed by the interfacial volume fraction, while the deformation mechanism itself remains invariant, establishing GGIs as preferred nucleation sites for shear transformations.

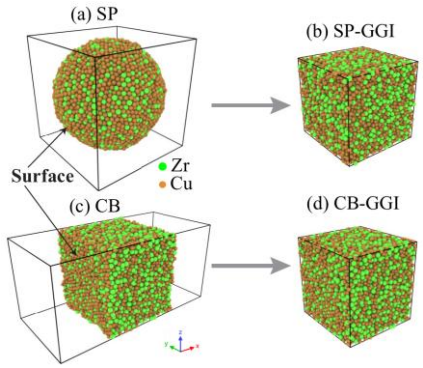

Fig. 1. $Cu_{64}Zr_{36}$ nanoglass models with glass-glass interfaces (GGIs). (a), (b) Spherical particle (SP) before and after isotropic compression. (c), (d) Cubic block (CB) before and after uniaxial compression. Adapted from Ref. 1.

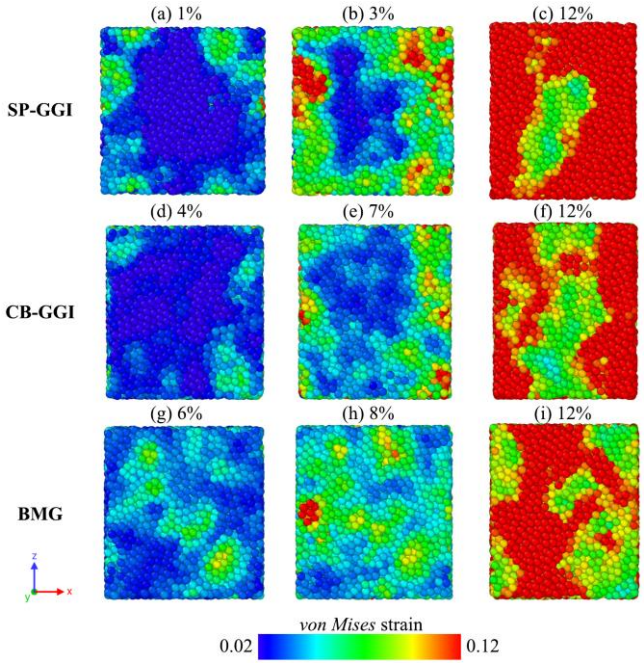

Fig. 2. Local von Mises strain maps under compression for SP-GGI, CB-GGI, and a reference bulk metallic glass (BMG): (a), (d), (g) preyield; (b), (e), (h) postyield; (c), (f), (i) larger strain. Plasticity nucleates and concentrates at GGIs in the nanoglasses. Adapted from Ref. 1.

Quantifying the structural memory of metallic glasses. Designing gradient architectures presupposes that a glassy state can be identified from structure alone, yet the absence of long-range periodicity and the finite sampling of medium-range environments obscure how thermal history is encoded. We define the representative information volume (RIV) as the smallest sampling volume that allows the thermal history of a glassy state to be identified with low error from its atomic

configuration [2]. MD simulations of $Cu_{64}Zr_{36}$ were run for five finite-rate quenches from 10^{13} to 10^{9} K/s, plus a direct-quench limiting state obtained by coupling the melt directly to a 50 K thermostat, giving six classes. GNNs trained on cubic cells of increasing size resolve these classes with accuracy rising from 78.7% at L = 2.2 nm to 91.9% at 3.2 nm and 99.8% at 4.4 nm (Fig. 3).

Composite-graph controls and descriptor baselines show that this crossover is dominated by variance reduction from sampling many local environments rather than by a single emergent long-range motif; the finite-size scaling therefore defines an operational sampling length, not a thermodynamic correlation length. Confusion matrices and t-SNE projections of the hidden-layer embeddings sharpen correspondingly, and the GNN outperforms logistic-regression and random-forest baselines built on Voronoi motif fractions at every box length. The consequence for this program is direct: the RIV is comparable to the glassy grain sizes used in NG and GNG design [3], so a nanoglass grain is close to the smallest volume in which a distinct thermal state can be said to exist, setting a floor on the length scale over which gradient architectures can meaningfully vary.

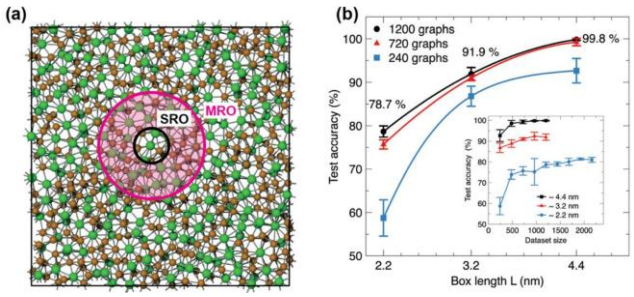

Fig. 3. Length scale for uniquely distinguishing $Cu_{64}Zr_{36}$ glassy states with a graph neural network (GNN). (a) Representative configuration showing the short-range order (SRO, first shell, r ≈ 3 Å) and the medium-range order (MRO) environment accessible to the GNN by message passing (r ≈ 9 Å). (b) Cross-validated test accuracy versus cubic box length L; curves are different training-set sizes and error bars denote the standard deviation over 5 folds. Adapted from Ref. 2.

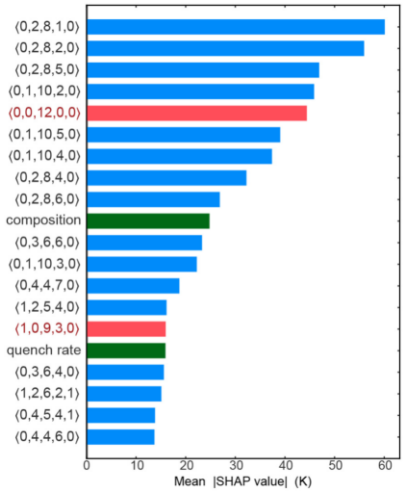

Fig. 4. Global feature importance from mean absolute SHAP values for the temperature-prediction network. Near-icosahedral Voronoi motifs dominate; the full icosahedron (0,0,12,0,0) and (1,0,9,3,0) are red, and the non-structural composition and quench-rate inputs green. Adapted from Ref. 5.

AI-driven characterization and design of glassy states. The graph-based analysis above builds on graph convolutional neural networks developed earlier in this program, spanning GraphSAGE, graph attention, and graph isomorphism architectures, which classify CuZr MG states directly from atomic configurations generated across a range of quench rates [4].

Explainable machine learning then identified which motifs carry the thermodynamic information [5]. A fully connected neural network trained on Voronoi motif populations across the Cu-Zr glass-forming range predicts the effective temperature of a configuration with a mean absolute error of 19.89 K over a 50–2000 K range, with $R^2 = 0.997$. SHAP analysis (Fig. 4) shows

the prediction is dominated not by a single descriptor but by a coupled family of near-icosahedral motifs with coordination numbers 11 to 13; the canonical full icosahedron ranks only fifth, while explicit composition and quench-rate inputs rank tenth and sixteenth. The model infers thermal history from local structure rather than from processing metadata. In parallel, we are developing diffusion models that generate MG configurations on demand at arbitrary quench rate, and foundation machine-learning interatomic potentials (MLIPs) for CuZr, NiZr, and NiNb.

Future Plans

Work in the coming period advances all four aims. For Aim 1, we will complete regeneration of the MG NP library with a revised embedded-atom potential, a necessary correction since preliminary tests with the previous potential produced anomalous mechanical behavior, and extend NP synthesis to NiZr and NiNb. These NPs will be assembled into GNG models whose GGI structure, composition, and free-volume distribution will be characterized against grain-size gradient and alloy composition, testing whether the size-dependent interfacial softness measured in CuZr is general. For Aim 2, we will begin impact-based synthesis simulations, depositing and consolidating glassy NPs at controlled impact energies and mapping how impact velocity and NP size distribution govern atomic rearrangement, GGI formation, and residual relaxation. Impact-driven consolidation accesses transient states unavailable to isothermal cold compression and has a direct experimental analogue.

For Aim 3, we will finalize the diffusion models and foundation MLIPs and close the design loop by coupling GNN surrogates of mechanical response to Bayesian optimization over gradient architectures. For Aim 4, we will conduct large-scale tensile, compressive, and nanoindentation simulations on the new GNG structures, quantifying Young's modulus, yield and ultimate strength, and fracture behavior while resolving STZ dynamics and strain delocalization. The spatially resolved activation-energy analysis demonstrated here will be extended to graded structures to test the central hypothesis that a grain-size gradient produces a graded PEL that activates deformation pathways hierarchically.

References

1. A. Liang, E. J. Gurniak, and P. S. Branicio, From surface segregation to glass-glass interfaces: Composition, activation-energy landscapes, and strength in CuZr nanoglasses, Physical Review Materials 10, 053604 (2026).
2. E. J. Gurniak and P. S. Branicio, Quantifying the structural memory of metallic glasses with graph neural networks, Digital Discovery, accepted (2026).
3. P. S. Joshi, X. Ren, and P. S. Branicio, Tailoring Cu-Zr gradient nanoglass structures: Influence of nanoparticle size and cooling rates on glass-glass interfaces, Intermetallics 178, 108633 (2025).
4. E. J. Gurniak, S. Yuan, X. Ren, and P. S. Branicio, Harnessing graph convolutional neural networks for identification of glassy states in metallic glasses, Computational Materials Science 244, 113257 (2024).
5. J. Wang, S. Yuan, and P. S. Branicio, Explainable machine learning reveals that local structural motifs encode the thermodynamic state across the Cu-Zr metallic glass-forming range, Computational Materials Science 272, 114836 (2026).

Publications

Publications from the previous two years supported by BES Award DE-SC0020295.

1. A. Liang, E. J. Gurniak, and P. S. Branicio, From surface segregation to glass-glass interfaces: Composition, activation-energy landscapes, and strength in CuZr nanoglasses, Physical Review Materials 10, 053604 (2026).
2. J. Wang, S. Yuan, and P. S. Branicio, Explainable machine learning reveals that local structural motifs encode the thermodynamic state across the Cu-Zr metallic glass-forming range, Computational Materials Science 272, 114836 (2026).
3. P. S. Joshi, X. Ren, and P. S. Branicio, Tailoring Cu-Zr gradient nanoglass structures: Influence of nanoparticle size and cooling rates on glass-glass interfaces, Intermetallics 178, 108633 (2025).
4. E. J. Gurniak, S. Yuan, X. Ren, and P. S. Branicio, Harnessing graph convolutional neural networks for identification of glassy states in metallic glasses, Computational Materials Science 244, 113257 (2024).
5. X. Ren, S. Yuan, E. J. Gurniak, and P. S. Branicio, Structural and thermodynamic characterization of CuZr metallic glass nanoparticles: Insights from atomistic simulations, Physical Review Materials 8, 046001 (2024).
6. E. J. Gurniak and P. S. Branicio, Quantifying the structural memory of metallic glasses with graph neural networks, Digital Discovery, accepted (2026)

Beyond Shear: Improving the Prediction of Plastic Deformation Activation in HCP Materials

Ashley Bucsek (University of Michigan); Huseyin Sehitoglu (University of Illinois at Urbana-Champaign)

Keywords: plastic deformation, hcp materials, titanium, non-Schmid behavior, X-ray microscopy

Research Scope

The advancement of lightweight structural metals remains one of the greatest potential contributions of the materials community to an energy-efficient future. Many lightweight metals have hexagonal close-packed (hcp) crystal structures and require improvements to ductility and formability while maintaining strength. Tuning the activation energies associated with competing plastic deformation mechanisms is a forward-looking methodology for these improvements, but there is a fundamental gap in our ability to predict and measure the activation of plastic deformation in hcp materials due to non-Schmid behavior. Under non-Schmid behavior, activation depends on additional stress components (i.e., beyond the shear stress). Because activation is non-Schmid, the activation threshold cannot be represented by a unique, orientation-independent CRSS. The goal of this program is to improve our understanding of the onset of plastic deformation in hcp materials by: (1) predicting the critical resolved shear stress (CRSS) for slip/twinning using a multiscale, atomistically informed framework that revisit atomic-scale configurations and energy barriers, (2) nanoscale experimental validation resolving individual dislocations, and (3) microscale experimental validation resolving subgrain-scale stress tensors.

Previously, we established an integrated theoretical-experimental framework, starting with slip in hcp titanium (Ti), including: (1) Predicted ab-initio CRSS values for dislocation slip at room temperature featuring a new fundamental understanding of the non-planar core structure under the influence of non-Schmid stresses; (2) Experimentally validated the CRSS predictions at the nanoscale using in-situ transmission electron microscopy (TEM); (3) Experimentally validated the CRSS predictions at the microscale using in-situ point-focused high-energy diffraction microscopy (pf-HEDM) at the Advanced Photon Source (APS). During the prior award period, we established this framework for slip in hcp Ti. During the current reporting period, we are extending it to cross-slip, deformation twinning in Ti and Mg alloys, and solute/order effects in Ti–Al alloys.

Recent Progress

Our research centers around the ability to predict non-Schmid plastic deformation activation, validated using a campaign of advanced in-situ experiments spanning from the nanoscale to the microscale. Our most recent efforts feature the extension of this theoretical-experimental framework to cross-slip, an important and pervasive source of non-Schmid behavior in hcp materials. We hypothesize that, when cross-slip occurs, the dislocation cores overlap and result in CRSS values that are much higher than the free glide case, as well as a CRSS dependence on orientation with some orientations not permitting cross-slip.

Applying our framework to cross-slip has enabled us to calculate cross-slip CRSS values that capture the orientation dependence of the cross-slip stress [1]. DFT-derived fault-energy landscapes are combined with anisotropic elasticity and an explicit dislocation-core model to predict activation thresholds without fitting to mechanical-test data. The theory also enables accurate calculation of the cross-slip energy barrier across temperatures and loading directions, reproducing the non-Schmid behavior of the mechanism. Furthermore, it explicitly incorporates anisotropic elastic interactions between partials, whereas much of the existing literature relies on isotropic approximations [2]. Together, these features constitute significant improvements over existing approaches and establish a foundation for analyzing cross-slip mechanisms across a broad range of materials, slip systems, and temperatures. For example, **Fig. 1** shows the cross-slipping process under a $[\bar{1}2\bar{1}0]$ loading direction, which is the same loading direction as was tested using in-situ TEM, discussed below [1]. The RSS, $\tau^{\pi\to \mathrm{Pr}}$, and the change in total energy, ΔE_{total}, are shown in **Fig. 1**. In the case of misfit energy, there are multiple cores; in the case of elastic energy, there are self-energy and interaction-energy terms. Starting from the locked pyramidal configuration, strongly interacting (superimposed) cores transition to a single prismatic fault with finite separation. The CRSS is governed by Stages (III)-(IV).

At the nanoscale, cross-slipping dislocations between the pyramidal-I and prismatic planes were observed experimentally using in-situ TEM with a specialized push-to-pull (PTP) device [1]. This technique has several advantages that make it suitable for studying deformation characteristics of materials to evaluate the precise critical stress values of the activated systems. First, the real-time observation of individual dislocations using electron transparent samples enables accurate identification of slip initiation. Moreover, extracting site-specific micro tensile samples allows for precise control over the Schmid factors in various systems, enabling independently study of a single system and identify cross slip

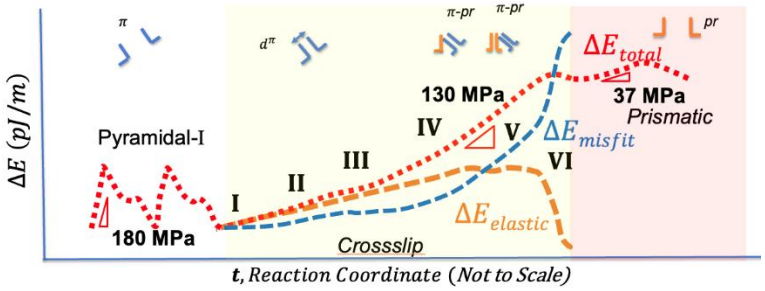

Fig. 1. Determination of CRSS for cross-slip and the evolution of total energy, misfit, and elastic energy components during pyramidal-to-prismatic transition.

activation. Before loading, we observed a sessile straight screw segment residing in the pyramidal plane, with a segment in the prismatic plane that appears more curved. This is due to the lower frictional forces on the prismatic plane compared to the pyramidal. As the load increases and stress reaches 110 MPa (resolved; see red star in **Fig. 2**), the dislocation becomes unlocked and glides in the prismatic plane, closely matching the model prediction of 130 MPa.

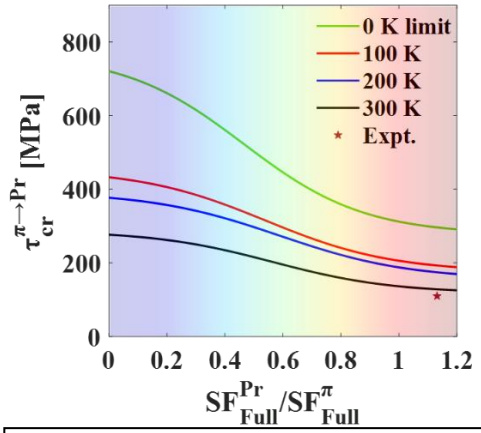

Fig. 2. Prismatic-to-pyramidal cross-slip CRSS vs. the Schmid factor ratio of prismatic/pyramidal, highlighting the orientation dependence of cross-slip. The red star is the in-situ TEM experiment that pinpoints the occurrence of cross-slip at 110 MPa, closely matching the predicted 130 MPa.

At the microscale, we used in-situ pf-HEDM at the APS to measure intragranular cross-slip CRSS values [6,7]. That is, by mapping orientation and elastic strain with subgrain-scale spatial resolution, these measurements are sensitive to intragranular stress concentrations. In addition, by probing many grains simultaneously, we can also investigate orientation dependence. The results are summarized in **Fig. 3**. One of the advantages of the pf-HEDM approach is that it allows us to measure a *CRSS distribution* rather than a single value (**Fig. 3a**). While the CRSS on the first peak had an average value of 42 MPa (corresponding to easy glide on the prismatic plane), a small second peak can also be observed at 106 MPa, closely matching the TEM measurement (110 MPa) and model predictions (130 MPa). The secondary population near 106 MPa is consistent with the pyramidal-I to prismatic cross-slip thresholds measured by TEM and predicted by the model, wherein the CRSS is elevated due to the effect of the pyramidal CRSS [7]. Finally, **Fig. 3b** shows the predicted orientation dependence of pyramidal-I to prismatic cross-slip, and **Fig. 3c** shows the experimentally measured orientation dependence. **Fig. 3c** shows only voxels belonging to the high-RSS population. These locations occur at

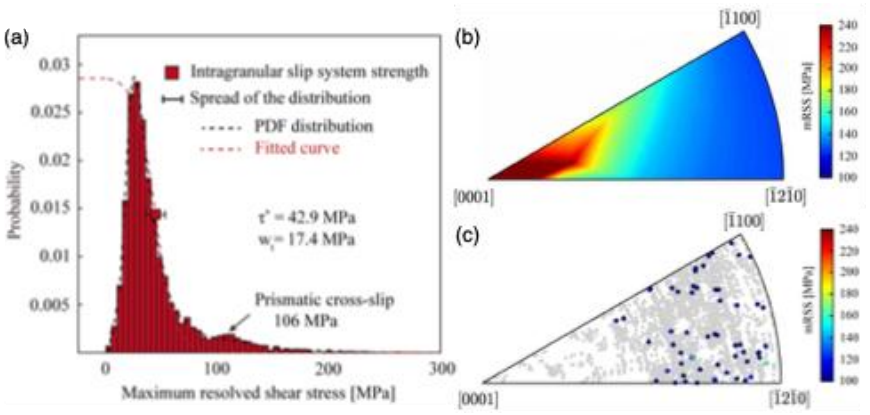

Fig. 3. In-situ pf-HEDM experiments during tensile loading of polycrystalline Ti showing (a) the distribution of prismatic mRSS values. The arrow points to a small population of orientations slipping at ~106 MPa, consistent with pyramidal-to-prismatic cross-slip. (b) Predicted CRSS values for pyramidal-to-prismatic cross-slip vs. (c) experimental CRSS values, highlighting the agreement between theory and experiment and the orientation dependence of cross-slip activation. (Gray = orientations with CRSS values below 80 MPa.)

orientations for which the model predicts relatively low cross-slip activation thresholds, suggesting that these orientations may cross-slip while the barrier is too high for others. The values also range from 100–130 MPa, closely matching the 110–130 MPa predicted for these orientations.

Future Plans

In the near-term, we are continuing to extend our integrated theoretical-experimental framework beyond pure metals to include solute effects. In Ti-Al alloys, coherent α_2 domains strongly influence the mechanical response. We combine in-situ TEM with a Wigner-Seitz-cell framework that incorporates generalized stacking fault energies, anisotropic elasticity, and dislocation core calculations to determine the CRSS for basal slip in Ti-7Al [3, 4]. The loss of ordering promotes repeated glide on previously activated basal slip bands, leading to planar slip localization and softening. Unlike classical APB-based strengthening models, the present framework derives strengthening from the complete generalized stacking fault energy landscape, including unstable stacking fault energies. The formulation is being further generalized to account for basal-prismatic screw-dislocation core spreading, providing orientation-dependent CRSS predictions.

We are also extending our framework to include deformation twinning in hcp-Ti, resolving key factors that contribute to CRSS [5]. We analyze the discrete lattice offsets defining the coherent twin boundary structure, which cannot be assumed a priori11/9/2026 8:53:00 AM since an incorrect boundary structure leads directly to erroneous twin boundary energies. We are determining the minimum-energy pathway (MEP) and identifying the shear-shuffle partitioning during twin growth. To validate the theory, in-situ TEM loading experiments are designed to activate specific twin systems on carefully oriented samples. These nanoscale experiments are complemented by microscale experiments: We have also successfully conducted in-situ pf-HEDM experiments to measure intragranular CRSS values for twinning, extending beyond Ti to Mg and Mg-Al alloys.

These extensions of our framework demonstrate its widespread usefulness in providing, predicting, and measuring accurate CRSS distributions for non-Schmid plastic deformation in hcp materials. More reliable activation laws can improve crystal-plasticity predictions used in forming and fatigue models for hcp Ti, Mg, and Zr alloys. Such models can reduce trial-and-error alloy/process development and enable lighter structural components without sacrificing durability.

References

[1] T.B. Celebi, O.K. Celebi, D. You, A.S.K. Mohammed, A. Bucsek, H. Sehitoglu, Cross-slip and Easy-glide CRSS in Titanium: Theoretical Predictions and in-situ TEM Measurements, International Journal of Plasticity (2026) 104605.
[2] O.K. Celebi, G. Gengor, D. You, A.S.K. Mohammed, A. Bucsek, H. Sehitoglu, Distorted dislocation cores and asymmetric glide resistances in titanium, Acta Materialia 274 (2024) 119967.
[3] T.B. Celebi, Daegun You, Orcun Koray Celebi, Ahmed Sameer Khan Mohammed,Ashley Bucsek, Huseyin Sehitoglu, Linking α_2-Domain Shearing to Slip Localization and Cyclic Softening in Ti–7Al, Submitted for Publication (2026).
[4] D. You, O.K. Celebi, A.S.K. Mohammed, A. Bucsek, H. Sehitoglu, The derivation of CRSS in pure Ti and Ti-Al alloys, International Journal of Plasticity 184 (2025) 104187.
[5] T.B. Celebi, Daegun You, Sena Pekol, Orcun Koray Celebi, Ahmed Sameer Khan Mohammed, Wenxi Li, Ashley Bucsek, Huseyin Sehitoglu, Distinct Structural and Energetic Origins of Compression Twinning in HCP Metals, Submitted for Publication (2026).
[6] W. Li, H. Sharma, P. Kenesei, S. Ravi, H. Sehitoglu, and A. Bucsek, Resolving intragranular stress fields in plastically deformed titanium using point-focused high-energy diffraction microscopy, J. Mater. Res. 1 (2023).
[7] W. Li et al., Intragranular critical resolved shear stress distributions in polycrystalline titanium using in-situ point-focused high-energy diffraction microscopy, Acta Mater. 122217 (2026).

Publications

[1] T.B. Celebi, O.K. Celebi, D. You, A.S.K. Mohammed, A. Bucsek, H. Sehitoglu, Cross-slip and Easy-glide CRSS in Titanium: Theoretical Predictions and in-situ TEM Measurements, International Journal of Plasticity (2026) 104605.
[2] O.K. Celebi, G. Gengor, D. You, A.S.K. Mohammed, A. Bucsek, H. Sehitoglu, Distorted dislocation cores and asymmetric glide resistances in titanium, Acta Materialia 274 (2024) 119967.
[3] T.B. Celebi, Daegun You, Orcun Koray Celebi, Ahmed Sameer Khan Mohammed,Ashley Bucsek, Huseyin Sehitoglu, Linking α_2-Domain Shearing to Slip Localization and Cyclic Softening in Ti–7Al, Submitted for Publication (2026).
[4] D. You, O.K. Celebi, A.S.K. Mohammed, A. Bucsek, H. Sehitoglu, The derivation of CRSS in pure Ti and Ti-Al alloys, International Journal of Plasticity 184 (2025) 104187.
[5] T.B. Celebi, Daegun You, Sena Pekol, Orcun Koray Celebi, Ahmed Sameer Khan Mohammed, Wenxi Li, Ashley Bucsek, Huseyin Sehitoglu, Distinct Structural and Energetic Origins of Compression Twinning in HCP Metals, Submitted for Publication (2026).
[6] W. Li, H. Sharma, P. Kenesei, S. Ravi, H. Sehitoglu, and A. Bucsek, Resolving intragranular stress fields in plastically deformed titanium using point-focused high-energy diffraction microscopy, J. Mater. Res. 1 (2023).
[7] W. Li et al., Intragranular critical resolved shear stress distributions in polycrystalline titanium using in-situ point-focused high-energy diffraction microscopy, Acta Mater. 122217 (2026).

AI-enabled real-time reconstructions and interpretation for rapid 3D Xray diffraction and imaging of materials under stress and extreme environments

Ashley Bucsek (University of Michigan); Reeju Pokharel (Los Alamos National Laboratory); Peter Kenesei (Argonne National Laboratory)

Keywords: X-ray microscopy, machine learning, artificial intelligence, variational autoencoders

Research Scope

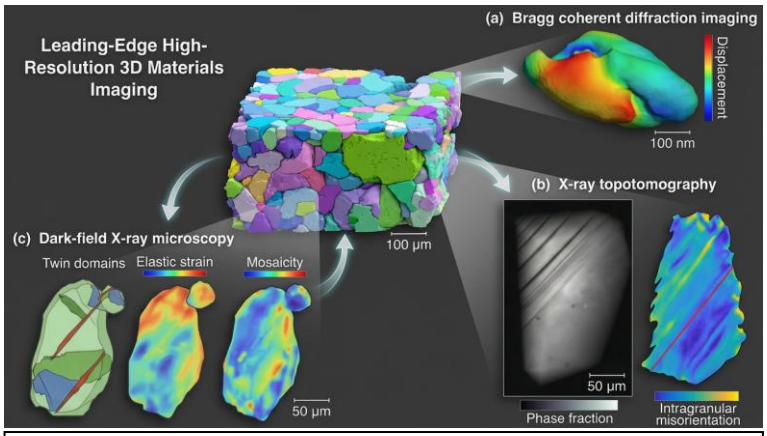

Fig. 1. Next-generation high-resolution 3D X-ray diffraction imaging techniques provide unprecedented capability to resolve 3D defect architectures and the local strain/stress fields that drive them.

Structural materials used in energy, transportation, and national security systems must withstand complex mechanical loads and extreme environments. The mechanical response of these materials emerges from the activation, motion, and interaction of discrete defects—dislocations, deformation twins, martensitic phase transformations—embedded within a three-dimensional (3D) polycrystalline grain network. Despite decades of research, our predictive capability remains limited: many widely used theories are rooted in single-crystal assumptions that neglect grain-network constraints, while high-fidelity simulations demand sample-specific calibration and prohibitive computational effort. Accelerating the discovery, qualification, and deployment of next-generation materials requires new scientific tools to directly connect mechanism-level physics to experimentally observed, bulk polycrystalline behavior.

Recent 3D diffraction imaging modalities—Bragg coherent diffraction imaging (BCDI), dark-field X-ray microscopy (DFXM), and X-ray topotomography (XRTT)—can resolve defect architectures and local stress/strain fields within embedded grains with spatial resolution approaching tens of nanometers (**Fig. 1**). However, data inversion and reconstruction remain a dominant bottleneck: DFXM and BCDI analyses can require months to years of expert effort, and stress-aware XRTT reconstructions are still immature. These limitations preclude real-time experimental decision-making, restrict measurements to one or a few grains, and slow translation of rich 3D data into actionable mechanistic descriptors for models and materials design.

Our goal is to develop artificial intelligence (AI) reconstruction methods that deliver rapid, accurate 3D maps of microstructure and internal stress/strain fields from high-energy X-

ray diffraction imaging experiments. The U.S. Department of Energy's synchrotron light sources—especially the Advanced Photon Source (APS) and its upgraded capabilities—provide uniquely bright X-rays and large working distances to enable in situ/operando imaging at sub-micrometer spatial scales. We leverage these national capabilities through an integrated team combining (i) new experimental developments and access across APS beamlines (Kenesei), (ii) advanced diffraction-based characterization and multimodal datasets spanning DFXM and XRTT (Bucsek), and (iii) AI and multiscale modeling expertise anchored in BCDI (Pokharel).

Our strategy is to develop variational autoencoder (VAE)-type generative AI models trained on physically realistic, simulation-generated data. Our main objectives include: (i) curating forward models for XRTT, DFXM, and BCDI that map a synthetic 3D microstructure to virtual diffraction datasets; (ii) generating synthetic 3D microstructures in elemental metals with different defect structures using molecular dynamics (MD); and (iii) generating virtual diffraction datasets for training and validation with known ground-truth microstructures and stress/strain fields; (iv) Using these paired datasets, we will develop and benchmark generative AI reconstruction models that incorporate physics-informed constraints (e.g., stress equilibrium) to improve fidelity and robustness. (v) Finally, we will transition from synthetic data to existing and newly collected experimental data. Basing our go/no-go decision on five carefully defined decision-gate metrics, we will shift to Phase II by testing and refining the approach on the existing and newly acquired experimental datasets.

The expected outcome is a step-change in reconstruction throughput while preserving quantitative accuracy and physical validity in the recovered microstructure and internal stress/strain fields. By enabling near–real-time feedback during beamtime, these new AI-based scientific tools have the potential to transform high-resolution 3D X-ray diffraction microscopy from an expert-driven, low-throughput capability into a scalable tool for multi-grain physics. Furthermore, this work creates a bridge between experiments and simulations, supporting rapid hypothesis testing, model refinement, and accelerated design of structural materials with predictable performance in demanding conditions.

References

[1] J. Kerby, The Advanced Photon Source Upgrade: A brighter future for x-ray science, (2023).
[2] Z. Liu, N. Vigano, H. Proudhon, and W. Ludwig, Theoretical Analysis of Topotomography Using Small Intragranular Strain Approximations, ArXiv Prepr. ArXiv251008712 (2025).
[3] H. Proudhon, N. Guéninchault, S. Forest, and W. Ludwig, Incipient Bulk Polycrystal Plasticity Observed by Synchrotron In-Situ Topotomography, Materials 11, (2018).
[4] J. Stinville, W. Ludwig, P. Callahan, M. Echlin, V. Valle, T. Pollock, and H. Proudhon, Observation of bulk plasticity in a polycrystalline titanium alloy by diffraction contrast tomography and topotomography, Mater. Charact. 188, 111891 (2022).
[5] H. F. Poulsen, A. C. Jakobsen, H. Simons, S. R. Ahl, P. K. Cook, and C. Detlefs, X-ray diffraction microscopy based on refractive optics, J. Appl. Crystallogr. 50, 1441 (2017).
[6] H. Simons, A. King, W. Ludwig, C. Detlefs, W. Pantleon, S. Schmidt, F. Stöhr, I. Snigireva, A. Snigirev, and H. F. Poulsen, Dark-field X-ray microscopy for multiscale structural characterization, Nat. Commun. 6, 6098 (2015).
[7] H. Simons, A. B. Haugen, A. C. Jakobsen, S. Schmidt, F. Stöhr, M. Majkut, C. Detlefs, J. E. Daniels, D. Damjanovic, and H. F. Poulsen, Long-range symmetry breaking in embedded ferroelectrics, Nat. Mater. 17, 814 (2018).
[8] A. Bucsek, H. Seiner, H. Simons, C. Yildirim, P. Cook, Y. Chumlyakov, C. Detlefs, and A. P. Stebner, Sub-surface measurements of the austenite microstructure in response to martensitic phase transformation, Acta Mater. 179, 273 (2019).
[9] S. Gustafson, W. Ludwig, P. Shade, D. Naragani, D. Pagan, P. Cook, C. Yildirim, C. Detlefs, and M. D. Sangid, Quantifying microscale drivers for fatigue failure via coupled synchrotron X-ray characterization and simulations, Nat. Commun. 11, 3189 (2020).
[10] S. Lee, T. D. Berman, C. Yildirim, C. Detlefs, J. E. Allison, and A. Bucsek, Multiscale in-situ characterization of static recrystallization using dark-field X-ray microscopy and high-resolution X-ray diffraction, Sci. Rep. 14, 6241 (2024).
[11] S. Lee et al., Three-dimensional nucleation and growth of deformation twins in magnesium, Science 389, 632 (2025).
[12] A. Scheinker and R. Pokharel, Enabling dynamic 3D coherent diffraction imaging via adaptive latent space tuning of generative autoencoders, Npj Comput. Mater. 10, 283 (2024).
[13] A. Scheinker and R. Pokharel, Adaptive 3D convolutional neural network-based reconstruction method for 3D coherent diffraction imaging, J. Appl. Phys. 128, (2020).
[14] M. J. Cherukara, R. Pokharel, T. S. O'Leary, J. K. Baldwin, E. Maxey, W. Cha, J. Maser, R. J. Harder, S. J. Fensin, and R. L. Sandberg, Three-dimensional X-ray diffraction imaging of dislocations in polycrystalline metals under tensile loading, Nat. Commun. 9, 3776 (2018).
[15] A. Pateras et al., Combining Laue diffraction with Bragg coherent diffraction imaging at 34-ID-C, Synchrotron Radiat. 27, 1430 (2020).
[16] S. Borgi, G. Winther, and H. F. Poulsen, Individual dislocation identification in dark-field X-ray microscopy, Appl. Crystallogr. 58, (2025).
[17] A. Scheinker, M. McBride, N. Brown, A. Mirabal, R. Pokharel, and D. E. Hooks, Conditional Latent Diffusion for High-Resolution Prediction of Electrochemical Surface Morphology, J. Electrochem. Soc. 173, 022502 (2026).
[18] S. Lee et al., Three-dimensional nucleation and growth of deformation twins in magnesium, Science 389, 632 (2025).

Elucidating the influence of bulk slip morphology on hydrogen environment-assisted cracking behavior in precipitation-hardened alloys

James T. Burns, University of Virginia

Keywords: Environmental cracking, nickel, dislocation, H-embrittlement, crack tip

Research Scope

The overarching objective of the proposed research is to elucidate the mechanistic influence of bulk slip morphology on the HEAC behavior of a model precipitation-hardened alloy by coupling high-fidelity fracture mechanics testing methods with a state-of-the-art multiscale characterization strategy. The following specific research questions will be addressed. First, for a constant global mechanical driving force (*e.g.,* stress intensity factor), grain size, grain orientation, and hydrogen uptake behavior, do differences in bulk slip morphology result in quantitatively different (both spatially and in intensity) near-crack plastic deformation distributions during HEAC? Addressing this question will rigorously establish the causal role of bulk slip morphology on HEAC susceptibility by controlling possible obfuscating factors. Second, how does the observed deformation distributions proximate to the crack at a constant stress intensity factor vary as a function of grain orientation and environmental severity (*e.g.*, hydrogen uptake behavior) for a given bulk slip morphology? Addressing this question will establish the sensitivity of observed deformation distributions for a given bulk slip morphology to two expected modifying influences. This will provide insights into (1) the mechanistic contribution of H content on crack propagation and (2) the impact of grain orientation on the deformation responsible for crack propagation. Third, differences in bulk slip morphology impact the deformation distribution *in front* of the crack tip for a constant applied stress intensity factor and hydrogen uptake behavior? Any observed variations in deformation distribution and grain boundary-deformation interactions proximate to the crack tip can provide a mechanistic pathway to understand *how* bulk slip morphology may induce differences in HEAC propagation metrics for a constant stress intensity factor and H uptake behavior.

Recent Progress

A full thermal treatment study of the model Ni-Cu system was completed to establish a system with a homogeneous grain size of 75-100 μm via annealing at 1323K and various strength levels via aging treatment at 923K. A full EBSD and TEM based microstructure analysis was completed to demonstrate consistency of the grain size and to document the size distributions of the gamma prime precipitates for non-aged, under-aged, peak-aged, over-aged, and highly over-aged conditions. Furthermore, TEM of each of samples from each of the aging conditions demonstrated that the non-aged and the highly over-aged conditions exhibited wavy slip and the underaged, peak-aged and over-aged conditions exhibited planarized bulk slip.

The primary focus of this reporting period was finalization and analysis of the LEFM based testing data in an inert environment (dry N_2) and 0.6 M NaCl for each of the aging conditions at polarization levels of -900, -1000, and -1100mV_{sce}. It is useful to note that increasingly cathodic (more negative) polarizations reflect higher levels of overpotential for H-production and thus more susceptible conditions. An example of the results of these ~25 LEFM-based tests is shown in Figure 1 that reports the full crack growth versus stress intensity relationships (da/dt vs. K) 1 for the 0.6 M NaCl and -1000 mVsce condition. The most salient aspects of the complete data-set are summarized in Figure 2, where the Stage II growth rate for each polarization level and material condition are reported. ***The results demonstrate that the materials that exhibit bulk planar slip (under-aged, peak-aged, and over-aged) exhibit a higher susceptibility than materials exhibiting bulk wavy slip (highly over-aged, and non-aged).*** This behavior is most pronounced at the intermediate levels of driving force (K) and polarization (e.g. moderately severe environments). This reasonably suggests that microstructural impacts can be muted by severe mechanical or environmental driving forces.

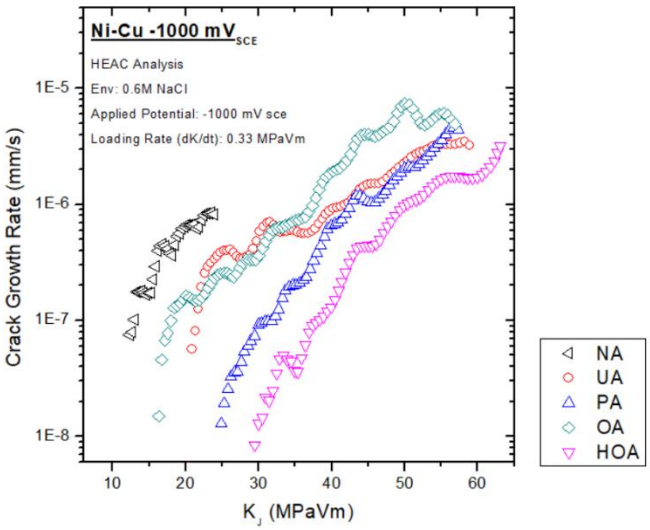

Figure 1: Crack growth kinetics for the model Cu-Ni alloy with different aging treatments in 0.6 M NaCl at -1000 mVsce.

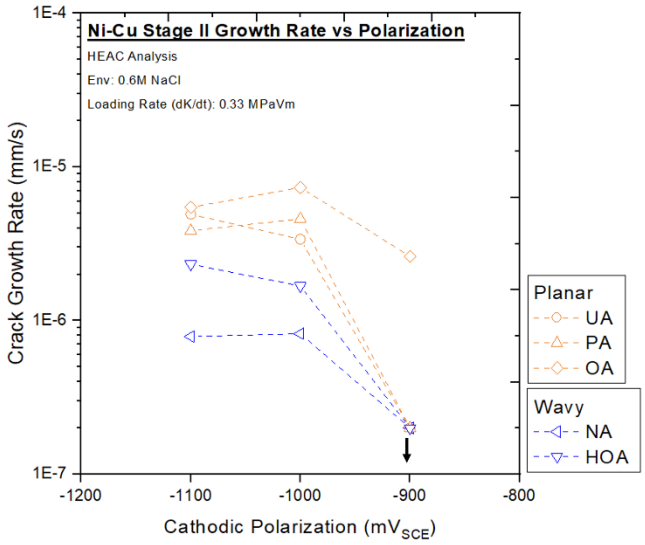

Figure 2: Stage II growth rates of the model Cu-Ni alloy as a function of polarization level for different aging treatments and bulk slip behavior.

The fundamental premise of the proposed effort is to employ a multiscale characterization effort on the crack tip and wake of the LEFM samples to explore the local plastic damage morphology as a function of the testing variables. With the completion of the testing program, the characterization efforts have commenced. A unique aspect of this effort is the recognition that the local plastic damage will be impacted by the K and grain orientation. As such, selection of the analysis areas will aim to hold these variables constant. This is demonstrated in Figure 3 where the dcPD-based crack lengths are plotted versus K for the highly over-aged (a) and under-aged (b) conditions and then transferred to a cross-sectional view of the crack wake. In

Figure 3(c,d) the crack lengths are marked on the cross-sections of the crack wakes for specific values and the pre-cracked (PC) and SCC regions are noted. Furthermore, regions (A) and (B) are marked in Figure 3(e,f) and have been selected for higher magnification analysis due to the fact that there are similar grain orientations and K values to compare the under-aged and highly over-aged conditions. Figure 3(g,h) show a moderate magnification KAM map to give a first order indication of the differences in plasticity between the two conditions.

Future Plans:

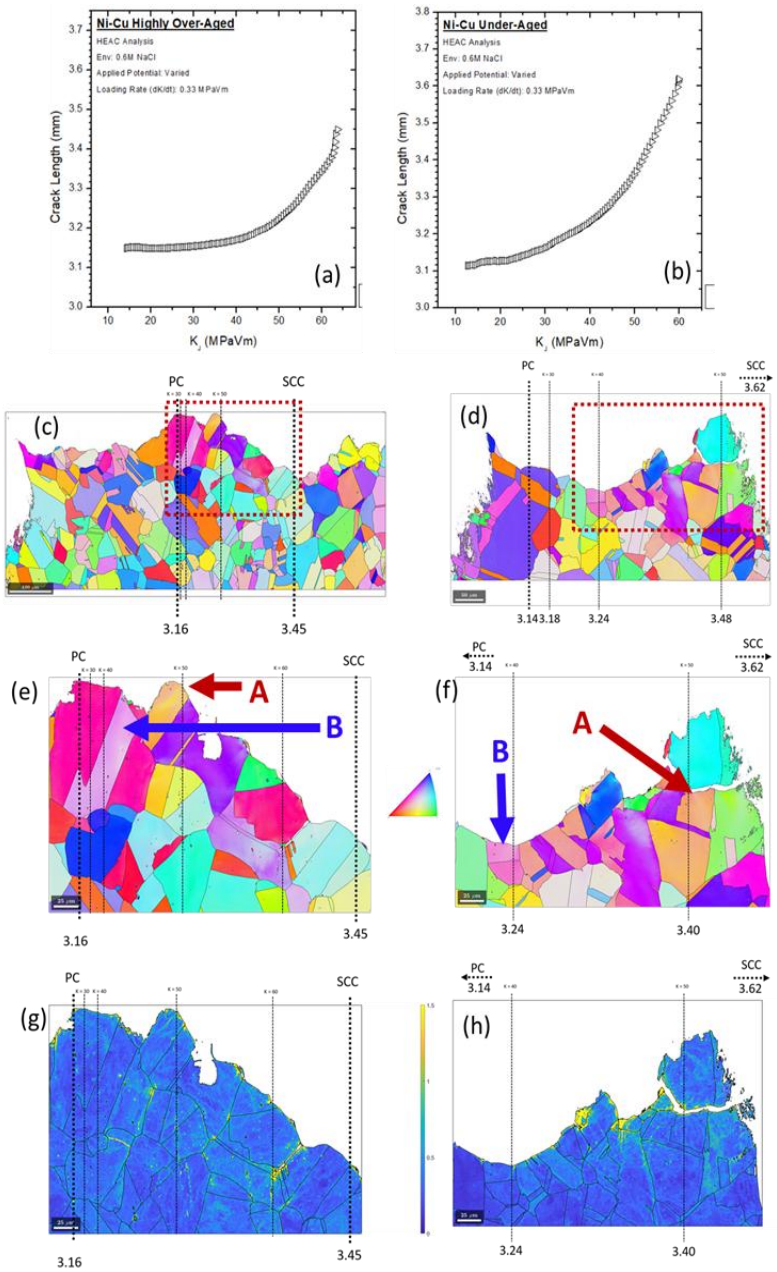

Figure 3: Crack length versus K relationships and EBSD/KAM cross-sections of highly over-aged (a,c,e,g) and under-aged (b,d,g,h) CuNi tested in 0.6 M NaCl at -1000 mVsce.

The program is poised to realize the proposed technical merit. Prior to the completion of the testing matrix extensive efforts were performed to develop, refine and validate the multi-scale characterization protocol on different material systems and samples. With the completion of the testing matrix and availability of the subject specimens the characterization will be executed on the samples of the interest. The highest priority will be put on comparisons of the highly over-aged and the under-aged samples at -1000 mVsce where significant differences in the growth kinetics were observed. This will include higher fidelity HR-EBSD characterization (with spot size sufficient for rigorous GND calculation) at the locations indicated in Figure 3(e,f) along with TEM to explore the details the dislocation structure. Furthermore, detailed analysis will be conducted at the intact crack tip to explore the gradient of plasticity and the transition region going from bulk deformation independent of H-effects transitioning to the crack tip damage structure. Exploration of these features and correlation of these features to the differences in crack growth kinetics will enable unprecedented evaluation of how and why the bulk deformation mode impacts the crack tip damage physics governing the growth kinetics.

Publications

1. Z.D. Harris, A.W. Thompson, J. Smith, R. Jayamohan, J.T. Burns, *Influence of grain boundary sulfur, local hydrostatic stress, and precipitate character on heat-to-heat variations in hydrogen environment-assisted cracking of Monel K-500*, Corrosion Journal, **In-revision**.

The Role of Local Chemical Order on Defect Kinetics in Alloys under Irradiation

Penghui Cao, University of California, San Diego

Keywords: Defect kinetics; Vacancy; Dislocation; Diffusion; Irradiation effect

Research Scope

High-energy particle irradiation often has detrimental effects on materials, but in certain cases, it can be beneficial. For example, it orients high-density magnetic alloys by promoting chemical order. The phenomenon of radiation-induced ordering, first postulated and demonstrated by Averbach over half a century ago, has been frequently observed in binary alloys. Multi-principal element alloys (MPEAs), which include medium- and high-entropy alloys with multiple principal elements in high concentration, are typically presumed to be random solid solutions that maximize configurational entropy. However, ideal random mixing in MPEAs may only be achievable at elevated temperatures. As temperatures decrease, the enthalpic contribution to the total free energy may dominate, leading to local chemical ordering. The emergence of chemical short-range order, whether due to material processing or irradiation, can play a vital role in radiation defect kinetics and material radiation tolerance.

This research project aims to understand the role of local chemical order on the kinetics of defects in MPEAs and to evaluate the mechanistic strategy for controlling radiation defect migration and evolution through tailoring local ordering at the nanoscale. The research focuses on single-phase MPEAs and addresses the questions regarding local ordering: (i) how does the local chemical order influence defect migration, coalescence, and growth; (ii) what are the new atomistic mechanisms and processes enabled by local order that could lead to radiation damage reduction; and (iii) is tuning the degree of local ordering able to promote defect recombination and to alleviate radiation-induced damage accumulation?

Specifically, research activities are driven by three mechanistic hypotheses pertaining to the role of local ordering on point defects, defect cluster, and interface: (1) the presence of local chemical order raises migration energy barriers of point defects and localizes their diffusion; a localized diffusion can promote defects recombination and mitigate defect cluster growth; (2) local chemical order roughens the potential energy landscape, which can locally pin a dislocation loop and reduce its diffusivity; and (3) the introduced local ordering in the grain matrix increases grain boundary migration energy and lowers its mobility. Evaluating these hypotheses will advance the fundamental understanding of atomistic mechanisms underlying the extraordinary properties of MPEAs, facilitate material design strategies to manipulate defect behaviors by tailoring nanoscale features, and enable tunable material properties.

Recent Progress

The project's major progress over the past two years has focused on advancing the fundamental understanding of vacancy and dislocation kinetic behaviors in concentrated solid solutions and the role of local chemical order.

Progress 1: Fragmenting diffusion pathways conferring extraordinary radiation resistance in refractory alloys

A critical degradation mode of materials under irradiation is the clustering of irradiation-induced vacancies, which drives void formation and structural instability. Conventional mitigation strategies rely on external defect sinks such as grain boundaries and precipitates, but these features inevitably evolve and saturate under sustained irradiation. In this research process [1], we show that a tungsten multicomponent alloy achieves intrinsic radiation resistance by fragmenting the vacancy diffusion network and kinetically trapping defects within localized domains. This fragmentation originates from a broad spectrum of migration barriers and substantial vacancy-jump heterogeneity, which reduces the interconnectivity of diffusion paths below the percolation threshold (Figure 1). Consistent with this discovered mechanism, irradiation experiments and atomic-scale defect characterizations show minimal defect growth even as the radiation dose increases by four orders of magnitude. These results provide a fundamental paradigm for percolation-engineered kinetics, offering a predictive pathway for tailoring defect diffusion and discovering inherently radiation-tolerant materials.

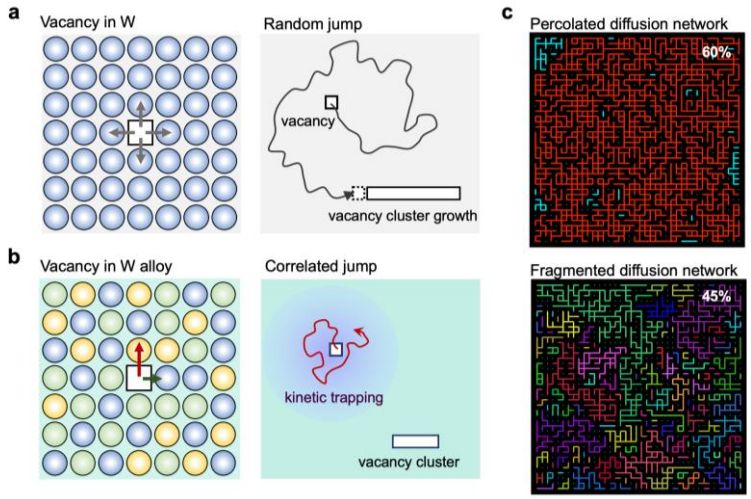

Figure 1. Diffusion pathways, network percolation and fragmentation, and diffusion barrier prediction in large compositional spaces.

Progress 2: Dislocation kinetics and collective motion in concentrated alloys

These unexpected findings emerged while evaluating Hypothesis 2, which posits that local chemical order and the associated roughened potential-energy landscape can locally pin dislocations. To assess this effect, we compared the stress–strain responses and slip behavior of quenched and annealed CrCoNi samples. The two conditions showed only minor differences in mechanical response, indicating that thermal treatments intended to modify local order have a limited effect on bulk dislocation slip and strength under the conditions studied.

In contrast, pronounced differences in slip morphology emerged among differently oriented samples, motivating us to investigate how atomic-scale collective dislocation processes give rise to microscopic slip-band formation.

Our work [2] reveals two distinct slip-band morphologies that share a common origin but evolve through different mechanisms. Confined slip bands are consistent with conventional Frank–Read source operation, whereas extended slip bands arise through dislocation glide-induced source deactivation followed by the dynamic generation of new dislocation sources (Figure 2). These findings expand the conventional understanding of slip-band formation and demonstrate the important role of collective source evolution in governing dislocation patterning in concentrated alloys. This unexpected outcome also refines our original hypothesis and motivates further investigation of how chemical complexity and local energy landscapes influence dislocation and defect motion.

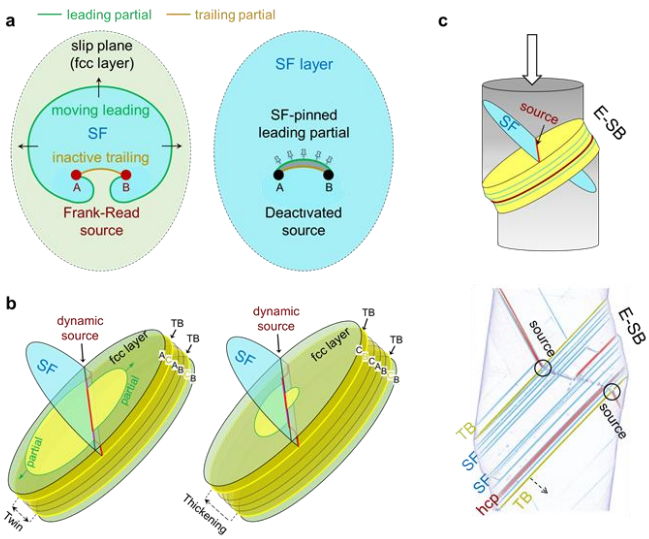

Figure 2. Dislocation mechanisms driving extended slip band formation. (a-b) Frank-Read source deactivation and dynamic dislocation source creation. (c) Atomistic modeling shows the resulting slip band.

Progress 3: Jerky one-dimensional diffusion of prismatic dislocation loops

In this effort, we reveal that prismatic dislocation loops in concentrated alloys (NbMoTaW) exhibit jerky one-dimensional diffusion that is significantly slower, up to three orders of magnitude, than in pure W. This reduction is driven by a rugged and non-periodic energy landscape shaped by chemical disorder and short-range order, leading to thermodynamic pinning and kinetic confinement. In contrast to conventional pure metals where loops diffuse

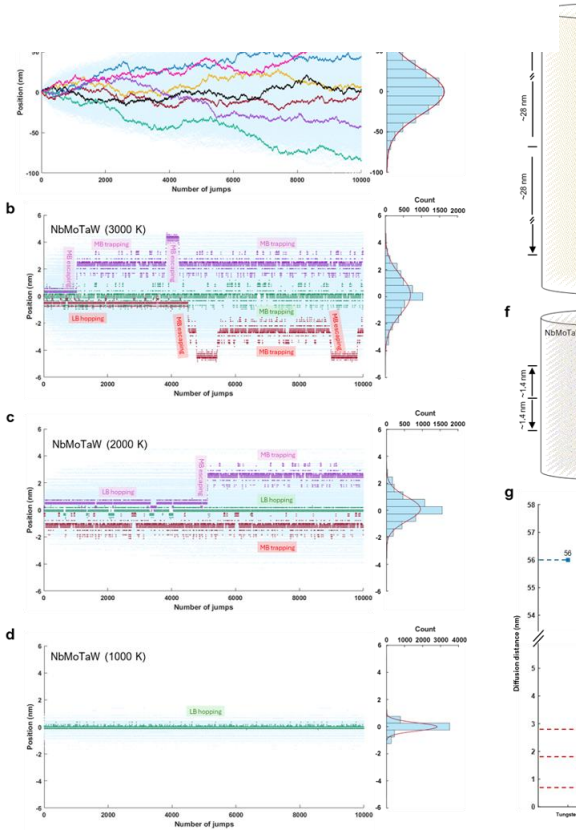

Figure 3. Diffusion trajectories of prismatic loops in W and NbMoTaW alloy. The dislocation loops in concentrated alloys exhibit jerky one-dimensional diffusion that is significantly slower than in pure W.

rapidly, in alloys such as NbMoTaW, loop motion is highly correlated and intermittent. Kinetic Monte Carlo simulations demonstrate these effects and elucidate the underlying mechanisms of jerky motion. Key findings are presented in Figure 3 and the manuscript is under preparation for submission.

Progress 4: Role of vacancy diffusion correlation and the diffusion-barrier spectrum in concentrated alloys

This study focuses on the essential question of how chemical complexity affects vacancy diffusion and what unique characteristics, if any, set concentrated alloys apart from traditional metals [3]. Studying vacancy diffusion in NbMoTa alloy across a broad temperature range from 2600 to 800 K, we reveal that, unlike pure metals, the two key diffusion parameters (diffusion correlation factor and activation energy) are not constant in alloys, but instead substantially decrease with decreasing temperature. This temperature dependence arises from a reduced number of active jump pathways at lower temperatures, leading to more correlated vacancy jumps. Compared to traditional metals, the diffusion correlation factor can be two orders of magnitude lower, which is believed to be the primary reason for the observed slow vacancy diffusion in concentrated alloys. Finally, we find that the vacancy diffusion rate drops noticeably in the presence of local chemical order in the NbMoTa system, particularly for MoTa alloys with long-range B2 order.

Progress 5: The ubiquitous chemical short-range order in MPEAs enabled by swift ion diffusion during solidification

Extensive research has been directed towards tailoring short range order through thermal processing and aging to modify material properties. However, recent experiments show that quenched and aged materials exhibit nearly identical strength, leading to an ongoing debate about the role of SRO. Our atomistic simulations have uncovered that a prevalent degree of order forms during solidification at the liquid-solid interface, even at extremely fast cooling rates [4]. This phenomenon stems from the rapid atomic diffusion in the supercooled liquid, which matches or even surpasses the rate of solidification. Consequently, short range order is an inherent characteristic of most face-centered-cubic (fcc) MPEAs, insensitive to variations in cooling rates and even annealing treatments. Unlike in dilute alloys where local ordering or precipitation necessitates long-range diffusion, local diffusion in concentrated solid solutions in MPEAs is sufficient to build a large degree of order.

Future Plans

As we move forward, we will focus on evaluating the remaining aspects of the hypotheses. Our primary objective in the near future is to demonstrate the mechanisms of chemical trapping of vacancies and dislocations, and defect cluster growth under irradiation. By coupling irradiation experiments with predictive atomistic modeling, we aim to show that vacancy-cluster growth can be effectively suppressed by tailoring chemical order and disorder.

Publications

1. B. Xing, B. Xie, W. Zou, E. Lang, E. Boltynjuk, H. Chen, M.P. Short, G. Tynan, T.J. Rupert, J. Trelewicz, H. Hahn, B.P. Uberuaga, K. Hattar, Penghui Cao, *Fragmenting diffusion pathways confers extraordinary radiation resistance in refractory multicomponent alloys*, arXiv:2603.02651 (2026, under review).
2. B. Xie, H. Chen, P. Wang, C. Zhang, B. Xing, M. Xu, X. Wang, L. Valdevit, J. Rimoli, X. Pan, and P. Cao, Divergent evolution of slip banding in CrCoNi alloys. Nature Communications, **16**, 3631 (2025).
3. B. Xing, W. Zou, T.J. Rupert, P. Cao, *Vacancy diffusion barrier spectrum and diffusion correlation in multicomponent alloys*, Acta Materialia, **266**, 119653 (2024).
4. Y. Han, H. Chen, Y. Sun, J. Liu, S, Wei, B. Xie, M. Li, J. Yang, W. Chen, P. Cao, Y. Yang. *Ubiquitous short-range order in multi-principal element alloys*. Nature Communications, **15**, 6486 (2024)
5. X. Wang, L. Valdevit, P. Cao. *Neural network for predicting Peierls barrier spectrum and its influence on dislocation motion*. Acta Materialia **267**, 119696 (2024).
6. A. Abu-Odeh, B. Xing, P. Cao, B. P. Uberuaga, M. Asta. *A simple model for short-range ordering kinetics in multi-principal element alloys*, Scripta Materialia **252**, 116224 (2024).
7. D. Aksoy, P. Cao, J.R. Trelewicz, J.P. Wharry, T.J. Rupert, *Enhanced radiation damage tolerance of amorphous interphase and grain boundary complexions in Cu-Ta*. JOM **76**, 2870–2883 (2024).

Deformation Twinning Networks in Metals with Hexagonal Close-Packed Crystal Symmetry

PI: Hi Vo, Laurent Capolungo, Khanh Dang and Rodney McCabe
Materials Science and Technology Division, Los Alamos National Laboratory

Keywords: Deformation twinning, twin networks, plasticity, hexagonal close-packed metals

Research Scope

Deformation twins play a key role in accommodating strain during plastic deformation in hexagonal close-packed (hcp) metals and their alloys. In polycrystals, twin nucleation, growth, transmission, and interaction produce complex, interconnected three-dimensional (3D) twin networks whose evolution is coupled to dislocation slip. Yet, how these networks form and influence plastic flow remains poorly understood. This gap is critical because twinning plays a dual role: it provides an additional pathway for deformation and strain accommodation, while also generating internal stresses and plastic incompatibilities that may promote strain localization and failure. How these competing effects emerge from the topology and mechanics of the 3D twin network remains an open question. To this end, we study the 3D character, evolution, and mechanics of deformation-twin networks using a combination of experiments, modeling, and theory.

Recent Progress

Complexity and features of 3D twin networks: A necessary first step toward understanding how twin network topology influences plastic deformation is to quantitatively characterize the structure and connectivity of these networks. To investigate differences in the structural fingerprint of twinned microstructures reconstructed through surface and 3D techniques, we performed a comparative analysis of 2D and 3D EBSD measurements of the same cryogenically compressed Ti microstructure. Insights into the topological structure of the networks were facilitated by combining a novel graph-based microstructure reconstruction framework with conventional statistical analysis of twin crystallography. The graph abstractions, illustrated in Figure 1 (a), reveal extraordinary differences in the fingerprint of the network when reconstructed using 2D surface slices compared to full 3D measurements. While 2D reconstructions depict the twin network as primarily dispersed, isolated twins with a few individual paired contacts, the 3D reconstructions instead show that the full network is composed of a highly interconnected scaffold of twin domains that spans across nearly the entire microstructure. Conventional 2D surface analysis also significantly underrepresents the frequency at which twins contact across grain boundaries and suggests that isolated twin nucleation events dominate the network evolution process, while in reality, we see that transmission across grain boundaries is both highly prevalent and likely an easy process. The 2D and 3D datasets were also analyzed using graph theory to assess the statistical characteristics of the networks and their evolution. As shown in Figure 1 (b), which

presents the frequency of observed cross-grain twin contacts as a function of alignment between the twins (represented here by $m' = (\eta_1^A \cdot \eta_1^B)(K_1^A \cdot K_1^B))$, twins commonly appear to intersect at grain boundaries in configurations that are unlikely to favor twin transmission. These frequent events are attributed to both co-nucleation of paired twins and incidental interactions between twins that formed through unrelated processes, the latter of which are commonly missed in 2D analyses and conventionally neglected in prior studies of twinned microstructures.

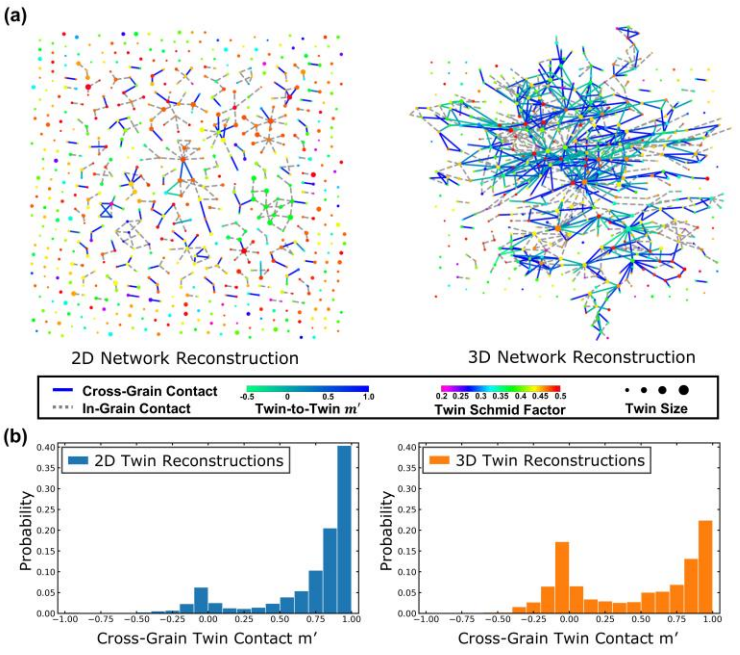

Figure 1. Differences in network topology identified in 2D and 3D twin network reconstructions. (a) Graph abstractions of the reconstructed twin networks in a 3D cubic volume and 2D surface area extracted from the same Ti test specimen cryogenically compressed to 2.6 % strain. (b) Histogram distributions of *m'* for cross-grain twin contacts identified in three 2D reconstructions (1938 contacts) compared to three 3D twin network reconstructions (1517 contacts).

The remarkable complexity of 3D twin networks was thus far highlighted solely by static snapshots of the microstructure at different steps during deformation, and our understanding of the formation and growth of networks was limited due to the multiple interrelated mechanisms involved in network dynamics. In particular, the individual domains and contacts between domains that underpin the topology of the network may form via multiple competing or unrelated processes such as isolated or co-nucleation, transmission or arrest at grain boundaries, short-range interactions within grains, and incidental interactions across grain boundaries. To predict network evolution and rationalize the relative contributions of different mechanisms, we developed a machine learning framework to predict the outcome of twin-grain boundary interactions using multilayer perceptrons trained on 2D and 3D EBSD datasets of twinned microstructures in high purity Ti. We then leveraged the trained model to virtually generate fingerprints of twin networks and explore the role of the aforementioned mechanisms on the evolution of the network structure. By integrating the crystallographic, geometric, and stress-based characteristics of the twins and twin-boundary contacts, the model predicts contact formation with high accuracy and reveals that while geometric alignment between the twin domains is a key factor for cross-grain contact formation, the role of internal stresses must be included to capture contact geometry in poorly aligned configurations. Further, by applying the model to the evolution of virtual twin networks, incidental interactions between unrelated twin domains are found to drive the high interconnectivity identified in 3D reconstructions of the studied Ti microstructures.

Insights into fundamental mechanisms underlying twin network formation: Building on these insights into the mechanisms governing 3D twin network connectivity, we next sought to establish the physical processes controlling the nucleation, growth, and co-deformation of the individual twin domains and junctions that comprise the network. In particular, the prevalence of cross-grain contacts suggests that twin transmission occurs readily, while the frequent occurrence of highly misoriented contacting twins indicates that mechanisms beyond geometrically favored transmission contribute to network formation. These observations are consistent with our previous modeling and simulations, which showed that twin transmission across grain boundaries is governed more strongly by energetic relaxation than by geometric alignment alone. We therefore focused our modeling efforts on two complementary questions: (i) *how do twin domains nucleate and grow in the presence of dislocation slip?* and (ii) *how do twin–twin junctions that form within the network subsequently co-deform and accommodate strain?*

To address the first question, we developed and leveraged a spectral twinning-crystal plasticity framework to systematically investigate the nucleation and stability of isolated $\{10\bar{1}2\}$ twin embryos while accounting for concurrent slip in the parent and twin phases. In the absence of plastic relaxation, nanometric twin embryos smaller than 100 nm become energetically favorable only at applied stresses exceeding approximately 500 MPa. In contrast, activation of profuse slip in the parent phase (akin to that observed in bulk polycrystals) relaxes the internal stresses associated with twin formation and reduces the predicted nucleation stress to approximately 250 MPa. Prior plastic deformation further generates favorable driving tractions for twin growth at applied stresses as low as approximately 100 MPa. The resulting traction distributions are strongly heterogeneous across twin facets, providing a mechanistic basis for the irregular and asymmetric twin morphologies observed experimentally. These findings demonstrate that dislocation-mediated plasticity fundamentally alters both the energetics and stability of twin embryos and helps reconcile the high twin volume fractions observed experimentally at relatively low applied stresses with previous estimates of twin nucleation stresses approaching 1 GPa.

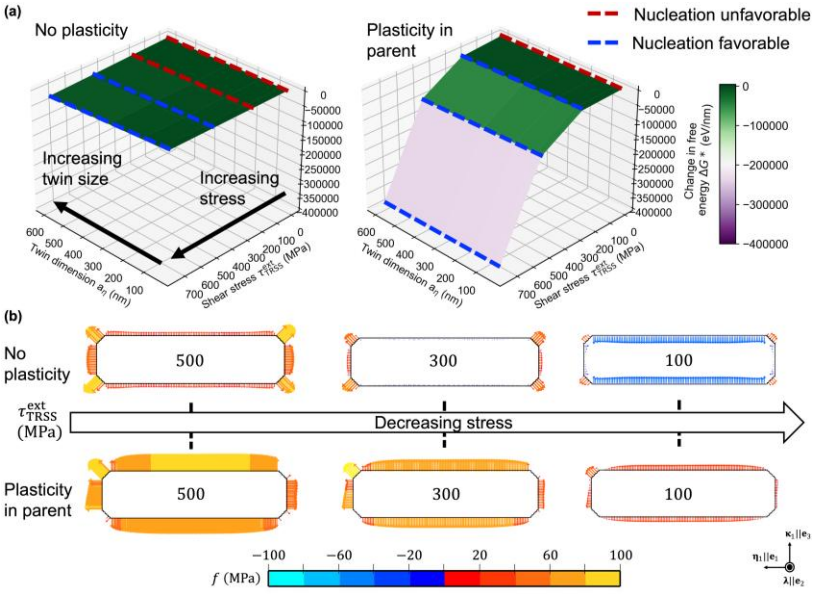

Figure 2. The influence of slip-mediated plasticity on twin nucleation in hcp Mg. (a) Gibbs free energy change curve for $\{10\bar{1}2\}$ twin nucleation at different applied stress states considering elasticity or profuse slip activity in the parent only. (b) Comparison of the driving traction profiles across different twin facets without active slip and with profuse slip activity in the parent grain at 100 to 500 MPa.

We next examined whether the twin–twin junctions formed as these domains intersect remain mechanically active during subsequent deformation. Using a coupled multi-phase field crystal plasticity framework, we simulated the co-deformation of different twin-twin junctions (TTJs) and dislocation slip in Mg. Contrary to the conventional view of TTJs as largely static or rigid features, the simulations reveal that these junctions are mobile and deformable, allowing intersecting twin domains to collectively evolve in response to the local mechanical fields. Their evolution produces substantial stress relaxation and redistributes the geometric incompatibilities associated with the intersecting twins. Importantly, concurrent activation of slip and twinning provides the most efficient pathway for stress relaxation and energy dissipation, while the degree of plastic accommodation depends strongly on junction geometry. Co-zone junctions exhibit greater plastic accommodation than non-co-zone junctions, demonstrating that the mechanical response of the network depends not only on its connectivity but also on the topology and deformability of the junctions comprising it. Together, these results establish a mechanistic link between the co-activation of slip and twinning at the scale of individual twin domains and junctions and the ability of a dense 3D twin network to accommodate deformation and relax local incompatibilities.

Future Plans

Our recent findings have established that 3D twin networks are highly interconnected and that both twin-grain boundary contacts and TTJs can actively evolve to accommodate deformation. Thus, our future efforts will be focused on how the topology of the networks and the co-deformation of their constituent interfaces and junctions govern the redistribution and localization of mechanical fields. Specifically, our next step is to determine how these fields evolve as twins grow toward grain boundaries, form contacts, and subsequently co-deform with the surrounding microstructure.

To this end, the influence of twin-network topology on the mechanical response of the microstructure will therefore be explored through a combination of tailored pre-deformation treatments (to generate networks with varied connectivity and structural characteristics) and *in situ* measurements of microstructural evolution via electron backscatter diffraction during small-scale mechanical testing. Further, the role of individual twin-grain boundary configurations in mediating local plastic accommodation will be investigated using high-resolution digital image correlation. In parallel, concurrent atomistic-continuum (CAC) simulations will be used to progressively bridge the mechanics of isolated twin domains to twin-grain boundary interactions. Our first focus will therefore be to establish the mechanical fields generated by isolated twin domains and how these fields depend on twin size and morphology. This will provide the mechanistic foundation needed for future studies of increasingly complex interactions, including the eventual interaction and co-deformation of twins with grain boundaries.

Publications

1. D.A. Greeley, H.T. Vo, R.J. McCabe, C.N. Tomé, and L. Capolungo, *Twin networks in hexagonal close-packed metals: Morphology, connectivity, and incompatibilities*, Acta Materialia, 286, 120595 (2025).
2. S. Wang, C. Ding, R.J. McCabe, L. Capolungo, and C.N. Tomé, *Three-dimensional faceted boundaries of {10-12} twins in hcp Ti and Mg*, Scripta Materialia, 260, 116579 (2025).
3. D.A. Greeley, H.T. Vo, R.J. McCabe, M. Schneider, C.N. Tomé, and L. Capolungo, *A quantitative comparison of the fingerprint of twinned microstructures through surface and three-dimensional techniques*, Nature Communications, 16, 9773 (2025).
4. K. Dang and L. Capolungo *The role of {10-12} tension and {11-22} compression twins on the α to ω phase transformation in Ti*, Scripta Materialia, 268, 116867 (2025).
5. D. Bamney and L. Capolungo, *Twin nucleation and growth in hexagonal close-packed metals: The role of slip-mediated plasticity on twin embryo formation and evolution*, Journal of the Mechanics and Physics of Solids, 206, 106407 (2025).
6. D. Bamney and L. Capolungo, *Deformation behavior of twin/twin junctions in hexagonal close-packed metals*, Scripta Materialia, 281, 117360 (2026).
7. V. Taupin, D. Bamney, J-J. Blandin, L. Capolungo, R. Daudin, M. Fivel, and A. Rovinelli. *A numerical spectral model for shear transformation zone dynamics in heterogeneous metallic glasses,* Journal of the Mechanics and Physics of Solids, 106604 (2026).
8. D.A. Greeley, P.O. Agbaje, H.T. Vo, and L. Capolungo. *Data-driven inference of twin network dynamics: nucleation, co-nucleation, transmission, and incidental contacts*. npj Computational Materials (accepted).

Dynamic Grain Boundary Chemistry for Efficient Defect Sinks in Irradiated Nanoceramics

Ricardo H. R. Castro, Lehigh University

Keywords: nanoceramics, sink efficiency, grain boundary, transition metal, doping

Research Scope

The goal of this project is to provide fundamental understanding on how dynamic grain-boundary chemistry controls radiation defect evolution in nanoceramics, creating a foundation for future interface-engineered materials for nuclear environments. We treat grain boundaries in fluorite oxides not as passive geometric sinks but as reactive chemical microenvironments whose redox state, space-charge, and segregation patterns set the local formation and migration energies of point defects. Under heavy-ion irradiation, these chemistries evolve far from equilibrium, changing sink efficiency in ways not captured by models that treat sink strength as mostly structural. By quantitatively linking redox-driven interfacial restructuring to defect annihilation, irradiation-induced grain growth, and mechanical response, the project will establish a predictive foundation for chemically activated defect sinks in nanoceramics.

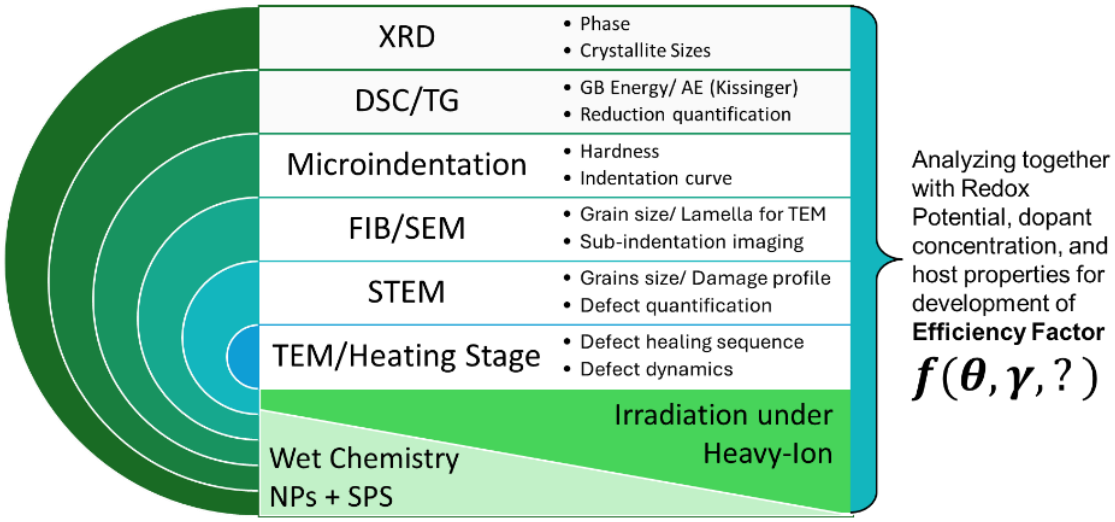

Figure 1. Workflow summary targeting unrevealing of sink efficiency factor of grain boundaries in oxide systems.

Nanocrystalline oxides such as yttria-stabilized zirconia and ceria sometimes resist amorphization, while other interface-rich ceramics show accelerated damage and early loss of crystallinity. These contrasts expose our limited understanding of the role of interfaces in radiation

tolerance (Figure 2), while pointing to a central role for interface chemistry in defining **sink efficiency**. The literature on experiments and simulations indicate that multivalent transition-metal dopants segregated to interfaces undergo irradiation-induced redox and strongly impacts defect populations near grain boundaries. The proposed work exploits our capability to fabricate dense fluorite oxides, from microcrystalline to ultra-nanocrystalline, with controlled dopant segregation to decouple the roles of grain-boundary area, thermodynamics, and (thermo)chemistry in radiation defect evolution. **We will perform systematic studies focusing on understanding the relationship between the chemistry of the interfaces and the sink efficiency factor used to describe the role of grain boundaries during irradiation. Our hypothesis is that multivalent dopants (Mn, Cr, Co, Ni), enriched at grain boundaries of dense fluorite oxides, act as redox-responsive modifiers of sink efficiency.**

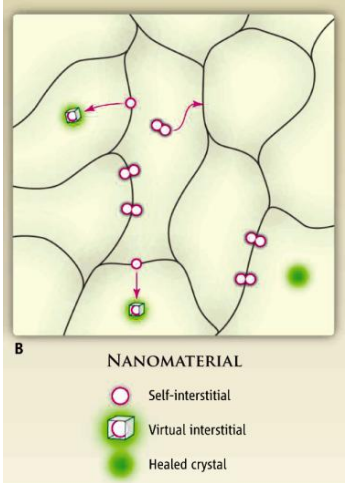

Figure 2. Schematic representation of self-healing mechanism in nanomaterials systems [1].

Changes in oxidation state and ionic radius alter grain-boundary energies, oxygen-vacancy content, and space-charge potentials, tuning driving forces for defect absorption and annihilation. We will synthesize model zirconia and ceria pellets in three grain-size regimes using high-pressure spark plasma sintering and introduce dopants via surface-enriched nanopowders. Heavy-ion irradiation with Lost Alamos National Laboratory collaborators will generate controlled damage, followed by advanced STEM/EELS mapping of chemistry, oxidation state, and defect clustering at and near grain boundaries. Differential scanning calorimetry will directly probe grain-boundary energies and defect-healing energetics in pristine and irradiated samples.

Tightly coupled tasks will link synthesis, irradiation, characterization, and modeling. We will (1) produce grain-size-tunable fluorite ceramics with reproducible segregation, (2) quantify grain-boundary energies, defect populations, and redox evolution across damage levels, and (3) integrate these data into a chemistry-aware efficiency function correlated with mechanical response and used as input for radiation-damage simulations. Mechanical testing of pristine and irradiated ceramics, combined with focused-ion-beam cross-sections of deformation zones, will connect grain-boundary chemistry to macroscopic performance relevant to nuclear structural and fuel-cycle applications. The resulting framework will enable predictive screening of dopant chemistries and interface states for radiation-tolerant oxides, directly supporting the DOE Basic Energy Sciences mission to understand and control matter under extreme, far-from-equilibrium conditions.

Recent Progress

This is a new project, with preliminary data and literature reports supporting the hypothesis. For example, although Cr doping in UO_2 is primarily recognized for enhancing fuel radiation

tolerance by promoting grain growth during high-temperature processing [2,3] more recent studies have demonstrated that Cr segregates to UO_2 grain boundaries during sintering and irradiation [4, 5]. Importantly, Cr is known to adopt multiple oxidation states in UO_2 (Cr^{2+}, Cr^{3+}, and Cr^{4+}) as documented in experimental and computational analyses [60–62]. One may speculate that Cr-segregated GBs in UO_2 may behave as chemically adaptable sinks, where redox-driven adjustments in ionic radius, charge state, and bonding environment improve the absorption, neutralization, and annihilation of point defects. This mechanistic pathway aligns with the broader hypothesis that multivalent transition metals can enhance radiation tolerance in oxides by activating *chemistry mediated* defect healing processes at grain boundaries.

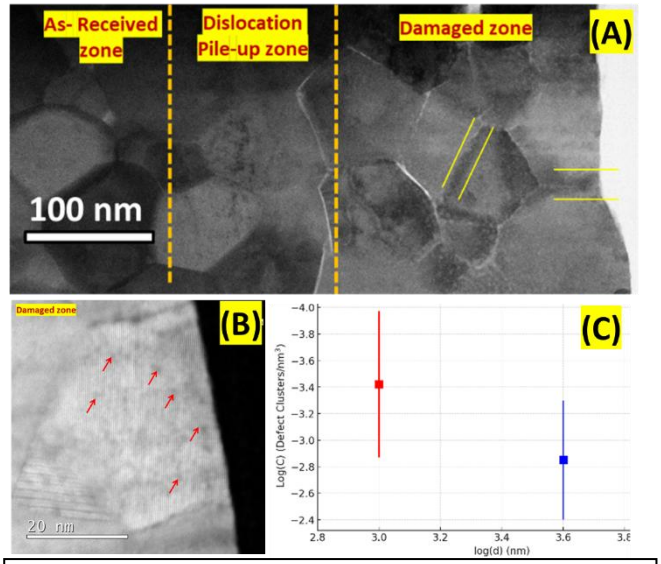

Fig. 3. (A) shows STEM image of Mn-doped CeO2 irradiated with heavy-ions. (B) shows high-magnification image of the damage zone, with red arrows showing defect clusters. (C) shows quantification of the defects for the Mn-doped (red) and the undoped CeO2 nanoceramics under similar radiation conditions.

As a preliminary study, we investigated radiation damage in Mn-doped nanocrystalline CeO_2, acting as a surrogate for UO_2, fabricated by spark plasma sintering. Manganese is known to segregate to the GBs of CeO_2, making this system a good preliminary platform for probing the influence of TM dopants on GB sink efficiency. The samples were irradiated with 400 keV Kr^{2+} ions in collaboration with Los Alamos National Laboratory, and Figure 3A presents representative scanning transmission electron microscopy (STEM) images of FIB-prepared lamellae after irradiation. The image shows three zones: one where damage is clearly observed near the surface, a region with dislocation pile-up, and an unaffected zone, bring consistent with the literature [7]. Interestingly, the BF-STEM shows the GB region in the "damage zone" has darker contrasts than the grain center, as indicated by the two parallel yellow lines. This could be explained by Mn-rich grain boundaries undergoing redox-driven structural distortion and oxygen-vacancy–assisted defect accumulation at the boundary. These changes increase static disorder and local strain, which scatter the electron beam more strongly and disrupt channeling, producing a darkened halo several nanometers into the adjacent grains. The observed contrast is therefore likely an indication of irradiation-enhanced GB chemistry and defect absorption, consistent with Mn acting as an active, redox-responsive defect sink under irradiation.

By using high magnification Dark and Bright Field images in STEM, we quantified the defect clusters presented in undoped and Mn-doped CeO_2, as seen in Figure 3B/C. Bright zones in

the STEM DF image indicate clusters comprised of higher thickness or accumulation of high Z elements (note that a high angle annular dark field (HAADF) detector was used for imaging and in a HAADF image, the intensity is proportional to square of Z, atomic number), while darker clusters suggest existence of vacancy rich zones. These clusters have reverse contrast in the BF images. While not enough area has been studied to narrow the error bars, the data suggests Mn-doped CeO_2 (red) shows reduced amounts of defects as compared to undoped. This is intriguing because Mn is expected to reduce the GB energy of CeO_2 [6], and as suggested in the sink *efficiency function*, lower grain boundary energies are expected to show reduced sink properties, indicating a missing term. This is further corroborated with literature data showing that while nanocrystalline YSZ exhibits improved radiation tolerance [7], lanthanum segregation, which lowers GB energy of YSZ [8,9], reduces the radiation tolerance. In that system, the large La^{3+} ions occupy energetically favorable sink sites, thereby diminishing overall sink strength [10].

The Mn-doped CeO_2 results therefore suggest a fundamentally different mechanism: rather than steric blocking of sink sites, the redox-active nature of Mn likely transforms the defect chemistry at GBs during irradiation, enabling more efficient point-defect annihilation.

While further atomic-scale characterization is required, the present findings strongly indicate that the irradiation-induced changes in oxidation state expected for Mn and other multivalent transition metals will directly influence how GBs function as point-defect sinks in nanocrystalline oxides.

The central vision of this project is to establish a fundamental connection between the redox behavior of TMs segregated to GBs and the radiation tolerance of GB-rich oxides by developing the *sink efficiency* concept.

References

1. G. Ackland, *Controlling Radiation Damage*, Science **327**, 1587 (2010).
2. A. Milena-Pérez, L. J. Bonales, N. Rodríguez-Villagra, M. B. Gómez-Mancebo and H. Galán, *Oxidation of accident tolerant fuel models based on Cr-doped UO_2 for the safety of nuclear storage facilities*, Journal of Nuclear Materials **582**, 154502 (2023).
3. A. J. Terricabras et al., *Performance and properties evolution of near-term accident tolerant fuel: Cr-doped UO_2*, Journal of Nuclear Materials **594**, 155022 (2024).
4. A. J. Terricabras et al., *Chromium doping effects on UO_2 grain-boundary chemistry: A combined experimental and modeling approach*, Journal of Nuclear Materials **617**, 156114 (2025).
5. S. C. Middleburgh et al., *Enrichment of chromium at grain boundaries in chromia-doped UO_2*, Journal of Nuclear Materials **575**, 154250 (2023).
6. L. Wu, S. Dey, M. Gong, F. Liu and R. H. R. Castro, *Surface segregation on manganese-doped ceria nanoparticles and relationship with nanostability*, Journal of Physical Chemistry C **118**, 30187 (2014).
7. S. Dey et al., *Radiation tolerance of nanocrystalline ceramics: Insights from yttria-stabilized zirconia*, Scientific Reports **5**, 7746 (2015).
8. A. Bokov, et al., *A strategy to mitigate grain-boundary blocking in nanocrystalline zirconia*, Journal of Physical Chemistry C **122**, 26344–26352 (2018).
9. A. Bokov et al., Energetic design of grain-boundary networks for toughening of nanocrystalline oxides, Journal of the European Ceramic Society 38, 4260–4267 (2018).
10. S. Dey et al., *Irradiation-induced grain growth and defect evolution in nanocrystalline zirconia with doped grain boundaries*, Physical Chemistry Chemical Physics **18**, 16921–16929 (2016).

Radiation-induced heterostructure formation

Marie A. Charpagne, Department of Materials Science and Engineering, University of Illinois at Urbana-Champaign, Urbana, IL.

Keywords: Irradiation, phase separation, immiscible alloys, correlative microscopy

Overview and scientific objectives

This project seeks to establish a new paradigm for the design of radiation-tolerant materials by leveraging irradiation as a tool for heterostructure formation, rather than solely viewing as a source of microstructure degradation. Conventional approaches to nuclear materials design focus on minimizing irradiation-induced microstructural evolution. In contrast, this work explores whether irradiation can be harnessed to create beneficial, chemical and defect architectures that are inaccessible through thermal processing alone. More specifically, his Early Career Faculty award focuses on the **fundamental mechanisms of phase separation in compositionally complex immiscible alloys during irradiation**, including identifying the role of ballistic mixing, thermal diffusion, radiation-induced segregation, and pre-existing microstructure features (grain boundaries, twins, etc.).

Starting steps

Our initial activities have focused on synthesizing metastable FCC alloys revolving around Fe-Cu as immiscible pair using DC magnetron sputtering. We target the model system FeNiCoCrCu and its binary, ternary, and quaternary subsets. The Ni/Co ratio allows to tune the stacking fault energy [1] while the Fe/Cu ratio tailors the width of the miscibility gap [2]. The first three alloys synthesized are $Ni_{80}Fe_{10}Cu_{10}$ (lattice parameter 0.365 nm), acting as a baseline system and a relatively simple ternary alloy with a well-documented equilibrium phase diagram [3], shown in fig.1a,b. The second alloy is $(Ni_{70}Co_{30})_{80}Fe_{10}Cu_{10}$, which exhibits a lower stacking fault energy hence a denser network of twin boundaries but a similar lattice parameter (0.36 nm), see fig.1c. Both alloys are grown to a thickness of 500-600 nm using >99.99% pure targets at room temperature, to achieve supersaturated single-phase FCC solid solutions (fig1b,c). The quinary NiCoFeCuCr high entropy alloy (HEA) was also synthesized, where contradicting findings have been reported previously regarding its phase separation during irradiation [4,5]. Irradiation experiments are conducted at UIUC's Materials Research Laboratory (MRL) using a Pelletron system and 2 MeV Ti ions at a 10° incidence angle. The irradiation chamber is maintained in a high vacuum with a base pressure $< 5 \times 10^{-8}$ torr at 450°C. The projected damage profile, generated using the SRIM software, is presented in fig1d. Each irradiation experiment is carried out using a shutter system, to pinpoint the effect of irradiation in light of thermal diffusion. Next steps include TEM characterization of annealed and irradiated samples across doses in the range 2-30 dpa, focusing on the topology of phase separation.

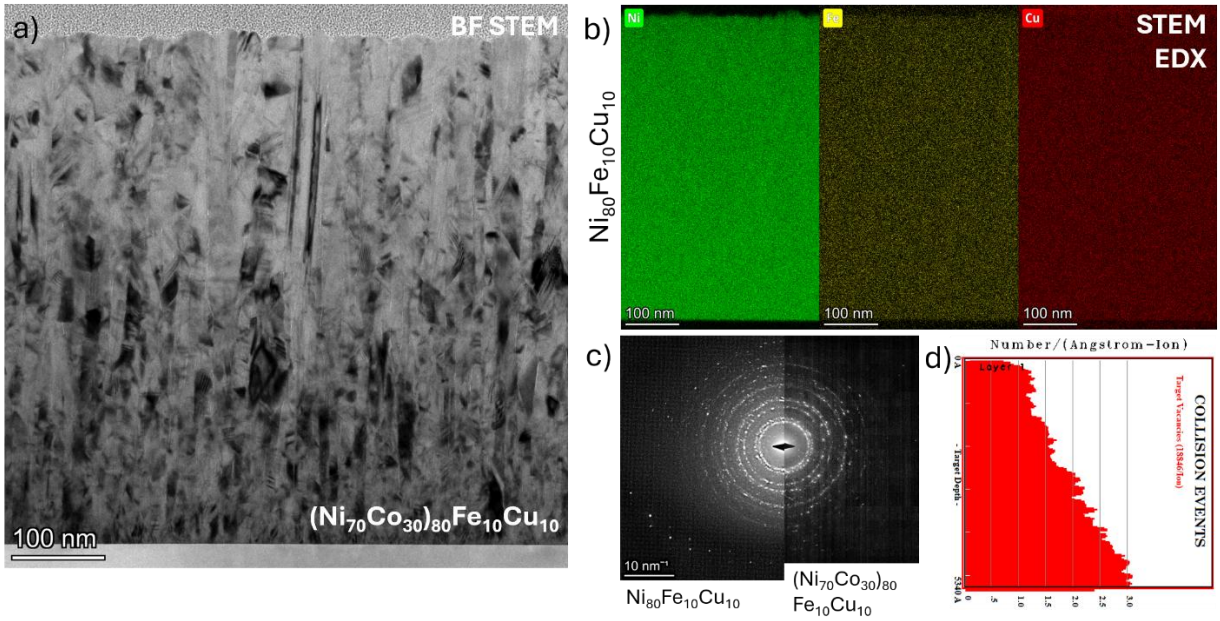

Fig.1. As-grown microstructures. a) bright-field STEM micrograph of $(Ni_{70}Co_{30})_{80}Fe_{10}Cu_{10}$, b) STEM EDS maps of $Ni_{80}Fe_{10}Cu_{10}$ showing a homogeneous solid solution, c) diffraction patterns of both ternary (left) and quaternary (right) alloys showing a single FCC phase, with similar lattice parameters d) SRIM simulations of irradiation damage in the ternary alloy with 2MeV Ti ions.

References

[1] Li-Yun Tian, Raquel Lizárraga, Henrik Larsson, Erik Holmström, Levente Vitos, A first principles study of the stacking fault energies for fcc Co-based binary alloys, Acta Materialia, Volume 136, 2017, Pages 215-223, https://doi.org/10.1016/j.actamat.2017.07.010 .

[2] Shichao Liu, Jinchuan Jie, Bowen Dong, Zhongkai Guo, Tongmin Wang, Tingju Li, Novel insight into evolution mechanism of second liquid-liquid phase separation in metastable immiscible Cu-Fe alloy, Materials & Design, Volume 156, 2018, Pages 71-81, https://doi.org/10.1016/j.matdes.2018.06.044.

[3] Liya A. Dreval, Mikhail A. Turchanin, Pavel G. Agraval, Thermodynamic assessment of the Cu–Fe–Ni system, Journal of Alloys and Compounds, Volume 587, 2014, Pages 533-543, https://doi.org/10.1016/j.jallcom.2013.10.223.

[4] Yanwen Zhang, Matheus A Tunes, Miguel L Crespillo, Fuxiang Zhang, Walker L Boldman, Philip D Rack, Li Jiang, Chen Xu, Graeme Greaves, Stephen E Donnelly, Thermal stability and irradiation response of nanocrystalline CoCrCuFeNi high-entropy alloy, Nanotechnology, Volume 30, Number 29, 2019 https://doi.org/10.1088/1361-6528/ab1605

[5] Li Jiang, Yong-Jie Hu, Kai Sun, Pengyuan Xiu, Miao Song, Yanwen Zhang, Walker L. Boldman, Miguel L. Crespillo, Philip D. Rack, Liang Qi, William J. Weber, Lumin Wang, Irradiation-Induced Extremes Create Hierarchical Face-/Body-Centered-Cubic Phases in Nanostructured High Entropy Alloys, Advanced Materials, 2020, https://doi.org/10.1002/adma.202002652

Role of nanoscale heterogeneities on charged species transport in oxide and oxide growth

Adrien Couet[1,2], Yongfeng Zhang[1,2], Jennifer T. Choy[3]

[1]Department of Nuclear Engineering and Engineering Physics, University of Wisconsin-Madison; [2]Department of Materials Science and Engineering, University of Wisconsin-Madison; [3]Department of Electrical and Computer Engineering, University of Wisconsin-Madison

DOE BES Award DE-SC0023873

Keywords: Corrosion, Space Charge, Metal/Oxide Interfaces, 4D-STEM, Charged-Species Transport

Program Scope

Classical high-temperature oxidation models treat the growing oxide as chemically and structurally homogeneous and reduce transport to one dimension [1], yet real oxide scales routinely contain embedded nanoscale heterogeneities, such as metallic and/or oxidized precipitates/clusters, and grain-boundary networks [2]. At each inclusion/oxide interface, Fermi-level alignment and interfacial defect chemistry generate space-charge regions whose fields can extend tens to hundreds of nanometers into the oxide, reshaping the coupled ionic and electronic transport that controls oxide growth. This project tests the hypothesis that such nanoscale heterogeneities induce heterogeneous fluxes of charged species through their interfaces. Using nanoscale metallic inclusions (NMIs) in ZrO_2 and model metal/semiconductor systems with controlled heterogeneity, we couple density functional theory (DFT) and continuum electrostatic modeling with a co-registered experimental toolkit: 4D-STEM center-of-mass (CoM) electric-field mapping [3], correlative electron microscopy and spectroscopy, ^{18}O isotopic tracing with atom probe tomography (APT), and nitrogen-vacancy (NV) center magnetometry. The award addresses three Science Questions: (SQ1) charge distribution at flat oxide/metal (O/M) interfaces, (SQ2) charge distribution around embedded NMIs as a function of their size, shape, and chemistry, and (SQ3) the resulting steady-state ionic and electronic flux distributions. The project has been recommended for a 3-year renewal that extends these questions from static space-charge landscapes to flux partitioning and their effects on O/M interface morphology evolution.

Recent Progress

Short- and long-range charge redistribution at O/M interfaces (SQ1, SQ2). We developed a unified multiscale description of charge redistribution at O/M interfaces by coupling DFT with a continuum electrostatic model, using ZrO_2 facing FCC metals (Au, Ag, Al) as model systems [P3]. DFT reveals a short-range redistribution confined to a few atomic layers whose character depends on the metal. For noble metals (Au, Ag) it is dominated by metal-induced gap states (MIGS) and the associated interfacial dipole while for reactive metals (Al), interfacial chemical bonding dominates and can reverse the direction of electron transfer expected from work-function arguments alone. The DFT-informed continuum analysis then propagates these interfacial boundary conditions into the oxide. Electron depletion layers develop for all metal contacts, with Schottky barrier heights controlled primarily by the metal work function and depletion-layer

widths controlled by the oxide doping level, extending from a few nanometers in heavily doped oxide to hundreds of nanometers in the weakly doped limit relevant to thermally grown ZrO_2 (see Fig. 1). These results quantify how NMI chemistry and oxide doping jointly set the extent of the electrostatic "impact zone" around an inclusion, and parameterize the mesoscale flux models developed under SQ3.

Direct measurement and decomposition of interfacial electric fields by 4D-STEM (SQ1). To validate CoM imaging as a quantitative probe of interfacial electrostatics, we measured the projected electric field across an epitaxial ZrN(111)/GaN(0001) heterojunction grown by Molecular beam epitaxy (MBE), an atomically sharp model metal/wide-bandgap-semiconductor analog of an NMI/oxide interface. Microcleaved cross-sections were mapped by 4D-STEM with an annular CoM mask and a vacuum-reference correction, yielding an abrupt interfacial field of $E_x \sim 5\times10^9$ V/m localized within ~1 nm of the interface. To interpret this signal, we constructed a quantitative decomposition of the measured CoM shift into its physical components, namely,

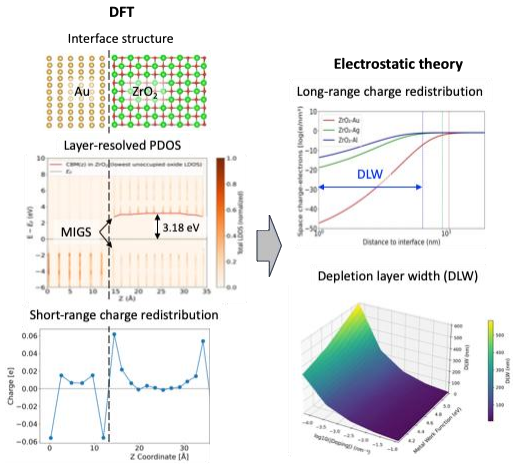

Figure 1. Combined DFT and continuum electrostatic description of metal/ZrO_2 interfaces: layer-resolved projected density of states showing metal-induced gap states (left) and long-range space-charge redistribution and depletion-layer width vs. oxide doping predicted by the DFT-informed continuum model (right) [P3].

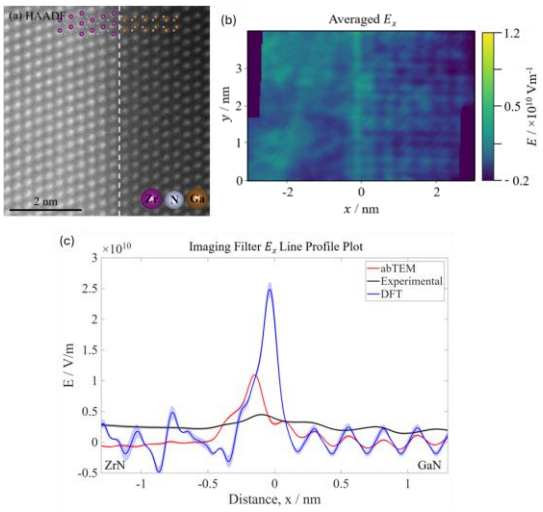

Figure 2. 4D-STEM CoM measurement of the ZrN/GaN interfacial electric field: (a) HAADF image of the interface and DFT relaxed structure; (b) experimental E_x map and (c) line profiles from experiment, abTEM, and DFT, agreeing in magnitude and sign of the MIP-dominated interfacial step.

the mean-inner-potential (MIP) step, the interfacial charge-transfer dipole, flexoelectric contributions, band bending in the GaN depletion region, and dynamical-scattering artifacts. Multislice simulations (abTEM) on the DFT-relaxed structure reproduce the thickness dependence of the measured field, showing that dynamical scattering and spatial averaging reduce the apparent interfacial field from $\sim1.2\times10^{10}$ V/m in the thin limit to $\sim5\times10^9$ V/m at the experimental thickness, in agreement with experiment (Fig. 2). Sign-consistent DFT slab calculations independently reproduce the MIP-dominated interfacial step. An analytic electrostatic budget anchored to literature polarization constants confirms the hierarchy that the MIP step ($\sim10^{10}$ V/m) dominates the interfacial response by roughly two orders of magnitude over

the polarization-induced interfacial dipole (~10^8-10^9 V/m), with flexoelectric contributions (≤10^8 V/m) and depletion-region band bending (~10^6 V/m over ~100s nm) well below the current single-scan detection limit. This workflow is the methodological foundation for quantitative space-charge mapping around NMIs in oxides, and a manuscript is in preparation.

Linking chemical and microstructural heterogeneity to electronic-defect landscapes in thermally grown ZrO_2 (SQ2). In parallel with the model-interface work, we demonstrated cross-sectional SEM-cathodoluminescence (SEM-CL) correlation microscopy as a mesoscale probe of electronic-defect heterogeneity in corrosion-grown oxides [P4]. By co-registering SEM-CL with electron backscatter diffraction (EBSD) and electron probe microanalysis (EPMA) on the same ZrO_2 cross-sections grown on Zr alloy, we showed that the CL response, dominated by the ~2.7 eV defect band, is strongly modulated by the underlying microstructure and chemistry. CL intensity increases with grain area and decreases in grain-boundary-rich regions, consistent with enhanced non-radiative recombination at microstructural disorder, and a substantial fraction of CL-dark features co-localize with Fe-enriched precipitates, the naturally occurring NMIs of Zr alloy corrosion (see Fig. 3). These results establish CL as a sensitive mesoscale technique to connect local electronic-defect landscapes to the heterogeneities hypothesized to bias charged-species transport, directly on realistic corrosion-grown oxides.

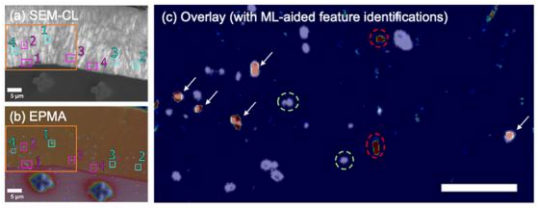

Figure 3. (a) SEM-CL and (b) EPMA Fe maps with (c) ML-aided overlay, showing CL-dark features co-localized with Fe-enriched precipitates; grain-boundary quenching is established by co-registered EBSD [P4]. The scalebar is 5 μm.

Toward flux quantification: tracer transport, heterogeneity libraries, NV magnetometry, and mesoscale modeling (SQ3). Three capabilities serving SQ3 matured over the reporting period. First, a correlative ^{18}O-tracer/APT/TEM study provided direct evidence that grain boundaries in autoclave-grown ZrO_2 act as preferential oxidizing species transport pathways [P1]. Second, we established engineered heterogeneity libraries in which monodisperse Au nanoparticles are spin-coated and encapsulated in PVD-grown ZrO_2 at Argonne's Center for Nanoscale Materials, with independently tunable NMI size, spacing, and volume fraction. Third, the NV-center widefield magnetometry platform for imaging current distributions is now operational on lithographically defined calibration circuits. The field-to-current inversion recovers the applied current-density distribution with peak amplitude within ~15% of the simulated ground truth, at a measured magnetic-field sensitivity of ~4 μT/√Hz and a projected current sensitivity of ~200 μA/√Hz. Our sensitivity is limited by the large (~5 μm) NV-to-conductor standoff distance and ODMR contrast and we are working on addressing both issues. The same ODMR platform resolves local Joule-heating features through the temperature dependence of the NV zero-field splitting, opening a route to simultaneous current and temperature mapping [4]. The experimental quantification of flux will be complemented by mesoscale modeling, for which a phase field model

of electrochemistry [5,6] is being extended to include NMIs for their impact on charge carrier transport and oxide growth.

Future Plans

The immediate priority is to transfer the validated 4D-STEM decomposition workflow from the flat ZrN/GaN benchmark to embedded NMIs. CoM mapping of the Au/ZrO_2 heterogeneity libraries is underway, targeting the space-charge "impact zones" around individual inclusions, with cross-sectional Kelvin probe force microscopy (with Prof. V. Brar, UW-Madison) providing an independent potential-sensitive cross-validation of the electrostatic length scales. In parallel, ^{18}O tracer exposures of the engineered NMI/ZrO_2 stacks will be performed and reconstructed in 3D by APT to map oxygen transport around NMIs. A feasibility campaign on Au-nanoparticle/ZrO_2 model tips (Fig. 4) is optimizing run parameters and trajectory-aberration corrections ahead of tracer runs. The NV magnetometry effort will reduce the sensor standoff with thinner diamond membranes, targeting ~1 μm resolution, and exploit the temperature dependence of the ODMR response for combined current/temperature imaging.

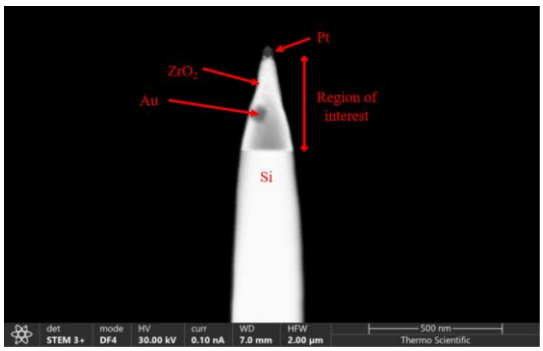

Figure 4. APT tip prepared from a PVD ZrO_2 film containing spin-coated Au nanoparticles on Si, used to optimize run parameters and analysis protocols so that trajectory aberrations around the inclusion do not obscure ^{18}O tracer visualization in corrosion-exposed samples.

Under the recommended renewal, these capabilities converge on three new SQs that move the program from static space-charge landscapes to transport and morphology: (SQ2.1) how NMI size, chemistry, and spatial statistics set steady-state ionic and electronic flux distributions, combining the co-registered field/tracer/current toolkit with self-consistent Poisson-drift-diffusion models parameterized by DFT; (SQ2.2) how oxide doping modulates NMI-induced space charge and flux channels, using dopant-controlled epitaxial analogs grown by MBE and ion-implanted ZrO_2/NMI libraries; and (SQ2.3) how heterogeneity-shaped fluxes, in competition with interfacial energies, select O/M interface morphology and growth kinetics, using a moving-boundary phase-field framework implemented in MOOSE [5,6]. The outcome will be an experimentally anchored multiscale framework linking nanoscale interfacial charge redistribution to macroscopic oxidation behavior in heterogeneous oxides.

References

[1]. D. D. Macdonald, The history of the Point Defect Model for the passive state: A brief review of film growth aspects, Electrochimica Acta 56, 1761–1772 (2011); [2]. J. Hu, A. Garner, N. Ni, A. Gholinia, R. J. Nicholls, S. Lozano-Perez, P. Frankel, M. Preuss, and C. R. M. Grovenor, Identifying suboxide grains at the metal–oxide interface of a corroded Zr–1.0%Nb alloy using (S)TEM, transmission-EBSD and EELS, Micron 69, 35–42 (2015). [3]. S. Toyama, T. Seki, B. Feng, Y. Ikuhara, and N. Shibata, Direct observation of space-charge-induced electric fields at oxide grain boundaries, Nature Communications 15, 8704 (2024) [4]. K. Chang, A. Eichler, J. Rhensius, L. Lorenzelli, and C. L. Degen, Nanoscale Imaging of Current Density with a Single-Spin Magnetometer, Nano Letters 17, 2367–2373 (2017). [5]. Q. C. Sherman and P. W. Voorhees, Phase-field model of oxidation: Equilibrium, Physical Review E 95, 032801 (2017). [6]. Kim, K., Sherman, Q. C., Aagesen, L. K. & Voorhees, P. W. Phase-field model of oxidation: Kinetics. Phys. Rev. E 101, 22802 (2020).

Publications resulting from work supported by the grant over the previous two years

P1. J. Liu, F. Xue, W. Zhang, H. Zhang, P. Frankel, G. Lucadamo, W. Howland, M. Moody, P. Bagot, C. Grovenor, E. A. Marquis, and A. Couet, Evidence for hydrogen and oxygen diffusion through grain boundaries in autoclave formed oxides on Zircaloy-4: A correlative APT and TEM study, Corrosion Science 253, 112981 (2025).
P2. Y. Tong, M. Zahedian, A. Zeng, R. Vidrio, M. Efremov, S. Yin, H. Mei, P. Heaney, and J. T. Choy, Tuning the surface energy of fluorinated diamond-like carbon coatings via plasma immersion ion implantation plasma-enhanced chemical vapor deposition with 1,1,1,2-tetrafluoroethane, Diamond and Related Materials 156, 112365 (2025).
P3. X. Wang, Y. Zhang, D. Skachkov, A. Das, J. Liu, A. Kvit, J. Choy, and A. Couet, Charge redistribution at metal–ZrO_2 interfaces: a combined DFT and continuum electrostatic study, Applied Surface Science 739, 166999 (2026).
P4. R. Vidrio, Y. Tong, J. Liu, B. Schneider, W. O. Nachlas, N. Curtis, M. Zahedian, A. Kvit, H. Zhang, Z. Yu, X. Wang, Y. Zhang, A. Couet, and J. T. Choy, Mapping optical, chemical, structural features in ZrO_2 via cross-sectional SEM-Cathodoluminescence correlation microscopy, Journal of Luminescence 298, 122104 (2026).

Understanding the effect of stress on complexion transitions and the interplay with creep in thermally stabilized nanocrystalline materials

Maarten P. de Boer, Gregory S. Rohrer, Elizabeth C. Dickey, Carnegie Mellon Univ.

Keywords: complexions, stress, creep, nanomechanical test platform

Research Scope

The structure and composition of a grain boundary comprise a grain boundary phase, also known as a complexion. Elemental segregation to grain boundaries can control material properties including ductility, strength and thermal stability. The amount of segregation can change with temperature, sometimes requiring diffusion. In this project we seek to determine if complexion transitions can be induced by stress, as is theoretically predicted. If so, we hypothesize that the material's mechanical behavior will be altered. We employ a newly-developed nanomechanical test platform to induce stress-assisted complexion transitions and measure their effect on creep.

Recent Progress

Solute segregation to grain boundaries is a well-known phenomenon. In all prior observations of grain boundary segregation in binary alloys, it is the minority component of the alloy (solute) that segregates to the grain boundary. However, it is also possible that solvent enrichment reduces the grain boundary energy, as shown by several theoretical models.

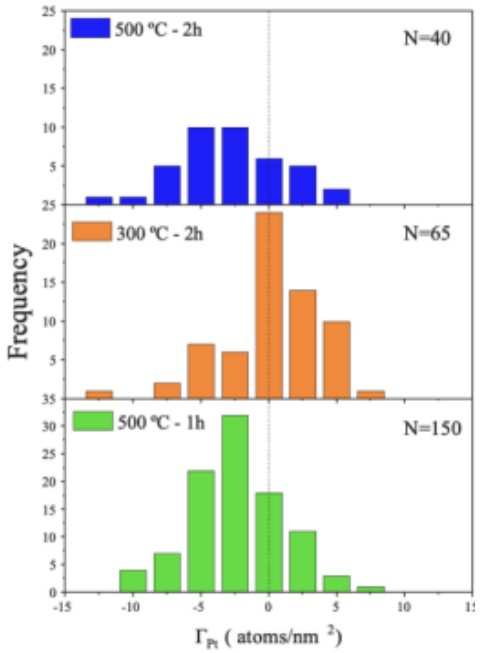

Fig. 1. EDS data of Pt interface concentration after anneals at three temperatures

Indeed, we have discovered a reversible solvent segregation-based complexion transition in a Au-rich Au-Pt binary alloy [1]. The top panel in **Fig. 1** shows a histogram of grain boundary composition, measured by energy dispersive spectroscopy, indicating that Pt is depleted from the grain boundaries in a Au-Pt alloy after annealing at 500 °C. The middle panel shows that on average, the Pt concentration after a subsequent 300 °C anneal is equal to its concentration in the bulk film. The bottom panel shows that the boundaries are again Au-rich after a second anneal at 500 °C. The data are taken on 50 nm thick sputtered Au-Pt films.

The transition from a stoichiometric boundary to a Au-rich boundary occurs heterogeneously. In other words, most, but not all, grain boundaries undergo this transition in a certain temperature range. This is reflected in the distribution of grain boundary compositions indicated in **Fig. 1**. We hypothesized that the anisotropy of grain boundary energy is responsible for the heterogeneity. To test this, we correlated the energies of about 90 grain boundaries with their compositions, and

found that at 500 °C, the highest energy grain boundaries were more likely to have transformed to the Au enriched state than the lower energy grain boundaries (see **Fig. 2**). This explains the heterogeneity of the transition. The finding is also consistent with the thermodynamic theory of complexions, but this aspect had not before been experimentally verified. A paper on this work is in preparation [2]. Another paper that explains why the Cu-Zr system originally proposed has been abandoned is under review [3].

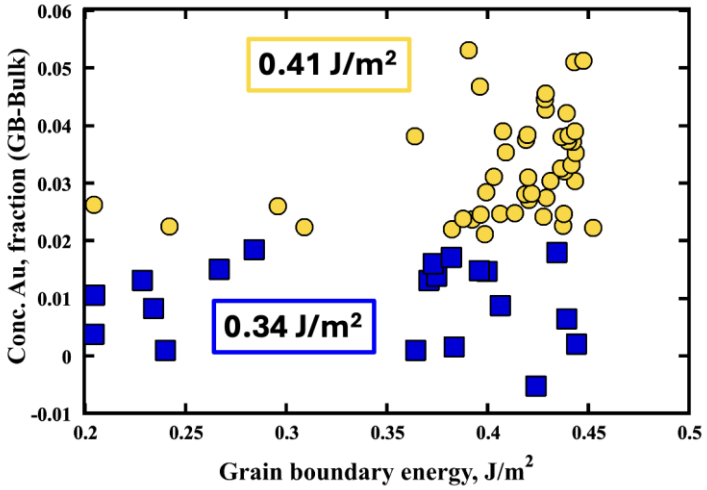

Fig. 2. Grain boundary Au-excess versus grain boundary energy. Each point represents a different observed grain boundary. Points with Au concentrations less than our threshold sensitivity, colored blue, are considered stoichiometric. Those enriched with Au by an amount greater than our sensitivity are colored yellow. The grain boundaries enriched in Au had an average energy of 0.41 J/m^2 while those that are stoichiometric had an average energy of 0.34 J/m^2, consistent with the hypothesis that higher energy grain boundaries preferentially transform to the Au enriched state.

The new phenomena documented by this research include solvent segregation, the reversibility of complexion transitions, and the relationship between grain boundary energy and complexion transitions. These findings advance our scientific knowledge of grain boundary complexion transitions and motivate our continued research.

While the complexion transition occurs by changing temperature, a stress change occurs at the same time, and cannot be ruled out. This is because the film is supported on a substrate with a different coefficient of thermal expansion (CTE).

We have developed a micromachined mechanical test platform allows us to decouple stress from temperature. **Fig. 3** shows an optical micrograph of an individual platform. It consists of a 100 nm thick specimen (here pure Au), a thermal actuator, a folded-beam load cell, and verniers. The thermal actuator is made with tantalum, with a ~2X larger CTE than the silicon substrate. As such, upon heating the platform, it is self-actuating and the specimen is isothermal.

About 8000 platforms are co-fabricated on a 4” wafer. Individual chips are cleaved for a test, and ten or more platforms are simultaneously tested. This is accomplished by continuously translating an xy stage in-plane to different platforms, auto-focusing with a high magnification optical microscope, and applying a pattern matching routine to detect specimen length changes over time. Platforms with load cells of different stiffnesses are co-fabricated side-by-side. At any given temperature, a wide range of stress is applied, thereby decoupling stress from temperature.

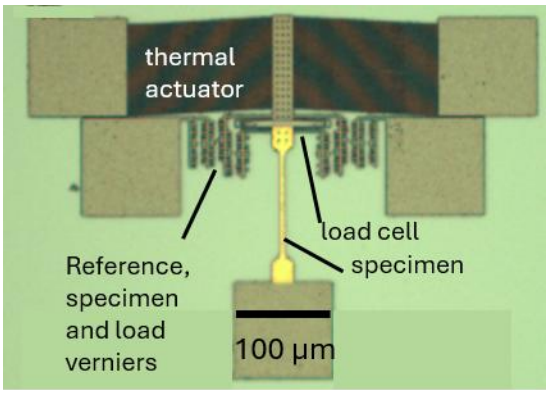

Fig. 3. Optical micrograph of a micromachined creep platform.

With this platform, the issues of gripping and alignment, which have been challenging for small scale mechanical testing since its inception, are solved. Focused ion beam milling is not used in the process flow, and therefore radiation damage is removed as a potential experimental artifact. As such, the platform represents an important advance in testing mechanical behavior at the nanoscale.

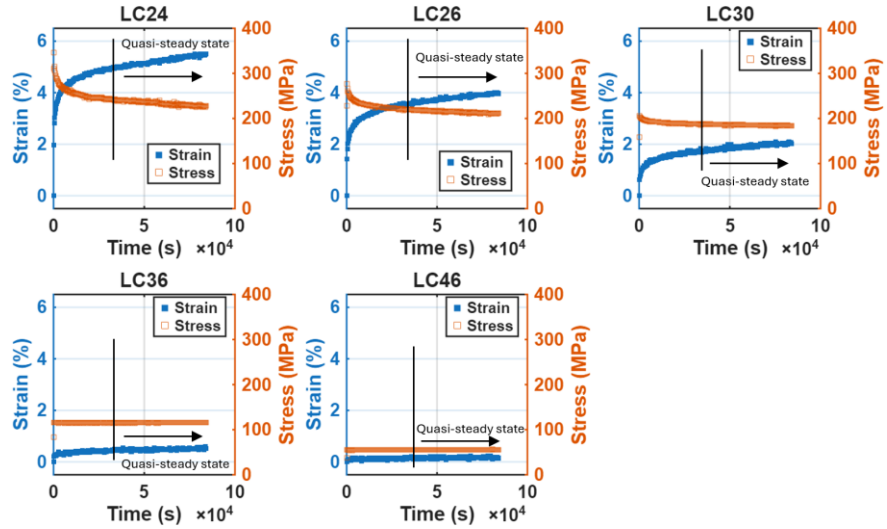

Fig. 4. Creep data from five co-fabricated platforms on a chip. The platforms are tested simultaneously in air at 100 °C. LCDD represents the length of the folded-beam load cell legs, where DD is in µm. The specimens are 100 nm thick Au sputtered at RT. The Au is annealed at 180 °C during the process flow but before release to densify and eliminate voids. The grain size is ~30-50 nm.

Example test results on five platforms tested in parallel are seen for an 80,000 s (0.93 day) test in **Fig. 4**. In this case, creep testing is conducted at 100 °C. Upon the initial temperature ramp to 100 °C, the Ta thermal actuators displace to impose a large stress. The specimen begins to creep. Stress σ decreases monotonically with load cell length, as expected. Likewise, the strain rate, $\dot{\varepsilon}$, decreases with stress. Rather than assuming a constant strain rate, the data is fit to a standard creep equation, $\dot{\varepsilon} = A\sigma^n$ after a quasi-steady state condition at 30,000 s is reached. This equation is integrated, and a stress exponent $n = 2.2$ is found.

Current work involves optimizing test protocols. In particular, it seems possible to gain data at multiple stresses and temperatures from a single chip. This will increase test throughput – always an issue in creep testing. From application of the thermally assisted glide model, it should be possible to extract the stress exponent at each temperature, apparent activation energy and apparent activation volume versus temperature, and 0 K energy barrier. We have recently processed Au-Pt platforms annealed to produce grain boundaries with two distinct complexion distributions, and will soon begin testing these devices.

We have published several papers on the platform that acknowledge support from this grant [4-6]. Papers on bend strength of anisotropically-etched Ta [7] and on Au creep with grain size 30 to 50 nm [8] are in preparation and will acknowledge this grant.

Future Plans

The overarching plan is to create microstructures with different grain boundary complexions, test them with the creep platform and gain understanding of the associated mechanisms. Distinctions due to complexion states can be most simply inferred from creep strain rates at similar conditions of stress and temperature. Scientifically, parameters from the thermally assisted glide model can also be extracted. We have at least two test approaches. The first is to leverage the discovery that thermal cycles induce complexion transitions. Accordingly, Au-Pt specimens annealed at 500 °C, and at 500/300 °C and then quenched will have different complexions. These can be tested to determine how different complexions affect creep. Second, Au-Pt specimens annealed at some lower temperature, e.g. 180 °C to remove voids, can be creep-tested at different temperatures below the anneal temperature. At each temperature, different stresses will be applied on adjacent platforms. A change in the activation energy or stress exponent for specimens at different stresses will be a direct signature that stress-induced complexion transition changes affect creep.

One focus will be on the mechanism for the difference in creep for the different complexions. It should be noted that a stress exponent $n \approx 2$, as observed for pure Au, is often associated with grain boundary sliding (GBS). However, a given stress exponent does not directly identify the actual mechanism. A standard model for GBS involves glide and climb of dislocations near grain boundaries, i.e., not necessarily deformation behavior within the boundary itself. If this is the mechanism, different complexions may not affect creep. However, GBS is a complicated phenomenon involving compatibility. The dislocations in this standard model must encounter and be transmitted at triple junctions, and this process is likely affected by the triple junction nature. The Rachinger model involves GBS and little grain shape change while the Lifshitz model invokes grain elongation. For sufficiently small grains, Coble creep is expected, which is associated with grain boundary diffusion. In that case the expected stress exponent is 1, no GBS is required, but this condition can lead to superplasticity. Other models for GBS invoke a glassy phase within the boundary that is amenable to sliding. In this case, the boundary structure is directly related to its viscosity. If understanding to control the stress exponent to a value well below 2 is gained, superplastic deformation near room temperature could be attained in a controllable way.

A second focus will be on the mechanism that causes a stress-induced complexion transition. To this end, we have made much progress on a platform process flow in which there is a through-wafer hole directly under the specimen. Multiple platforms will be in an TEM specimen holder. Using a Gatan double tilt holder with temperature control, it should be possible to examine in-situ which temperature and stress conditions, and which grain boundaries therein, give rise to a complexion transition.

Publications supported by this grant (3 published, 1 under review, 4 in preparation)

[1] S. Calderon, W.-Y. Chen, M. S. Islam, S. S. Tripathy, M. P. de Boer, E. C. Dickey, and G. S. Rohrer, "A reversible solvent segregation transition at grain boundaries in gold-platinum alloys," *Scripta Materialia,* vol. 269, p. 116902, 2025.

[2] W. Y. Chen, M. S. Islam, J. W. Pan, M. P. de Boer, G. S. Rohrer, and E. C. Dickey, "Grain boundary heterogeneity in Au-Pt films subjected to varying anneal temperatures " *To be submitted,* 2026.

[3] W. Y. Chen, M. S. Islam, M. P. de Boer, E. C. Dickey, and G. S. Rohrer, "Influence of Zr and O on the morphological stability of Cu-Zr thin films," *submitted,* 2026.

[4] R. M. Pocratsky, M. S. Islam, L. Ni, E. J. Fox, and M. P. de Boer, "Oxygen diffusion in freestanding body centered cubic tantalum structural thin films in air and in high vacuum," *Thin Solid Films,* vol. 800, p. 140392, 2024.

[5] M. S. Islam, L. Ni, and M. P. de Boer, "Anisotropic reactive ion etching of 2.5 micrometer thick alpha phase tantalum films for surface micromachining," *Micro and Nano Engineering,* vol. 28, p. 100305, 2025.

[6] M. S. Islam and M. P. d. Boer, "Uniform Whole Wafer Anisotropic Etching of Structural Ta Thin Films," *Journal of Microelectromechanical Systems,* vol. 35, no. 3, pp. 429-439, 2026.

[7] X. P. Li, J. W. Pan, and M. P. de Boer "In-situ in-plane bend strength measurement of structural tantalum films using a self-actuating MEMS test platform," *to be submitted,* 2026.

[8] X. P. Li, J. W. Pan, and M. P. de Boer "Creep of ultrathin gold films using a self-actuating nanomechanical test platform," *to be submitted,* 2026.

No effect of curvature on the radiation response of Cu-Nb phase boundaries

M. J. Demkowicz[1], K. Y. Xie[1]

[1]Department of Materials Science and Engineering, Texas A&M University, College Station, TX 77843

Keywords: Radiation, interfaces, curvature, metal composites, TEM

Research Scope

The objective of this work is determine whether curvature affects the response of solid-state interfaces. We are motivated by the hypothesis that interface curvature increases interface sink efficiency by introducing additional, atomic-level defect sites that attract and absorb radiation-induced defects.

Our work focuses on phase boundaries between copper (Cu) and niobium (Nb). These elements do not form compounds and exhibit negligible solid solubility. Thus, interfaces between them are atomically sharp and easy to image. Previous investigations have shown that flat Cu-Nb interfaces are effective at reducing radiation-induced damage. Moreover, nanocomposites with curved Cu-Nb interfaces have been prepared by annealing nano-layered samples. Future nuclear materials call for intricate, hierarchical microstructures, whose ultimate performance depends on highly curved interfaces. However, the effect of curvature on radiation response of interfaces (including those between Cu and Nb) has not been investigated before. Our work fills this gap.

Our work assesses radiation response by measuring the size, density, and distribution of radiation-induced voids at phase boundaries and within their vicinity. Radiation-induced void formation originates from the generation of vacancies and self-interstitial atoms (SIAs) by atomic displacements caused by incident high energy particles. SIAs are rapidly absorbed by sinks while the remaining vacancy supersaturation drives void nucleation and growth. Void density at a given location is therefore an indirect indicator of the local radiation-induced vacancy supersaturation. Planar sinks, such as boundaries or free surfaces, are often flanked by void depleted zones (VDZs). In VDZs, vacancy supersaturation is reduced by vacancy absorption by the sink. Void distributions within VDZs may therefore be analyzed to quantify the effectiveness of planar sinks for absorbing vacancies.

Recent Progress

We examine void densities in the Cu-Nb tri-layer composite shown in Fig. 1. This sample exhibits a wide range of local phase boundary curvatures. We develop algorithms for determining local void densities in the interior of the Cu layer and at Cu-Nb interfaces. We also determine local

interface curvatures numerically. A key aspect of our work is uncertainty estimation and propagation.

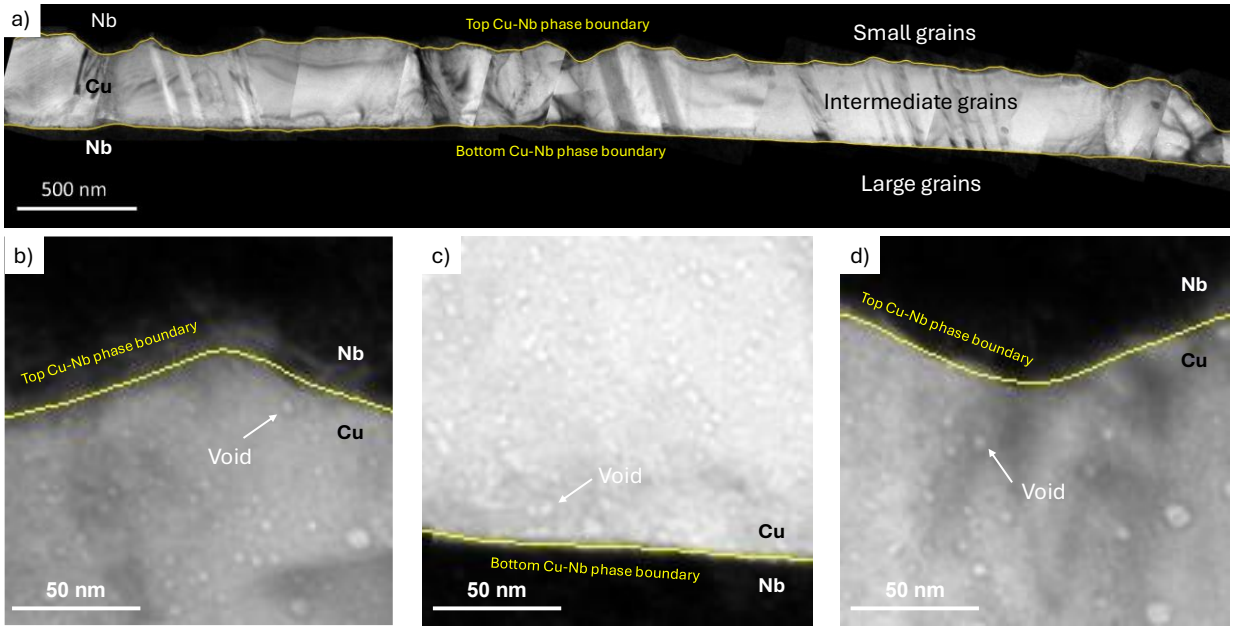

Fig. 1 a) Stitched BF-TEM images of the irradiated Nb-Cu-Nb tri-layer sample. Interfaces are marked with yellow lines. Images are taken in under-focus (800 nm) to reveal nanoscale voids. Examples of void distributions near interfaces of b) positive, c) zero, and d) negative curvature are shown.

Our analysis shows that neither void densities at Cu-Nb interfaces—shown in Fig. 2)—nor the characteristics of VDZs flanking Cu-Nb interfaces show any statistically significant dependence on interface curvature. This observation indicates that changes in the structure of Cu-Nb interfaces induced by curvature have no measurable effect on the void nucleation rate, void growth rate, interface sink efficiency, or the range of interaction between interfaces and radiation-induced vacancies. The implication of this finding for the design of radiation resistant nanocomposites is that interface curvature may be varied freely without affecting radiation response. Consequently, interface curvature in such composites may be adjusted to optimize other properties, such as mechanical response or thermal stability, while maintaining high radiation resistance.

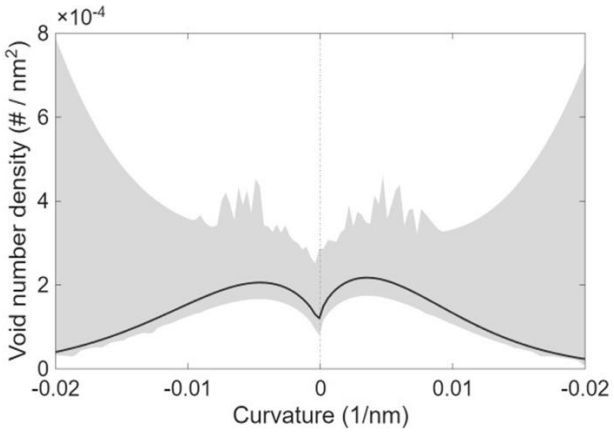

Fig. 2 Void density per unit interface area computed as a function of curvature. Gray bands denote uncertainties.

Our experiments also permit us to estimate void nucleation rates. We find that they are far greater than the rates predicted by classical nucleation theory. We are able to obtain a good match between experiments and theory if we assume a substantially reduced surface energy of voids in Cu. Our conclusions align with prior work of S. Zinkle and colleagues, who showed that impurities—such as oxygen (O)—promote void nucleation by reducing void surface energy.

Future Plans

This project is sunsetting, so our goals are to finish all our analyses, submit papers, present results at conferences, etc.

Publications

1. G. A. Turner, E. Sheu, D. Yadav, J. Singh, Y. Q. Wang, K. Xie, and M. J. Demkowicz, *No effect of curvature on the radiation response of Cu-Nb phase boundaries*, Acta Materialia **submitted** (2026).
2. K. Y. Xie, D. Yadav, K. Cooper, Y. Lu, J. Howard, M. Hansen, R. R. Chauhan, J. H. Park, S. Lee, Y. Park, A. Phong, G. D. Sim, Y. Wu, L. Shao, and M. J. Demkowicz, *Abnormal Grain Growth Driven by Proton Irradiation in Nanocrystalline Ni*, Nuclear Instruments and Methods B **572**, 166009 (2026).
3. T. Y. Liu, E. Sheu, M. Tavakolzadeh, D. J. Williams, J. K. Baldwin, and M. J. Demkowicz, *Reduction of vanadium diffusivity within copper grain boundaries due to enhanced binding*, Scripta Materialia **258**, 116515 (2025).
4. D. Yadav, B. K. Derby, M. Powers, J. K. Baldwin, Y. Q. Wang, A. Misra, K. Y. Xie, and M. J. Demkowicz, *Influence of implantation temperature and He implantation-induced defects on morphological evolution of co-deposited Cu-Mo nanocomposites*, Journal of Nuclear Materials **607**, 155645 (2025).

Fundamental Insights into Defect Generation and Transport at Extended Defects for Resilient Energy Materials

S. Dillon[1], W. Neilson[2], J. White[2], M. Cooper[2], D. Andersson[2], Y. Wang[2], B. Uberuaga[2], K. Burke[3], S. Finkeldei[3]
[1]University of California, Irvine, Department of Materials Science and Engineering;
[2]Los Alamos National Laboratory, Materials Science and Technology Division;

[3]University of California, Irvine, Department of Chemistry

Keywords: grain boundaries, nucleation kinetics, interface mediated creep, swelling/bubble growth

Research Scope

Grain boundary (GB) transport controls many processes that determine the evolution of structural and nuclear materials. Classical models for interface mediated strain treat point-defect sources and sinks as continuously available [1]. That approximation fails when climb mediating sinks must first be nucleated. Our recent bicrystal creep experiments show that finite defect-nucleation times significantly affect creep rates [2]. In oxides the activation energy for GB source/sink nucleation is significantly lower than for that of the lattice, which causes the broad stress regime over which non-Newtonian creep is observed and the relative narrow but observable Coble regime. In simple metal, the activation energy for GB sources and sinks is comparable to lattice dislocation nucleation, which causes the Coble regime to be absent in most cases and the lattice and GB non-Newtonian creep regimes to overlap. The large activation energies for GB climb-mediating sources/sink observed experimentally indicate that these effects must be integrated into continuum constitutive laws and that their role in affecting irradiation induced creep processes warrants investigation.

Recent Progress

The present work treats creep as a renewal process. A completed strain increment requires a sequence of kinetic steps. The sequence includes nucleation of a climb-mediating grain boundary disconnection, local point-defect exchange, grain boundary transport, and surface transport. The corresponding waiting times add within one renewal cycle. Bubble growth is inherently a creep process that under irradiation may be irradiation induced creep. Radiation-enhanced point-defect transport and line defect creation can facilitate strain when the displacement-damage rate is high. Dislocation/disconnection nucleation becomes important when irradiation induced damage rates are low. In this work, we developed an analytical framework for treating combined effects of

source/sink nucleation, point defect diffusion, and point defect creation/annihilation and applied it in investigating bubble growth at model Cu/Ag interfaces.

We represent interface-normal strain as a renewal process in which each climb-mediating grain-boundary dislocation or disconnection carries a finite strain increment $\Delta\varepsilon_{\mathrm{q}}$ during an active sink lifetime τ_{q}. The active sink population is renewed at rate η. The activity coefficient is Λ and is defined by $\Lambda = \eta\tau_{\mathrm{q}}$. The sink lifetime contains the time for local point-defect creation or annihilation τ_{ex} and the time for long-range transport τ_{tr}. The mean strain rate is the strain increment divided by the sink lifetime and multiplied by the steady activity factor $\frac{\Lambda}{1+\Lambda}$. This form gives a single constitutive description that contains the nucleation-limited, defect-creation or annihilation-limited, and Coble regimes.

$$\dot{\varepsilon} = \chi_{\max}\frac{\Delta\varepsilon_{\mathrm{q}}}{\tau_{\mathrm{q}}}\frac{\Lambda}{1+\Lambda}, \qquad \Lambda = \eta\tau_{\mathrm{q}}\,, \qquad \tau_{\mathrm{q}} = \tau_{\mathrm{ex}} + \tau_{\mathrm{tr}}$$

When $\Lambda \ll 1$, sink renewal is slow and the strain rate is controlled by nucleation. When $\Lambda \gg 1$, the eligible sinks remain nearly continuously active and the rate is controlled by completion of the active event. Point-defect creation or annihilation controls this limit when $\tau_{\mathrm{ex}} \gg \tau_{\mathrm{tr}}$. Long-range GB transport controls the rate when $\tau_{\mathrm{tr}} \gg \tau_{\mathrm{ex}}$. The conventional Coble response is recovered when the active sink population is also sufficiently dense that $g_{\mathrm{N}} \to 1$.

$$\Lambda \ll 1 \Rightarrow \dot{\varepsilon} \simeq \chi_{\max}\Delta\varepsilon_{\mathrm{q}}\eta$$

$$\Lambda \gg 1 \; and \; \tau_{\mathrm{ex}} \gg \tau_{\mathrm{tr}} \Rightarrow \dot{\varepsilon} \simeq \chi_{\max}\frac{\Delta\varepsilon_{\mathrm{q}}}{\tau_{\mathrm{ex}}}$$

$$\Lambda \gg 1 \; and \; \tau_{\mathrm{tr}} \gg \tau_{\mathrm{ex}}, g_{\mathrm{N}} \to 1 \Rightarrow \dot{\varepsilon} \simeq \chi_{\max}\frac{C_{\mathrm{tr}}\delta D_{\mathrm{gb}}\Omega\sigma_{\mathrm{d}}}{k_{\mathrm{B}}Td^3}$$

Here $\dot{\varepsilon}$ is the interface-normal strain rate, $\chi_{\max}$ is the geometrically eligible fraction of source and sink configurations, $\Delta\varepsilon_{\mathrm{q}}$ is the finite strain increment carried by one completed event, η is the nucleation rate per eligible inactive site, τ_{q} is the active sink lifetime, τ_{ex} is the point-defect creation or annihilation time, τ_{tr} is the long-range transport time, and Λ is the dimensionless activity coefficient. In the Coble limit, C_{tr} is the transport geometry factor, δ is the effective GB width, D_{gb} is the grain-boundary diffusivity, Ω is the atomic or molecular volume, σ_{d} is the driving stress, k_{B} is the Boltzmann constant, T is the absolute temperature, d is the characteristic grain or transport length, and g_{N} is the discrete-sink correction that approaches unity in the continuum Coble limit. The model can be generally fit to polycrystalline creep data to extract reasonable barrier parameters and diffusivities, see Figure 1.

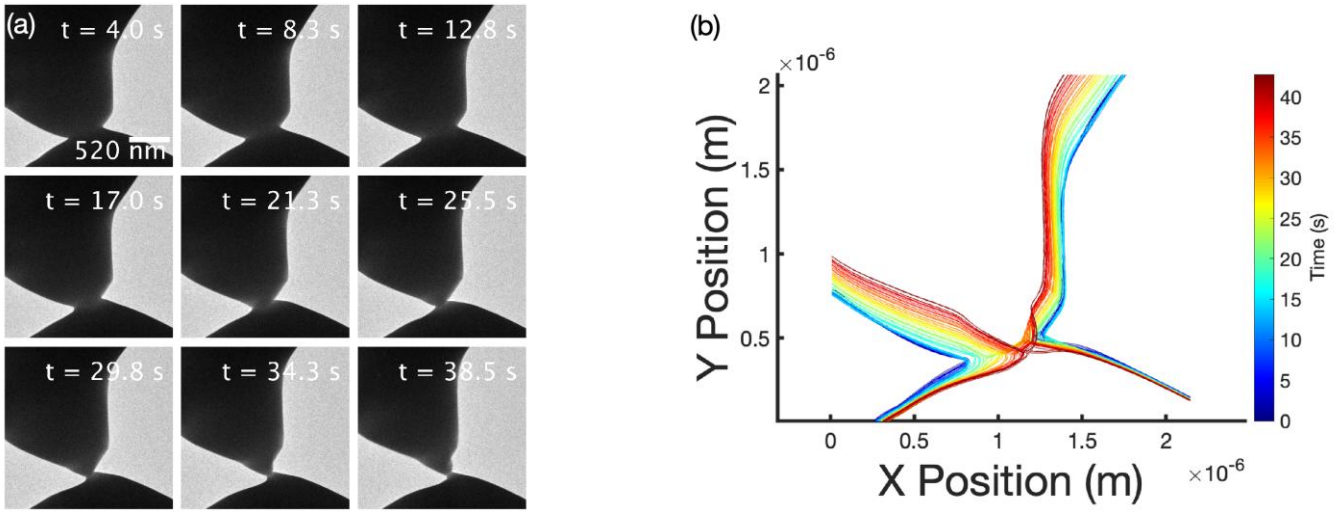

Figure 1. Example bicrystal tensile creep performed on a fluorite oxide [2].

Additionally the model can be fit to bicrystal creep data to directly extract activation free energies and volumes for sink nucleation, see Figure 2, and diffusivities.

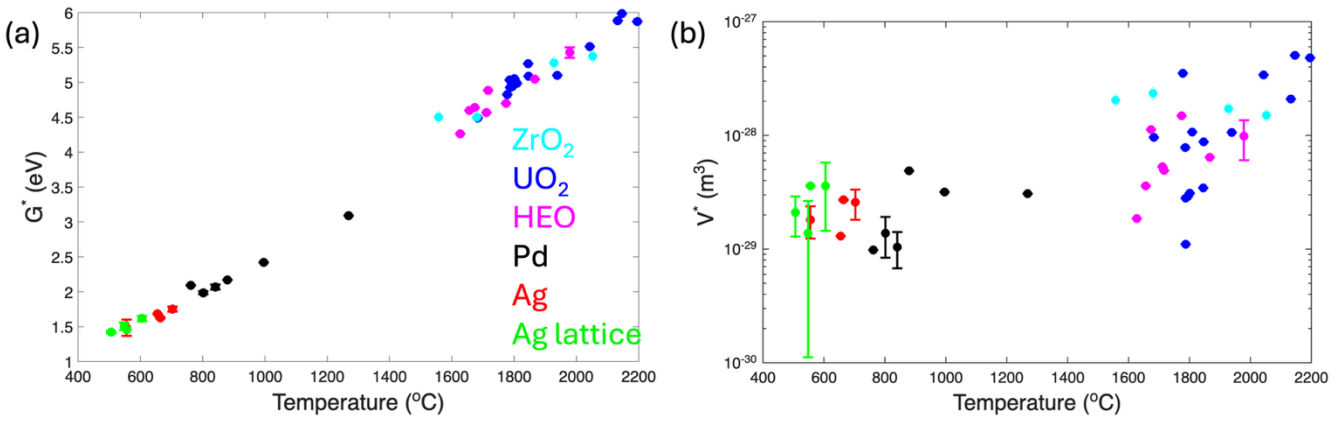

Figure 2. Temperature dependent activation free energy (a) and activation volume (b) at approximately the activation stress for GB sink nucleation kinetics, and lattice dislocation nucleation, for Ag. The slope highlights the large negative activation entropy.

The competition between line defect nucleation and point defect mediated diffusion motivated an examination of strain accommodation during gas-bubble growth at Cu/Ag interfaces. Prior studies have not tracked the growth kinetics of individual bubbles at interfaces and related them to mechanism dependent scaling laws. Plan-view in-situ transmission electron microscopy was used to track individual bubbles during ion implantation. Kr and He implantation conditions placed the

implanted gas near the Cu/Ag interface while generating substantially different displacement-damage rates. Kr irradiation produced damage rates on the order of 10^{-3} to 10^{-2} dpa s^{-1}. He irradiation produced damage rates of the order of 10^{-5} dpa s^{-1}.

Kr irradiation produced continuous bubble growth at 300 and 400 ˚C (Figure 3a) and generally followed power law growth kinetics consistent with

$$\frac{RdR}{dt} = 2K_{eff}(t)$$

R is the mean bubble radius, t is irradiation time, K_{eff} is the effective time-dependent growth coefficient that contains the transport and irradiation-assisted accommodation terms.

He irradiation between 200 and 400 ˚C produced early nucleation followed by a long period of weak radius evolution. Rapid growth began only after an extended incubation period (Figure 3b). The measured trajectory is consistent with a stress-gated dislocation-nucleation process at the bubble surface. The gas pressure supplies the mechanical driving force and the nucleation event retains an activated rate.

$$\frac{dR}{dt} = (2\pi R) \cdot \upsilon_o \cdot exp\left(-\frac{G^*}{k_B T}\right) \cdot exp\left(\frac{v^* \sigma_{net}}{k_B T}\right)$$

ν_0 is the dislocation-nucleation attempt frequency, G^* is the activation free energy for dislocation nucleation, v^* is the activation volume, σ_{net} is the net mechanical driving stress, k_B is the Boltzmann constant, and. T is the absolute temperature.

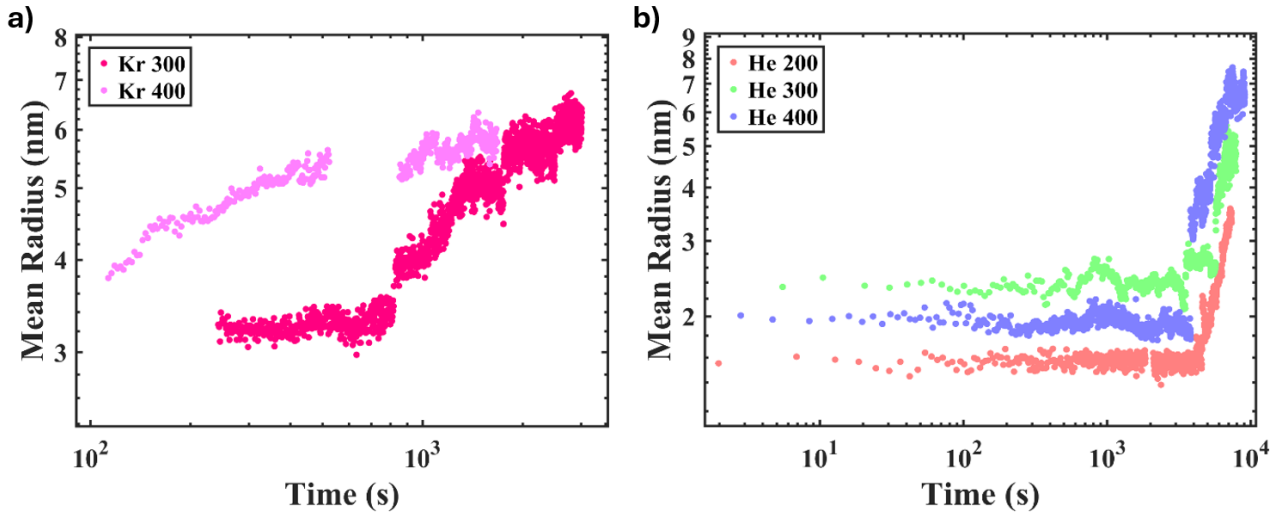

Figure 3. Log-log plots of mean bubble-radius versus time for Kr (a) and Helium (b) bubble growth at Cu-Ag interfaces.

Figure 3 highlights the distinct scaling kinetics associated with bubble growth in the two systems. Phase field simulations were employed to reproduce the measured response under the assumed mechanisms, and data fitting produce physically reasonable diffusivities and line defect nucleation activation energies. The analysis also suggests that the initial He bubbles are under-pressured, consistent with expectations that He stabilize vacancies and vacancy clusters.

Analyses of interface mediated creep and swelling/bubble growth phenomena typically presuppose diffusion-controlled kinetics. The current work demonstrates that nucleation kinetics control the response over a broad range of conditions. The results demonstrate how systems evolving under both thermomechanical driving forces and under irradiation driven conditions both fall into nucleation rate limited and diffusion limited kinetic regimes, depending on the availability of stress or irradiation induced line defect concentration and point defects. The work also provides an analytical framework for integrating three necessary and potentially rate-limiting mechanisms into a single formalism that can account for both thermomechanical and irradiation induced creep strain.

Future Plans

Future plans involve understanding the atomic nature of strain mediating interfacial defects, especially those evolved under irradiation, the effects of oxide stoichiometry, and the role of electric fields towards affecting nucleation and transport. In parallel, we seek to understand how extended defects evolve in the lattice and organize under thermomechanical driving forces and irradiation.

References

[1] B. Burton, *Interface reaction controlled diffusional creep: A consideration of grain boundary dislocation climb sources*, Materials Science and Engineering, **10**, 9-14 (1972).

[2] D. K. Coffman, J. T. White, J. Brown, D. Zhang, A. J. Terricabras, J. Luo, K. Hattar, S. Finkeldei, S. Dillon, *Nucleation rate controlled grain boundary and lattice creep*, Acta Materialia, **300**, 121485 (2025).

Publications

1. A. R. Miles, B. Monserrat, S. C. Finkeldei, *Machine-learned potential for fission gas diffusion in uranium oxide nuclear fuels*, Physical Review B, https://doi.org/10.1103/d775-mmsy, accepted (2026).
2. S. J. Dillon, *A case for non-steady-state grain growth kinetics*, Scripta Materialia, **271**, 116963 (2026).
3. A. J. Terricabras, C. O. T. Galvin, M. Kosmidou, M. Pena, A. Van Veelen, W. D. Neilson, S. J. Dillon, M. W. D. Cooper, D. A. Andersson, S. C. Finkeldei, J. T. White, *Chromium doping effects on UO_2 grain boundary chemistry: A combined experimental and modeling approach*, Journal of Nuclear Materials, **617**, 156114 (2025).
4. S. J. Dillon, R. M. Schoell, A. Wright, J. Luo, E. Rabkin, K. Hattar, *Creep and failure at metal-oxide interfaces*, Acta Materialia, **283**, 120563 (2025).
5. W. D. Neilson, C. O. T. Galvin, M. W. D. Cooper, D. A. Andersson, *Chromium Accommodation at UO_2 Grain Boundaries: Defect Chemistry Insights into Cr-Induced Grain Growth*, The Journal of Physical Chemistry C, **129**, 22163 (2025).
6. I. Martinez, C. O. T. Galvin, R. M. Schoell, M. W. D. Cooper, D. A. Andersson, K. Hattar, S. J. Dillon, *The effect of grain boundary yield and disconnections on grain boundary fracture strength*, Journal of the European Ceramic Society, **45**, 117680 (2025).

7. C. O. T. Galvin, D. A. Andersson, R. T. Sweet, L. Capolungo, M. W. D. Cooper, *Diffusional creep model in UO_2 informed by lower-length scale simulations*, Journal of Nuclear Materials, **607**, 155659 (2025).
8. S. J. Dillon, S. C. Finkeldei, E. Lang, K. Hattar, A. T. Nelson, *Using in situ UO_2 bicrystal sintering to understand grain boundary dislocation nucleation kinetics and creep,* Journal of the American Ceramic Society, **107,** 6701 (2024).
9. W. D. Neilson, J. Rizk, M. W. D. Cooper, D. A. Andersson, *Oxygen potential, uranium diffusion, and defect chemistry in $UO_{2\pm x}$: a density functional theory study*, The Journal of Physical Chemistry C, **128**, 21559 (2024).
10. W. D. Neilson, C. O. T. Galvin, S. J. Dillon, M. W. D. Cooper, D. A. Andersson, *Irradiation-induced creep in UO_2: The role of grain boundaries*, Physical Review Materials, **8**, 103602 (2024).

Understanding the Mechanics of Reverse Phase Transformation and Detwinning in BCC Metal Microstructures

Avinash M. Dongare, University of Connecticut

Keywords: Molecular dynamics, BCC, Non-Schmid effects, phase transformation, anti-twinning, diffraction

Research Scope

Pure BCC metals such as Ta, Mo, Nb, and Fe typically exhibit poor twinnability due to their high SFE values, and dislocation slip dominates plasticity. However, TWIP in pure BCC metals is activated at the nanoscale in single-crystal systems and in nanocrystalline microstructures under quasistatic loading conditions. In addition, Fe-based BCC metals undergo a pressure-induced BCC-to-HCP transformation, and the reverse transformation results in a distribution of transformation twins in an unloaded microstructure, even at the coarser grain sizes. However, predicting grain-scale twinnability in BCC metals still remains a challenge, as BCC metals do not obey Schmid's law and non-Schmid effects (twinning anti-twinning asymmetry) can complicate predictions of slip vs twin contributions to the plastic deformation. This program uses a novel computational framework to gain fundamental insights into the governing rules that determine the nucleation/formation of {112}<111> and {332}<113> twins during plastic deformation or reverse phase transformation and their contributions to grain-scale deformation behavior in polycrystalline BCC microstructures, whether formed as twins, anti-twins, or transformation twins. This research program investigates whether a framework with Schmid factor values, loading directionality, and modifications due to neighboring grain misorientations can provide a predictive, mechanistic basis for assessing twinnability in individual grains in nanocrystalline and coarse-grained BCC metals and their contributions to plastic deformation. The program uses a novel combination of (a) large-scale molecular dynamics (MD) simulations at the atomic/nanoscales, (b)newly developed virtual texture analysis (VirTex) to create simulated EBSD maps, (c) virtual x-ray diffraction (XRD) and selected area diffraction (SAED), and (d) Quasi-coarse-grained dynamics (QCGD) simulations at the mesoscales. The insights obtained will provide a rationale for the twinnability of individual grains in polycrystalline BCC during plastic deformation and during reverse transformation. This understanding is the essential foundation for building predictive models of TWIP in other BCC metal microstructures, such as those observed in β-titanium alloys.

Recent Progress

The program has established a novel framework that uses MD simulations and VirTex analysis to investigate grain-scale deformation twinning behavior in polycrystalline microstructures [1]. The program has established that the various embedded atom method (EAM) potentials for Fe [2], Ta [3], Nb [4], and W [5] can predict the respective mechanical behavior (stacking fault energy curves and barriers for twinning and anti-twinning), as well as the $\alpha \rightarrow \varepsilon \rightarrow$

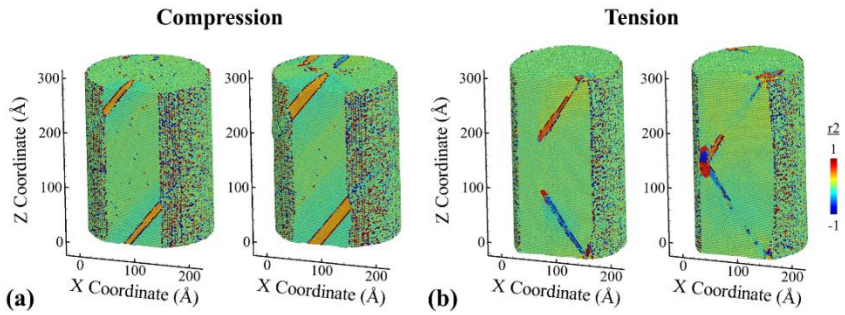

Figure 1. Formation of {112} (a) twins and (b) anti-twins in Fe nanowires loaded along [110] orientation [6]. Time between snapshots (left, right) is two picoseconds. Atoms are colored by orientation analysis in VirTex.

α phase transformation-induced transformation twinning behavior in Fe. The analysis of deformed polycrystalline microstructures suggests that individual grains do not twin strictly according to Schmid factor (SF) predictions and requires further understanding of Schmid (orientation) and non-Schmid (asymmetry) effects, as well as the influence of neighboring grain misorientations [1]. The investigation of Schmid and non-Schmid effects on the twinning vs anti-twinning vs dislocation-slip behavior is carried out using cylindrical nanowires with a diameter of 20 nm with varying loading orientations [6] to compare with the experimental studies. Loading along the [110] direction results in twinning in compression and anti-twinning in tension. Snapshots in Figure 1(a) and (b) reveal twin formation in compression and anti-twin formation in tension, respectively, when loaded. Deformation twins have a large fraction of coherent boundaries and contain only twinning partial dislocations (1/6<111>). Continued deformation of systems with a twin leads to twin growth, which contributes to ductility. Deformation anti-twins have complex structures, a larger fraction of incoherent boundaries, and leave traces of pure-slip dislocations alongside anti-twinning partials (1/3<111>). Continued deformation of systems with an anti-twin results in slip-anti-twin interactions inducing strain hardening through detwinning. Similarly, loading along [112] activates shear banding in compression, as observed experimentally, and also activates the less common {332}<113> twinning system when loaded in tension. Twinnability at the nanoscale is also observed across different BCC metals, but variations in energy barriers lead to changes in volume fractions and dislocation densities [6]. The slip, twin, and anti-twin interplay is observed to be modified due to the presence of neighboring grain misorientations, wherein the stresses for twinning can be increased/decreased, and anti-twinning is largely suppressed and dominated by dislocation slip [7].

Similarly, MD simulations investigate the role of variant selection in pressure-induced α → ε → α phase transformation and twinning in Fe single crystals with varying orientations and polycrystalline microstructures attributed to the ε-phase variant selection and the loading/unloading pathways [8]. For example, variant selections during loading a [110]-oriented Fe crystal under uniaxial strain compression are shown by snapshots in Figure 2(a), which result in the formation of a {112}<111> transformation twin. However, when loaded under quasi-hydrostatic loading, as shown in Figure 2(b), the system exhibits modified variant selections and instead forms a {332}<113> transformation twin. VirTex characterization suggests that the same dominant ε-variant yields a {112}<111> twin under uniaxial strain but a {332}<113> twin under quasi-hydrostatic loading of the same orientation. While the {112} < 111> transformation twin is

observed to de-twin during deformation, as shown in Figure 2(c), suggesting an anti-twin character, the {332}<113> transformation twins remain sessile and allow the nucleation of additional {112}<111> deformation twins, as shown in Figure 2(d). These corresponding contributions are evident in the stress-strain curves shown in Figure 2(e). While the {112}<111> transformation twin increases flow stress compared to the pure system, the {332}<113> twin serves as a barrier for slip/twinning and yields significantly higher strength and flow stress values, contributing to enhanced strength and toughness responses, as observed in β-titanium alloys.

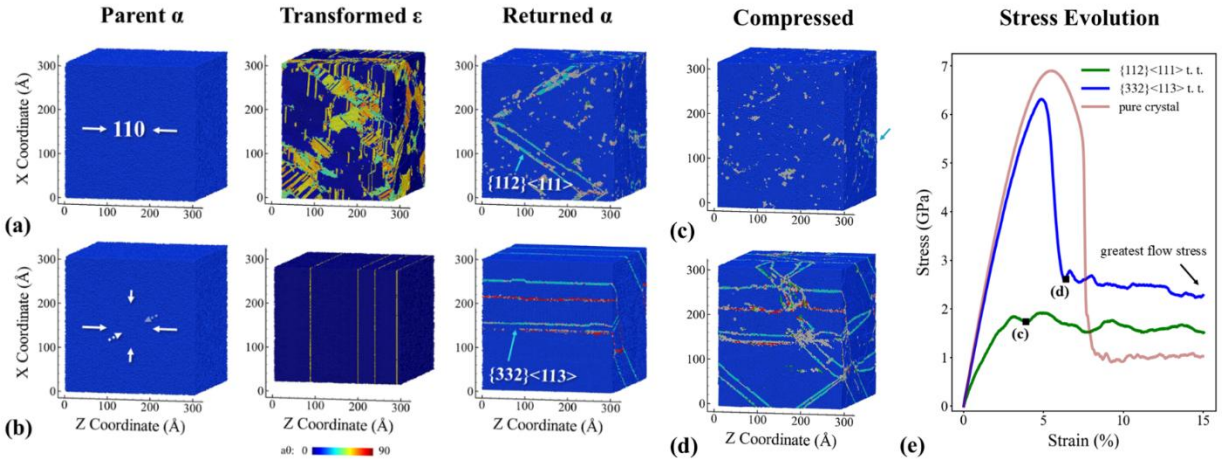

Figure 2. Snapshots showing parent [110] Fe α phases, transformed ε phase, and returned α phases when loaded under (a) uniaxial strain compression resulting in a {112}<111> twin, and (b) quasi-hydrostatic compression rendering a {332}<113> twin [8]. Parent and returned α phases are colored by structure type, where blue is BCC, cyan is coherent twin boundary, and grey is disordered. Transformed ε systems are colored using VirTex analysis. The same snapshots with pre-existing (c) {112}<111> twin and (d) {332}<113> twins after uniaxial stress compression along [110] and the corresponding (e) Stress-strain curves are shown in (e) compared to those for a pure (defect-free) crystal loaded along [110].

Future Plans

While BCC twinnability studies have largely focused on {112}<111> twinning and its asymmetry, {332}<113> twinning is also established as a fundamental deformation mode in bcc metastable β titanium alloys and in pure Fe. Although prior work links {332}<113> to diffusionless phase transformations [9 - 11], preliminary results from this program show it can also form during plastic deformation alone, independent of any phase transformation. The proposed program therefore aims to develop a fundamental, mechanistic understanding of the competition between {112}<111> and {332}<113> twinning, both during plastic deformation and during reverse (ε→α) transformation, governed by Schmid and non-Schmid effects, loading stress state, grain misorientation, and alloying chemistry. The computational framework will be applied across Two Objectives to address these questions:

Objective A: Investigate the factors that activate/suppress {112}<111> twinning and dislocation slip in BCC metals. The {332}<113> twinning involves a combination of shear and atomic shuffling, which is likely accompanied by a higher intrinsic nucleation barrier as compared to {112}<111> twinning. *As a result, identifying pathways and barriers to compare with* {112}<111> twinning is extremely difficult. *This objective tests the hypothesis that {332}<113> twinning is activated when other deformation modes are suppressed.* This is the case observed for loading along the [112] orientation. This study will investigate the role of (a) neighboring grain misorientations and grain boundary structures, and (b) the stress state of loading (uniaxial, biaxial, and triaxiality) that are likely to activate/suppress {112}<111> twinning and anti-twinning during plastic deformation.

Objective B: Investigate the factors that activate/suppress transformation twinning in BCC metals. The {332}<113> twinning has been linked with diffusion-less phase transformations such as the $\alpha \rightarrow \varepsilon$ phase transformation in Fe. This Objective will test the hypothesis that several factors can influence phase-transformation thresholds and either activate less-dominant ε-phase variants or suppress dominant ε-phase variants and, in turn, the competition between {112}<111> and {332}<113>transformation twin formation. These factors include the role of (a) alloying chemistry-induced threshold modifications, and (b) the stress state of loading (triaxiality) in determining which transformation twin mode forms.

References

1 Kannan, A., P. Tsurkan, and A.M. Dongare, Virtual texture analysis to understand microstructure effects on deformation twinning and detwinning behavior in BCC metals. Comp. Mater. Sci. **249**, 113636 (2025)

2. Gunkelmann, N., et al., Polycrystalline iron under compression: Plasticity and phase transitions. Phys. Rev. B **86**, 144111 (2012)
3. Ravelo, R., et al., Shock-induced plasticity in tantalum single crystals: Interatomic potentials and large-scale molecular-dynamics simulations. Phys. Rev. B **88**, 134101 (2013)
4. Li, P., et al., Crystallographic-orientation-dependence plasticity of niobium under shock compressions. Int. J. Plast. **150**, 103195 (2022)
5. Marinica, M.C., et al., Interatomic potentials for modelling radiation defects and dislocations in tungsten. Journal of Physics: Condensed Matter **25**, 395502 (2013)
6. P. Tsurkan, E. Byers, C. Sabatini, A. M. Dongare, Twinning and Anti-twinning Plasticity in BCC Metal Nanowires, Journal of Materials Research, accepted, in press, (2026)
7. Byers, E., P. Tsurkan, and A.M. Dongare, Misorientation effects on Deformation Twinning and Antitwinning Behavior of BCC Metals, Journal of Applied Physics, (in preparation for submission).
8. P. Tsurkan, A. M. Dongare, Pressure-Induced Phase Transformation and Transformation Twinning in Fe: Insights from Atomic Scale Simulations, Scripta Materialia, (submitted, in review).
9. M. J. Lai, C. C. Tasan, D. Raabe, On the mechanism of {332} twinning in metastable β titanium alloys, Acta Materialia 111, 173-186 (2016).
10. S. J. Wang, M. L. Sui, Y. T. Chen, Q. H. Lu, E. Ma, X. Y. Pei, Q. Z. Li, H. B. Hu, Microstructural fingerprints of phase transitions in shock-loaded iron, Scientific Reports 3, 1086 (2013).
11. L. M. Dougherty, G. T. Gray Iii, E. K. Cerreta, R. J. McCabe, R. D. Field, J. F. Bingert, Rare twin linked to high-pressure phase transition in iron, Scripta Materialia 60, 772-775 (2009)

Publications

1 Kannan, A., P. Tsurkan, and A.M. Dongare, Virtual texture analysis to understand microstructure effects on deformation twinning and detwinning behavior in BCC metals. Comp. Mater. Sci. **249**, 113636 (2025)

2. P. Tsurkan, E. Byers, C. Sabatini, A. M. Dongare, Twinning and Anti-twinning Plasticity in BCC Metal Nanowires, Journal of Materials Research, accepted, in press (2026)
3. Byers, E., P. Tsurkan, and A.M. Dongare, Misorientation effects on Deformation Twinning and Antitwinning Behavior of BCC Metals, Journal of Applied Physics, (in preparation for submission).
4. P. Tsurkan, A. M. Dongare, Pressure-Induced Phase Transformation and Transformation Twinning in Fe: Insights from Atomic Scale Simulations, Scripta Materialia, (submitted, in review).

The Origins of Strain Localization and Crack Nucleation in Complex Alloys Under Cyclic Loading

J. A. El-Awady and **S. I. Rao, Johns Hopkins University**

Keywords: refractory multi-principal element alloys, slip localization, screw-dislocation cross-slip, fatigue crack initiation, in situ SEM micromechanics

Research Scope

Refractory multi-principal element alloys (RMPEAs) are among the most promising structural materials for high-temperature service in next-generation energy systems, yet their fatigue behavior remains poorly understood. For example, it is not understood how alloy composition and crystal orientation govern slip localization and the transition to fatigue crack initiation in these alloys. As such, the objective of this project is to identify the origin of slip localization in RMPEAs under cyclic loading. Our central hypothesis is that slip localization is controlled by screw-dislocation cross-slip: in bcc RMPEAs, the elementary kinks carrying screw motion form on {112}- or {110}-type planes depending on composition, and slip confines to a single plane only when the maximum resolved shear stress lies on that same kink-plane family, suppressing cross-slip onto equivalent planes. We test this in two model bcc RMPEAs: MoNbTi where kinks expected on {112}; and MoNbTa where kinks are expected on {110} by tightly coupling in situ scanning electron microscopy (SEM) micromechanical experiments with large-scale atomistic simulations: (i) in situ micropillar compression with quantitative slip-trace analysis to resolve the active slip systems and their orientation dependence; (ii) molecular dynamics (MD) simulations with a machine-learning interatomic potential (MLIAP) to resolve the screw-dislocation core structure and glide trajectory underlying the measured traces; and (iii) in situ SEM cyclic loading experiments, with high-resolution transmission electron microspecies (HRTEM) of the resulting slip bands and crack tips, to link the atomistic mechanism to where and how irreversible slip accumulates and leads to crack initiation. The project outcome is a mechanistic link between composition, slip mechanisms, and fatigue crack initiation to guide the design of fatigue-resistant refractory alloys.

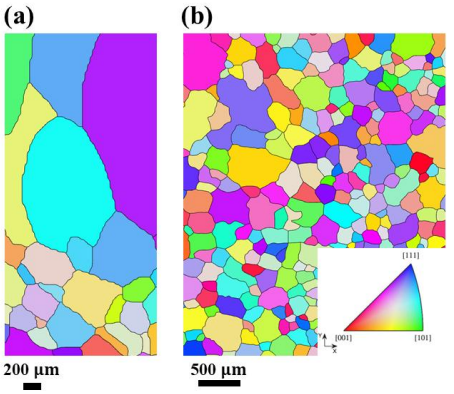

Figure 1. EBSD orientation maps of as-cast, equiatomic (a) MoNbTa and (b) MoNbTi, showing randomly oriented, equiaxed grains with no crystallographic texture.

Recent Progress

We synthesized equiatomic MoNbTa and MoNbTi by arc melting. Electron backscatter diffraction (EBSD) across the as-cast microstructures showed randomly oriented, equiaxed grains with no texture in either alloy (Fig. 1). From these, 23 single-crystal micropillars (14 MoNbTa, 9 MoNbTi) were fabricated by FIB

milling into grains selected to maximize the difference in Schmid factor between the {112} and {110} slip families. Throughout, we label each pillar by the plane carrying the maximum Schmid factor (MSF): a "{112}-MSF" pillar is loaded so that a {112} plane has the highest Schmid factor, and a "{110}-MSF" pillar so that a {110} plane does. This designation defines the loading geometry only and does not imply which plane has predominant slip. Compression loading was limited to <5% engineering strain to isolate early-stage dislocation activity from subsequent strain hardening and entanglement.

Slip-trace analysis was performed on every pillar by comparing measured surface-trace angles on each face against the trace angles predicted for {112} and {110} slip from the loading direction and Schmid factors (Fig. 2). Two morphologies were distinguished: confined traces, lying on a single well-defined plane within 5° of the predicted active plane; and fanning traces, in which an initially confined trace progressively broadened into a diverging band as strain accumulated.

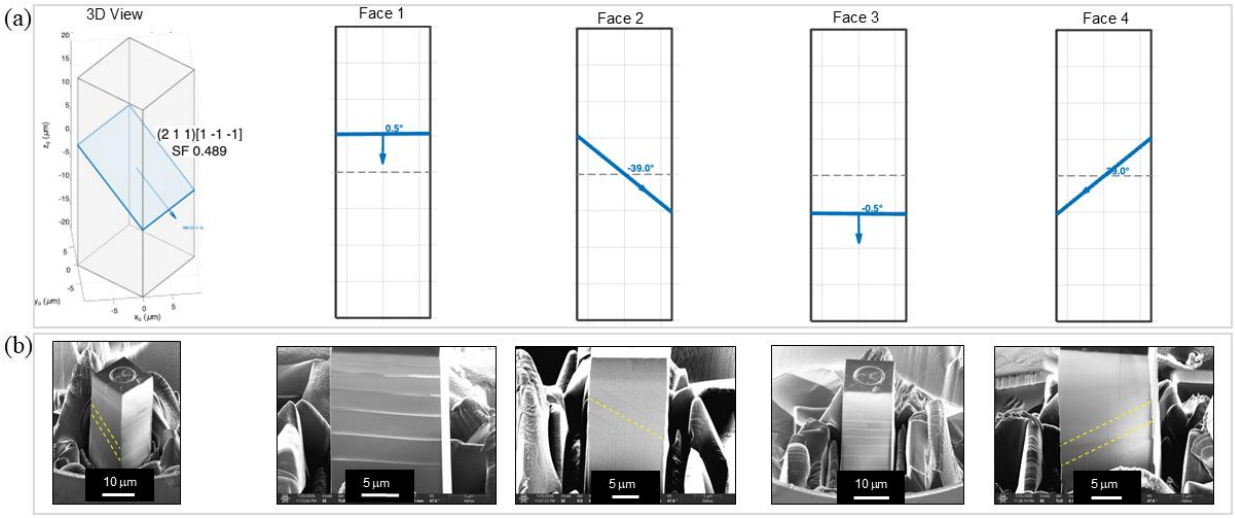

Figure 2. Slip-trace analysis methodology. (a) Schematic single-crystal micropillar showing the geometric relationship between the loading axis and the maximum-Schmid-factor slip plane, and the predicted trace angles on each face; the arrow is the Burgers vector and its projections. (b) SEM image of a deformed pillar; measured trace angles are compared with the predicted {112} and {110} angles to identify the active slip system.

The two alloys showed a systematic, composition- and orientation-dependent difference in slip confinement (Fig. 3). In MoNbTi, {112}-MSF pillars (max {112} SF = 0.49; nearest {110} SF = 0.42) exhibited slip sharply confined to a single {112} plane (Fig. 3f), whereas {110}-MSF pillars (max {110} SF = 0.50; nearest {112} SF = 0.44) showed fanning traces and higher flow stress, indicating greater resistance to {110} glide (Fig. 3d). MoNbTa showed the inverse: {110}-MSF pillars (max {110} SF = 0.50; nearest {112} SF = 0.43) show confined slip on a single {110} plane (Fig. 3c), while {112}-MSF pillars (max {112} SF = 0.49; nearest {110} SF = 0.43) showed pronounced fanning (Fig. 3e); no significant flow-stress difference was measured between the two MoNbTa orientations.

Across both alloys, slip is confined when the maximum-Schmid-factor plane coincided with the composition's expected kink-plane family ({112} for MoNbTi, {110} for MoNbTa), while

fanned slip traces occur when it did not. Progressive fanning is consistent with screw dislocations consistently cross-slipping off their initial plane, leading to a broadened slip trace. For MoNbTi, this is in agreement with Balbus *et al.* [1], who attribute the primary atomistic glide to {112} and the apparent {110} response to sequential cross-slip on {110}. Slip-trace analysis alone, however, cannot uniquely quantify the underlying mechanism since fanning could also reflect near-simultaneous activation of multiple systems given the small Schmid-factor differences (e.g., on {123} or {134} slip plans), or lattice rotation bringing a second system into a favorable orientation. However, the small strains in the current study and our SEM analysis suggest the latter is unlikely. The traces thus establish that slip becomes progressively less confined on {110} in MoNbTi and on {112} in MoNbTa, but not why. To test the cross-slip hypothesis, we compared these observations against atomistic simulations of screw-dislocation core structure and mobility in the following.

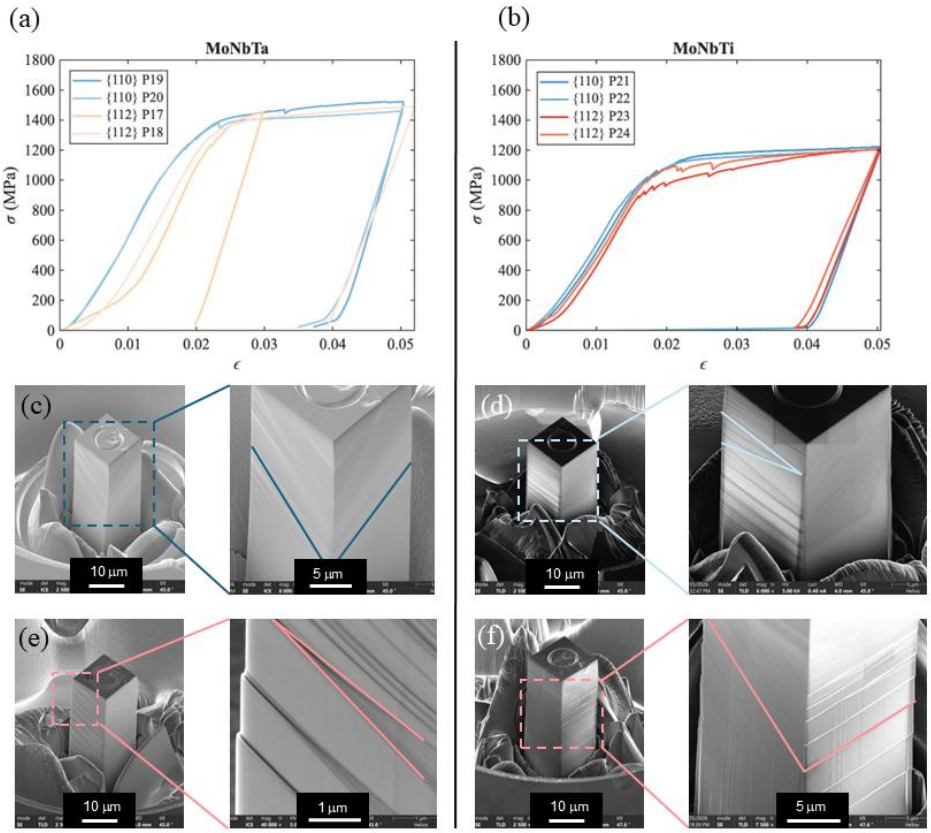

Figure 3. Mechanical and deformation behavior of the two alloys. (a–b) Engineering stress–strain curves for representative {112}-MSF and {110}-MSF pillars of (a) MoNbTa and (b) MoNbTi. (c–f) Post-deformation SEM images: (c) {110}-MSF MoNbTa pillar showing confined planar slip on a single {110} plane; (d) {110}-MSF MoNbTi pillar showing fanning slip; (e) {112}-MSF MoNbTa pillar showing pronounced slip trace fanning; (f) {112}-MSF MoNbTi pillar showing confined slip on a single {112} plane.

To determine the screw-dislocation core structures and glide trajectories under shear resolved on {110} and {112} in MoNbTa and MoNbTi, we utilize MD simulations using an MLIAP for the Cr-Hf-Mo-Nb-Ta-Ti-V-W-Zr system [2]. Before introducing any dislocation, we computed the lattice constants, elastic constants (C11, C12, C44), and the generalized stacking-fault energy (GSFE) along ⟨111⟩ on both {110} and {112} (Fig. 4) for three random seeds per alloy. Relaxed lattice parameters are 3.2545 Å for MoNbTa and 3.2251 Å for MoNbTi.

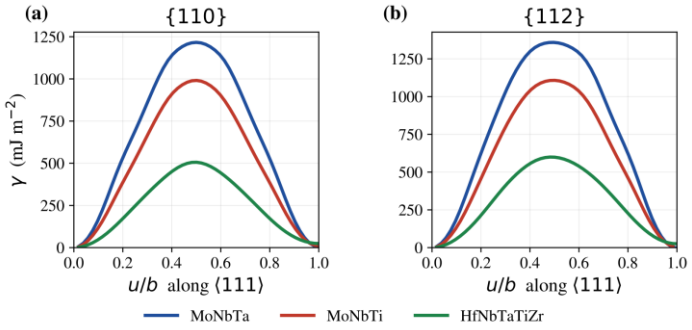

Figure 4. Generalized stacking-fault energy along ⟨111⟩ for shear on (a) {110} and (b) {112}; the distance is normalized by the Burgers vector magnitude of each alloy. HfNbTaTiZr is included as a third composition from the same refractory family.

A single ½⟨111⟩ screw dislocation was then introduced into the simulation cell as a periodic array of dislocations (PAD) [3], with the dislocation line parallel to the x-axis, glide direction parallel to the y-axis, and slip-plane normal parallel to the z-axis. The simulation cell included ~1.2×10^5 atoms, ~200×200 Å cross-section dimensions, and ~50 Å line length. Constant-shear-stress loading at 5 K was imposed to isolate the intrinsic glide-plane preference and the core trajectory while suppressing thermal fluctuations. The simulated trajectories are therefore compared qualitatively with the experimentally measured slip morphologies, while the simulated stresses and kink-pair kinetics are not intended to be quantitatively representative of room temperature in the current analysis.

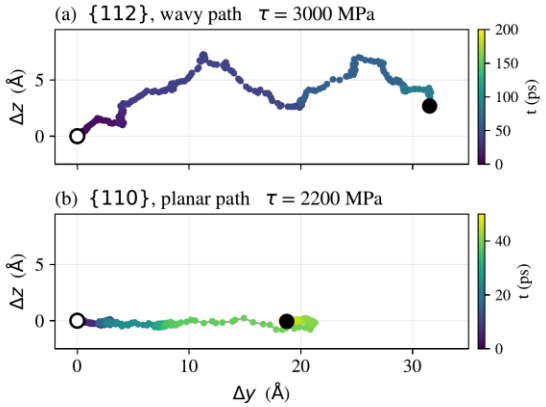

Figure 5. Slip trajectories in the MoNbTa alloy as predicted from MD simulations at 5K. Open circle indicates the dislocation's initial position, and the solid-filled circle represents the final position. In (a), the applied shear is on the {112}; while in (b), the applied shear is on the {110}.

These simulation results are observed to reproduce the experimental observations for the MoNbTa orientation dependence (Fig. 6). When the applied shear is imposed on the {110} plane, the dislocation core glides at a critical stress of 2200 MPa in a planar manner on the (110) plane. On the other hand, when shear is applied to the {112} plane, the core follows a wavy, cross-slipped trajectory. This observation supports the conclusion that the experimentally observed fanning traces in {112}-MSF MoNbTa pillars are induced by cross-slip on {112} planes. The simulations

thus provide sub-resolution core information that slip-trace measurements cannot access and directly support cross-slip as the origin of fanning. Simulations for MoNbTi and the remaining loading conditions are ongoing.

Future Plans

To probe slip localization under cyclic loading, we will fabricate single-crystal microcantilevers by plasma-FIB milling in grains selected to maximize the {112}-versus-{110} Schmid-factor difference along the beam axis, again yielding {112}-MSF and {110}-MSF orientation classes. High-angular-resolution EBSD of the top and side faces will enable direct comparison of predicted and observed slip traces. In situ SEM high-cycle fatigue testing will then track the evolution of slip localization, crack initiation, and early crack growth, and HRTEM will relate the dislocation structure within the slip bands to the onset of cracking — closing the loop between the atomistic cross-slip mechanism and observed fatigue damage.

References

[1] G. H. Balbus, S. I. Rao, O. N. Senkov, E. J. Payton, Orientation-dependent plasticity of the refractory multi-principal element alloy MoNbTi investigated via micropillar compression, Acta Mater. 262 (2024) 119401.

[2] J. Byggmästar, T. Lopes, Z. Fan, T. Ala-Nissila, Nine-element machine-learned interatomic potentials for multiphase refractory alloys, arXiv:2603.04147 (2026).

[3] Y. N. Osetsky, D. J. Bacon, An atomic-level model for studying the dynamics of edge dislocations in metals, Model. Simul. Mater. Sci. Eng. 11 (2003) 427.

Computational and Experimental Study of Slip Transfer in a BCC-B2 alloy

Maryam Ghazisaeidi (PI) and Michael Mills (Co-PI), The Ohio State University

Keywords: Refractory alloys, B2 ordering, slip transfer

Research Scope

Energy efficiency requires the development of new materials with excellent high temperature performances. A possible alternative to the current leading Ni-based superalloy is the refractory multicomponent alloys with a BCC/B2 microstructure. Our previous studies [P1] successfully identified potential B2 formers among 11 refractory metals. We explained the trends based on bonding nature and provided guidelines for identifying simplified compositions that can form the desired microstructure and validated the theory by experimentally confirming the presence of the B2 phase in TaRe system [P2], which has never been reported before. This binary TaRe system is further used as a testbed to study the slip transfer between the BCC matrix and B2 precipitates. We trained a machine learning interatomic potential for the Ta-Re system, using first-principles calculations and applied it to a large scale molecular dynamics simulations with over a million atoms targeting dislocation activity across the BCC/B2 interface. We also conducted micropillar compression tests for <111> slip on {110}, {112} and {123} planes targeting single slip systems. Further analysis of slip systems and comparison between simulations and experiments is currently ongoing.

Recent Progress

Computational effort

To fully understand the deformation mechanisms in the TaRe alloy, large-scale atomistic simulations at finite temperatures are required. However, such simulations are usually beyond the reach of density functional theory (DFT). Recent advances in the application of machine learning algorithms to materials modeling has facilitated the development of machine learning interatomic potentials (MLIPs) [1]. When trained properly, MLIPs can achieve DFT level accuracy at much lower computational cost. We trained a binary TaRe moment tensor potential (MTP) [2] based on training data from DFT calculations and applied it to study the dislocation motion between BCC solid solution and B2 TaRe phases, using the experimental composition of Ta65Re35 for the matrix. The training data was generated to span a broad range of the phase space between Ta and Re, including the ground state structures, strained structures, and *ab initio* molecular dynamics simulations for pure elements and compounds of various compositions and space groups.

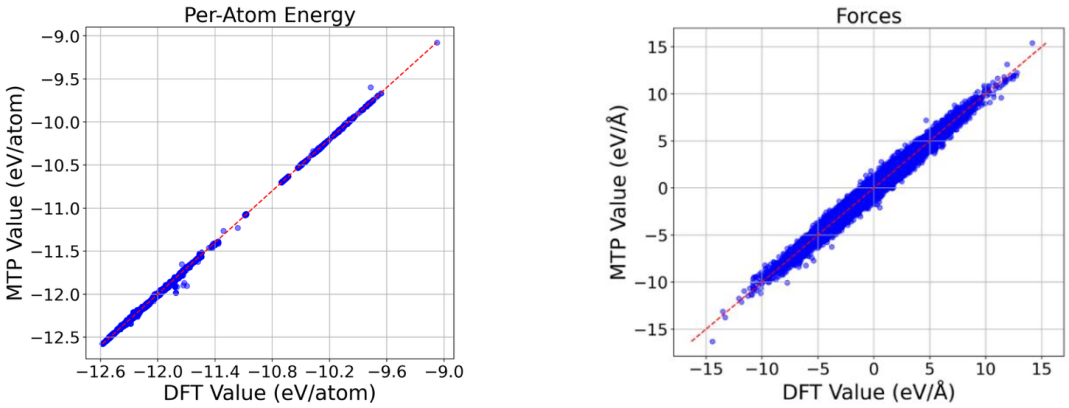

Fig.1 Parity plot of the trained potential. X-axis shows the DFT reference value while Y-axis shows the MTP predicted value. The trained model achieved an overall mean absolute error of *7.25 meV* for the energy and *72.6 meV/Å* for the force. The red dotted line indicates the perfect fit.

The trained potential achieved an overall mean absolute error of *7.25 meV* for the energy and *72.6 meV/Å* for the force. Without being explicitly included in the training data, the elastic constants of the B2 TaRe and BCC Ta as well as the 1/2<111> screw dislocation core structure in B2 TaRe and BCC Ta produced by the potential matches the DFT reference value very well,

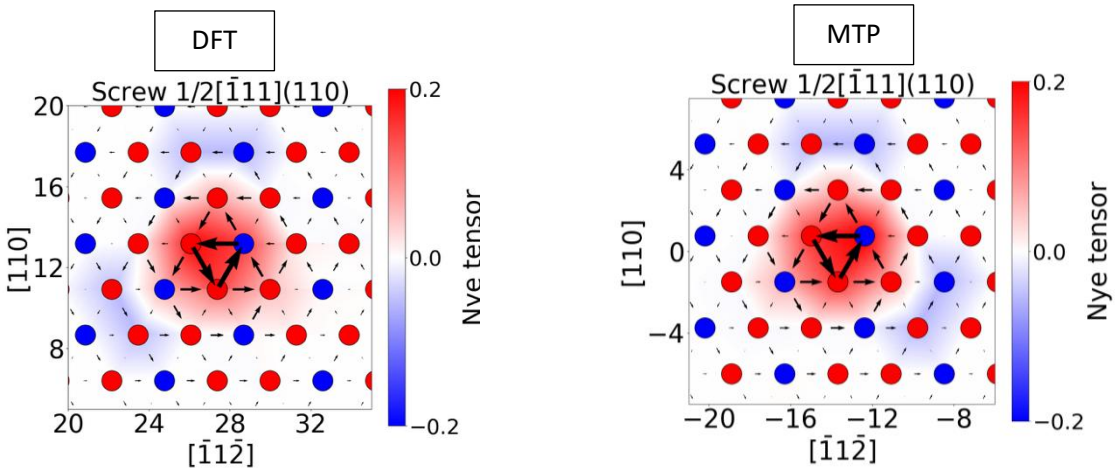

Fig.2 Comparison of the differential displacement map for screw ½ <111> dislocation in B2 TaRe.

validating the potential for studying dislocations. The validated potential was then used to perform molecular dynamics simulations. We first simulated the ½ <111> screw dislocation in different slip systems at 0K, including pure Ta, BCC solid solution, and B2 TaRe with {110}, {112}, and {123} glide planes. It is observed that, the dislocation tends to move on the {110} planes. The motions on {112} and {123} planes constitute of alternating {110} and {112} motions.

We also modeled the interface between the BCC Ta65Re35 and B2 TaRe using different setups, one with a straight dislocation line while the other with a dislocation loop. The straight

dislocation simulation was conducted on a cell with 1.08 million atoms. The box dimension is 469Å in [-2 1 1] (dislocation moving direction), 244 Å in [0 1 -1] and 166 Å in [1 1 1]

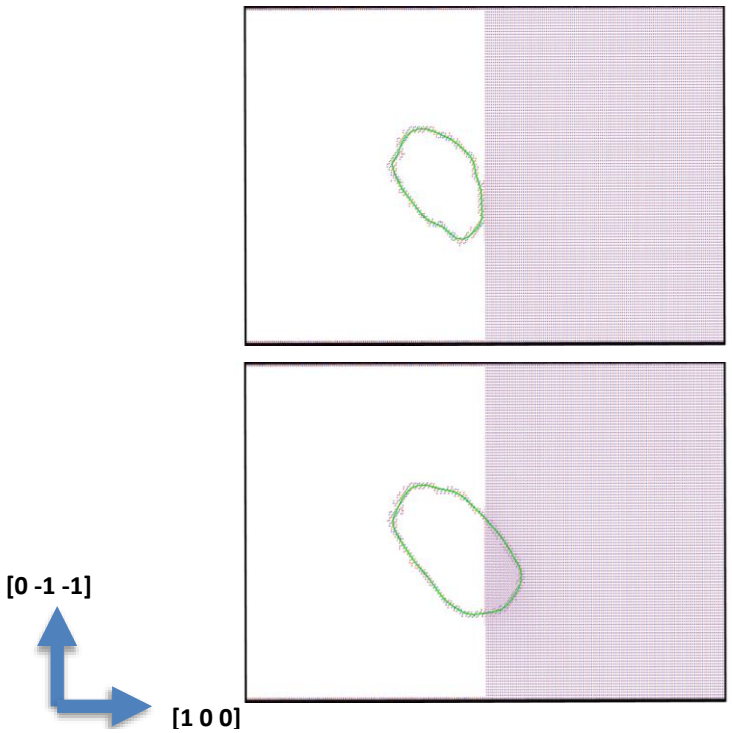

Fig.3 ½<111> Dislocation Loop (green) top: at the interface; bottom: entered the TaRe B2 region (right) from BCC Ta65Re35 solid solution (left, bulk atoms are not shown). Ta is shown in red while Re in blue.

(dislocation line direction). The BCC/B2 interface is the (100) plane. The T=0K simulation of the straight dislocation shows that the dislocation, when inserted in the BCC region, is not a straight line due to local composition variations. Under applied shear strain, the dislocation line moves in different {110} planes in the BCC region with multiple kinks and jogs. However, when the dislocation penetrates the interface and enters the B2 region, it moves as a straight line and on one single {110} plane with anti-phase boundaries (APB) forming behind it. The dislocation loop simulation was conducted on a cell with 1.152 million atoms. The box dimension is 386 Å in [1 0 0], 273 Å in [0 -1 -1] and 182 Å in [0 1 -1]. The BCC/B2 interface is the (100) plane. At T=78K with 6% resolved shear strain, the loop expands and approaches the interface, it first aligns itself with the interface and then penetrates the B2 phase. While in the B2 region, the loop clearly shows a preference for pure edge and screw segments. It creates an APB as both segments moves further into the B2 region.

Snapshots of these simulations are shown in Figures 3. At the current simulation temperature, the dislocation loop dynamics appears to be dominated by the stress required expand the loop. Whenever the loop expands sufficiently to reach the interface, it always penetrates into the B2

phase. Simulations at higher temperatures may reveal a different balance between loop expansion and interface resistance. These simulations are currently ongoing.

Experimental effort

Micropillar compression testing [3-5] was performed to study the single crystal mechanical properties in collaboration with Tresa Pollack and Dan Gianola at UCSB. For the Ta65Re35, alloy EBSD was used to select grains with favorable Schmid factors for <111> slip on {110}, {112}, and {123} planes targeting single slip systems. Taper-free radial micropillars roughly 5 μm in diameters and 12μm in length were fabricated. At least three pillars per condition were deformed to 5% strain and one pillar to 20 % strain. All the pillars exhibited significant plasticity in compression with most reaching 20% without cracking. Pillars deformed to 5% strain for the <111>{110}, <111>{112}, and <111>{123} in a twinning and anti-twinning configuration to assess slip asymmetry can be seen in Figure 4 A-D. Only the pillar in the <111>{123} twinning configuration exhibited more than one active slip system (Figure 4 C). Determination of the exact slip systems and post-mortem STEM characterization of the dislocation-precipitate interactions are ongoing.

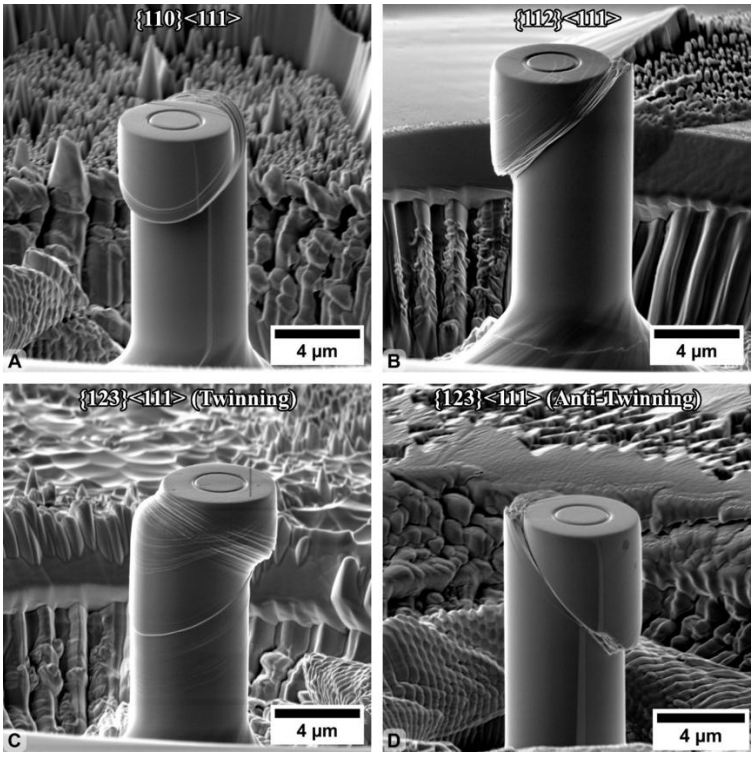

Figure 4: For the Ta65Re35 alloy, deformed micropillars to ~2% strain targeting single slip orientations for the (A) {110}<111>, (B) {112}<111>, and (C, D) {123}<111> slip systems. For the {123}<111> (C) and (D) target slip systems in the twinning and anti-twinning orientation to assess slip asymmetry reported in literature. Despite targeting a single slip orientation for all pillars, the {123}<111> twinning condition, (C), exhibited two active slip systems.

Future Work

We will perform additional simulations at higher temperatures, further analyze dislocation behavior, and investigate how the critical stresses associated with different mechanisms vary with temperature. We will also compare the experimental characterization of the slip systems and atomistic simulations which will provide a comprehensive understanding of the deformation mechanisms.

References:

[1] Jacobs, R., Morgan, D., Attarian, S., Meng, J., Shen, C., Wu, Z., ... & Wood, B. M. (2025). A practical guide to machine learning interatomic potentials–Status and future. Current Opinion in Solid State and Materials Science, 35, 101214.

[2] Novikov, I. S., Gubaev, K., Podryabinkin, E. V., & Shapeev, A. V. (2021). The MLIP package: moment tensor potentials with MPI and active learning. Machine Learning: Science and Technology, 2(2), 025002.

[3] A.S. Schneider, B.G. Clark, C.P. Frick, P.A. Gruber, E. Arzt, Effect of orientation and loading rate on compression behavior of small-scale Mo pillars, Materials Science and Engineering: A 508 (2009) 241–246. https://doi.org/10.1016/j.msea.2009.01.011.

[4] G.H. Balbus, S.I. Rao, O.N. Senkov, E.J. Payton, Orientation dependent plasticity of the refractory multi-principal element alloy MoNbTi investigated via micropillar compression, Acta Mater. 262 (2024). https://doi.org/10.1016/j.actamat.2023.119401.

[5] C. Frey, H. You, S. Kube, G.H. Balbus, K. Mullin, S. Oppenheimer, C.S. Holgate, T.M. Pollock, High Temperature B2 Precipitation in Ru-Containing Refractory Multi-Principal Element Alloys, Metall. Mater. Trans. A Phys. Metall. Mater. Sci. 55 (2024) 1739–1764. https://doi.org/10.1007/s11661-024-07368-x.

Publications:

1. Junxin Wang; Ali Barooni; Maryam Ghazisaeidi, “Stability of the B2 phase among refractory metals", *Acta Materialia*, 279, 120323 (2024).
2. Crossman, Bryan J., Junxin Wang, Loic Perrière, Si Athena Chen, Jean-Philippe Couzinié, Maryam Ghazisaeidi, and Michael J. Mills. "Multi-modal characterization of the B2 phase in the Ta-Re binary system." Acta Materialia 293, 121097 (2025).
3. Julian Brodie; Junxin Wang; Jean-Philippe Couzinie; Milan Heczko; Veronika Mazanova; Michael J Mills; Maryam Ghazisaeidi, “Stability of the B2 phase in refractory high entropy alloys containing aluminum", *Acta Materialia* 268, 119745 (2024).

Electro-Chemo-Mechanical Fatigue in Lithium

Wendy Gu, William Chueh, Stanford University

Keywords: Microstructure, solid-state battery, high homologous temperature

Research Scope

Lithium is a lightweight bcc metal with a high electrochemical potential that is mechanically soft and ductile near room temperature[1]. Lithium and its alloys have been intensely investigated for use as anodes in solid-state batteries. One of the main challenges is mechanical instabilities that form within the metal anode during cycling, that lead to contact loss, the formation of dendrites and short circuiting, and eventual failure of the battery[2]. These instabilities and failure events have been documented at different pressures, temperatures, and charging rates, but a detailed understanding of the underlying deformation mechanisms remain elusive. Recent observations show that fatigue damage within the lithium anode corresponds to electrochemical degradation of the solid-state battery[3]. An improved understanding of fatigue within lithium and lithium alloys, and its relationship to creep and microstructural evolution at small length scales, high homologous temperatures and coupled mechanical and electrochemical fields is needed to resolve these issues.

As in structural alloys, major mechanistic questions are the microscopic processes that lead to crack initiation and propagation and the role of microstructural features under cyclic loading. In this project, the research objectives are to: 1) Understand the formation of defect structures during cyclic loading, 2) Determine microstructure and mean stress dependence in lithium under fatigue, 3) Investigate length scale effects on creep-fatigue interactions, 4) Understand deformation at bi-metallic interfaces in lithium alloys.

Future Plans

Our approach is to perform air-free fatigue testing of lithium and lithium alloys, and compare the resulting microstructure and mechanical properties to the structure, mechanical and electrochemical performance of lithium and lithium alloys cycled within solid-state batteries. We will develop methods to 1) perform fatigue testing on lithium and lithium alloys that can be compared to the stresses and strains that form during electrochemical cycling, 2) analyze the defect structure within lithium and lithium anodes, and 3) enable long-term electrochemical cycling of model metallic anodes in order to study fatigue within solid-state batteries. Additional mechanistic insights will be obtained through advanced in-situ electro-chemo-mechanical testing within a scanning electron microscope, which will enable the direct imaging of fatigue defects (e.g. slip traces and microcracks) under different mechanical and electrochemical driving forces[4].

References

1. Boehler, R. Melting Temperature, Adiabats, and Gruneisen Parameter of Lithium, Sodium and Potassium versus Pressure. *Phys. Rev. B 27*, 11, 6754–6762 (1983).
2. Zaman, W.; Zhao, L.; Martin, T.; Zhang, X.; Wang, Z.; Wang, Q. J.; Harris, S.; Hatzell, K. B. Temperature and Pressure Effects on Unrecoverable Voids in Li Metal Solid-State Batteries. *ACS Appl. Mater. Interfaces, 15*, 31, 37401–37409 (2023).
3. Wang, T.; Chen, B.; Liu, Y.; Song, Z.; Wang, Z.; Chen, Y.; Yu, Q.; Wen, J.; Dai, Y.; Kang, Q.; Pei, F.; Xu, R.; Luo, W.; Huang, Y. Fatigue of Li Metal Anode in Solid-State Batteries. *Science*, *388* (6744), 311–316 (2025).
4. G. McConohy, X. Xu, *T. Cui*, E. Barks, S. Wang, E. Kaeli, X.W. Gu, W.C. Chueh, "Mechanical Regulation of Lithium Intrusion Probability in Garnet Solid Electrolytes." *Nature Energy, 8, 241-250 (2023).*

Publications

1. T. Cui, S. Wang, S. Lee, E. Barks, J. Cattermull, C. Melamed, Z. Jiang, L. Narun, Y. K. Tzeng, S. H. Kim, X. Xu, G. McConohy, P. Wallace, A.C. Lee, X. Cui, J.H. Lee, W.C. Chueh, X.W. Gu. "Dendrite initiation and deflection in biaxially compressed solid electrolytes." *Nature*. 655, 631-637 *(2026).*
2. Xin Xu, Teng Cui, Geoff McConohy, Harsh D. Jagad, Samuel S. Lee, Sunny Wang, Celeste Melamed, Yufei Yang, Edward Barks, Emma Kaeli, Leah Narun, Yi Cui, Zewen Zhang, Hye Ryoung Lee, Rong Xu, Melody M. Wang, Levi Hoogendoorn, Ajai Romana, Alexis Geslin, Robert Sinclair, Yi Cui, Yue Qi, X. Wendy Gu, William C. Chueh, "Heterogeneous Doping *via* Nanoscale Coating Impacts Mechanics of Li Intrusion in Brittle Solid Electrolytes." *Nature Materials, 25, 627-634 (2026).*
3. C. Wu, M.M. Wang, M. Shuai, T. Cui, X.W. Gu, "Ultrafast High Temperature Sintering of Porous Sandwich Metals." *Materialia. 42, 102492 (2025).*
4. M.M. Wang, R. Dang, A. Parakh, A.C. Lee, Z. Li, S. Chariton, V.B. Prakapenka, J. Kang, Y.W. Zhang, A. Hodge, H. Gao, X.W. Gu, "Nanotwinned Alloys Under High Pressure." *Acta Materialia. 285, 120654 (2025).*

Understanding the role of temperature on grain boundary migration

Eric R. Homer (Brigham Young University), Gregory B. Thompson (University of Alabama), Oliver K. Johnson (Brigham Young University)

Keywords: grain boundary migration, disconnections, cryogenic and elevated temperatures

Research Scope

The major goal of the project is to understand the role of temperature on grain boundary (GB) migration to create microstructural networks in polycrystals that possess enhanced mechanical properties. The most recently completed funding period focused on cryogenic temperatures. For the upcoming funding period, we now focus on applying the gained expertise to elevated temperatures.

The cryogenic effort was aimed at determining the feasibility of controlling microstructure evolution through select GBs that migrate at cryogenic temperatures rather than the majority that migrate only at elevated temperatures. Past funding periods revealed how ordered atomic mechanisms were the source of the cryogenic mobility (Priedeman, 2017) and how a classical model reconciles non-Arrhenius behaviors with a thermally activated model (Homer, 2022). Recent experimental work has reaffirmed cryogenic coarsening (Robinson, 2023), and nearly completed experiments and simulations are focused on observing cryogenic motion and its corresponding mechanisms.

In the process of determining the extent to which cryogenic GB migration is observed in simulations of different GB types, we found that a theorized Kosterlitz-Thouless (KT) topological transition in disconnection migration behavior (Chen, 2020) could reconcile some of the elevated temperature transitions in GB migration; this is the subject of our forward work starting July 2026. Furthermore, our preliminary results make it clear that this transition has significant implications for traditional thermal processing that impacts many polycrystalline engineering metals.

Recent Progress

Recent progress in the cryogenic effort includes advances on several fronts. First, we have unpublished simulations focused on validating the very small activation energies associated with the non-Arrhenius migration; these appear to support the expectations that the motion is thermally activated but frustrated by thermal energy (Homer, 2022). Second, we observed an interesting phenomenon where a grain boundary comprised of more than one type of dislocation/disconnection can decompose into two grain boundaries if the applied stress leads to differential Peach-Koehler forces causing only one type to move. We published a demonstration of this in low-angle grain boundaries (Wan, 2026). Third, considerable effort has gone into providing direct experimental observation of the in situ cryogenic migration as well as efforts to fully resolve the mechanisms associated with experimental evidence. Fourth, as noted above,

efforts to determine the extent to which cryogenic boundary migration is observed have now led to insights about a theorized KT transition. These third and fourth efforts are described in more detail below.

The goal of in situ observation is crucial to validate cryogenic coarsening because post-mortem characterization could be sensitive to microstructural evolution events that occur during ambient temperature preparation following cryogenic processing. For example, we have found that magnetron-sputtered Cu that is composed of incoherent nanotwins just after fabrication will self-anneal to an equiaxed, twin-free microstructure in just 24 hours at ambient conditions. For this reason, our past nanotwinned samples have been Cu-Al alloys (Robinson, 2023), since incoherent twin boundaries (ITBs) are a GB type that simulations show to be non-Arrhenius (antithermal).

The current experimental setup combines the Bruker Hysitron PI89 SEM Picoindenter with a push-to-pull (PTP) MEMS device and the Bruker OPTIMUS on-axis transmission Kikuchi diffraction (tKD) detector. This enables us to load an electron-transparent lamella in tension and perform orientation mapping in situ at the given temperature. This setup has now overcome challenges present in previous experiments and enables stress calculations from the load-displacement curves. Furthermore, tKD resolution is superior to the EBSD maps collected from heavily deformed nanopillar compression tests that have been previously reported (Frazer, 2020).

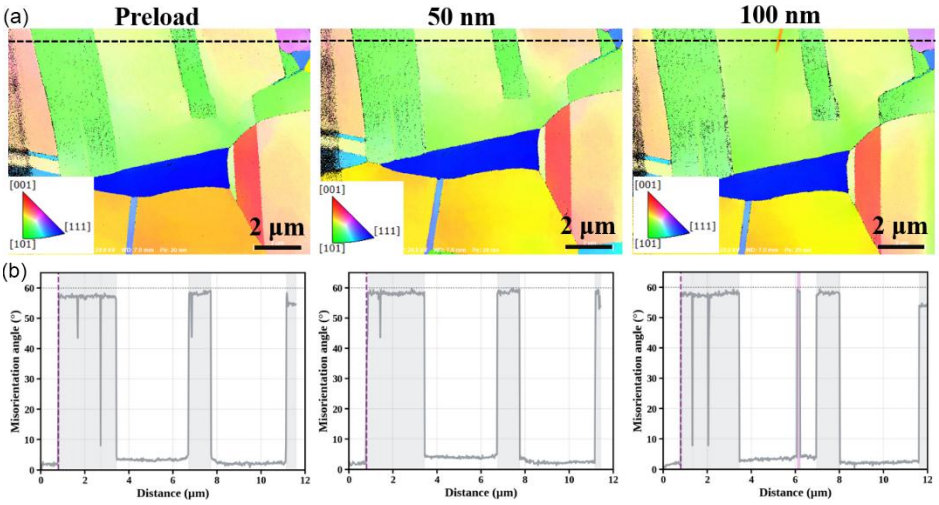

Fig 1. (a) IPFZ maps of the PTP unit at fixed displacements. (b) Misorientation angle line profiles across the dotted black line in (a).

The sample in Fig. 1 is a 100 nm thinned cross section of a FIB liftout. It was obtained from a split Hopkinson pressure bar which deformed pure copper creating a microstructure with a high density of {112} ITBs within micron sized grains. The sample was loaded at ambient conditions in displacement-control to three stages (50 nm, 100 nm, and 250 nm). tKD scans were done at preload and at the end of each displacement cycle while the PTP unit was in tension such that the migration of the ITB could be tracked. Fig. 1 shows IPFZ maps at preload and two displacements as well as a misorientation angle line profile for the same region at the different increments. The most interesting feature is the new ~100 nm thick grain with ~60° misorientation angle that appears at the 100 nm displacement cycle. This is clear ITB migration in these

experiments and there is even a slight retreat (0.1 μm) of the ITB when the load is released at the 250 nm displacement cycle (not shown).

Reaching this stage required overcoming several significant challenges including optimized PTP design compatible with tKD, a stable/viable specimen for this test, minimizing FIB Ga+ damage, and carbon contamination due to repeated tKD scans. With these challenges now resolved, we are in the process of running these tests at cryogenic and elevated temperature conditions, with the latter supporting our upcoming work.

In searching for GBs with cryogenic mobility, we came across some particularly interesting transitions in GB migration behaviors. As GB migration is increasingly understood in terms of disconnections, a recent theory has proposed that GBs can undergo a KT-type topological transition (Chen, 2020) that fundamentally changes disconnection behavior. Below the KT transition, migration is dominated by a single disconnection mode nucleating as bound pairs. Above the transition, multiple modes of unbound disconnections proliferate, leading to boundary roughening, a sliding transition, and a change in the GB mobility. While this transition has been predicted theoretically and demonstrated in disconnection-based mesoscale simulations (Chen, 2020), its actual occurrence and characteristics have remained largely unexplored.

Here, we investigated the theorized KT transition using molecular dynamics simulations of Ni GBs across a range of temperatures and driving forces. We examined the three predicted signatures of the transition: changes in boundary roughness, shear-coupling behavior, and the temperature dependence of mobility.

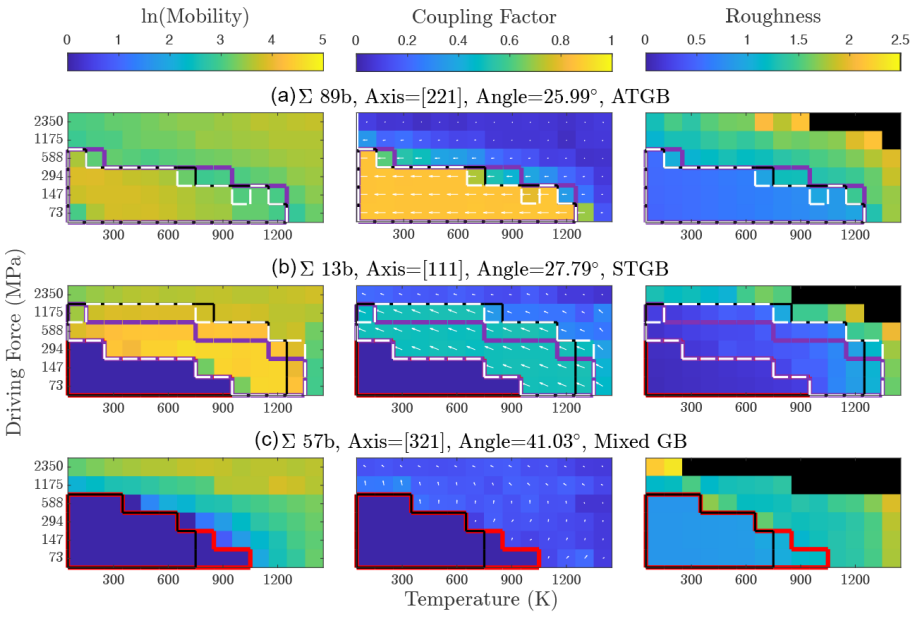

Fig. 2 Migration characteristics of three Ni GBs as a function of temperature and driving force. The white, red, black, and purple lines enclose simulation with clear single-mode, immobile, low roughness, elastically constrained conditions.

Fig. 2 shows these quantities for three representative boundaries and illustrates both compelling evidence for KT-like transitions and substantial differences in how they manifest. For example, the Σ89b boundary (Fig. 2a) provides the clearest example. Increasing temperature or driving force produces coincident changes in roughness, shear coupling, and mobility, with the inferred transition temperature decreasing with increasing driving

force as predicted for a KT transition. The Σ13b boundary (Fig. 2b) exhibits similarly strong signatures but with distinctly different mobility behavior. At low temperature and driving force it is initially immobile, becomes mobile in a strongly shear-coupled single-mode regime, and then undergoes a second transition associated with roughening and reduced coupling. Finally, the Σ57b boundary (Fig. 2c) provides a third manifestation, where roughening coincides with the onset of detectable mobility with no observed single-mode regime.

Thus, the principal result is not simply the observation of signatures consistent with a KT transition, but that those signatures are strongly GB dependent. Some boundaries display all predicted characteristics simultaneously, while others only demonstrate a subset. This distinction also appears important under polycrystalline-like elastic constraints; GBs inferred to be above the KT transition, with access to multiple disconnection modes, appear to migrate independent of polycrystalline constraints, while GBs below the KT transition have reduced mobility in the single-mode regime if polycrystalline constraints are enforced. Importantly, the inferred KT transitions at low driving forces span approximately 0.35–0.75 (T_m) in observed GBs (not all shown), overlapping typical thermomechanical processing temperatures. These results suggest that KT transitions may provide an important framework for understanding the diverse migration behavior of GBs and ultimately predicting their behavior in constrained polycrystalline microstructures.

Future Plans

The cryogenic efforts will conclude soon with an anticipated three manuscripts to be submitted on the topics described above. Importantly, and as noted above, the efforts to provide in situ observations of cryogenic GB migration will now benefit the proposed work to understand the nature of the KT transition and provide experimental evidence for the transition characteristics. Simulations over a wider range of GB types are also planned, including GBs examined in these new experiments. As noted above, the implications of the KT transition for thermal processing could be significant as GBs in a polycrystalline network are able or unable to evolve because of connected boundaries that may or may not be above their KT transition.

References

1. J. L. Priedeman, D. L. Olmsted, and E. R. Homer, *The role of crystallography and the mechanisms associated with migration of incoherent twin grain boundaries*, Acta Mater **131**, 553 (2017).
2. K. Chen, D. J. Srolovitz, and J. Han, *Grain-boundary topological phase transitions*, PNAS **117**, 33077 (2020).
3. D. Frazer, J.L. Bair, E. R. Homer, and P. Hosemann, *Cryogenic Stress-Driven Grain Growth Observed via Microcompression with in situ Electron Backscatter Diffraction*, JOM **72**, 2051 (2020).
4. E. R. Homer, O. K. Johnson, D. Britton, J. E. Patterson, E. T. Sevy, G. B. Thompson, *A classical equation that accounts for observations of non-Arrhenius and cryogenic grain boundary migration*, npj Comput Mater **8**, 157 (2022).
5. A. Robinson, A. Verma, E. R. Homer, and G. B. Thompson, *Nanotwin stability in alloyed copper under ambient and cryo-temperature dependent deformation states*, Mater Sci Eng A **871**, 144866 (2023).

Publications

1. W. Wan, C. Tang, and E. R. Homer, *Decomposition of low-angle grain boundaries,* Acta Mater **316**, 122478 (2026).

Understanding the Role of Surface Energy in the Deformation of Metal Nanoparticles

Tevis D.B. Jacobs (University of Pittsburgh) & Ashlie Martini (University of California, Merced)

Keywords: Nanoparticles, Deformation mechanisms, Dislocations, Surface diffusion, Surface energy

1. Research Scope

Surfaces play a critical role in nanoscale deformation both due to surface-dislocation nucleation and surface diffusion; however, fundamental understanding of these mechanisms and their competitive or cooperative role in the mechanical behavior of nanoparticles is lacking. The long-term goal of this research program is to achieve fundamental understanding of how surface energy modifies (and is modified by) "bulk" deformation in nanoparticles. In service of that long-term goal, the current objective of this research is to understand how surface energy affects the deformation of small metal nanoparticles under compression. This research is carried out through a combination of *in situ* compression testing of nanoparticles inside of a transmission electron microscope with complementary atomistic simulations using molecular dynamics.

2. Methods: Combining *in situ* TEM experimentation and atomistic simulation.

In the *in situ* experiments, metal nanoparticles are deposited directly onto the substrate of an *in situ* nanomanipulator and are then compressed inside of a transmission electron microscope. The high-resolution video acquired during compression enables characterization of the shape and size of each experimental nanoparticle, calculation of the true strain, and direct visualization of the operative deformation mechanisms; simultaneous real-time force measurement enables calculation of the true stress. Molecular dynamics simulations are designed to complement the experiments, using a modeling protocol and set of force fields that we previously developed and validated for these metals. Model nanoparticles of varying size, shape, and crystallographic orientation are equilibrated at the temperature of interest and then compressed between two parallel virtual walls, with stress and strain calculated in several ways, including to match the experiments. The two techniques are complementary (Fig. 1): the simulations resolve atom-by-atom rearrangement that cannot be seen experimentally, while the experiments provide a direct measurement of the interatomic forces that are prescribed (rather than measured) in the simulations.

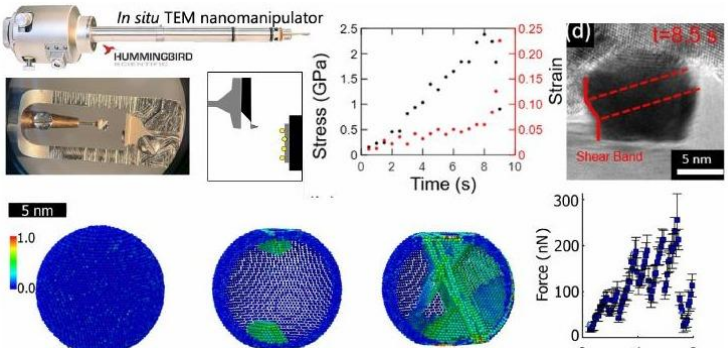

Fig. 1. In situ compression of metal nanoparticles (top) is combined with complementary atomistic simulations (bottom).

3. Recent Progress

3.1 A new understanding of the complex behavior of size-dependent strength. We compressed nanoparticles to failure across an unprecedented range of size and material, linking measured strength to observed failure mechanism. More than 250 *in situ* tests on Pt, Au, and Ag particles from 3 to 130 nm reveal a complex, non-monotonic dependence of strength on size (Fig. 2). Large particles (130 down to 15 nm) fail by surface-nucleated dislocations and—without a change in mechanism—first strengthen with decreasing size, reach a peak strength near 30–60 nm, and then weaken. Intermediate particles (about 15 to 5 nm) exhibit a mix of displacive plasticity and diffusive deformation, while the smallest, single-digit-nanometer particles deform homogeneously by surface-atom migration. This comprehensive, mechanism-linked dataset—spanning three materials and a wide range of size scale—provides the largest-ever set of nanoparticle compression tests and establishes the empirical foundation for a unified description of nanoparticle deformation.[1]

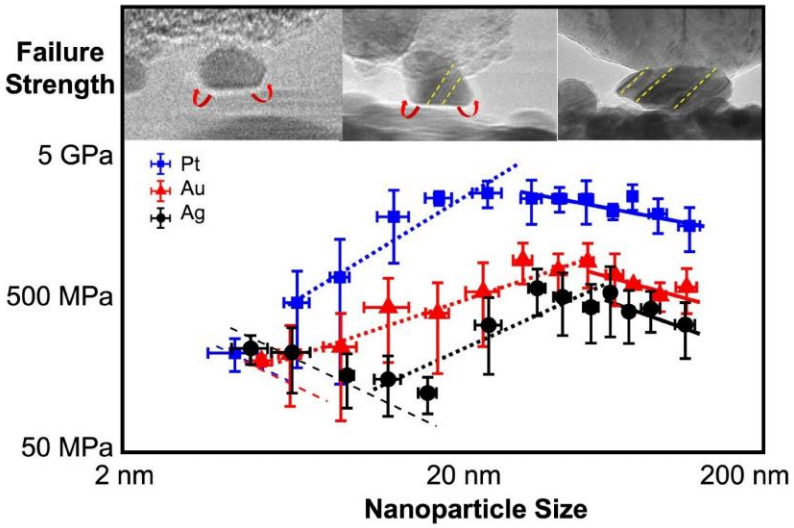

Fig. 2. Failure strength has a non-monotonic dependence on size for Pt, Au, and Ag across sizes from 3 to 130 nm, with the deformation mechanism confirmed by TEM (insets).

3.2 The deformation of larger particles demonstrates how crystallographic orientation governs strength anisotropy. For plasticity-controlled deformation, we have compressed single-crystalline Pt, Au, and Ag nanoparticles along different crystallographic orientations and combined *in situ* TEM with classical molecular dynamics (MD) simulations to directly link strength anisotropy to deformation mechanism. Nanoparticles compressed along [111] predominantly exhibit dislocation slip, whereas those compressed along [001] primarily deform through twinning, as revealed by direct observation of dislocation nucleation and evolution in both experiments and simulations. These deformation pathways are broadly consistent with Schmid-factor predictions for leading and trailing partial dislocations in FCC metals; however, the magnitude of difference in the yield strength as a function of orientation (Fig. 3) *cannot* be explained by the simple Schmid-factor analysis. Instead, these observations are consistent with a stacking fault energy (SFE) modification to the orientation-dependent deformation behavior. These findings provide the first direct experimental validation of the impact of orientation on deformation in small freestanding metallic nanoparticles, and demonstrate the complex interplay between crystallography and energetics that governs nanoscale strength.

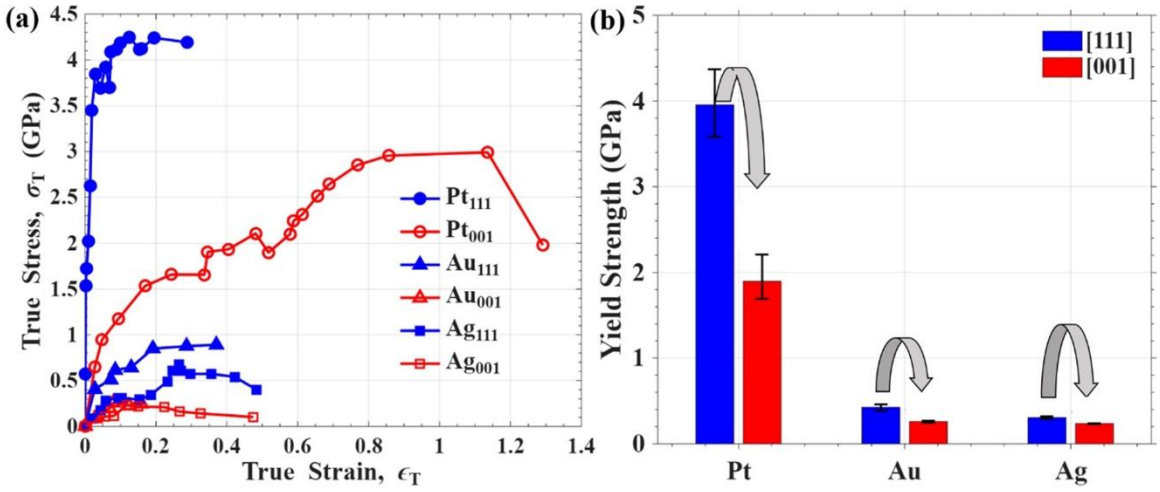

Fig. 3. (a) True stress-strain curves of Pt, Au, and Ag nanoparticles compressed along the [111] and [001] crystallographic orientations. (b) Bar chart showing the corresponding yield strength values extracted from (a), along with the percentage decrease in strength from [111] to [001] orientations.

3.3 The deformation of small particles suggests a thermodynamic framework for deformation. For ultra-small particles, we reveal the driving force for homogeneous deformation. Contrary to the prevailing "Coble-creep-like" model, the deformation of these smallest particles is neither time-dependent nor well fit by the associated kinetic equation. Instead, the behavior is time-independent and consistent with a zero-creep thermodynamic analysis that balances the work done against the change in whole-particle surface energy as the particle deforms (Fig. 4). Strikingly, this

framework predicts a smaller-is-stronger trend within the purely diffusive regime—a counterintuitive result that, for the first time, we confirmed experimentally in silver particles.[1]

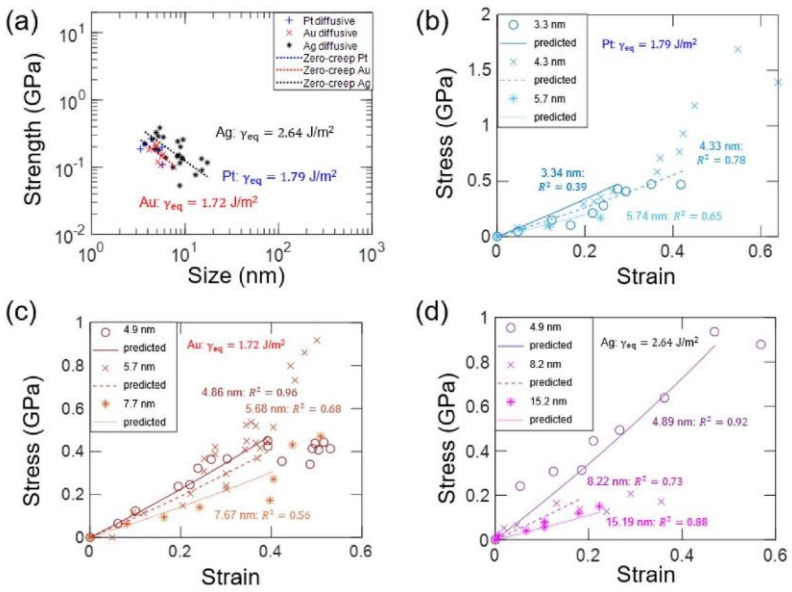

Fig. 4. Experimental results in the diffusive regime are accurately described by the zero-creep analysis: size-dependent strength (a) and stress–strain response with predicted fits for Pt, Au, and Ag (b–d).

4. Future Plans

The results above motivate a unifying description of nanoparticle deformation. Historically, the displacive ("smaller-is-stronger") and diffusive ("smaller-is-weaker") regimes have been treated with separate governing equations, with no physically motivated theory for the intermediate "mixed" regime or for the boundaries between regimes. Our central hypothesis for the ongoing work is that these regimes can be harmonized within a single equilibrium-thermodynamics framework, in which small particles represent the surface-controlled limit, large particles represent the defect-controlled limit, and—unlike prior formulations—the transition region can be predicted. This framework combines the classical thermodynamics of slip with the zero-creep analysis, treating deformation as an energy balance among elastic, defect, and surface/interfacial contributions and shifting the emphasis from "nanoparticle strength" to "equilibrium under load."

4.1. Quantify the energetics of size-dependent transitions in deformation behavior. We are quantifying how particle size modifies the balance among elastic, defect, and surface/interfacial energy, using silver as a model material. Similarly shaped silver particles spanning 4 to 64 nm are compressed in both experiments and simulations, and a "time-lapse" analysis—building atomistic models from individual TEM frames of matched size, shape, and structure—is used to extract each instantaneous contribution to the Helmholtz free energy, along with the total work done and the dissipation over the course of the test. The expected outcome is a theoretically grounded, and even predictive, description of the transition from displacive to diffusive plasticity.

4.2. Alter material and structure to test the predictions of the framework. To test and generalize the framework, we are deliberately varying the relative energy contributions through changes in material and structure. Comparing gold and silver isolates the role of defect energy; compressing gold between different oxide substrates isolates the role of interfacial energy; and comparing pristine and pre-defected particles probes the role of pre-existing defects. Combined with our prior platinum data, these experiments and simulations will enable, for the first time, a quantitative size- and material-dependent energy (phase) diagram for gold, silver, and platinum nanoparticles—removing the current reliance on system-specific models and ad hoc scaling arguments.

5. Publications in the last two years

1. R. Ding, A. Martini, and T. D. B. Jacobs, Mechanical Behavior and Size–Dependent Strength of Small Noble-Metal Nanoparticles, Acta Materialia, 293, 121092 (2025).
2. C. Zhang, A. K. Prasad, T. Liu, T. D. B. Jacobs, and A. Martini, Effect of Reversible Dislocation-Based Deformation on Nanoparticle Strain at Failure, Nanoscale, 17, 9297–9307 (2025).
3. R. Ding, S. Azadehranjbar, I. M. Padilla Espinosa, A. Martini, and T. D. B. Jacobs, Separating Geometric and Diffusive Contributions to the Surface Nucleation of Dislocations in Nanoparticles, ACS Nano, 18, 4170–4179 (2024).

Understanding the Interplay between Hydrogen and Chemical Short-Range Order in Multi-Principal Element Alloys

Miaomiao Jin (PI) and Yang Yang (Co-PI), The Pennsylvania State University, University Park, PA 16802

Keywords: Chemical short-range order, hydrogen, dislocations, multi-principal element alloys

Research Scope

Hydrogen embrittlement (HE) poses a serious challenge for structural alloys used in hydrogen-bearing environments, and metallurgical strategies that increase strength and ductility often compromise resistance to HE. Multi-principal element alloys (MPEAs) provide an emerging materials space in which this conventional trade-off may be altered, but their responses to hydrogen vary substantially across alloy systems. Some MPEAs remain highly susceptible to hydrogen-assisted degradation, whereas others, such as equiatomic CoNiV, exhibit an unusual combination of high strength, ductility, and resistance to HE at ambient temperature [1]. The origin of these contrasting hydrogen responses remains poorly understood. An important characteristic of MPEAs is chemical short-range order (CSRO), arising from statistically preferred local atomic arrangements and producing nanoscale variations in chemical environment [2]. CSRO can modify local energetics, planar-fault behavior, and dislocation motion [3]. Hydrogen is likewise highly sensitive to its local chemical and structural environment. Their coupling therefore introduces a fundamental question for MPEAs: how does local chemical order regulate hydrogen energetics and hydrogen–defect interactions, and how do these interactions ultimately influence hydrogen-assisted plasticity?

This program tests the central hypothesis that **CSRO regulates hydrogen partitioning and modifies the interactions of hydrogen with planar faults and dislocations, thereby influencing the susceptibility of MPEAs to hydrogen-assisted deformation and embrittlement**. Three scientific questions (SQs) organize the work: SQ1. Will hydrogen be trapped at CSRO? SQ2. How will hydrogen impact the stacking-fault energy in MPEAs with pre-existing CSRO? SQ3. How will hydrogen impact dislocation motion in MPEAs with pre-existing CSRO? Through tightly coupled atomistic simulation and advanced characterization, the objective is to establish a fundamental understanding of the coupling among local chemical order, hydrogen, and deformation mechanisms in MPEAs.

Recent Progress

1. Enabling Computational and Experimental Capabilities

Addressing the three scientific questions requires both atomistic models that describe chemical ordering and hydrogen at the scale of dislocations and experimental capabilities that directly observe hydrogen-driven microstructural evolution. Three interatomic potentials have been developed and validated: a moment-tensor machine-learning interatomic potential (MLIP) for Co–

Ni–V–H, a parallel MLIP for Ni–Co–Cr–H, and an embedded-atom-method (EAM) potential for Co–Ni–V–H. For example, the Co–Ni–V–H MLIP reproduces DFT energies to 11.35 meV/atom and forces to 162.5 meV/Å on a highly structurally disordered validation set, with elastic constants within 1–9% of DFT. In parallel, an in situ environmental TEM (E-TEM) capability for hydrogen exposure at elevated temperature has been established, together with correlative STEM approaches for connecting local chemical order and defect structure with hydrogen behavior. These capabilities provide complementary insights where simulation resolves the local energetics and dynamics that are difficult to measure directly, while microscopy provides direct evidence of the defect evolution that the atomistic mechanisms must explain.

2. CSRO Reshapes Hydrogen Energetics in a Motif-Dependent Manner (SQ1)

Hybrid Monte Carlo/Molecular dynamics sampling yields pronounced V-centered CSRO in CoNiV, characterized by strong Ni–V and Co–V preference and first-neighbor V–V avoidance, consistent with experimental interpretation. We note that the ordering is robust from 300 to 1000 K and essentially unchanged by 1 at.% H. Sampling the hydrogen resident octahedral interstitial sites, it is found that CSRO shifts the mean hydrogen solution energy from 0.11 ± 0.004 eV to 0.18 ± 0.005 eV and reduces the fraction of negative-energy (deep-trap) sites (Figure 2a–c). Mapping solution energy against first-nearest-neighbor composition identifies that V-rich octahedral coordination supplies the favorable sites, and V–V avoidance under CSRO statistically reduces them. Grand-canonical Monte Carlo sampling independently confirms the same trend: at 1 at.% H, the six nearest metal neighbors show normalized Ni, Co, and V enrichments of 0.84, 0.71, and 1.45, respectively, where the enrichment is defined as the average local atomic fraction divided by the bulk atomic fraction. Hydrogen therefore preferentially occupies locally V-rich octahedral environments.

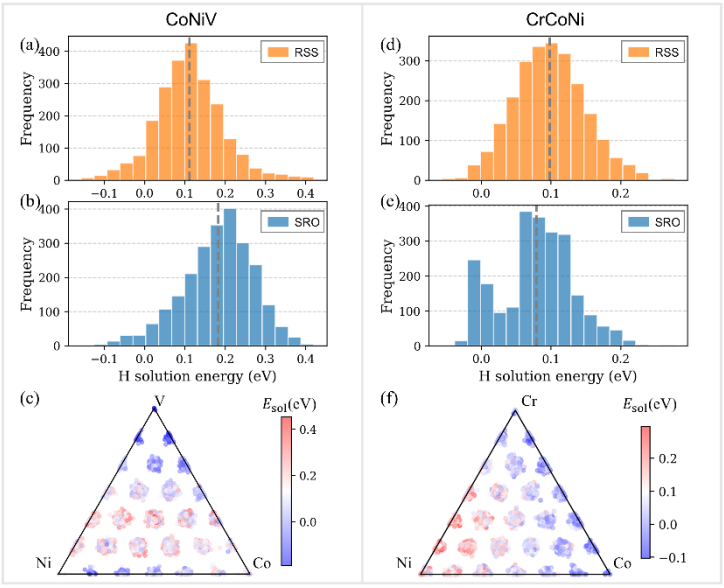

Figure 1. Hydrogen solution-energy landscape in CoNiV (a–c) and CrCoNi (d–f), computed with the newly developed Co–Ni–V–H and Ni–Co–Cr–H MLIPs. (a, d) Solution-energy distributions in the random solid solution (RSS) and (b, e) in the CSRO state; dashed lines mark means. (c, f) Ternary composition maps positioning each site by its first-nearest-neighbor shell composition, colored by solution energy.

Applying the same analysis to CrCoNi produces the opposite trend: CSRO lowers hydrogen solution energies and broadens the distribution toward more favorable hydrogen environments, implying enhanced bulk uptake (Figure 2d–f). Thus, CSRO is not intrinsically beneficial or detrimental to hydrogen accommodation. Instead, its effect depends on the local chemical motifs produced by ordering. In

CoNiV, V-centered ordering reduces favorable V-rich hydrogen environments, whereas ordering in CrCoNi promotes environments that enhance hydrogen accommodation. The answer to SQ1 is therefore more general than the original hypothesis: CSRO regulates hydrogen energetics, but the direction and magnitude of this regulation depend on the chemistry of the ordered motifs.

3. Stacking-Fault Energetics are Dominated by CSRO (SQ2)

CSRO has a pronounced effect on stacking-fault energetics and dislocation structure. In relaxed CoNiV dislocation dipoles, the separation between Shockley partials contracts from approximately 4 nm in the random solid solution to 2 nm after development of CSRO. Direct generalized stacking-fault calculations likewise show a substantial increase in intrinsic SFE, from (1.2±17.8) mJ/m² in the random state to (136.1±16.2) mJ/m² under CSRO. Our independent EAM study across an increasing degree of CSRO reproduces the trend: increasing CSRO raises both the running-average SFE and the stress required for dislocation motion. Artificial Ni–V- and Co–V-rich domains placed on the slip plane act as discrete obstacles to dislocation motion. The independently developed MLIP and EAM descriptions therefore support the same qualitative dependence on CSRO.

Hydrogen, however, has little direct effect on the stacking-fault ribbon in CoNiV at the dilute concentrations. Hydrogen solution energies within the fault are generally higher than those of favorable bulk environments. Instead, the increase in SFE is primarily a CSRO effect, whereas hydrogen–CSRO coupling must occur through other aspects of dislocation structure and dynamics.

4. Hydrogen–Dislocation Coupling Emerges Dynamically (SQ3)

In CoNiV, static calculations show that hydrogen segregates to the tensile fields of Shockley partial cores, but the effective trapping strengths are modest, approximately 0.03 eV in the random state and 0.06 eV under CSRO, with the interaction localized within several angstroms of the core. These values suggest that static core trapping alone may not produce a strong effect on dislocation behavior. In CrCoNi, however, in situ E-TEM reveals pronounced hydrogen-associated changes in dislocation evolution. In addition, hydrogen exposure produces pronounced surface reconstruction in CrCoNi, revealing that hydrogen can dynamically reorganize the local surface structure rather than simply occupy pre-existing trapping sites. This reconstruction is accompanied by changes in

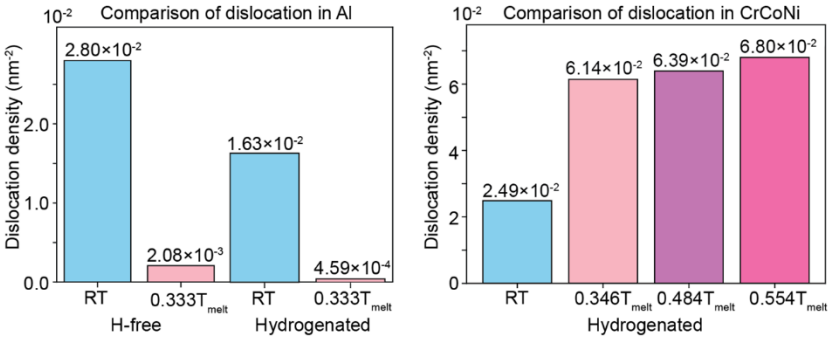

Figure 2 Anomalous hydrogen-induced dislocation accumulation in CrCoNi compared with conventional behavior in aluminum. Left: in Al, dislocation density decreases sharply upon thermal annealing both with and without hydrogen, consistent with conventional defect annihilation. Right: in hydrogenated CrCoNi, dislocation density instead increases monotonically with annealing temperature.

near-surface defect behavior, further indicating that hydrogen–defect interactions in MPEAs can be strongly kinetic and structurally coupled. During annealing, the dislocation density increases monotonically with temperature instead of undergoing conventional thermal recovery (Figure 2). Although these results involve different MPEAs, together they raise the broader question of whether hydrogen–dislocation interactions are controlled mainly by trapping energetics or by dynamic coupling between mobile hydrogen and evolving dislocations.

To directly examine this behavior, we have initiated stress-driven MD simulations of dislocation motion in CoNiV using chemical configurations with and without hydrogen. The emerging results show a strong CSRO-dependent response. Hydrogen can decrease, increase, or have little effect on dislocation velocity and on the critical shear stress required for sustained motion. We speculate that hydrogen couples strongly with local CSRO on the slip plane to modify dislocation mobility. The dislocation motion is driven by competition among the driving stress, local chemical barriers, interactions between the two partials, and hydrogen redistribution. These dynamic simulations provide a possible bridge between the weak static core binding predicted atomistically and the observed substantial changes in dislocation behavior. More broadly, they suggest that hydrogen–dislocation interactions in MPEAs cannot necessarily be represented by a universal hardening or softening mechanism, but instead emerge from the coupling among local chemical order, hydrogen residence and redistribution, and the evolving dislocation structure.

Future Plans

The atomistic energetics underlying SQ1 and SQ2 are now largely established, while the next phase will experimentally test these predictions and place greater emphasis on the kinetic processes underlying SQ3. This effort will combine stress-driven dislocation simulations with in situ E-TEM and correlative STEM characterization in CoNiV and CrCoNi. A complementary cryogenic atom-probe tomography effort will directly test whether deuterium partitioning correlates with specific CSRO motifs. Building on our established APT analysis capability and prepared specimens, the next phase will compare measured deuterium distributions with atomistic predictions of CSRO-dependent hydrogen energetics. CoNiV and CrCoNi provide a particularly useful contrast because CSRO shifts bulk hydrogen energetics in opposite directions. Direct comparison of hydrogen partitioning, dislocation evolution, and local defect structure will test whether these different energetics lead to systematically different hydrogen–dislocation responses. Integrating cryo-APT, in situ microscopy, and atomistic modeling across these two alloys will enable development of local-chemistry descriptors linking CSRO motifs to hydrogen partitioning and defect response, providing predictive insights for hydrogen-tolerant MPEAs.

References

1. H. Luo, S. S. Sohn, W. Lu, L. Li, X. Li, C. K. Soundararajan, W. Krieger, Z. Li, and D. Raabe, A strong and ductile medium-entropy alloy resists hydrogen embrittlement and corrosion, Nature Communications 11, 3081 (2020).
2. X. Chen, Q. Wang, Z. Cheng, M. Zhu, H. Zhou, P. Jiang, L. Zhou, Q. Xue, F. Yuan, J. Zhu, X. Wu, and E. Ma, Direct observation of chemical short-range order in a medium-entropy alloy, Nature 592, 712–716 (2021).
3. J. Ding, Q. Yu, M. Asta, and R. O. Ritchie, Tunable stacking fault energies by tailoring local chemical order in CrCoNi medium-entropy alloys, Proceedings of the National Academy of Sciences 115, 8919–8924 (2018).

Publications

1. B. Chen, D. M. Sayed Ahmed, Y. Yang, and M. Jin, *Chemical Short-Range Order Regulates Hydrogen Energetics and Hydrogen–Dislocation Interactions in CoNiV*, npj Computational Materials (2026).
2. H. Kim, H. Lee, K. Kim, Y. Fan, S. Kim, M. Jin, and Y. Yang, *Kinetic Interplay between Chemical Short-Range Order and Grain Boundaries in NiCoCr Alloys under Irradiation*, Materials Research Letters 14, 642 (2026).
3. D. M. Sayed Ahmed, Y. Sun, Y. Yang, and M. Jin, *Impact of Chemical Short-Range Order on Planar-Fault and Dislocation Properties in NiCoV Alloys*, Physical Review B (2026), under review.
4. X. Xu, B. Chen, Y. Sun, D. M. Sayed Ahmed, T. Wang, Y. Yang, and M. Jin, *Dynamic Hydrogen–Dislocation Interactions in CoNiV*, in preparation (2026).

Elucidating Grain Growth in Thermo-Magnetic Processed Materials by Transfer Learning and Reinforcement Learning

Amanda R. Krause (Carnegie Mellon University), Michael R. Tonks (University of Florida), Joel B. Harley (University of Florida), Michael S. Kesler (Oak Ridge National Laboratory)

Keywords: Grain growth, microstructure, machine learning, x-ray diffraction microscopy

Research Scope

The goal of this research program is to establish the mechanisms governing local grain boundary motion, which is needed to design and process desirable microstructures for better performance, by identifying the relative contributions of grain boundary (GB) energy, mobility and stiffness to grain growth. Classical models for grain growth assume that the primary mechanism for reducing the total interfacial energy is area reduction and that GB restructuring is not significant. This assumption implies that grain growth is locally driven by curvature. However, recent experimental observations using new non-destructive 3D x-ray diffraction microscopy techniques (3D-XRM) reveal that classic descriptors (i.e., curvature, number of neighbors, grain size) do not predict real grain growth [1,2]. Instead, local GB motion appears to be governed by its energy relative to its neighbors such that low-energy boundaries replace those of higher energy [3]. A significant challenge to testing this assumption is due to anisotropic GB mobility. Anisotropic mobility has been hypothesized to cause abnormal grain growth or affect the final grain shapes or growth rate but its true contributions are unknown because it is difficult to measure. As mobility and energy both control GB motion, it is challenging to isolate the local driving forces necessary to test the common assumption that the primary mechanism is area reduction.

The novelty of this work is the use of machine learning tools to capture GB mobility and energy from laboratory-based diffraction contrast tomography (LabDCT, a type of 3D-XRM) measurements in polycrystals to test the common assumption used in grain growth models. Machine learning can capture high-order correlations in dynamic systems like those found in the evolving GB topology. The PIs have previously developed a physics-regularized interpretable machine learning microstructure evolution (PRIMME) model that accurately replicates the grain growth behavior of its trained data set [4,5]. In the current work, PRIMME is being expanded to capture energy and mobility independently from noisy, non-continuous microstructural data from LabDCT. The developed anisotropic PRIMME model will be used to interpret the grain growth behavior of alumina and iron and assess whether GB energy reduction is a primary mechanism for microstructure evolution.

Recent Progress

This study has compared grain growth in untextured to textured undoped alumina, which have unique grain boundary character distributions, to identify the role of grain boundary replacement mechanism in grain growth. In this work, textured and untextured undoped alumina is prepared by slip casting inside and outside, respectively, a magnetic field at Oak Ridge National Laboratory and then sintered and heat treated for 1hr at 1600°C outside the magnetic field.

Laboratory x-ray diffraction contrast tomography was used to track grain growth at subsequent heat treatments completed in argon at 1800°C. The unique grain boundary character distribution (lower misorientation angles and high population of the crystallographic *C*- and *A*-planes) of the textured alumina was found to reduce the grain growth rate (Fig. 1). This finding agrees with hypothesis that low energy grain boundaries will reduce the overall driving force for grain growth and reduce the growth rate. However, the grain boundaries of lowest energy (basal) are found to be the fastest moving boundaries in the textured alumina, rejecting the classical equation that says grain boundary velocity is proportional to energy. Instead, the slow grain growth rate is attributed to the network effects (i.e., the spatial arrangement of low energy boundaries) that reduce the grain boundary replacement mechanism during grain growth.

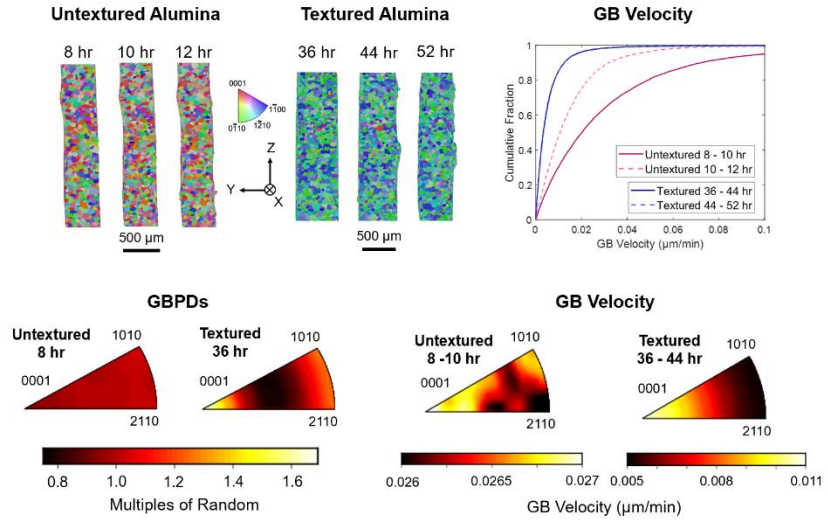

Figure 1: Grain growth in untextured and textured undoped alumina at 1800°C as measured with LabDCT: the LabDCT micrographs, grain boundary (GB) velocity distributions, GB plane distributions and the GB velocity distributions plotted with respect to GB plane.

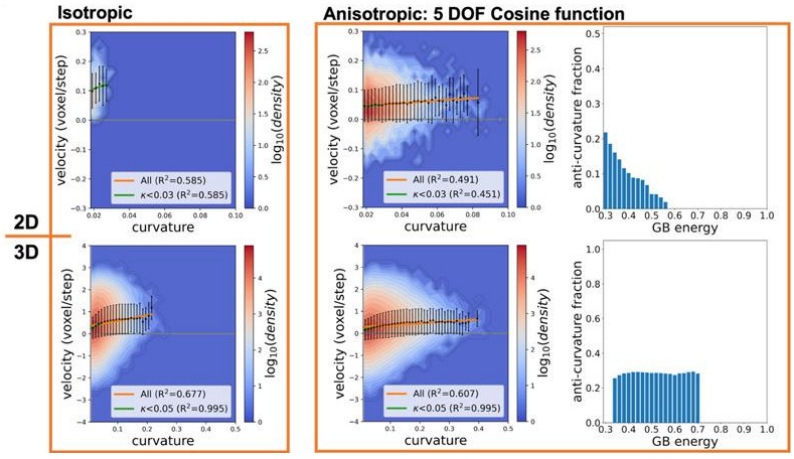

Figure 2: The grain boundary velocity with respect to curvature and energy distributions for isotropic and anisotropic Monte Carlo Potts simulations in 2D and 3D.

The role of the grain boundary network on microstructure evolution is also exemplified by our study investigating curvature-driven grain growth with fully anisotropic Monte Carlo Potts simulations[6]. 2D and 3D Monte Carlo Potts simulations with differing grain boundary energy anisotropy were evaluated for anti-curvature motion (i.e., boundaries moving away from their center of curvature). Unlike 2D simulations, anti-curvature motion is found in 3D isotropic simulations and with increasing frequency depending on the anisotropic GB energy function (shown in Fig. 2). The anti-curvature motion is attributed to the constrained freedom of motion of boundaries within a 3D network. These results further support experimental observations that find simple curvature-driven models are insufficient for describing grain growth in 3D polycrystals.

To learn the network effects on grain growth, we have developed a machine learning-based grain growth model (PRIMME) that can capture grain growth dynamics purely from temporal microstructural data [5]. Previously, we have demonstrated that PRIMME, when trained with Monte Carlo Potts simulations (using either isotropic or anisotropic grain boundary properties), can reproduce metrics used to validate grain growth models. We developed PRIMME to now work with non-continuous temporal, 3D microstructural data, which is necessary to learn from experiments. Following the successful validation of the developed model on simulation data, we extended the framework to experimental LabDCT microstructure data. LabDCT measurements of undoped (untextured) alumina microstructure captured during growth at 1800°C were used to train and test model. The measured microstructure volume was divided into smaller volumes reserved for training, validation, and testing. Preprocessing procedures, including temporal registration, segmentation refinement, and spatial normalization, are applied prior to model training. The machine learning-based model is then trained using just the grain structure data from these two consecutive time steps. For one-step prediction, the trained model achieves 87.31% accuracy compared with the ground-truth microstructure as shown in Figure 3. Future work will focus on improving the alignment between experimental time steps and enhancing long-term temporal prediction stability and physical consistency by including misorientation data in the training. In addition, physically meaningful evaluation metrics, particularly those characterizing local microstructural behavior, will be developed and systematically analyzed.

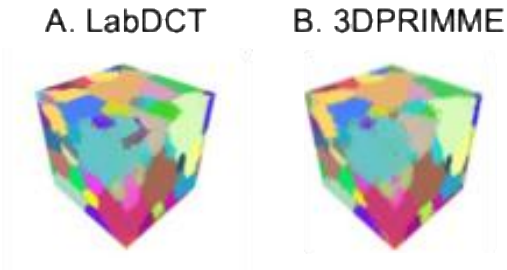

Figure 3: Comparison of the (a) LabDCT measurement and (b) 3DPRIMME prediction (trained from experimental data) from the same initial experimentally determined microstructure.

Future Plans

The future of this work will focus on comparing the fully 3D anisotropic multi-step machine learning model when trained with anisotropic grain growth simulations and experimental datasets. Additional anisotropic phase field simulations will be completed and experimental data will be collected from textured alumina to help in the training process to investigate the role of

grain boundary anisotropy on grain growth. After training, the trained models will be compared to experiments and simulations to identify the effects of anisotropic grain boundary character on grain growth. The goal is to interpret the machine learning model to identify what is the mechanistic difference between experiments and simulations. Thus, the model's architecture was built to highlight microstructural features used in learning to help in this process. If successful, this work will elucidate the governing law for grain growth in polycrystals.

References

[1] V. Muralikrishnan, H. Liu, L. Yang, B. Conry, C.J. Marvel, M.P. Harmer, G.S. Rohrer, M.R. Tonks, R.M. Suter, C.E. Krill, A.R. Krause, Observations of unexpected grain boundary migration in SrTiO3, Scripta Materialia 222 (2023) 115055. https://doi.org/10.1016/j.scriptamat.2022.115055.

[2] A. Bhattacharya, Y.F. Shen, C.M. Hefferan, S.F. Li, J. Lind, R.M. Suter, C.E. Krill, G.S. Rohrer, Grain boundary velocity and curvature are not correlated in Ni polycrystals, Science 374 (2021) 189–193. https://doi.org/10.1126/science.abj3210.

[3] Z. Xu, Y.-F. Shen, S.K. Naghibzadeh, X. Peng, V. Muralikrishnan, S. Maddali, D. Menasche, A.R. Krause, K. Dayal, R.M. Suter, G.S. Rohrer, Grain boundary migration in polycrystalline α-Fe, Acta Materialia 264 (2024) 119541. https://doi.org/10.1016/j.actamat.2023.119541.

[4] J. Melville, V. Yadav, L. Yang, A.R. Krause, M.R. Tonks, J.B. Harley, Anisotropic physics-regularized interpretable machine learning of microstructure evolution, Computational Materials Science 238 (2024) 112941. https://doi.org/10.1016/j.commatsci.2024.112941.

[5] W. Yan, J. Melville, V. Yadav, K. Everett, L. Yang, M.S. Kesler, A.R. Krause, M.R. Tonks, J.B. Harley, A novel physics-regularized interpretable machine learning model for grain growth, Materials & Design 222 (2022) 111032. https://doi.org/10.1016/j.matdes.2022.111032.

[6] L. Yang, V. Muralikrishnan, V. Yadav, Z. Tian, J.B. Harley, A.R. Krause, M.R. Tonks, Beyond curvature-driven grain growth: Insights from fully anisotropic Monte Carlo Potts simulations, Acta Materialia 302 (2026) 121672. https://doi.org/10.1016/j.actamat.2025.121672.

Publications

1. D.P. DeLellis, Y. Wang, V. Muralikrishnan, J.B. Harley, M.R. Tonks, A.R. Krause, *3D Analysis of Abnormal Grain Growth in Calcia Doped Alumina in the Presence of Large Pores*, Journal of the European Ceramic Society **46**[8], 118173 (2026).
2. L. Yang, V. Muralikrishnan, V. Yadav, Z. Tian, J.B. Harley, A.R. Krause, M.R. Tonks, *Beyond Curvature-Driven Grain Growth: Insights from Fully Anisotropic Monte Carlo Potts Simulations*, Acta Materialia **302**, 121672 (2025).
3. Y. Wang, Z. Xu, V. Muralikrishnan, J.B. Harley, M.R. tonks, G.S. Rohrer, A.R. Krause, *4D Observations of the initiation of abnormal grain growth in commercially pure Ni*, Scripta Materialia **264**, 120876 (2025).
4. D.P. DeLellis, A.R. Krause, *Large Pores Promote Abnormal Grain Growth Behavior in Calcia Doped Alumina,* Scripta Materialia **245**, 116058 (2024).
5. J. Melvile, V. Yadav, L. Yang, A.R. Krause, M.R. Tonks, J.B. Harley, *Anisotropic physics-regularized interpretable machine learning of microstructure evolution*, Computational Materials Science **238**, 112941 (2024).
6. B. Conry, M. Kole, W.R. Burnett, J.B. Harley, M.R. Tonks, M.S. Kesler, A.R. Krause, *The evolution of grain boundary energy in textured and untextured Ca-doped alumina during grain growth*, Journal of the American Ceramic Society, **107**, 1725-1735 (2024).
7. L. Yang, V. Yadav, J. Melvile, J.B. Harley, A.R. Krause, M.R. Tonks, *A triple junction energy study using an inclination-dependent anisotropic Monte Carlo Potts grain growth model*, Materials & Design **239**, 112763 (2024).
8. J. Melville, V. Yadav, L. Yang, A.R. Krause, M.R. Tonks, J.B. Harley, *A new efficient grain growth model using a random Gaussian-samples mode filter*, Materials & Design **237**, 112604 (2024).

9. I.D. Khurjekar, B. Conry, M.S. Kesler, M.R. Tonks, A.R. Krause, J.B. Harley, *Automated, high-accuracy classification of textured microstructures using a convolutional neural network*, Frontiers in Materials **10**, 1086000 (2023).
10. W. Yan, J. Melville, V. Yadav, K. Everett, L. Yang, M.S. Kesler, A.R. Krause, M.R. Tonks, J.B. Harley, *A novel physics-regularized interpretable machine learning model for grain growth.* Maerials & Design. **222,** 111032 (2022).
11. B. Conry, J.B. Harley, M.R. Tonks, M.S. Kesler, A.R. Krause, *Engineering grain boundary anisotropy to elucidate grain growth behavior in alumina*, Journal of the European Ceramic Society **42** [13], 5864-5873 (2022).
12. L. Yang, F. Hilty, V. Muralikrishnan, K. Silva-Reyes, J.B. Harley, A.R. Krause, M.R. Tonks, *Calculating the grain boundary inclination of voxelated grain structures using a smoothing algorithm*. Scripta Materialia **218**, 114796 (2022).

Mechanical Behavior of Materials at the Micrometer Scale under Different Environments

Seok-Woo Lee (University of Connecticut)

Keywords: Micromechanical test, Dislocation, Plasticity, Fracture, Size effect

Research Scope

Mechanical behavior of metals at the micrometer scale is often different from that of bulk metals because the plasticity at the micrometer scale is controlled by the intermittent operation of dislocation sources, while the plasticity in bulk scale is controlled by continuous and collective evolution of dislocation structures. This intermittent, source-controlled plasticity is the finite-size signature of the same scale-free, collective dislocation dynamics that operate in the bulk, now truncated by the sample dimension. Temperature is an important factor that affects the motion of dislocation, but the effect of temperature on the source-controlled plasticity at the micrometer scale has not been understood well. For the past decade, the combined effect of temperature and sample dimension on compressive strength and plastic flow has been widely investigated. However, the combined effect of temperature and sample dimension on tensile plasticity and fracture has not been explored. To advance the knowledge on metal plasticity, it is crucial to understand how the interplay between temperature and sample dimension influences dislocation dynamics, the tensile ductility, as well as fracture. In this project, therefore, we study the tensile plasticity of body-centered-cubic (BCC) metals at the micrometer scale using in-situ cryogenic mechanical testing and theoretical calculation. This project aims to understand how the interplay between temperature and sample dimension affects tensile plasticity and fracture of BCC metals at the micrometer scale. We also propose a unifying theme of these size-dependent responses that can be organized within a finite-size scaling framework, in which sample dimension truncates the correlated dislocation activity that governs strength and flow at different temperatures. Research outcomes of this project will provide an important insight into understanding of mechanical behavior of metals at low temperature.

Recent Progress

We have developed and validated a finite-size scaling (FSS) theory of micropillar plasticity in which the applied stress plays the role of the control parameter, the accumulated plastic strain the order parameter, and the pillar diameter D the finite size that truncates the growing correlation length of collective dislocation activity. From the canonical FSS hypothesis [1] we derived a single constitutive law in which strain hardening and the size effect appear as two independent power laws, one in plastic strain and one in diameter, coupled through a single universal scaling function. The strain-hardening exponent m and the size exponent n are not fitting parameters; they are fixed by the underlying critical exponents of the transition.

The theory makes three falsifiable predictions, each of which we have confirmed against published data. First, because the scaling function factorizes, the size exponent n must be independent of the plastic strain at which the flow stress is evaluated. Using eleven micropillar datasets spanning FCC (Ni, Au) and BCC (Fe, Ta, V, Mo, Nb, W) single crystals in multiple orientations, we find that n

is nearly constant with strain in every system examined. This model-free experimental fact proves that strain and size enter the flow stress as strictly separable factors, exactly the factorization the FSS form demands. Second, the stress-strain data for all pillar diameters within a given material collapse onto a single universal master curve when expressed in FSS coordinates, with coefficients of determination ranging from 0.91 to 0.99 across the nine datasets examined (Figure 1). To our knowledge, this is the first demonstration that the constitutive response of a deforming crystal obeys finite-size scaling, the same scaling structure that governs magnetic systems, percolating networks, and interfaces at depinning. This collapse is the defining signature of criticality: material identity enters only through non-universal amplitudes and the numerical exponent values, not through the scaling structure itself, so FCC and BCC crystals, whose microscopic mechanisms could hardly differ more, obey the same law. Third, once the exponents and the amplitude are fixed, which requires stress-strain data from only two pillar diameters of adequate separation, the framework reconstructs the statistically averaged stress-strain response at any size within the source-controlled regime [2], capturing the correct ordering of strength with diameter, the magnitude of size-dependent strengthening, and the systematically stronger hardening of FCC relative to BCC.

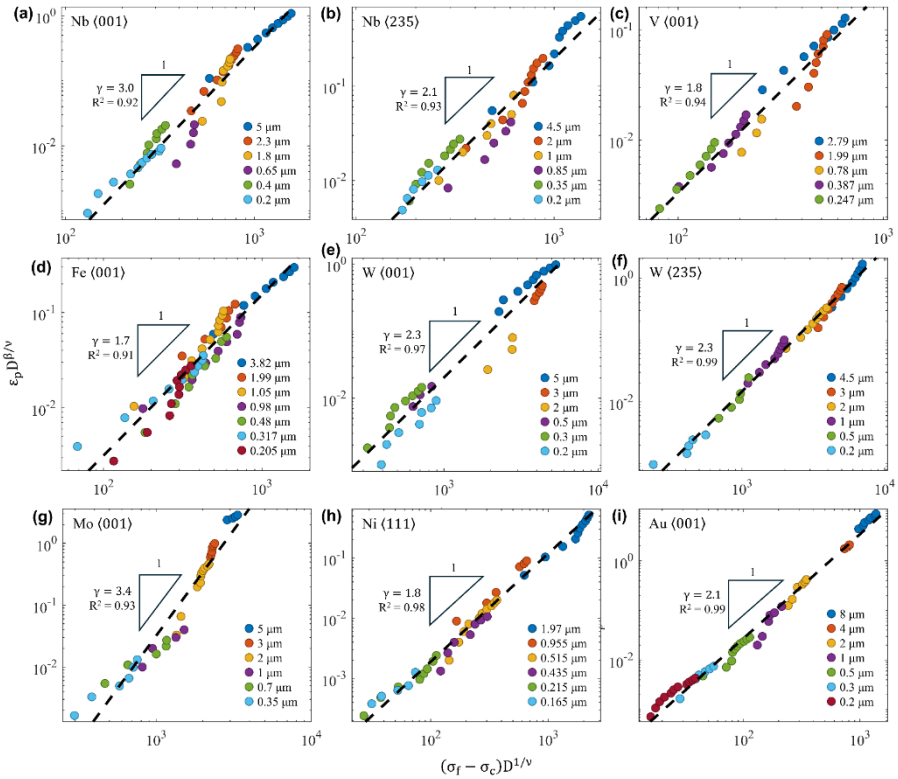

Figure 1. Universal data collapse confirming finite-size scaling. When expressed in finite-size-scaling coordinates (rescaled plastic strain versus rescaled excess stress), stress-strain data for all micropillar diameters within each material system fall onto a single master curve, shown here in logarithmic space for nine FCC (Ni, Au) and BCC (Nb, V, Fe, W, Mo) single-crystal datasets. Black dashed lines are power-law fits with slope γ; coefficients of determination R^2 range from 0.91 to 0.99. This universal function can obtained from stress-strain data with two different diameters only and can produce statistically-averaged stress-strain curves at any other diameters.

Two further results deepen the physical picture. First, we established a closed exponent algebra that locks the smooth constitutive law to the intermittent avalanche statistics [3]: the size exponent (n) obtained from the flow stress equals the ratio of the size (δ) and stress cutoff (κ) exponents of the avalanche-size distribution, $n = \delta/\kappa$. This link is an identity required by criticality rather than an empirical correlation, and it is independently testable by acoustic-emission and displacement-burst measurements. Second, the extracted exponents cluster by crystal structure rather than by material, with FCC and BCC occupying distinct regions of exponent space. This separation reflects how strongly the correlated dislocation trajectories of each structure couple to the specimen boundary: the extended, planar glide of FCC reaches the free surface readily and is strongly truncated (large n), whereas the more internal, kink-pair-controlled screw motion of BCC couples to the boundary weakly (small n). These findings point toward a small number of distinct universality classes of crystalline plasticity. Taken together, the work recasts "smaller-is-stronger" [4] as the finite-size truncation of correlated dislocation activity, and strain hardening as the continuous motion of a critical point that the deforming crystal tracks, or "surfs," throughout loading [5].

Future Plans

In the remaining period of this project, we will pursue two directions. First, we will generate realistic, discrete (jerky) stress-strain curves by superposing scale-free strain bursts, sampled from the same critical exponents and cut off by the pillar diameter, onto the smooth averaged response of the constitutive law, thereby turning the statistical variability of small-scale plasticity into a predicted rather than merely observed quantity. Second, we will map the boundaries of the source-controlled regime, characterizing the crossovers to dislocation starvation in the smallest pillars and to bulk Taylor storage in the largest, where the single-exponent scaling is expected to break down. We will also extend the analysis from compression to tensile data, applying the same finite-size scaling framework to the tensile plasticity of BCC metals to test whether the size-dependent tensile response obeys the same universal scaling structure. Together, these efforts will consolidate the finite-size scaling framework as a practical route to the size-dependent plasticity of BCC metals at the micrometer scale.

References

1. M. E. Fisher and M. N. Barber, Scaling Theory for Finite-Size Effects in the Critical Region, Physical Review Letters 28, 1516 (1972).
2. T. A. Parthasarathy, S. I. Rao, D. M. Dimiduk, M. D. Uchic, and D. R. Trinkle, Contribution to size effect of yield strength from the stochastics of dislocation source lengths in finite samples, Scripta Materialia 56, 313 (2007).
3. D. M. Dimiduk, C. Woodward, R. LeSar, and M. D. Uchic, Scale-Free Intermittent Flow in Crystal Plasticity, Science 312, 1188 (2006).
4. M. D. Uchic, D. M. Dimiduk, J. N. Florando, and W. D. Nix, Sample Dimensions Influence Strength and Crystal Plasticity, Science 305, 986 (2004).
5. M. Zaiser, Scale invariance in plastic flow of crystalline solids, Advances in Physics 55, 185 (2006).

Publications

1. Zhongyuan Li, Alexander J. Horvath, Sarshad Rommel, Shuyang Xiao, Gyuho Song, Mark Aindow, Seok-Woo Lee, Tensile behavior of micron-sized niobium single crystals: the effect of sample dimension, low temperature, and dislocation density, Scripta Materialia 277, 117248 (2026).
2. Kyle P. Wade, Mark Aindow, Seok-Woo Lee, Finite-size scaling unifies strain hardening and the size effect in small-scale crystal plasticity, submitted to Acta Materialia (2026).

Understanding The Influence of Ca and Zn on Twinning-Detwinning Behavior in Mg Alloys During In-SEM Cyclic Loading

Aeriel Leonard, Department of Materials Science and Engineering, The Ohio State University, Columbus, OH

Keywords: transmission electron microscopy; Twinning; Mg Alloys; Fatigue; Cyclic Stress-Strain Behavior

Research Scope

The research objective of this project is to understand and quantify the role of twin and twin boundary types on natural crack initiation in unalloyed Mg, Mg-RE, Mg-Zn, Mg-Ca, and Mg-Zn-Ca alloys. The core hypothesis of this work is that damage near and within twin and grain boundaries is driven by dislocation interactions and accumulations (i.e., pileups, penetrated dislocations, slip irreversibility) near these regions leading to a local stress concentration. It is well established that many wrought Mg alloys show a strong initial basal texture, where the c-axis in most grains is aligned normal to the working direction[1]. During cyclic loading the grains with this initial texture favor twinning during compression and the c-axis of the twinned regions are rotated 86.3° toward the working direction. When the load is reversed detwinning occurs and the twins either narrow or are removed altogether. Recent studies have shown that twinning is greatly reduced through the addition of RE elements and/or the combination of Ca and Zn [2,3]. However current research fails to collectively link dislocation interactions and structures at the nano and micro scale to meso-scale damage accumulation or macro-scale mechanical behavior. To improve the understanding of fatigue crack initiation, this study will involve a multi-scale and multi-modal systematic investigation to understand the mechanisms of damage accumulation leading to crack initiation.

Recent Progress

In recent progress[4,5], the project has focused on elucidating the fatigue deformation mechanisms in rare-earth (RE) containing Mg alloys and Mg–Zn–Ca alloys to identify the key similarities and differences governing their fatigue behavior. This understanding is imperative to discovering if the addition of Ca could produce Mg alloys with comparable or superior fatigue performance to RE containing alloys. The low-cycle fatigue behavior of an extruded, solution-treated Mg–2Nd–1Y–0.1Zr–0.1Ca alloy was investigated under fully reversed, strain-controlled loading at amplitudes of 0.4–0.8%. A multimodal characterization approach combining SEM, EBSD, FIB nanofabrication, STEM, and STEM-EDS was used to elucidate the influence of rare-earth (RE) elements on deformation mechanisms. The initial microstructure exhibited a RE texture with basal (0001) poles tilted ~30–45° from the loading direction, promoting non-basal slip activity. Cyclic hardening was observed across all strain amplitudes, accompanied by increases in

plastic strain amplitude and energy with increasing total strain. Site-specific STEM revealed that deformation was accommodated by basal ⟨a⟩ and pyramidal ⟨c+a⟩ slip. HAADF-STEM and center-of-symmetry analysis identified I_1 intrinsic stacking faults arising from ⟨c+a⟩ dislocation dissociation, along with dense fault aggregates in the postmortem microstructure. These findings provide new insight into the role of complex dislocation mechanisms in governing the cyclic response of rare-earth Mg alloys. The fatigue life (N_f) as a function of total strain amplitude (ε_A) is shown in Figure 1 for 0.4%, 0.5%, 0.6%, and 0.8%. The loading direction was parallel to the extrusion direction of the sample. The plastic strain amplitude ($\Delta\varepsilon_p/2$) at the half-life as a function of total strain amplitude is shown in Table 1. It was found that the fatigue life decreased as the total strain amplitude increased because of the increase in the amount of plastic strain induced at higher ε_A.

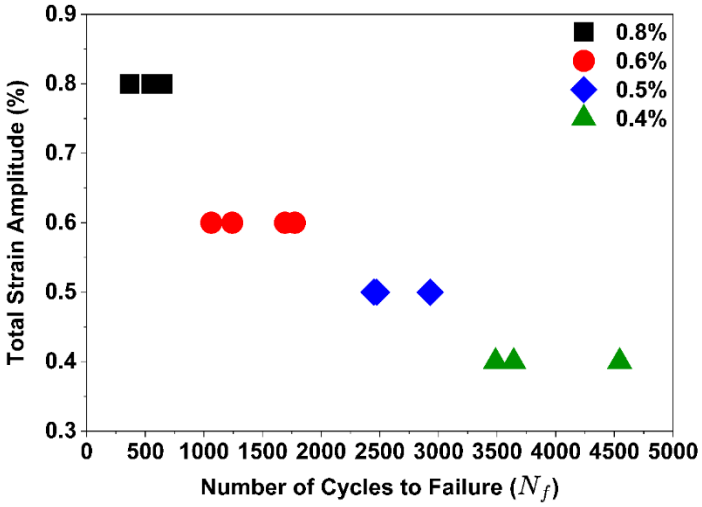

Figure 5: The total strain amplitude vs fatigue lifetime at total strain amplitudes of 0.4% (green triangle), 0.5% (blue diamond, 0.6% (red circle), and 0.8% (black square).

To investigate dislocation interactions within the microstructure during low-cycle fatigue, TEM lamellae were extracted from beneath the specimen surface after post-mortem cycling at a total strain amplitude of 0.6%. This strain amplitude was selected as it represents an intermediate level that exhibited gradual hardening throughout the test. Figure 2a shows a BF-STEM DCI image acquired in the $[\bar{1}2\bar{1}0]$ zone axis. The direction of the basal (0001) plane is indicated on the image. Under these conditions several planar dislocation slip marks were observed parallel to the basal plane. At the orientation where $g = [0002]$, is excited (Figure 2b), dislocations outlined by red solid circles are also visible at $g = [10\bar{1}0]$ (Figure 2c) indicating that these are <c+a> type dislocations. At $g = [10\bar{1}0]$ dislocations outlined in white solid lines are only visible under this orientation vector indicating that these are $\langle a \rangle$ type dislocations with

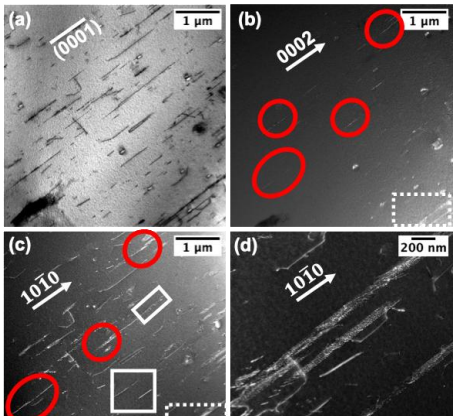

Figure 6:(a) BF-STEM DCI image of a region of interest (ROI) showing the activation of several dislocation acquired in the $[\bar{1}2\bar{1}0]$ zone axis, (b) – (c) DF-STEM DCI images of the ROI revealing the presence of <a> and <c+a> dislocations, and (d) a high magnification DF-STEM image of the area outlined by white dashed lines in (b) and (c) showing several slip bands oriented parallel to the (0001) plane. Individual <c+a> dislocations are piled up within the slip bands.

majority oriented parallel to the basal plane. Figure 2d is a high-resolution DF-STEM DCI image of the region outlined by a white dashed square in Figures 2b-c. Three planar slip bands oriented parallel to the (0001) planes are visible at both $g = [10\bar{1}0]$ and $g = [0002]$, conditions showing that these are <c+a> dislocations. Individual <c+a> dislocations piled up within the slip bands are observed in Figure 2d. In addition to slip bands, stacking fault fringes were also observed within the deformed microstructure. HAADF-STEM revealed the presence of a stacking fault bundle containing an aggregate of two intrinsic stacking faults (I_1 SF_1 and I_1 SF_2) which is shown in Figure 3a. The left, center, and right ends of the I_1 SF_1 are shown in Figures 10b, 10c, and 3d, respectively. COS mapping of FFT-filtered HAADF-STEM images was carried out to investigate disruptions in the stacking sequence in the matrix and are shown directly below each HAADF-STEM image. The COS map confirmed that the dissociation of the full dislocation into partial dislocations resulted in the formation of an I_1 intrinsic stacking fault where the stacking transitioned from ABABAB to ABABCBC. Through Burger's Circuit analysis (Figure 3h) it is confirmed that the partial dislocations are frank partial dislocations with $b = \frac{1}{6}\langle 02\bar{2}3\rangle$ *and* $b = \frac{1}{6}\langle 0\bar{2}2\bar{3}\rangle$. Stacking fault bundles are a concentrated array of multiple, closely spaced planar defects. Like the surrounding matrix, multiple stacking fault (SF) fringes were observed within the twin interior (Figure 4). However, the SFs did not propagate across the twin boundaries, indicating that they were nucleated at one twin boundary and subsequently pinned by the opposing boundary. The twin boundaries are outlined by red arrows, and the stacking faults are denoted by white arrows.

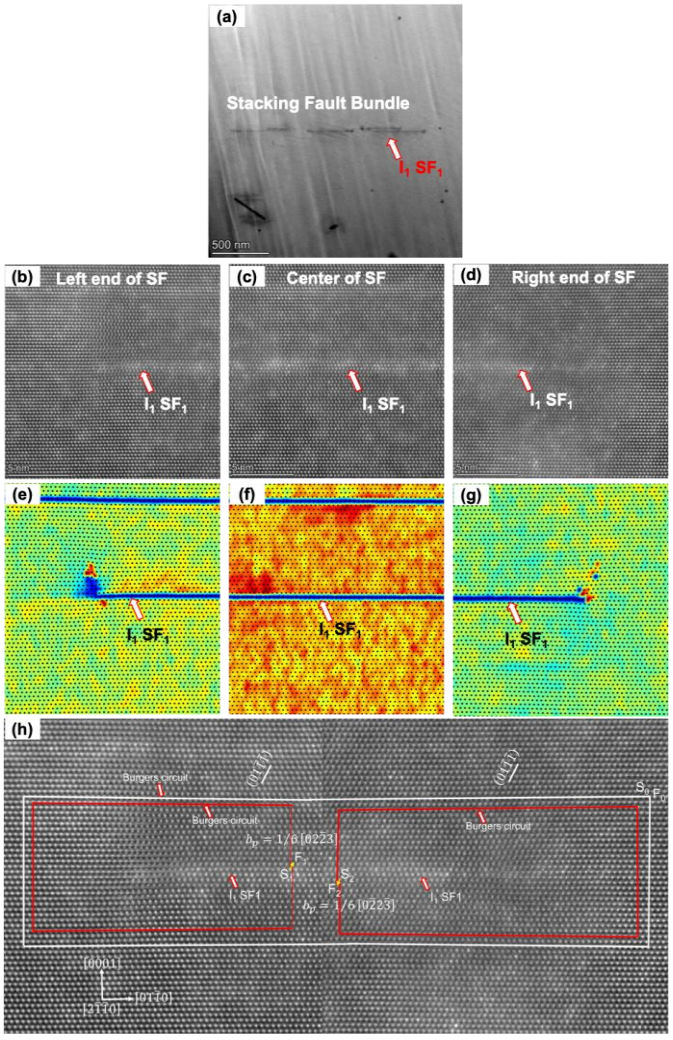

Figure 7::HAADF-STEM images of (a) stacking fault bundle containing two intrinsic stacking faults (I_1 SF_1 and I_1 SF_2), (b-d) the left, center, and right ends of I_1 SF_1 showing the Burgers and the corresponding (e-g) COS map are also shown. (h) Burger's Circuit analysis revealed that the partial dislocations are frank partial dislocations.

Future Plans

The previous project period focused primarily on elucidating the fatigue deformation mechanisms in rare-earth-containing magnesium alloys. Building on these findings, future work will shift toward Mg–Zn–Ca alloys to determine whether similar mechanisms govern their fatigue behavior. Recent results revealed that, as in rare-earth-containing Mg alloys, stacking faults nucleate within deformation twins and play a key role in controlling detwinning. In addition, calcium segregation and ordering were observed along extension twin boundaries, suggesting a previously unrecognized role of solute ordering in twin boundary stability and deformation. Future studies will investigate how these nanoscale defect–solute interactions influence cyclic deformation, fatigue crack initiation, and overall fatigue resistance in rare-earth-free Mg alloys.

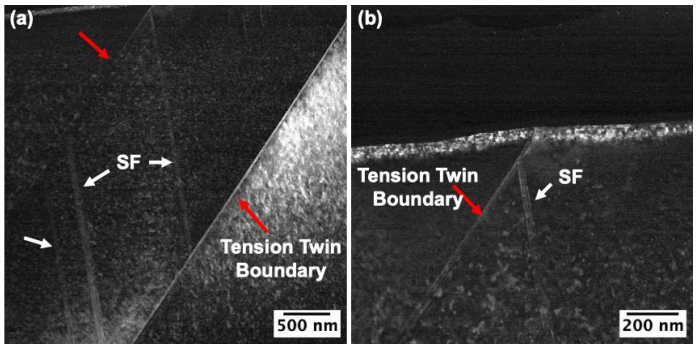

Figure 8: DF-STEM micrographs showing the (a) formation of stacking faults within deformation induced deformation twins and (b) the interaction between the SF and the twin boundary.

References

[1]Murphy-Leonard AD, Pagan DC, Beaudoin A, Miller MP, Allison JE. Quantification of cyclic twinning-detwinning behavior during low-cycle fatigue of pure magnesium using high energy X-ray diffraction. Int J Fatigue 2019; 125:314–23. https://doi.org/10.1016/j.ijfatigue.2019.04.011.
[2]Berman TD, Allison JE. Coupling Thermomechanical Processing and Alloy Design to Improve Textures in Mg-Zn-Ca Sheet Alloys. Jom 2021. https://doi.org/10.1007/s11837-021-04630-0.
[3]Roumina R, Lee S, Berman TD, Shanks KS, Allison JE, Bucsek A. Mg-3. 2Zn-0. 1Ca wt.% alloy using in-situ far field high-energy diffraction microscopy. Acta Mater 2022:118039. https://doi.org/10.1016/j.actamat.2022.118039.
[4]Smith J, Miao J, Murphy-Leonard AD. The role of rare earth additions on low cycle fatigue behavior of a Mg-2Nd-1Y-0.1Zr-0.1Ca alloy. Journal of Magnesium and Alloys 2026. https://doi.org/10.1016/j.jma.2026.102151.
[5]Mena A, Miao J, Veghte D, Williams B, Murphy-Leonard AD. In-situ observations of cyclic deformation in an extruded Mg-2Nd-1Y-0.1Zr-0.1Ca alloy. Int J Fatigue 2026:109489. https://doi.org/10.1016/j.ijfatigue.2026.109489.

Publications

Smith J, Miao J, Murphy-Leonard AD. The role of rare earth additions on low cycle fatigue behavior of a Mg-2Nd-1Y-0.1Zr-0.1Ca alloy. Journal of Magnesium and Alloys 2026. https://doi.org/10.1016/j.jma.2026.102151.

Mena A, Miao J, Veghte D, Williams B, Murphy-Leonard AD. In-situ observations of cyclic deformation in an extruded Mg-2Nd-1Y-0.1Zr-0.1Ca alloy. Int J Fatigue 2026:109489. https://doi.org/10.1016/j.ijfatigue.2026.109489.

Discovering the Mechanisms of Photoplasticity in Semiconductors

Lin Li, Arizona State University

Qi An, Iowa State University

Keywords: Photoplasticity; CdTe; Dislocations; Atomistic Modeling; Deformation Mechanisms

Research Scope

Photoplasticity in semiconductors refers to the reversible changes in mechanical properties, such as flow stress and hardness, caused by the interactions between photoexcited charge carriers and extended defects. II-VI semiconductors commonly exhibit a positive photoplastic response as illumination hardens the material; however, this is modulated by several factors, including doping, accumulated plastic strain, and temperature [1]. Understanding photomechanical behavior in semiconductors is of both fundamental and technological importance, as it involves complex interactions between electronic states and defect mobility and has important implications for photovoltaic and optoelectronic materials and their associated manufacturing processes. Studying photoplasticity is inherently multiscale, requiring an understanding of how photoexcitation modifies electronic structure and bonding at defect cores, how these changes affect the energetics and kinetics of dislocation motion, and ultimately how altered dislocation behavior governs plastic deformation at experimentally relevant length and time scales. Using CdTe as a prototype II–VI semiconductor, this project integrates ground- and excited-state density functional theory (DFT), machine-learning interatomic potentials, atomistic simulations, and mesoscale crystal plasticity modeling to establish these connections and uncover the fundamental mechanisms governing photoplasticity.

Our major progresses in the last year have advanced fundamental understanding of photoexcitation on the elastic fields and mobility of partial dislocations in CdTe through simulation of kink-pair mechanisms and revealed a critical role of chemically passivated grain boundaries in the enhancement of the photomechanical performance of polycrystalline CdTe thin-films.

Recent Progress

Machine-learning potentials for ground- and excited-state CdTe

A major enabling accomplishment of this project has been the development of the machine-learning interatomic potentials (MLIPs) for CdTe in the ground-state (dark) and two excited-state (light) conditions [2]. The potentials are trained on databases obtained from ground-state density-functional theory (DFT) calculations or from excited-state constrained DFT calculations, with the latter introducing an explicit electron-hole (e-h) pair concentration to simulate the photoexcited state in CdTe. The newly developed MLIPs have been systematically validated against DFT (and constrained DFT) calculations of elastic constants, dislocation core structures, generalized stacking-fault energies, and Peierls energy landscapes, providing the computational foundation for

the project's subsequent studies of kink-pair nucleation and migration, dislocation mobility, and photoexcitation-dependent deformation in CdTe.

Effect of photoexcitation on the kink pair mechanisms of partial dislocations

As an initial effort into studying the effects of photoexcitation on dislocation mobility in CdTe, simulations of kink-pair mechanisms were performed in the ground- and excited-states. The 30° partial dislocation was selected as a representative dislocation structure due to its lack of predicted core reconstruction, remaining in the single-periodic (SP) configuration, irrespective of excitation conditions. Energetic barriers for kink-pair nucleation and single kink migrations, as distinct processes, were performed using nudged elastic band (NEB) calculations alongside our recently developed MLIPs. A primary objective of this research was to discern how photoexcitation modifies the activation energies for kink-pair mechanisms as these energies are proportional to the velocity of dislocations in the material and, therefore, to the rate of macroscopic plastic deformation.

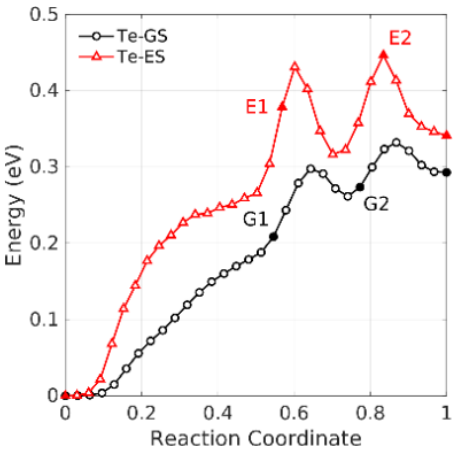

Figure 1. Minimum energy pathways for kink-pair nucleation on 30°-SP Te-core dislocation in the ground-state (GS) and excited-state (ES) conditions.

Results from the simulations indicate that the effects of photoexcitation at the specific charge carrier concentration examined (0.5 e-h pairs per 100 atoms) is predominantly energetic in nature. No significant bond reconstruction is introduced by photoexcitation in the 30°-SP partial dislocations and, as such, structural changes associated with the nucleation or migration of kinks are remarkably similar between the ground- and excited-state conditions. Despite this, however, significant differences in the activation energies for the processes are measured. This is exemplified by the differences in the minimum energy pathways for kink-pair nucleation of Te-core (β) dislocations in CdTe, as shown in Figure 1. In the ground-state, Te-core dislocations exhibit an overall activation energy for dislocation motion, that is, the addition of the single kink formation energy and the average single kink migration barrier, of 0.252 eV while under photoexcitation this value increases to 0.371 eV. Conversely, Cd-core (α) dislocations (not shown) exhibit an elevated activation energy in the ground-state of 0.673 eV reducing under photoexcitation to 0.278 eV, compared to that of the Te-core dislocation in the ground-state. The results for the excited-state activation energies are qualitatively consistent with experimental observations of core-dependent dislocation mobility in CdTe, with Cd-core (α) dislocations being generally accepted to be the more mobile species under photoexcitation. These results suggest that macroscopic photoplasticity observed in CdTe may be partially governed by changes in the mobility of the Te-core dislocation while the increased mobility of Cd-core dislocations under photoexcitation may hint towards an increase in dislocation interactions during prolonged plastic deformation events leading to modifications of the work-

hardening rate and increase in immobile dislocation density that diminishes the effects of photoplasticity, as have been experimentally demonstrated for CdTe.

Defect-mediated photoplasticity in polycrystalline CdTe thin-films

Polycrystalline CdTe thin-films are regularly treated with $CdCl_2$ to reduce non-radiative recombination and increase overall photovoltaic device efficiency. Studies on photoplasticity are generally constrained to bulk semiconductor materials, typically single-crystalline, and the photoexcitation modification of defect states or dislocation mobility while neglecting the contributions of grain boundaries (GBs). GBs in CdTe act as both barriers to dislocation motion and as active centers for non-radiative recombination. As such, photoexcitation effects in as-deposited thin-films of CdTe may be constrained by recombination at GBs as they reduce the charge carrier population available to interact with extended defects. Nanoindentation experiments were carried out on as-deposited and $CdCl_2$-treated thin-films of CdTe to understand how GB passivation and microstructural changes induced from the treatment impact the photoplastic effect in polycrystalline thin-films.

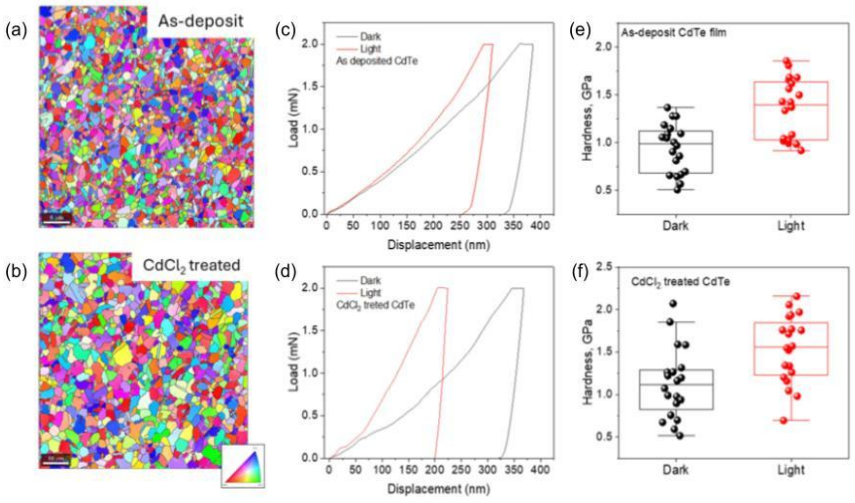

Figure 2. EBSD scans of (a) as-deposited and (b) $CdCl_2$ treated thin-films. Representative load-displacement curves in dark and light conditions on the (c) as-deposited and (d) $CdCl_2$ treated thin-films. Box and whisker plots showing the measurements of hardness in dark and light conditions on the (e) as-deposited and (f) $CdCl_2$ treated thin-films.

Treated thin-films exhibit a larger grain size (~3 μm) compared to as-deposited thin-films (~1 μm) and reduced residual strain due to microstructural changes from the treatment. Post-processing analysis of electron backscatter diffraction (EBSD) area scans of the thin-film surfaces (Figs. 2a,b) showed that Σ3 GBs constituted a significant portion (~30%) of the GB networks. Time-resolved photoluminescence measurements confirmed that the treatment increased the carrier lifetime to ~100 ns from ~20 ns in the as-deposited thin-films which is consistent with previous studies that have shown that Cl can passivate defect states at GBs in polycrystalline CdTe. Representative nanoindentation measurements show that photoexcitation only modestly affects the load-displacement response of as-deposited CdTe (Fig. 2c) while the treated thin-film is substantially enhanced (Fig. 2d). This weak photomechanical response in the as-deposited thin-films corresponds to an average 5 GPa increase in reduced modulus and 0.2 GPa increase in hardness (Fig. 2e). After treatment, the thin-film exhibits an average 21 GPa increase

in modulus and 0.5 GPa increase in hardness (Fig. 2f), a strong photomechanical response, corresponding likely to the combined effects of chemical passivation and increased GB stability due to the incorporation of Cl_{Te} defects.

Supporting DFT calculations were performed to confirm the effects of Cl segregation on GB cohesion by systemically introducing Cl_{Te} substitutional defects into both Σ3 and Σ5 GBs. Segregation of Cl is observed to weaken or eliminate Te-Te dangling bonds resulting in passivation of the GBs. Work of adhesion calculations are performed for the pristine and solute-segregated GBs with the Σ3 GBs exhibiting a marked increase from 0.36 J/m^2 to 0.51 J/m^2, respectively, while the Σ5 GBs had a negligible increase from 0.60 J/m^2 to 0.61 J/m^2, respectively. From this, we found that the interfacial fracture toughness of the Σ3 GB increases with segregation by 17.5% while the Σ5 GBs increased by only 1.2%. This increase for the Σ3 GB is significant as both thin-films exhibit a large fraction of Σ3 GBs in their GB networks suggesting an outsized effect on bulk photomechanical performance may arise from the chemical passivation of the Σ3 GB.

Future Plans

In the next year, we plan to extend the study of kink pair mechanisms to shuffle-set perfect (0° and 60°) dislocations while pursuing in parallel the computation of the mobilities of these same dislocations in CdTe under photoexcitation. The use of shuffle-set dislocations is motivated by their ability to remain undissociated at elevated temperatures (conversely, glide-set dislocations dissociate at temperatures as low as 5 K [3]) and their relatively lower dislocation core energy when compared to glide-set perfect dislocations [3]. This effort will provide much needed dislocation mobility data to support the development of atomistically-informed crystal plasticity models of photoplasticity.

Our recent findings also highlighted the complex interplay between chemical passivation and grain boundary cohesion on the photomechanical response of CdTe. For polycrystalline thin-film photovoltaic and optoelectronic materials, GBs are critical targets for processing strategies to both improve carrier transport and light-dependent mechanical reliability. As such, fundamental calculations establishing the effects of photoexcitation on the cohesion of various low- and high-energy CSL-type grain boundaries is to be pursued leveraging a combination of MLIPs and density-functional theory calculations.

References

1. C. Cao, and Q. An, *Photoplasticity behavior in inorganic semiconductors: unraveling fundamental mechanisms across ionic and covalent systems*, Mater. Horiz. **13**, 2767-2785 (2026).
2. K. Luo, R. Zhou, and Q. An, *Mechanistic insights into photoplasticity of CdTe*, International Journal of Mechanical Sciences **305**, 110765 (2025).
3. J. Li, K. Luo, and Q. An, *Atomic structure, stability, and dissociation of dislocations in cadmium telluride*, International Journal of Plasticity **163**, 103552 (2023).

Publications in the recent 2-years

1. C. Cao, and Q. An, *Photoplasticity behavior in inorganic semiconductors: unraveling fundamental mechanisms across ionic and covalent systems*, Mater. Horiz. **13**, 2767-2785 (2026).
2. X. Han, J. Cappola, C. Cao, Y. Wang, D. Li, Y. Zheng, Q. An, L. Li, and F. Yan, *Defect-mediated photoplasticity in polycrystalline CdTe thin films*, Matter & Light **1**, 100070 (2026).
3. J. Cappola, K. Luo, Q. An, and L. Li, *Kink-pair nucleation and migration barriers of 30°-SP partial dislocations in photo-excited CdTe via machine-learning potentials*, Under review.
4. XG. Huang, K. Luo, J. Cappola, L. Li, Q. An, *Effective eigenstrain contribution to photoexcited dislocation elastic fields in CdTe*, Under review
5. J. Cappola, J. Carbajal, F. Yan, Q. An, L. Li, *Grain boundary strengthening in CdTe induced by solute segregation from $CdCl_2$ passivation*, In preparation.
6. L. Kulundu, C. Cao, K. Luo, L Li, Q. An, *Coupling of Electronic Excitation and Grain-Boundary Disorder in the Inverse Hall–Petch Plasticity of Nanocrystalline CdTe,* In preparation.

Influence of 3D heterophase interface structure on deformation physics

Prof. Nathan A. Mara, University of Minnesota-Twin Cities

Prof. Irene J. Beyerlein, University of California, Santa Barbara

Keywords: Dislocation-interface interactions; Phase Field Dislocation Dynamics; Crystal Plasticity; Nanolayered Composites; Electron Microscopy; Enhanced Strength and Ductility

Research Scope: The goal of this program is to develop an **understanding of the mesoscopic effects of biphase interfaces on their interactions and reactions with dislocations and slip bands**. Interfaces play a profound role in the response of materials to mechanical deformation through the localized strains and stresses they develop and their resulting effects on the defects that enable plasticity. Not all interfaces produce the same effect and the outcome of their interactions and reactions with defects depends on the structure of the interface. Detailed work into the defect-interface interactions enabling the enhanced mechanical behavior of two-phase or multiphase materials have only begun to investigate the rich parameter space of heterophase interface character, morphology, and chemistry. To date, heterophase interfaces are generally regarded as two dimensional (2D), and chemically and structurally abrupt. Yet for decades, studies have pointed to the enormous influence that interface properties in the out-of-plane dimension can have on strength and mechanical behavior.

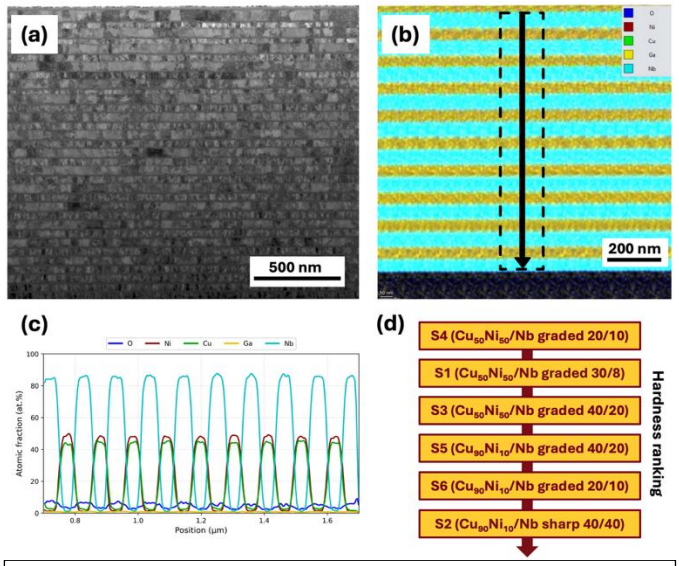

Figure 1: **(a)** Bright field TEM micrograph of $Cu_{50}Ni_{50}$/Nb nanoscale multilayer with 40 nm constituent layer thickness and 20 nm 3D interface thickness. **(b)** STEM-EDS map of same multilayer as in (a) with the corresponding EDS line scan in **(c)**. **(d)** Ranking of hardness from highest (top) to lowest (bottom) of CuNi alloy/Nb nanolayered composites. The graded interfaces show increased strength over the reference with sharp interfaces, and the composites containing 50/50 Cu/Ni alloy as one of the constituents ranks highest amongst samples tested (S4, S1, S3).

In this project, we aim to understand defect-interface interactions and their effects on mechanical behavior using composites containing *3D interfaces*. 3D interfaces are heterophase interfaces that extend out of plane into the two adjacent crystals. They are chemically, crystallographically, and topologically divergent, from the crystals they join. Such interfaces influence not only the unit processes of single dislocations that can be understood at the atomic scale, but also mechanical behavior at the scales of a few to tens of dislocations and the resulting bulk behavior. The types of 3D interfaces studied encompass those containing chemical gradients and/or boundary curvature, and are of relevance to particle-strengthened materials, irradiated materials, lamellar composites, and more.

For 3D interface effects, the scientific issues concern attaining a multiscale understanding of defect physics from the unit process (e.g., alterations in the dislocation core as it reacts with an interface) to impinging dislocation arrays that can transform the interface structure to the collective processes of multiple slip interactions. Each process can be profoundly altered by varying the chemical composition and structure of the 3D interface. In this program, we converge synthesis, measurement, and modeling efforts to elucidate basic, controllable structural variables of the 3D interface that affect structural material performance. The materials containing interfaces are synthesized via physical vapor deposition, a process by which the composition and/or structure may be systematically varied in the out-of-plane direction. Microstructural characterization consists of a suite of techniques that addresses structure at the atomic level (TEM, Atom Probe), as well as mesoscales (X-ray). Mechanical behavior is investigated at length scales ranging from atomic-level dislocation-interface interactions (in-situ TEM) to micro scales (in-situ SEM and ex-situ nanomechanical testing). A combination of atomic-scale simulation and mesoscale modeling are employed to simulate dislocation interactions with the 3D interfaces we synthesize. The calculations together aim to uncover fundamental mechanistic details underlying the dislocation reactions, to extract the energies and critical stresses associated with them, and to relate them to the morphology and chemistry of the 3D interfaces. At present, the methods for simulating the dynamic evolution of many discrete dislocations in crystals with interfaces that span this broad range of length scales include molecular dynamics (MD), discrete dislocation models and crystal plasticity (CP). In this program, we exploit phase field dislocation dynamics (PFDD) to simulate multiple dislocation interactions with 3D interfaces, and their collective behavior informs CP-fast Fourier transform (CP-FFT) models capable of understanding and predicting the propensity for slip localization and premature failure [2, 3]. PFDD uses density functional theory and MD calculations as input into simulation models. PFDD can model single or multiple dislocations within a single crystal or nanolaminate or nanocrystalline polycrystal. Further, the output of PFDD can be linked to experimentally determined stress-strain responses, as can CP-FFT.

Recent Progress: Recently, we discovered that $Cu_{50}Ni_{50}$-Nb nanocomposites containing 3D interfaces with layer thickness h = 40 nm and 3D interfacial thickness of h’ = 20 nm provide enhanced hardness over their 2D counterparts. **(See Figure 1)**. One of the constituent layers is a Cu_xNi_{1-x} alloy that forms a FCC solid solution. The other constituent layer is pure Nb, with a continuously graded interface between them. While Ni and Nb may form intermetallics, the sputtering process provides for quenching-in metastable structures, with no intermetallic phase evident via XRD or STEM-EDS. We observe that a decrease in Ni content is accompanied by a decrease in hardness, showing that even at these relatively coarse layer thicknesses alloy content can strengthen. As layer thicknesses decrease, the role of alloying may present a weaker strengthening effect compared to local interfacial structure and chemistry.

In conventional 2D-interface nanolaminate materials, reducing layer thickness historically causes an increase in strength, but a decrease in deformability [4]. As such, we investigating interface thickness h′ effects on strength and shear localization in Ti/Nb [5] and a companion paper on

Cu/Nb [1], showing that 3D interface h′ substantially suppresses shear localization and promotes delocalized deformation. For Ti/Nb, our findings demonstrated a strong asymmetry in slip transfer direction, with thicker h′ increasing the critical stress for transfer and modulating the degree of directional asymmetry. An extended PFDD model for the hcp Ti/bcc Nb 3D interface system incorporating a gradient interface approximation and the same interfacial character was used to determine the role the interfacial gradient plays in slip transmission pathways and associated critical stresses. **Figure 2** depicts the complexity of the gradient structures found within the 3D interface and how they can be captured in PFDD models containing regions of differing composition or crystal structure.

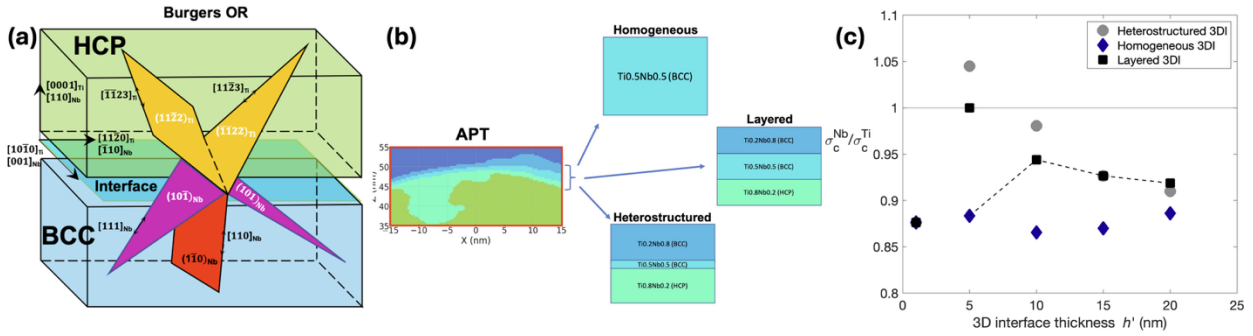

Figure 2**: (a)** Schematic representation of the dominant Ti/Nb Burgers orientation relationship and relevant crystallographic slip planes and directions. **(b)** Schematic of homogeneous, and APT-informed heterostructured gradient and layered gradient approximations for the 3DI. In the heterostructured case, the 50-50 layer always has a thickness of 1 nm. In the layered case, the thickness of the three sub-layers is the same. **(c)** Asymmetry ratio-the ratio of the critical stress for slip transfer for dislocations starting in Nb to dislocations starting in Ti for the homogeneous (blue diamonds), gradient layered (black squares) and gradient heterostructured (gray circles) approximations. The dashed line tracks the interfaces seen in APT. *(publication in review)*

The APT observations motivated dislocation dynamics simulations consisting of Ti and Nb crystals in the Burgers orientation and 3DI in-between. In the model, the 3DI is segmented into Ti-rich, Nb-rich, and 50/50 regions. Directly embedding either gradient or homogeneous 3D interfaces into the calculation shows that the critical slip transfer stress is sensitive not only to 3DI thickness but also to its compositional gradients. The structural and chemical gradient interface representations exhibit asymmetric behavior not predicted for the homogeneous interface. Notably, gradient representations lead to up to a 10% increase in the directional independence of slip transmission. These 3D interface structures open a new design space for tuning dislocation-interface interactions. Thickness, morphology, chemical gradients, lattice structural gradients are just some of the features that can be altered to affect dislocation-based mechanisms and processes. In the case of Cu/Nb **(Figure 3)** [1], the PFDD model was set up to predict the stresses and energies associated with slip transmission across the Cu/Nb 3D interfaces of different h′. The model was informed by data from APT and TEM and by atomistic simulations for the moduli and gamma surfaces of the 3D interface material. The 3D interfaces were mostly crystalline but the relatively thicker ones contained amorphous precipitates, in agreement with experiment. Our work revealed a critical insight: as h′ increases in Cu/Nb systems, the 3DIs transition from facilitating strain

redistribution to adopting metallic glass-like behavior. While these interfaces can arrest shear bands, after a critical length-scale they sacrifice uniform deformability, resulting in brittle failure.

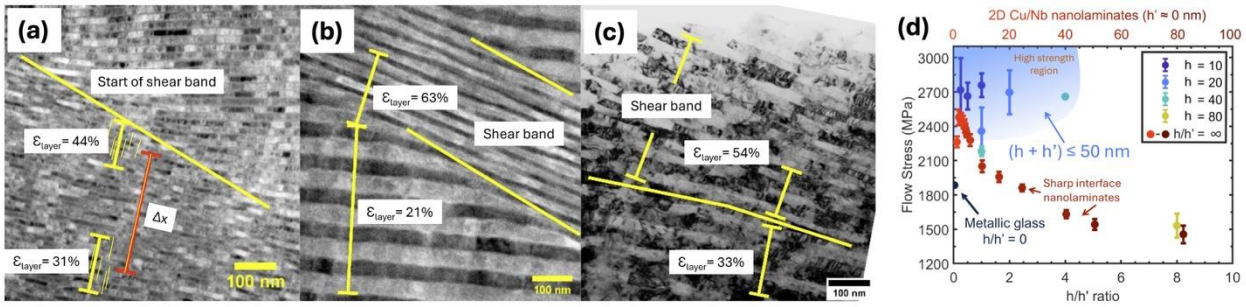

Figure 3: **(a)** Comparative shear band formation in different Cu/Nb nanolaminates. a) 10- 10 Cu/Nb broad shear band snapshot at 0.27 strain. Strain is accommodated over a large volume and the layer-to-layer change in strain happens gradually, as can be seen in the 10-10 stress-strain curve (not shown), where the onset of plasticity occurs over a strain range. Small yellow lines in (a) denote measurement overlays performed through ImageJ for reasonable quantitative backing. **(b**) 40-10 Cu/Nb exhibits a narrower shear band, indicative of stress localization. **(c)** 2D 40 Cu/Nb. Shear band is found between the yellow lines. ε_{layer} is calculated both inside and outside the shear band as there is plastic deformation outside the shear band. **(d)** Micropillar compression flow stress of nanolaminates with various combinations of h + h′. The sky blue region denotes a region where most combinations of (h + h′) ≤ 50nm have superior strength than their sharp interface counterparts. The data suggests that specific layer and interface thicknesses combinations promote enhanced strength. The red spectrum data was involves only 2D interface Cu/Nb nanolaminates, which saturate in the lower high strength region at h ≈ 2nm. [1]

Future Plans: In the second half of this grant cycle, we will continue work into the deformation physics of Cu-Ni/Nb nanolaminate composites containing 3D interfaces. **(a)** We will continue studying slip band development using the SB-FFT model in combination with machine learning algorithms to predict mechanical stability. The role of gradient properties of 3D interfaces in the dispersion of slip bands within layers, across layers, and their connectivity. **(b)** We plan to apply the MD and PFDD modeling to study the role of Cu-Ni alloy concentration on the 3D interface properties, dislocation core structure, and slip transmission process. **(c)** Continue microstructural characterization and nanomechanical testing of Cu-Ni/Nb multilayers using TEM/STEM, STEM-EDS, and XRD to establish the relationship between deposition conditions, 3D interface structure, and resulting properties. This will better inform PFDD and SB-FFT modeling.

References

1.De Leo, M., N. Fuchs-Lynch, J.Y. Cheng, S. Xu, I.J. Beyerlein, and N.A. Mara, *Interface thickness size effects on strength and shear localizations in Cu/Nb nanolaminates.* International Journal of Plasticity, 2026. **199**: p. 104640. DOI:https://doi.org/10.1016/j.ijplas.2026.104640
2.Ahmadikia, B., M.A. Kumar, and I.J. Beyerlein, *Effect of neighboring grain orientation on strain localization in slip bands in HCP materials.* International Journal of Plasticity, 2021. **144**: p. 103026. DOI:https://doi.org/10.1016/j.ijplas.2021.103026
3.Ahmadikia, B., L. Wang, M.A. Kumar, and I.J. Beyerlein, *Grain boundary slip – twin transmission in titanium.* Acta Materialia, 2023. **244**: p. 118556. DOI:https://doi.org/10.1016/j.actamat.2022.118556
4.Beyerlein, I.J., Z. Li, and N.A. Mara, *Mechanical Properties of Metal Nanolaminates.* Annual Review of Materials Research, 2022. **52**(1): p. 281-304. DOI:10.1146/annurev-matsci-081320-031236
5.Fuchs-Lynch, N., M. De Leo, P. Garg, S. Xu, N.A. Mara, and I.J. Beyerlein, *3D interface size effects on slip transfer in Ti/Nb nanolaminates.* International Journal of Plasticity, 2025. **186**: p. 104246. DOI:https://doi.org/10.1016/j.ijplas.2025.104246

Publications (10 most relevant, 2024-present):

1. N. Fuchs-Lynch, M. de Leo, J.D Poplawsky, B.K. Derby, N.A. Mara ,I.J. Beyerlein, "Slip bands in Cu/Nb nanolaminates with thick 3D interfaces", *under review at the Journal of Applied Physics (2026)*
2. M. de Leo, "Interface-driven mechanical response of Titanium-Niobium HCP/BCC nanocomposites" University of Minnesota PhD Dissertation (2026).
3. M. de Leo, N. Fuchs-Lynch, I.J. Beyerlein, N.A. Mara "Designing 3D interfaces for enhanced mechanical performance in nanolaminates", *JOM, (2026).*
4. N. Fuchs-Lynch, M. de Leo, J.D Poplawsky, B.K. Derby, N.A. Mara ,I.J. Beyerlein, "Chemical and structural gradients in thick interphases in Ti/Nb nanolaminates", *under review at Materials Science and Engineering A (2026).*
5. M. de Leo, N. Fuchs-Lynch, J.Y. Cheng, S. Xu, I.J. Beyerlein, N.A. Mara, "Interface thickness size effects on strength and shear localizations in Cu/Nb nanolaminates", *International Journal of Plasticity,* Vol. 199, 104640 (2026).
6. M. de Leo, N. Fuchs-Lynch, B. Derby, Y. Chen, I.J. Beyerlein, N.A. Mara, "Extending interfaces in 3D to achieve superior nanoscale strength in Ti/Nb nanolaminates", *Nano Letters,* Vol. 25, issue 21, 8503-8510 (2025).
7. N. Fuchs-Lynch, M. de Leo*, P. Garg, S. Xu, N.A. Mara, I.J. Beyerlein, "3D interface size effects on slip transfer in Ti/Nb nanolaminates", *International Journal of Plasticity*, Volume 186, 104246 (2025).
8. J.Y. Cheng, A. Hamilton, M. Odlyzko, M. De Leo, J.K. Baldwin, N.A. Mara, "Thick graded interfaces increase wear resistance in Ti/TiN nanolayered thin films", *Thin Solid Films*, Volume 816, 140653 (2025).
9. J.Y. Cheng, Z. Li, D.L. Poerschke, J.K. Baldwin, B.L. Bresnahan, N.A. Mara, "Thermal Stability of 3D Interface Cu/Nb Nanolaminates", *Scripta Materialia*, Volume 254, 116319 (2025).
10. J.Y. Cheng, J. Wang, Y. Chen, S. Xu, J.G. Barriocanal, J.K. Baldwin, I.J. Beyerlein, N.A. Mara, "3D interfaces enhance nanolaminate strength and deformability in multiple loading orientations", *Acta Materialia*, Volume 267, 119697 (2024).

Interplay between radiation-induced segregation and irradiation-induced grain boundary migration

Emmanuelle Marquis (University of Michigan), Fadi Abdeljawad (Northwestern University), Enrique Martinez (Clemson University), Suveen Mathaudhu (Colorado School of Mines)

Keywords: Irradiation, grain boundaries, segregation

Research Scope

In the context of developing an understanding of materials behavior under irradiation to support the continued advancement of reliable nuclear energy, this project seeks to uncover, understand, and model the interplay between chemical species and structural defects that governs chemical partitioning and grain boundary evolution. Specifically, we focus on radiation-induced segregation (RIS) at defect sinks in alloys and its role in controlling microstructural evolution during irradiation. The coupling between grain boundary motion and radiation damage has been studied in the literature with conflicting conclusions, mainly at intermediate temperatures and grain sizes beyond hundreds of nm, where the basic mechanisms leading to the migration of the boundary are not well established. Through integrated ex-situ and in-situ experimental, theoretical and computational approaches, the PIs aim to challenge commonly held assumptions regarding the interplay between RIS, defect fluxes and grain boundary motion, and develop new knowledge and tools to understand, model, and predict the co-evolution of chemistry and microstructure of metallic alloys by:

- Explaining the fundamental mechanisms for grain boundary migration under irradiation (radiation-induced grain boundary migration) at intermediate temperatures and relatively large grain sizes (> hundreds of nms).
- Quantifying the role of displacement cascades in grain boundary migration at intermediate temperatures and grain sizes.
- Establishing the correlation between RIS and grain boundary migration.
- Uncovering the relation between grain boundary structure, defect fluxes and boundary migration.

Recent Progress

Diffusion calculations

A new kinetic Monte Carlo (KMC) method has been developed to allow for the calculation of the transport coefficients induced by vacancy jumps. It relies on a tensor-contraction cluster expansion (TCE) (recently developed in the project) that renders the calculation of energy differences trivial. We have added the saddle point configurations to the TCE to be able to compute the rates for every possible event in the system, in this case for a vacancy to exchange with a first nearest neighbor. TCE can estimate the energy of any concentrated alloy provided there is data to fit it and the calculation of the activation energy is fast enough to run long enough trajectories to accurately compute the transport coefficients. A paper with results for the model W-Ta system is under review. We are currently working on adding self-interstitial jumps, which is crucial for materials under irradiation. The goal is to generalize the model to work for a wide range of materials, although the number of potential configurations to deal with in this case is significantly large and depends quite strongly on the specific alloy.

Revisiting the notion of RIS steady state.

The existence of a steady state for RIS requires that the alloy grain interiors, away from grain boundaries, also reach some form of steady state. However, prior RIS literature did not directly quantify microstructures away from grain boundaries, be it dislocation loop, cavity or possible phase separation such as precipitation. Consequently, our approach focused on the full quantification of RIS evolution up to high doses under our working hypothesis that a lack of steady state in the grain interior can prevent RIS at grain boundaries from reaching a steady state.

Using two model Fe-Ni-Cr alloys that were ion irradiated at 400 ºC, we showed that the evolution of RIS at grain boundaries correlates with phase evolution in grain interiors. In the alloy undergoing irradiation-accelerated spinodal decomposition, grain boundary chemistry was dominated by RIS at low doses with the expected Ni enrichment and Fe and Cr depletion (Figure 1). RIS, however, evolved significantly at higher doses as phase separation evolved in the grain interior from mid (15 dpa) to high doses (70 dpa). The behavior was reproduced using a phase-field approach. In the second alloy, the extent of the phase separation did not evolve from low (5 dpa) to high dose (70 dpa), correlating with no notable changes in the RIS response at grain boundaries. The findings highlight the synergy between grain

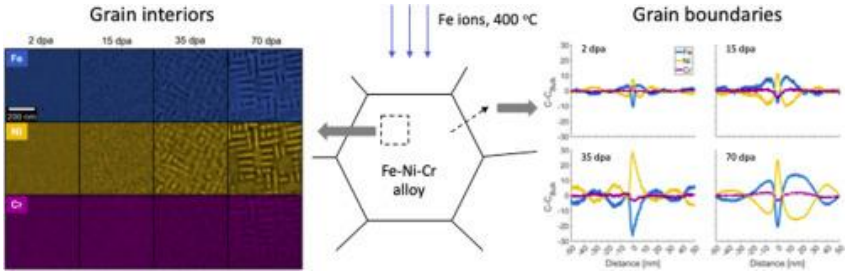

Figure 1: STEM-EDS maps of grain interiors showing the development of spinodal decomposition while RIS evolves concomitantly at grain boundaries. From ref. [8].

interior and grain boundaries during irradiation.

Role of grain size on RIS

One goal of our project was to understand RIS behavior as a function of grain size, or equivalently GB density. Martinez et al. had reported that RIS should decrease with decreasing grain size, but no experimental evidence was available in the relevant grain size range. Using Fe-9Cr and Fe-40Ni-10Cr alloys, we confirmed that the extent of RIS for high angle grain boundaries decreases with decreasing grain sizes over the studied range. No measurable grain growth was noted for the larger grain sizes, while the ultrafine-grains in the samples prepared by high pressure torsion to decrease the starting grain size grew from an average of 110 to 190 nm during ion irradiation. From a mesoscale modeling perspective, phase field simulations (see Figure 2) indicate that RIS exhibits a non-linear dependence on grain size. Under identical irradiation conditions, the magnitude of RIS is predicted to be significantly greater in materials with larger grain sizes than in the fine-grained limit. A combined experimental-computational manuscript on RIS as a function of grain size is currently under review.

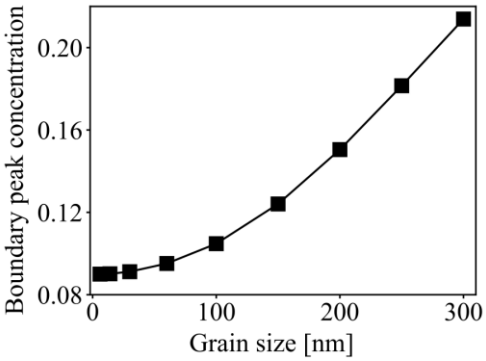

Figure 2: Phase field simulations of the dependence of RIS on grain size.

Irradiation-induced grain boundary migration

Grain boundary migration in irradiated metals and alloys can take place via two distinct phenomena: radiation-induced grain growth and radiation-induced grain boundary migration (RIGM). We focus on RIGM that applies to large grain materials for which grain growth is negligible. RIGM has previously been observed in different metallic systems. However, the mechanisms and dependence on irradiation conditions remained unclear. We found that in a coarse-grain Fe-Ni-Cr-Mn austenitic alloy irradiated with Fe ions at 400 ºC to 15, 35, and 70 dpa, grain boundary migration is only observed in the irradiated regions and exhibits a linear dependence on the locally delivered dose, as estimated from SRIM calculations (Figure 3). Notably, the same linear dependence is noted across the nominal doses. The evidence points to grain boundary migration being mediated by the flux of point defects to grain boundaries and motivates additional systematic studies of RIGM in these systems.

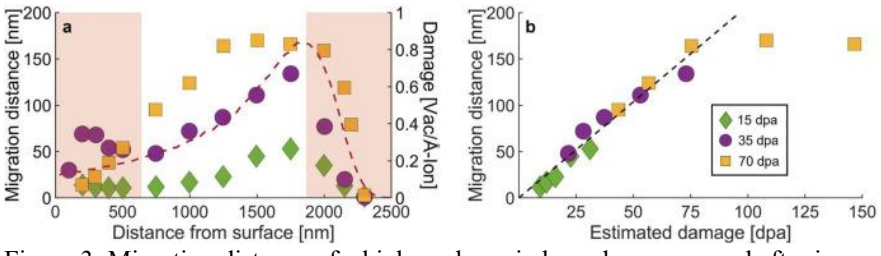

Figure 3: Migration distance of a high angle grain boundary measured after ion irradiation in a Fe-Cr-Ni-Mn alloy. a) as a function of distance to the irradiated surface; b) as a function of damage (estimated from SRIM). From Ref. [7].

Future Plans

Current and future tasks include: 1) quantifying RIGM in model alloys to understand dependence with alloy chemistry and irradiation conditions; 2) revisiting the mechanisms behind W-shaped RIS concentration profiles across grain boundaries; 3) atomistic and theoretical study of bias in defect absorption at grain boundaries; 4) implementation of interstitials in the KMC and calculation of transport coefficients for the alloys of interest; 5) continue the development of a GPU-accelerated mesoscale phase field model of RIS and boundary migration using implicit numerical schemes for the governing equations (intended to become an open-source predictive modeling capability of RIS and microstructure evolution), 6) triple junctions effects on RIS, and 7) extend a recently developed multi-component phase field model to explore multi-element RIS and boundary migration.

Publications

1. D.F. Offidani, E. Martinez, E.A. Marquis, *On the analysis of radiation-induced segregation at ion-irradiated grain boundaries*, Journal of Nuclear Materials **605**, 155533 (2025)

2. MJ Thomas, D Fattó Offidani, M Dhoriya, EA Marquis, E Martinez, SN Mathaudhu, *Decoupling thermal and irradiation effects on grain boundary segregation*, Materialia 102607 (2025).

3. J Jeffries, F Abdeljawad, S Mathaudhu, E Marquis, E Martinez, Prediction of defect properties in concentrated solid solutions using a Langmuir-like model, Physical Review Materials **9** (3), 033803

4. Y Wang, J Jeffries, R Roumina, E Martinez, S Mathaudhu, E Marquis, F Abdeljawad, *Grain boundary segregation and chemical ordering in CoCrFeMnNi multi-principal element alloy*, Journal of Materials Science, **60** 20095–20109 (2025)

5. J Jeffries, B Sun, E Martinez, *A generalized and adaptable tensor-contraction-based cluster expansion formalism for multicomponent solids*, Computational Materials Science **262**, 114338 (2025)

6. 1. D.F. Offidani, E. Martinez, E.A. Marquis, *On the analysis of radiation-induced segregation at ion-irradiated grain boundaries*, Journal of Nuclear Materials **605**, 155533 (2025)

7. D.F. Offidani, E.A. Marquis, *Irradiation-induced grain boundary migration in an ion irradiated Fe-Ni-Cr-Mn alloy*. Scripta Materialia **275**, 117182 (2026)

8. DF Offidani, Y Wang, M Thomas, J Jeffries, S Mathaudhu, F Abdeljawad, E Martinez, EA Marquis, *Evolution of radiation-induced grain boundary segregation in an ion irradiated Fe-Ni-Cr alloy undergoing spinodal decomposition*, Acta Materialia, **317**, 122523 (2026)

9. M Taghizadeh, M Alkayyali, F Abdeljawad, *Grain boundary segregation and solute drag in multicomponent alloys,* Nature Communications, **17**, 4896 (2026)

10. J Jeffries, H Lee, A El-Azab, E Martinez, *General statistical framework for vacancy and self-interstitial properties in concentrated multicomponent solids*, Physical Review Materials **10** (6), 063802 (2026)

Metal-ceramic interfaces at high temperatures

Yuri Mishin, George Mason University, Fairfax, Virginia

Keywords: Interfaces, metals, ceramics, modeling, deformation, dislocations, stacking faults

Research Scope

This program aims to improve the fundamental understanding of metal-ceramic interfaces and develop new methods for computational prediction of their structure, thermodynamics, kinetics, and mechanical responses. One of the key components of the methodology is the development of machine-learning interatomic potentials based on first-principles calculations. Such potentials will enable reliable predictions of energy and atomic forces in mixed-bonding systems. We focus on Al-Si alloys as prototypical composite materials. However, our long-term goal is to expand this program to other classes of metal-matrix composites. The project can significantly advance fundamental understanding of metal-ceramic interfaces and provide a theoretical foundation for designing new composite materials in the future. The current research focuses on the mechanical behavior of the interfaces.

Recent Progress

1. Development of a machine-learning interatomic potential for the Al-Si system

We have generated a reliable machine-learning interatomic potential for the Al-Si system in the moment tensor potential (MTP) format. A large database of energies, atomic forces, and stress tensors has been generated via DFT calculations for elemental Al and Si, as well as Al-Si supercells with varying structures and chemical compositions across the entire concentration range. The training on this database was performed in active learning mode. The root-mean-square error of training is 2 eV/atom relative to the DFT energies and accurately reproduces a large set of properties of Al and Si and Al-Si liquid solutions. Most importantly, the potential reproduces the Al-Si phase diagram with reasonable agreement with experiment (Figure 1). This gives us confidence that our simulations correctly capture the thermodynamics of the Al-Si system. The potential also reproduces the DFT data for point defects in Al and Si, including the energies of

impurity atoms with substitutional and interstitial occupation.

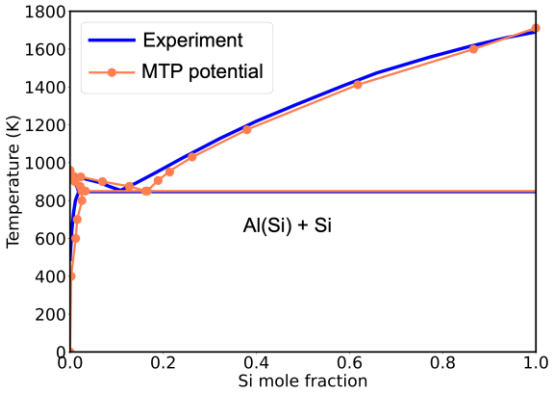

Figure 1: Al-Si phase diagram predicted by the new machine-learning interatomic potential developed in this project. The blue lines represent the experimental phase diagram. The phase diagram calculation required large-scale thermodynamic simulations combining MD and Monte Carlo methods. All previous interatomic potentials for the Al-Si system failed to reproduce the phase diagram quantitatively.

2. Atomistic modeling of Al-Si interfaces at high temperatures.

Considering the relevance to the experiments, we focused on the $\{111\}_{Al} \parallel \{111\}_{Si}$ and $\{110\}_{Al} \parallel \{100\}_{Si}$ boundaries. After the deposition and thermodynamic equilibration, the diffusion coefficients of Al and Si atoms at the boundary were measured by tracking their motion and using the Einstein equation. The diffusivity in Al–Si interfaces is below that of even the slowest-diffusing grain boundaries in Al and Al(Si). The diffusion mechanisms observed so far are dominated by collective atomic rearrangements, with significant dynamic heterogeneity and the formation of mobile clusters exhibiting string-like atomic displacements (Figure 2). Since string formation is one of the mechanisms of interface diffusion, we have studied it in greater detail. It has been found that strings grow by a sequence of dynamically uncorrelated increments. Each increment of growth involves a displacement of a single atom or 2-3 atoms. There are two types of strings: (1) Positive density peaks moving by forward propagation, like an interstitial atom; and (2) Negative density peaks moving by back-propagation, like a vacancy. We call the defects driving string growth positive and negative densitons, which generalize interstitials and vacancies. Densiton dynamics can play a role in interface diffusion and interfacial creep.

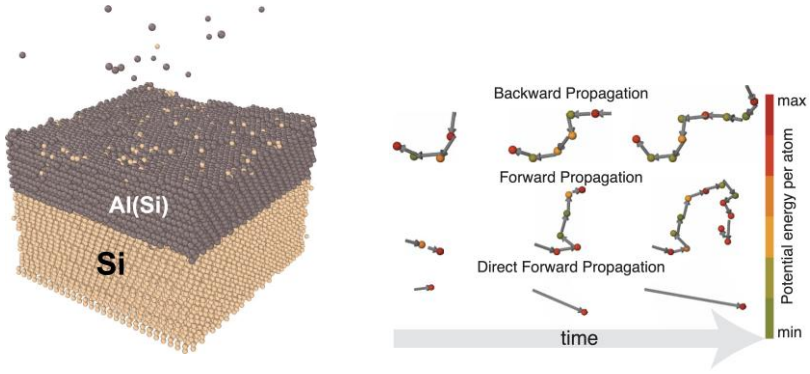

Figure 2: *Left:* Example of simulated deposition on Al(Si) alloys on (111)Si substrate using the new machine-learning interatomic potential developed in this project. *Right:* Back-propagating and forward-propagating strings found in the Al(Si)/Si interface. The strings are signatures of densiton migration responsible for the interface diffusion and interfacial creep.

3. Dislocation nucleation at metal-ceramic interfaces

We have studied the onset of plastic deformation at Al(110)/Si(001) interfaces under tension and compression applied parallel to the interface plane at room temperature (300 K). The key and surprising observation was the pronounced asymmetry in dislocation nucleation at the interface (Figure 3). Under tension, only a Shockley partial dislocation nucleated. The critical stress of nucleation was about 3-5 GPa, depending on the stress orientation within the interface. The trailing partial dislocation did not nucleate on the scale of our MD simulations. In contrast, under compression, the trailing dislocation nucleated almost immediately after the leading one, and the two formed a full dislocation. The latter was only narrowly dissociated into partials and exhibited significant cross-slip into alternative (111) planes. The critical stress of dislocation nucleation was on the order of 20 GPa, much higher than under tension. The tension asymmetry can have significant implications for the mechanical behavior of metal-matrix composites such as Al-Si.

Our hypothesis is that this asymmetry arises from stress-induced changes in the stacking-fault (SF) energy in Al. If tensile stress applied normal to the SF plane reduces the SF energy, then a leading Shockley partial can nucleate more easily and create a large SF area without enforcing the nucleation of the trailing partial. Conversely, if the SF energy increases under compression, the dislocation nucleation barrier will be higher, and both partials will nucleate together, forming a

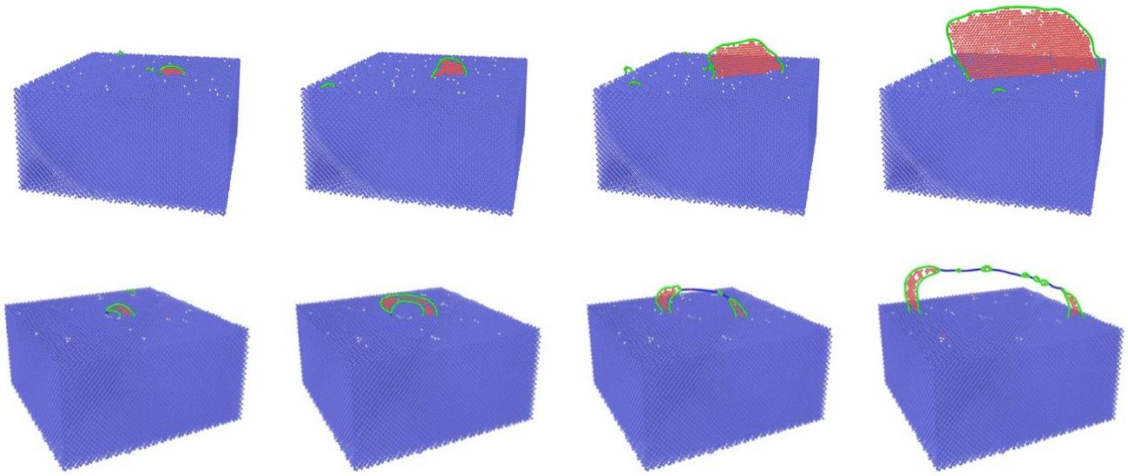

Figure 3: Examples of mechanical testing of Al/Si interfaces by lateral tension/compression. The time increases from left to right. The blue atoms are Si. The FCC Al atoms are invisible for clarity. Color coding: black for a perfect dislocation, green for a Shockley partial dislocation, red for an intrinsic stacking fault. *Upper row:* Tension. The dislocation nucleates as a Shockley partial with a large stacking fault. *Lower row:* Compression. The dislocation nucleates as a full [110] dislocation with a narrow stacking fault. The images demonstrate the strong tension-compression asymmetry of the plastic deformation at these interfaces.

full dislocation with a narrow separation. Furthermore, the narrow separation will favor cross-slip behavior, as observed in the MD simulatio

4. Stress effect on stacking fault energy

To test this hypothesis, we performed DFT calculations to assess the effects of stress on the stable and unstable SF energies in FCC metals, including Al (Figure 4). Note that under a compressive stress of 5-15 GPa, the SF energy increases by about 30-50% relative to the stress-free value. More dramatically, under a tensile stress of the same magnitude, the SF energy decreases to near 10-20% of its stress-free value! Although Al is a high-SF energy metal, it becomes a low-SF energy metal under a tensile stress of 10-15 GPa. Furthermore, a normal stress of 5-15 GPa significantly alters the elastic moduli of Al and other FCC metals. The general trend revealed by DFT calculations is that strong compression makes FCC metals tougher and significantly increases the planar fault energies (both stable and unstable), whereas tension produces the opposite effect.

Stress-induced changes in SF energies can affect many dislocation-controlled processes in FCC metals under high stress, such as cross-slip and dislocation nucleation at interfaces. The tension-induced decrease in the intrinsic SF energy causes wider dissociation of full dislocations into Shockley partials, which affects the dislocation mobility and raises the barrier to cross-slip into other (111) planes. The tension-induced reduction in unstable SF energy lowers the barrier to dislocation nucleation at interfaces. Under high compression, FCC dislocations are predicted to dissociate into partials with much narrower widths, thereby promoting their cross-slip behavior. These trends explain the mechanism behind the observed tension-compression asymmetry in the nucleation of Al dislocations at the Al/Si interface.

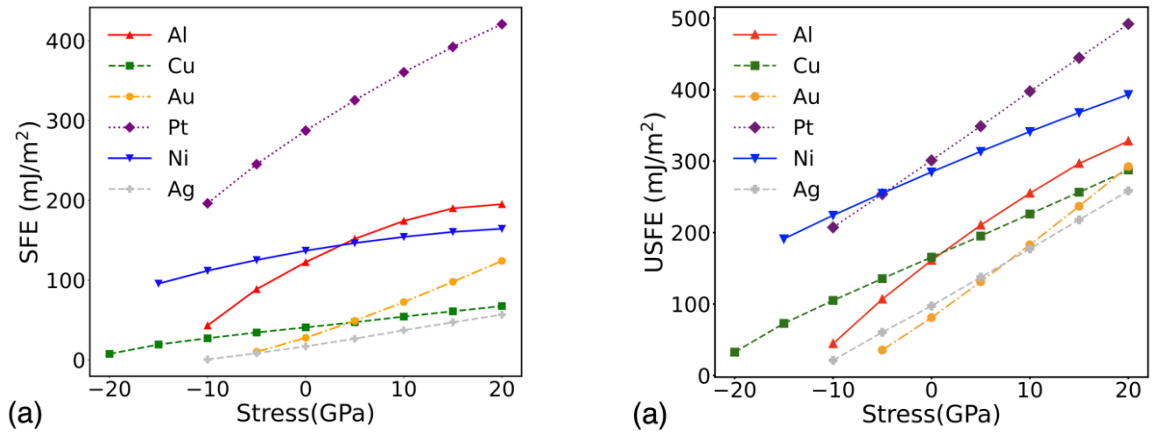

Figure 4: DFT calculations of the stable (left) and unstable (right) stacking fault energy in FCC metals as a function of stress normal to the fault plane. Compressive stress is considered positive and tensile stress negative. For Al, compression significantly increases the stacking fault energy, while tension strongly decreases it.

4. A model of dislocation nucleation at interfaces

We are currently developing a quantitative model to explain the observed asymmetry in dislocation nucleation at interfaces. The model predicts the energy of the leading and trailing half-loops as a function of the loop radius R, the applied stresses, and the SF energy:

$$E_{\text{lead}}(R) = AR\ln\left(\frac{\alpha R}{r_c}\right) + \frac{\pi R^2}{2}\gamma_{\text{SF}} - \frac{\pi R^2}{2}b_p\tau_{\text{lead}}$$

$$E_{\text{trail}}(R;\rho) = AR\ln\left(\frac{\alpha R}{r_c}\right) - \frac{\pi R^2}{2}\left[b_p\tau_{\text{trail}} + \left(1-\frac{1}{\rho}\right)\gamma_{\text{SF}}\right].$$

The model predictions for the critical stresses of nucleation agree well with MD simulations and confirm our hypothesis regarding the origin of the tension-compression asymmetry in dislocation nucleation at interfaces. The model is general and can be applied to other interfaces between dissimilar phases when dislocations nucleate into the softer phase.

Future Plans

- Continue investigating the mechanical responses of Al-Si interfaces, with a focus on dislocation and twin nucleation at high temperatures.
- Extend the investigation of mechanical properties of interfaces to interfacial creep under shear stresses applied parallel to the interface plane. Understand the creep mechanisms.

Publications

1. Y. Li, R. K. Koju and Y. Mishin. Atomistic modeling of diffusion processes at Al/Si(111) interphase boundaries obtained by vapor deposition. *Acta Materialia* 289, 120937 (2025). This research was supported by the U.S. Department of Energy, Office of Basic Energy Sciences, Division of Materials Sciences and Engineering, under Award # DE-SC0023102.
2. Y. Li and Y. Mishin. Atomistic modeling of the structure and diffusion processes at Al(110)/Si(001) interphase boundaries obtained by vapor deposition. *Physical Review Materials* 9, 053401 (2025). This research was supported by the U.S. Department of Energy, Office of Basic Energy Sciences, Division of Materials Sciences and Engineering, under Award # DE-SC0023102.
3. Omar Hussein, Yang Li and Yuri Mishin. The origin of strings and rings in the atomic dynamics of disordered systems. *Acta Materialia* 296, 121212 (2025). This research was supported by the U.S. Department of Energy, Office of Basic Energy Sciences, Division of Materials Sciences and Engineering, under Award # DE-SC0023102.
4. Yang Li and Yuri Mishin. The effect of normal stress on stacking fault energy in face-centered cubic metals. *Acta Materialia* 312, 122243 (2025). This research was supported by the U.S. Department of Energy, Office of Basic Energy Sciences, Division of Materials Sciences and Engineering, under Award # DE-SC0023102.

Plasticity of High-Strength Multiphase Metallic Composites

Amit Misra
University of Michigan, Ann Arbor, MI 48109

Keywords: dislocations, interfaces, nanoscale eutectics, nanomechanics, electron microscopy.

Research Scope

The goal of this research program is to elucidate thermally activated energy barriers for dislocation emission in the hard phase from the interphase boundaries (interfaces) in high-strength, multi-phase microstructures with disparate phases, particularly in terms of the synergy between the interface spacing and atomic structures, confinement-induced internal stresses and alloy chemistry of the hard phase. In single-phase microstructures involving soft phases, plastic deformation can be interpreted in terms of slip transmission across interface barriers [1]. However, in multi-phase microstructures with hard phases with a high activation energy for dislocation glide at low homologous temperatures, slip transmission may not be favored, resulting in cracking of hard phase. Plasticity in such microstructures has been interpreted in terms of conflicting mechanisms: i) micro-cracks in hard phase arrested by softer phase where phase morphology was crucial factor in enhancing ductility [2], and ii) transmission of slip across interfaces, although the atomistic mechanisms were not elucidated [3]. Research in this program has identified slip transmission across interfaces as well as slip reflection from interfaces as active unit mechanisms in different model systems (Al-Al_2Cu and Al-Si, respectively) in fine-scale multi-phase microstructures, and is developing a fundamental understanding of the critical mechanism in terms of the relative energy barriers for slip transmission across and slip reflection from interface.

The key hypothesis is that the dimensional confinement of hard phase in multi-phase microstructure, atomic structure of interphase boundary and local chemical environments in hard phases act synergistically in multi-phase microstructures to lower the thermally activated dislocation glide barrier in the hard phase at low homologous temperatures. An integrated approach is used that involves electron and laser beam melt processing, nanomechanical testing, scanning transmission electron microscopy (STEM) characterization (*in situ*, high-resolution), and dislocation theory and modeling. Model eutectic systems such as Si(Ge)-Al and Cr-Ni, including additional solute elements, are used that involve hard/soft phases with/without, respectively, strong temperature dependence of yield stress at low homologous temperatures. The scientific knowledge from this study will elucidate how the fundamental energy barriers that limit dislocation glide can be modified to enhance plasticity in high-strength, multi-phase microstructures at low homologous temperatures. Atomistic modeling task, supported in the past grant period through a sub-contract to Jian Wang (Nebraska-Lincoln), is currently an unfunded collaboration.

Recent Progress

Model systems of Al-Ge and Al-(Si,Ge) binary eutectics were refined to nanoscale via laser rapid solidification (LRS) to explore mechanisms of glide dislocations in Al interacting with the hard diamond cubic (DC) phase. It is shown that, similar to Al-Si studied earlier, slip reflection dominates in the Al-Ge system that also exhibits novel metastable phases as summarized below. On the other hand, alloyed eutectic, Al-(Si,Ge), exhibited slip activation in the hard phase supporting the hypothesis that the chemical effects synergistic with interface confinement in fine-scale microstructures can change the dominant unit mechanism from reflection to transmission.

i) Discovery of metastable phases and unusual deformation mechanisms in Al-Ge

Al-Ge eutectic, following equilibrium phase diagram, solidifies with lamellar morphology involving FCC Al and DC Ge phases. However, in LRS Al-Ge, the constituent phases were Al- Al_6Ge_5 (β-1, monoclinic <C 2/c>), and Al-AlGe (β-2, monoclinic <P 2_1>), both still exhibiting lamellar morphologies. The Al phase (in both cases) exhibited a distribution of fine Ge-rich solute clusters. The β-2 AlGe intermetallic phase showed a growth-induced nano-twinned structure suggesting this structure may have lower stacking fault energy (SFE) than β-1 Al_6Ge_5 that did not show any faults or twins. The conversion of DC Ge to monoclinic Ge_xAl_y intermetallic phases in the Al-Ge eutectic led to unusual mechanical behavior at room temperatures, Fig.1. Both Al-Al_6Ge_5 and Al-AlGe with eutectic spacings refined to below 100 nm, show high compressive flow strengths >1 GPa with enhanced plasticity, whereas the as-cast Al-Ge has lower strength (≈400 MPa) and lower plastic deformability [4]. The measured flow strengths, e.g., ≈1200 MPa for Al-AlGe (Fig. 1a), may appear very high for Al-based alloy but it should be noted that in Al-Ge LRS systems, the volume fraction of the intermetallic is higher than Al. The deformation mechanisms that enable plasticity at these strength levels are novel. First, in Al, in both cases, a high density of stacking faults was observed post deformation (Fig. 1b) intersecting the metastable Ge-rich solute clusters. DFT calculations (Fig.1c) show that SFE of Al is reduced by Ge addition. Second, the nanotwinned AlGe exhibited

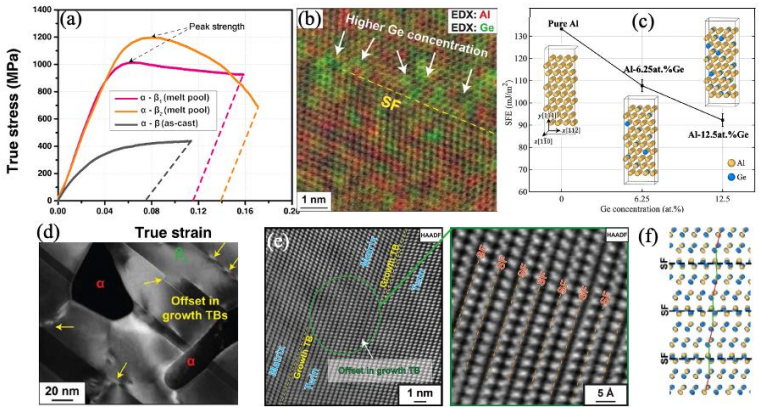

Figure 1(a) Compression stress-strain response of (a-b_1) Al-Al_6Ge_5 and (a-b_2) Al-AlGe LRS eutectics compared to as-cast Al-Ge eutectic. (b) Deformed samples revealed stacking faults in the Al phase intersecting the Ge-rich solute clusters. c) DFT calculations show that Ge lowers the stacking fault energy of Al. (d) Deformed (a-b_2) Al-AlGe eutectic shows fine shear bands in the b_2 phase creating offsets across growth nanotwin boundaries. e) Atomic structure within the shear offset regions revealed a faulted structure with planar fault every 3rd (1 0 -1) plane. f) DFT relaxation indicated that the faulted structure was stable.

fine shear bands that initiated from the Al-AlGe interface and extended in a zig-zag path across the AlGe nanotwins to the next Al-AlGe interface (Fig. 1d), manifested as a gradual strain softening after a peak compressive flow strength of 1200 MPa. The shear offsets created at the twin boundaries revealed a periodic atomic arrangement with planar faults every 3rd atomic layer (Fig.1e). DFT relaxation found the faulted structure to be stable with energy comparable to structure with a single fault or no faults (Fig. 1f). Similar to Al-Si and Al-Si(Sr), the interfaces in Al-Ge_xAl_y, are "slip reflection" dominated where the strain hardening in the Al phase provides the plasticity as dislocations are not directly transmitted into the hard phase. But the nano-twinned structure (seen only in the β-2 AlGe case, not in the β-1Al_6Ge_5) provides an additional strain accommodation mode. These findings are consistent with our observations in Al-Si and Al-Si(Sr) confirming the validity of our hypothesis.

The LRS Al-Si(Ge) eutectic exhibited tensile strength of ~790 MPa and plastic strain to failure of ~15%, higher than binary Al-Si, revealing that Ge alloying has profound effect on deformation behavior. The (Si,Ge) fibers participated locally in strain accommodation through planar-fault-mediated deformation. Unlike the Si fibers in the binary Al–Si reference, that crack due to lack of slip transmission, the Ge-containing fibers remained crack-free after tensile straining and developed deformation-induced stacking faults, twin-boundary offsets, and occasional 9R-like faulted regions. These defects are consistent with localized Shockley partial-dislocation activity at stress concentration sites like faceted interfaces, and twin-boundaries, rather than homogeneous plasticity of the covalent phase. These results highlight that the interface behavior changed from "slip reflection" dominated in Al-Si to "slip transmission" dominated in Al-(Si,Ge). An approach to develop mechanism maps is described next.

ii) Interface Energy Barriers for Slip Transmission and Reflection

For interfaces involving soft metals, the dislocation transmission depends on geometry of incoming and outgoing slip systems, and dislocation core relaxation along interface. However, for metal-hard phase systems, glide dislocation transmission across interface is generally difficult. A computational approach is developed to estimate the energy barriers for slip transmission and reflection in terms of the plastic deformation incompatibility between soft (Al) and hard (Si) phases [5]. Using $(111)_{Al}||(111)_{Si}$ semi-coherent interfaces, the simulation box had the coordinates along x-$[11\bar{2}]$, y-[111] and z-$[1\bar{1}0]$ directions. Dislocations were then introduced by applying the anisotropic Barnett-Lothe solutions. A mixed dislocation $b_{in} = \frac{a_{Al}}{2}[0\overline{11}]$ was introduced in the Al layer that became trapped at the interface. Two mechanisms were considered: (A) slip transmission, where a synchroshear dislocation $b_{out-T} = \frac{a_{Si}}{3}[\overline{112}]$ is emitted into the Si layer, gliding along the $(11\bar{1})_{Si}$ plane and leaving a residual dislocation $b_{res-T} = b_{in} - b_{out-T}$ at the interface; (B) slip reflection, in which a dislocation $b_{out-R} = \frac{a_{Al}}{2}[\overline{110}]$ reflects into the $(001)_{Al}$ plane.

The transmitted/reflected dislocation was introduced at different positions along the glide plane. Molecular statics simulations were used to compute energy variations as a function of distance of the transmitted/reflected dislocation from the interface. Boundary conditions were fixed along x and y, and periodic along z direction. As the applied load is increased, the soft Al undergoes plastic deformation (ε^p_{soft}) while the hard Si phase remains elastically deformed ($\varepsilon^p_{hard} = 0$), a plastic deformation incompatibility, quantified as $\varepsilon^p_{S-H} = \varepsilon^p_{soft}$, develops. Such an incompatibility can be accommodated by GNDs accumulated at the Al/Si interface, that leads to load transfer to the hard phase (Fig. 2a-b). For atomistic simulation, it is reasonable to assume that the hard phase bears the addition load corresponding to the plastic strain ε^p_{S-H}.

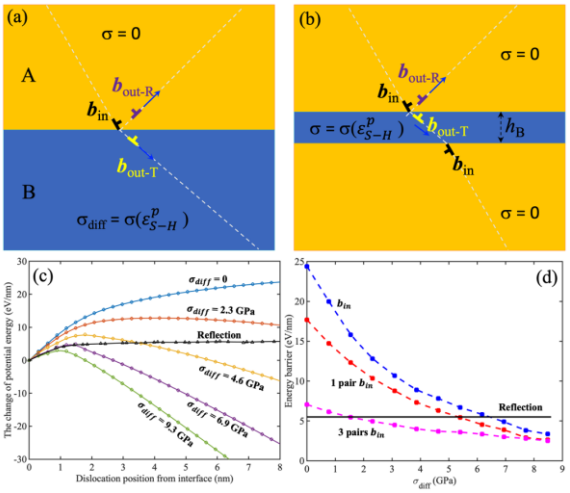

Figure 2. Schematic of dislocation transmission and reflection in (a) a bilayer model and (b) a confined layer model. (c) The energy variation associated with a reflected or transmitted dislocation moving away from the interface at different levels of stress σ_{diff}. (d) Variation of energy barrier for slip transmission with the stress σ_{diff} due to plastic deformation incompatibility.

The additional load is referred to as σ_{diff}, which evolves rapidly with increasing plastic strain in soft phase. The energy change for a transmitted or reflected dislocation moving away from the interface under zero applied load was computed (Fig. 2c), and reflection barrier (5.61 eV/nm) was lower than transmission (23.5 eV/nm), implying that reflection is energetically favored. The initial barrier may evolve with increasing σ_{diff}. Fig. 2c shows the energy variation associated with a dislocation moving away from the interface at different level of stress σ_{diff}. Note that this reflection energy barrier remains constant since the stress in soft phase is assumed to be constant while load transfers to the hard phase. However, with increasing plastic strain incompatibility, the barrier for transmission decreases, and for σ_{diff} > 6.9 GPa, the transmission barrier becomes comparable to reflection. This implies that the specific dislocation unit mechanism assumed in this calculation for transmission, (A) above, could be activated provided a high enough local stress can build without fracture in a confined system. Using the confined layer model, Fig. 2b, the effects of local stress concentration in Si due to accumulation of Al glide dislocations at the interface on the relative transmission vs reflection barriers is computed. The three-layer model calculation was set up with a cube-on-cube orientation relationship between Al and Si, featuring $(111)_{Al}||(111)_{Si}$ semi-coherent interfaces with negligible misfit strain. Fig. 2d shows the variation in the transmission barrier as a function of stress σ_{diff} under different levels of stress concentration. The barrier (black line) for slip reflection under zero stress difference is also shown for comparison. The critical stress difference σ^c_{diff}, is defined as the intersection between the transmission and reflection

energy barrier curves. For the case with three pairs of dislocation dipoles at interfaces, σ_{diff}^{c} is significantly reduced to 1.2 GPa, compared to 6.5 GPa for the single dislocation case. This suggests that σ_{diff}^{c} decreases with increasing local stress concentration. The implication is that the emission of glide dislocation in the hard phase from the interface becomes equally favorable to reflection from the interface with increasing density of soft phase dislocations deposited at the interface and a reduction in thickness of the confined hard phase. The results in Fig. 2 were based on a model with ≈14 nm thick confined Si layer (Fig. 2b). At lower thickness, 2 nm Si, zonal edge partial dislocations were emitted in Si leading to the formation of stacking faults.

Future Plans

The recent results highlight activation of unusual dislocation mechanisms in metal-hard phase nano-eutectics leading to enhanced flow strength, strain hardening and tensile ductility. However, the current work is limited to room temperature behavior. Ongoing work involves investigation of interface-glide dislocation interaction mechanisms as a function of temperature in model systems such as Al-(Si,Ge) and Cr-Ni (where hard phase is a body-centered cubic refractory metal).

References

1. M.D. Sangid, T. Ezaz, H. Sehitoglu, I.M. Robertson, *Energy of slip transmission and nucleation at grain boundaries,* Acta Materialia, **59**, 283 (2011).
2. P. Shi, R. Li, Y. Li, Y. Wen, Y. Zhong, W. Ren, Z. Shen, T. Zheng, J. Peng, X. Liang, P. Hu, N. Min, Y. Zhang, Y. Ren, P. K. Liaw, D. Raabe, Y.-D. Wang, *Hierarchical crack buffering triples ductility in eutectic herringbone high-entropy alloys,* Science, **373**, 912 (2021).
3. D. Röhrens, N. Navaeilavasani, O. Stryzhyboroda, F. Swientek, P. Pavlov, D. Meister, A. Genau and U. Hecht, *Microstructure and Mechanical Properties of BCC-FCC Eutectics in Ternary, Quaternary and Quinary Alloys from the Al-Co-Cr-Fe-Ni System*, Frontiers in Materials, **7**, 567793 (2020).
4. A. Ghosh, W. Wu, J. Wang, A. Misra, *High strength ultrafine eutectic composites with metastable intermetallic phases*, Journal of Materials Science & Technology, **235**, 174 (2025).
5.W. Wu, J. Wang, A. Misra, *Maps for Glide Dislocation Transmission and Reflection from Interphase Boundaries in Heterostructured Materials*, Scripta Materialia, **272,** 117069 (2026).

Publication list from the current grant (2024-2026)

*PhD student supported by this grant. ^postdoc supported by this grant.

1. A Ghosh*, M Tobah, J Zhou, J Wang, A Misra, *Strengthening and interface-mediated plastic co-deformation in an ultrafine Cr-Ni eutectic: A nanomechanical investigation*, **Acta Materialia**, (2026) in review.
2. A Ghosh*, T Ma, A Hunter, J Wang, A Misra, *A method for STEM tomography of nanocomposites with close-atomic number crystalline phases*, **MRS Commun**., **16**, 735-745 (2026).
3. W. Wu*, J. Wang, A. Misra, *Maps for Glide Dislocation Transmission and Reflection from Interphase Boundaries in Heterostructured Materials*, **Scripta Materialia**, **272**, 117069, (2026)
4. M. Tobah, A. Ghosh*, X. Hu^, R. Race, A. Misra, *Printing Cr-Ni Binary Eutectic Microstructures via in situ Alloying in Electron Beam Powder Bed Fusion*, **Journal of Alloys and Compounds**, (2026) in review.
5. A. Ghosh*, W. Wu*, J. Wang, A. Misra, *High strength ultrafine eutectic composites with metastable intermetallic phases*, **Journal of Materials Science & Technology**, **235**, 174 (2025).
6. W. Wu*, B. Wei*, C. Zhou, A. Misra, J. Wang, *The influence of twin boundary on character and motion of dislocations in silicon*, **Acta Materialia**, **284**, 120649 (2025).
7. A. Ghosh*, W. Wu*, T. Ma, J. Wang, A. Misra, *Systematic discovery of new nanoscale metastable*

intermetallic eutectic phases in laser rapid solidified Aluminum-Germanium alloy, **Journal of Alloys & Compounds**, **1011**, 178413 (2025).
8. W. Wu*, S. Yang, J.F. Nie, A. Misra, J. Wang, *Slip transmission across plate-shaped Ω nano-precipitates in Al-Cu-Mg-Ag alloys*, **Scripta Materialia 259**, (2025) 116539.

9. W. Wu*, B. Wei*, A. Misra, J. Wang, *Atomistic Simulations of Dislocation Activity in Si Nanofibers in Al-Si Eutectics*, **Acta Materialia**, **264** (2024), 119569.
10. B. Wie*, W. Wu*, A. Ghosh*, M. Kayitmazbatir*, A. Misra, J. Wang, *In situ SEM characterization of tensile behavior of nano-fibrous Al-Si and Al-Si-Sr eutectics*, **Journal of Materials Science**, **59** (2024) 5233-46.
11. E. Song^, A.-A. Bogno, J. Valloton, H. Henein, J. Wang, A. Misra, *Nanomechanical Behavior of Impulse Atomized Al-Ce Eutectic Particles*, **Materials Science & Engineering A**, **915** (2024) 147296.
12. B.P. Sahu^, M.T. Andani, A. Ghosh*, J. Wang, A. Misra, *Crystallography and Interface Structures in As-Arc Melted and Laser Surface-Remelted Aluminum–Silicon Alloys with and without Strontium Addition*, **Crystals**, **14**, 283 (2024).

Mechanistic, Quantitative Understanding of the Dynamics of Many, Interacting Defect Clusters for Tailoring Irradiation Responses

Dane Morgan and Paul M. Voyles, University of Wisconsin-Madison; Kevin G. Field, University of Michigan-Ann Arbor

Keywords: irradiation damage; defect-cluster mobility; in situ electron microscopy; machine learning; atomistic simulation

Program Scope

Defect clusters move, interact, and change as an irradiated material evolves, but limited data prevent us from understanding and predicting these dynamics. Conventional microscopy and manual analysis capture only a few defects at widely spaced time points, missing rapid motion, intermittent pinning, rare interactions, and population-level correlations. Our long-term goal is to overcome this limitation for cavities/bubbles and dislocation loops and to determine how their motion and evolution depend on key variables such as size, temperature, composition, irradiation, helium, strain, grain boundaries, free surfaces, and nearby defects. Our present focus is on model nickel-chromium (Ni-Cr) alloys.

We are addressing this challenge by combining high-speed transmission electron microscopy (TEM), rapid three-dimensional imaging, artificial-intelligence-assisted defect detection and tracking, and atomic simulations guided by machine-learning potentials. Fast imaging (>1,000 frames per second [fps]) captures motion and pinning that conventional measurements (e.g., <100 fps) miss, while automated analysis tracks thousands of defects over time and across viewing angles. These data can reveal fundamental distributions in size, shape, depth, and motion, including potentially rare or correlated events such as trapping, release, interaction, and merging. These data are at spatiotemporal scales approaching state-of-the-art molecular simulation, creating new opportunities to merge simulations with experiments to identify the underlying atomic mechanisms controlling these processes.

Recent Progress

Loop Dynamics from Atom-by-Atom Simulation and High-Speed Electron Microscopy

We have combined atomistic simulations with high-speed TEM to resolve the structure and intrinsic migration physics of self-interstitial clusters in face-centered-cubic nickel [1].

We have identified three recurring configurations (Fig. 1): disordered dumbbell clusters, sessile faulted Frank loops, and mobile perfect loops. Perfect loops reorganize into compact, aligned dumbbell arrays that are lower in energy

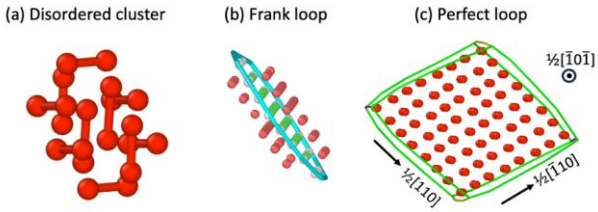

Figure 1. Simulation-predicted self-interstitial cluster structures in face-centered-cubic nickel: (a) a disordered dumbbell cluster, (b) a sessile faulted Frank loop, and (c) a mobile ordered perfect loop. From Ref. 1.

and more mobile. Above 14 interstitials, the perfect-loop branch is lower in energy, but reorganization barriers can keep Frank loops metastable. This agrees with irradiation experiments showing temperature-dependent unfaulting without a universal critical size, while contrasting with first-principles calculations that favored Frank loops in nickel up to about 20 interstitials. Together, these comparisons show that the energetics depend on model and geometry and that kinetic trapping can allow both loop types to persist.

For compact perfect loops containing 16–400 interstitials, we have found Arrhenius diffusion and a migration barrier near 0.02 electron volts that is nearly independent of size. A significant size dependence of diffusivity does occur and arises almost entirely from the prefactor, $\underline{D}_0$. Our trajectory analysis has shown that loops do not translate as rigid objects: rows of dumbbells advance through relay events, and the average participating segment grows approximately as $N^{0.82}$, where N is the number of interstitials in the loop. Based on mass arguments, this suggests $D_0 \propto N^{-0.41}$. Thus, the growth of the participating segment with loop size can account for most of the observed $D_0 \propto N^{-0.56}$ dependence. The remaining size dependence may reflect deviations from the harmonic approximation, as well as correlation effects not captured by a simple mass-scaling picture, including forward-backward correlations between successive relay events. The nearly size-independent 0.02 electron-volt barrier and $D_0 \propto N^{-0.56}$ scaling agree with earlier crowdion-cluster results in iron and copper (0.02–0.03 electron volts and $N^{-0.6}$) [2]. We have now identified a quantitative relay mechanism that relates this known scaling to the number of atoms moving in each event.

Using high-speed in situ TEM at 500 °C and 1,100 frames per second, we have observed one-dimensional motion of nanoscale black-dot defect clusters, with 33–104 millisecond pinning intervals between segments moving at about 270–410 nanometers per second (Fig. 2). To our knowledge, this experimental measurement has the highest time resolution reported for loop migration in a nickel alloy. Examining motion between pinning events and fluctuations within pinned regions, we estimate effective diffusivities to be 10^{-18}–10^{-14} m^2/s, five to nine orders of magnitude below the intrinsic perfect interstitial loop simulation result of 10^{-9} m^2/s. The one-dimensional motion agrees with earlier in situ observations [3], and the repeated trapping and release resemble results in copper [4]. Unresolved sub-frame pinning and solute-atmosphere drag are plausible explanations for the gap and will be studied further.

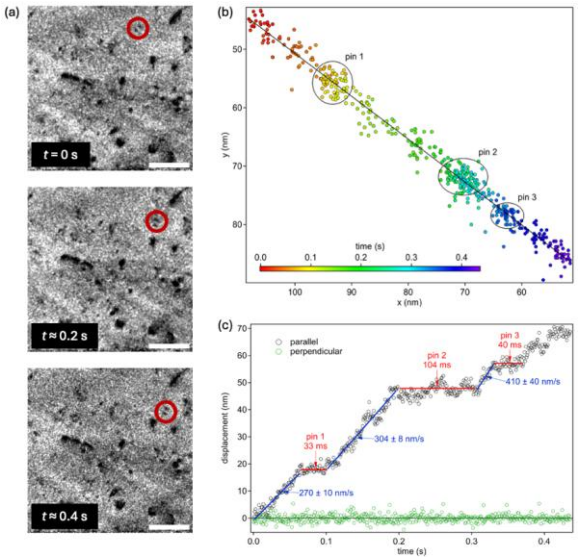

Figure 2. Intermittent one-dimensional loop motion at 500 °C, with three pinning intervals separating mobile segments. From Ref. 2.

Taken together, we have found that microstructural trapping and drag, rather than the small intrinsic migration barrier, control loop motion in experiments. Our STAR and loop-mobility studies are key steps toward a mechanistic understanding of defect-cluster motion in heterogeneous energy landscapes.

Small-Tilt Automated Reconstruction (STAR)

The number of defects we could track in the above work was greatly limited by the significant human analysis required. To overcome the experimental bottleneck of obtaining time-resolved three-dimensional information from dense defect populations, we have developed the small-tilt automated reconstruction (STAR) technique [5]. STAR combines pairs of electron microscopy images taken from slightly different viewing angles with deep-learning vision tools that enhance the image sequence, locate defects, and automatically match the same defect across views. We then use the matched observations to reconstruct each defect's depth, position, size, and orientation and place the results in a common sample-based coordinate system. Full technical details are provided in Ref. 5. The use of deep learning enables reconstructions with combined acquisition and analysis times of 2 s or less, enabling future deployments for high temporal resolution 3D reconstructions of evolving microstructures.

We have tested the geometric reconstruction accuracy against controlled synthetic data. We recovered loop centers with a pairwise root-mean-square error of about 0.51% of the image width, latex-sphere positions with an average error of about 0.73% of the image width, and assigned 97% of synthetic loops to the correct habit-plane family. These benchmarks show that the geometric reconstruction is accurate when correct cross-view matches are supplied. Depth remains the most sensitive coordinate because the small viewing-angle difference amplifies small in-plane errors.

Figure 3 shows the population of defects in irradiated nickel identified and classified with STAR. We tested pure nickel irradiated in situ with krypton ions under conditions dominated by cavities (510 °C, 5.93 displacements per atom) or loops (500 °C, 0.39 displacements per atom). We

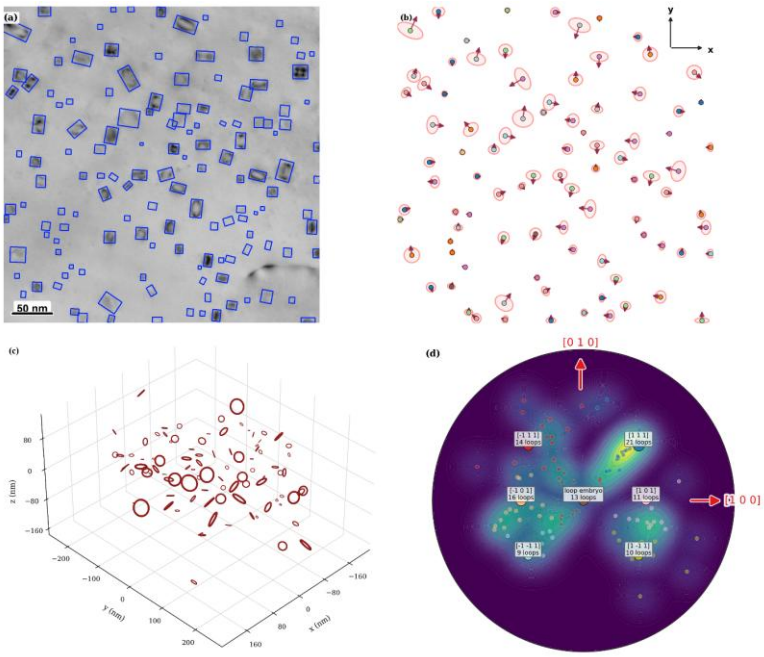

Figure 3. STAR reconstruction of irradiated-nickel loops: (a) detections, (b) projected loop geometries and plane normals, (c) the three-dimensional population, and (d) the aligned pole-density map. From Ref. 5.

identified nearly 1,000 defects in this dataset, including 787 cavities and 178 loops. Of 94 reconstructed loops, 54 were automatically assigned to the {111} family, 27 to {110}, and 13 to a small-loop or black-dot category. We have also begun applying STAR to three-dimensional snapshots of pure nickel and alloys containing 2.5 or 15 weight percent chromium irradiated at 500 °C. Although the two available dose points do not yet establish a dose trend, we have observed a composition-dependent loop-family balance: the alloy with 15 weight percent chromium has a larger fraction of {110} perfect-type loops, whereas the alloy with 2.5 weight percent chromium remains more strongly {111} Frank-type dominated. These initial results directly connect to our goal of determining how alloy composition affects defect evolution. Representative pure-nickel loop results are shown in Fig. 3.

We have found that matching the same defect across views, rather than the subsequent three-dimensional calculation, is now the main limitation. Deep-learning frame interpolation increased cavity matching from 46.9% to 71.2%, but loop matching improved only from 50.0% to 52.8%, as loop appearance varies with imaging conditions. These results have given us concrete targets for improved image acquisition and tracking. We have also upgraded the workflow from box-based detection to contour-based segmentation so that it can preserve the shapes of the larger, anisotropic loops in the nickel-chromium experiments.

Future Plans

During the next project year, we will refine our three-dimensional microscopy to measure defect populations more reliably across viewing angles and alloy compositions. We will extend the reconstruction to multiple views, automate classification of vacancy- and interstitial-type loops, and use automated tracking to identify common and rare defect events under irradiation in pure nickel and nickel-chromium alloys. We have recently found that agentic artificial intelligence tools can substantially accelerate the development of these analysis workflows, and we are pursuing this approach. These measurements will test how chromium changes loop size, character, mobility, pinning, and interactions while clarifying when imaging contrast or cross-view matching limits the physical interpretation.

We will also deepen the comparison between intrinsic and microstructure-limited loop motion. Atomistic simulations will examine how chromium changes loop structure and migration, while high-speed microscopy will provide pinning-time and velocity distributions, beginning with low-defect-density pure nickel and extending to nickel-chromium once the workflow is robust. Comparing these results will help us distinguish intrinsic migration from trapping and solute drag and identify the mechanisms that produce the large gap between simulated and observed mobility.

References

1. Ajay Annamareddy, Ibrahim Momohjimoh, Hangyu Li, Kevin G. Field, Paul M. Voyles, and Dane Morgan, *Morphology and Dynamics of Self-interstitial Clusters in Irradiated Nickel*, submitted (2026).

2. Y. N. Osetsky, D. J. Bacon, A. Serra, B. N. Singh, and S. I. Golubov, *One-dimensional Atomic Transport by Clusters of Self-interstitial Atoms in Iron and Copper*, Philosophical Magazine **83** (2003) 61–91, doi:10.1080/0141861021000016793.

3. K. Arakawa, K. Ono, M. Isshiki, K. Mimura, M. Uchikoshi, and H. Mori, *Observation of the One-dimensional Diffusion of Nanometer-sized Dislocation Loops*, Science **318** (2007) 956–959, doi:10.1126/science.1145386.

4. K. Ono, M. Miyamoto, and K. Yamahaku, *In-situ Observation of the Dynamic Behavior of Cascade Defect Clusters Formed by Irradiation with High-energy Self-ions at 50 K in Cu*, Journal of Nuclear Materials **511** (2018) 122–127, doi:10.1016/j.jnucmat.2018.09.001.

5. Hangyu Li, Benjamin P. Eftink, Kai Sun, Ethan M. Polselli, and Kevin G. Field, *Small-Tilt Automated Reconstruction (STAR): A Machine-Learning-Based Stereo Method for Realization of Real-Time 3D Microscopy Characterization*, submitted (2026).

Publications

No peer-reviewed BES-supported publications for the previous two years; Ref. 1 and 5 are submitted.

Modeling the Molecular Mechanisms of Interfacial Welding in Self-Healing Polymers

Thomas C. O'Connor, Materials Science & Engineering, Carnegie Mellon University

Keywords: Polymers, Self-Assembly, Self-healing, Thermoplastic Elastomers, Mechanical Welding

Research Scope

The objective of this research project is to combine molecular dynamics simulations and self-tack adhesion experiments to identify the molecular mechanisms that mediate bulk failure and interfacial healing in self-assembling thermoplastic elastomers. The hypotheses driving our recent work focus on how the incorporation of associative chemical bonds into block-copolymers alter the molecular mechanisms mediating their yield, cavitation, failure, and interfacial adhesion. To test this, we have been applying molecular dynamics simulations to resolve the molecular-scale dynamics of associative polymers and TPEs undergoing nonlinear uniaxial and triaxial deformatio. Our simulations have been carried out conjunction with collaborative mechanical experiments. Our work is organized into three thrusts studying: (1) bulk mechanical properties, (2) mechanical recovery during welding, and (3) nanostructure reorganization at interfaces in nanostructured self-healing polymers. We've focused on expanding our modeling tools to encompass a much wider range of self-assembling polymer materials and stakeholders, validating that our models can reproduce experiments and relate mechanical data to molecular mechanisms in polyelectrolyte coacervates, block copolymers, and associative polymer networks.

Recent Progress

Model Development: Data-Driven Particle Dynamics for Thermally Accurate Coarse-Grained Molecular Models

We have engaged in collaborative research with fellow DOE ECRP recipient and applied mathematician, Prof. Nathaniel Trask (UPenn) to apply Scientific Machine Learning to create thermodynamically self-consistent coarse-grained models. These methods have enabled us to use molecular dynamics simulation data to train coarse-grained models that accurately capture the structure and dissipative dynamics of complex polymeric systems at mesoscopic scales, enabling us to accurately model their dissipative mechanics. This has culminated in a timely manuscript that has just been accepted for publication in the *Proceedings of the National Academy of Sciences.*

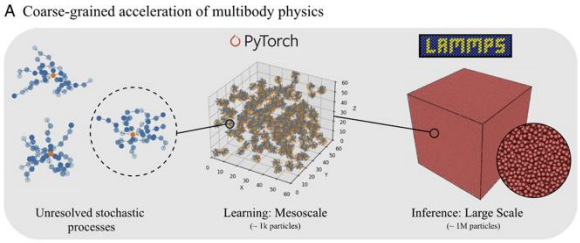

Figure 1 – Schematic illustrating our DDPD modeling approach which successfully coarse grained multi-arm star polymers with N=50 atoms into single point-particles, while accurately preserving their many-body free energy and dissipative forces.

Bulk Mechanics: Anomalously Low Extensional Stresses in Silk-Inspired Associative Polymers

Natural silks – made by spiders and silkworms – have long been a focus of research due to their exceptional toughness, high crystallinity, and high extensibility. These materials are made of polymer chains that self-assemble into a network via associative bonds. A major open question has been how is it possible for worms to manipulate and form these viscoelastic materials at room temperature with the power output of their bodies. We addressed this question in a recent simulation study that is now published as an ***Editors Selection*** in ***Physical Review Letters***. Our study revealed that the viscoelastic behavior of associative polymer networks is governed by fundamentally distinct molecular relaxation processes than those of traditional synthetic polymers. Specifically, while synthetic polymer chains respond to extensile strains by stretching uniformly, associative polymer chains display a much more stochastic response dominated by broad fluctuations in local chain tension. This dramatically decreases the dissipative stresses within the material, enabling them to creep at much lower stress levels – like those produced by worms. This work has established our ability to reproduce experiments and settle foundational mechanistic questions in self-assembling materials undergoing highly nonlinear deformations.

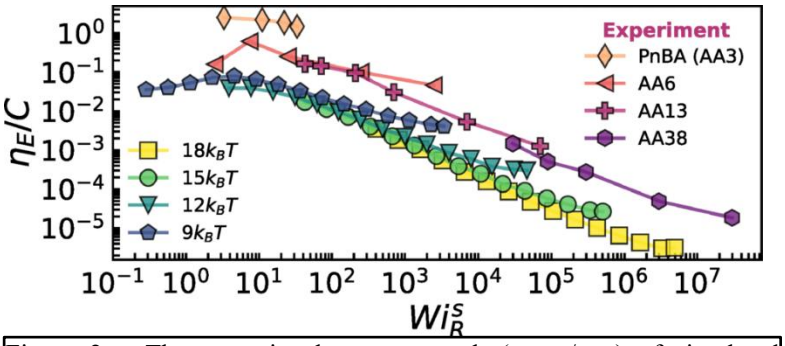

Figure 2 – The extensional stress growth (stress/rate) of simulated (green/yellow) and experimental (pink/purple) associative polymer networks.

Bulk Mechanics: Molecular Modeling of Saloplasticity in Polyelectrolyte Complex Coacervates

Polyelectrolyte complex coacervates (PECCs) are concentrated polymer materials consisting of oppositely charged polycations and polyanions. These concenrtrated gels of oppositely charged polymers form highly charge correlated soft materials. PECCs have become a major focus of research due to their excellent performance as *underwater adhesives*. Recent work by our collaborator Prof. Sarah Perry has shown that PECCs composed of very short polyelectrolyte chains can display substantial strain hardening behavior, enabling the formation of adhesive bonds that are much tougher than expected for their short molecular weights. PECC viscoelasticity is also highly sensitive to the to the presence of

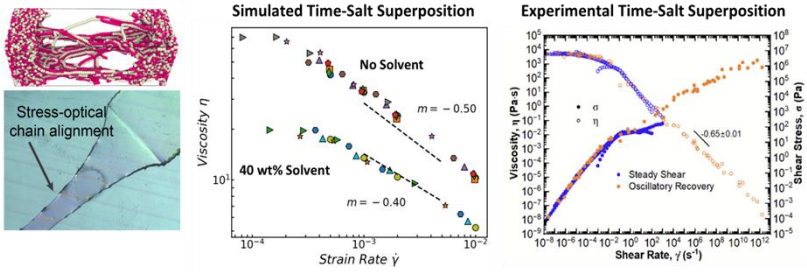

Figure 3 – Preliminary experimental and simulation results for the mechanics of PECC films (left). Both simulations (middle) and experiments (right) demonstrate analogous time-salt-superposition master curves for the non-linear shear deformation of PECs. Both methods predict power-law decreases viscoelastic stresses with increasing strain rate, and exponential decreases with increasing counterion concentration, consistent with our hypothesis that salt is disrupting supramolecular charge complexes.

mobile salt counterions, such that increasing salt concentration can dramatically accelerate viscoelastic relaxation times. This *saloplasticity* is well established, but the mechanisms by which it occurs remain debated, with multiple models able to fit experimental data over the range that can be measured. Distinguishing these requires molecular scale information.

To investigate this physics, we have been performing joint experiments and simulations of the rate-dependent shear deformation of PECC materials as we systematically vary the ionic strength of the material by addition of monovalent salts. Our simulations have shown that the monovalent salts bind to polyelectrolyte backbones and disrupt the formation of supramolecular complexes, leading to an exponential reduction in stresses and a distinctive rate-dependent power-law in viscous stresses. These trends are consistent with experimental data collected by Prof. Simon Roger's at UIUC for Perry's films (**Figure 3**). These results have resulted in a manuscript that will soon be published.

Bulk Mechanics: Mechanisms of Strain Hardening In Tetrablock Copolymer Membranes

Through an invited talk at the M-WET EFRC we've begun collaborating with Prof. Gabriel Sanoja to establish the molecular mechanisms governing the toughness of thermoplastic elastomer filtration membranes. These functional assemblies are used to for ion and foulant filtration, but they are prone to brittleness. Sanoja has been systematically varying the molecular architecture of these assemblies to create composite-like nanostructures containing soft rubbery and hard glassy domains in highly ordered arrangements. We have applied our modeling methods to test the <u>*working hypothesis:*</u> that the self-assembled rubbery domains act like traditional rubber toughening additives and uniformly nucleate microcracks across the material, leading to enhanced fracture toughness. Our preliminary results (**Figure 4**) are consistent with this hypothesis. We are currently preparing a collaborative manuscript for publication.

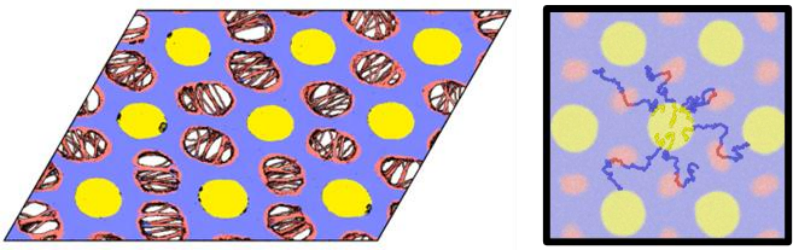

Figure 4 - Simulation snapshots of tetrablock copolymer membranes. The incorporation of a rubbery midblock (red) leads to the formation of rubbery domains at interstitial sites in the 2D HEX lattice. Simulations reveal that these rubbery domains uniformly cavitate during tensile deformation, distributing damage uniformly across membranes and enhancing membrane toughness

Interfacial Mechanics: Interfacial Welding of Precisely Sequenced Copolymers

Our most recent studies of interfacial mechanics are motivated by experimental results by *(Kim et al.*[1] which showed that associative block copolymers display simultaneously enhanced bulk toughness and interfacial welding during additive manufacturing. To understand how these hierarchically self-assembling systems break this tradeoff, we prototyped new models for these

materials and have verified that our models accurately capture the scattering structure and mechanical trends produced by these hierarchical assembly of associative TPEs and have progressed to establishing the molecular mechanisms mediating the simultaneously enhanced toughness and welding in these systems.

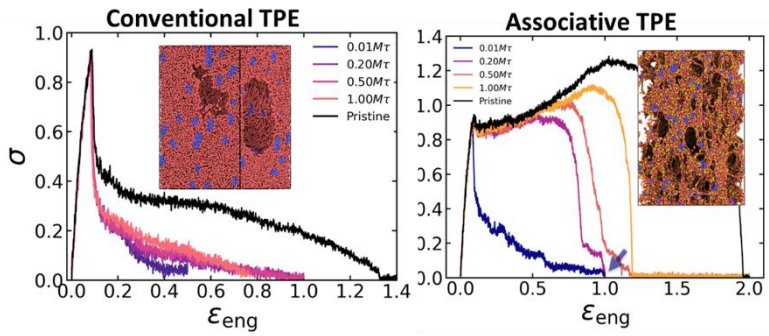

Figure 5 – Self-tack tests (triaxial tension tests) during the interfacial healing of conventional TPEs (left) and associative TPEs(right) at ambient temperature. Simulated stresses are reported in reduced Lennard-Jones units. The conventional TPE cannot reform its physical network across the interface and shows almost no recovery of its pristine toughness. The associative TPE also cannot reform its physical network across the interface, but it almost immediately reforms its associative network, which strengthens to interface sufficiently to suppress failure.

Our preliminary work has revealed that incorporating associative bonds into a traditional TPE materials creates two interdigitating networks: the conventional *physical network* linking chains together through microphase separated glassy domains, and a new *associative network* that links chains together through a network of intermolecular associative bonds. In conventional TPEs, only the physical network is present, and this network cannot heal at interfaces unless the material is heated above the T_G of the glassy domains that form the physical crosslinks. In the associative TPE, while the physical network is similarly immobilized, the network of associative bonds is not and can rapidly reform across the interface. This leads to a rapid recovery of interfacial strength that is sufficient to suppress interfacial failure (**Figure 5**).

Future Plans

Our aim for the coming year is to publish our now complete studies of polyelectrolyte coacervate saloplasticity, tetrablock polymer fracture, and associative copolymer welding. These collaborative studies are all complete and collaborative publications are being drafted, with several soon to be submitted. These will demonstrate the broad applicability of our modeling methods across the spectrum of self-assembling polymer chemistries. In tandem, we are developing fundamental simulation and experimental studies of the associative copolymers and aim to systematically investigate how the placement of associative bonds within the existing microphases of a block polymers can be used to manipulate the mechanisms governing mechanical yield, cavitation, fracture, and interfacial healing. Last, we aim to continue refining our MD simulation workflows to more accurately and efficiently replicate experimental structures and predict their mechanical response. This will include exploring emergent opportunities to apply generative ML techniques to more efficiently and accurate generate polymer models and polymer molecular structures from continuum field theories and/or experimental structural data.

References

1. M. Kim, S. Nian, B. Huang, J. Zhu, G. Freychet, M. Zhernenkov, L.-H. Cai, *3D Printable Elastomers from Physically Cross-linked Homogeneous Associative Polymers*, ACS Polymers Au **4**, 98-108 (2024).

Publications

1. S. Liu and T.C. O'Connor, *Modeling the Flow-Driven Disassembly and Extensional Rheology of End-Linking Telechelic Polymers*, J. Chem. Phys. **164** (2026)
2. Q. Hernández, M. Win, T.C. O'Connor, P.E. Arratia, N. Trask, *Data-driven particle dynamics: Structure-preserving coarse-graining for emergent behavior in non-equilibrium systems*, Proc. Nat. Acad, Sci., **123**, (2026)
3. B. Mei, G.S. Grest, T.C. O'Connor, K.S. Schweizer, *Intermediate time sub-diffusion and stress relaxation in ring polymer melts*, J. Chem. Phys., **164**, (2026)
4. S. Liu, T.C. O'Connor, *Flow-Driven Stretch Fluctuations Govern the Nonlinear Viscoelasticity of Elongating Associative Polymer Networks*, Phys. Rev. Lett. **135**, 098101 (2025)
5. N. Chongvimansin and T.C. O'Connor, *The Work of Mechanical Degradation in Elongating Polymer Melts*, Macromolecules, **58**, 1787-1794 (2025)

Understanding Irradiation-Assisted Plasticity in Complex Concentrated Alloys: Aging-Enhanced Ductility in Ti-Zr-Nb-O

Hyunseok Oh, University of Wisconsin-Madison

Keywords: complex concentrated alloys; irradiation-assisted plasticity; ordered oxygen complexes; strain localization; dislocation channeling

Research Scope

This project aims to address the strength-toughness trade-off in structural metals under irradiation at intermediate temperatures (<0.4 melting point). Under these conditions, irradiation and mechanical stress result can lead to hardening and embrittlement through significant strain localization within dislocation channels [1]. Leveraging recent advancements in complex-concentrated alloys (CCAs), this project investigates the effects of multi-scale structures on irradiation-assisted plasticity in CCAs and identifies scientific principles for enhanced resistance to irradiation embrittlement while maintaining hardening. Our focus is on reducing strain localization by tailoring the unique deformation mechanisms of CCAs, a process referred to in this project as planar defect-mediated delocalized plasticity (PMDP).

PDMP has been shown to strongly influence mechanical behavior in unirradiated CCAs. The mechanisms typically initiate from planar slip, which facilitates strain localization through the glide-plane softening effect. However, in some CCAs, synergetic interactions between planar defects and other features, such as dislocation cross-slip tendencies from different stacking fault energies (SFEs) or non-shearable precipitates, can lead to unprecedented strain delocalization and work hardening effects [2,3].

The present work establishes the unirradiated mechanistic baseline for the body-centered-cubic (BCC) branch of the project using oxygen-containing Ti-Zr-Nb CCAs. Ordered oxygen complexes (OOCs) are attractive nanoscale obstacles because their interaction with screw dislocations can promote double cross-slip, Frank-Read source, and dislocation multiplication [2], providing a potential PDMP mechanism. Their benefit effects, however, are thermally fragile. In Ti-Zr-Nb-O alloys, intermediate-temperature exposure can transform oxygen-associated environments into ω or HCP-related precipitates, or promote oxygen segregation at grain boundaries, causing aging embrittlement. To activate the PMDP mechanism, the BCC matrix must be sufficiently stable for irradiation at intermediate temperatures, while retaining local OOCs.

In this work, we designed Zr/Nb-rich Ti44Zr30Nb–2X–2O alloys (at.%; X = Al or Mo; Ti = balance) and selected a 300 °C aging window to tune oxygen-associated order without detectable ω/HCP precipitation. The alloys not only retained ductility after aging but also exhibit increased ductility and work hardenability. A series of characterization studies was conducted to identify the mechanistic origin of this improvement. The working hypothesis emerging from these results is that edge-rich planar bands form the initial deformation skeleton, while a smaller population of mobile screw-dislocations interact with OOCs to populate the inter-band regions and activate

additional slip. Ion irradiation will determine whether this coupled planar-wavy slip mechanism persist in the presence of irradiation defects and mitigate channel-dominated localization.

Recent Progress

Two non-equiatomic alloys, Ti44Zr30Nb–2Mo–2O (R-Mo) and Ti44Zr30Nb–2Al–2O (R-Al), were vacuum arc-melted, cold-rolled by ~90%, recrystallized at 950 °C for 30 min, water-quenched, and aged at 300 °C for 48 h. Electron backscatter diffraction and synchrotron high-energy X-ray diffraction (Fig. 1, left) show equiaxed BCC microstructures with no detectable secondary phase after water quenching, furnace cooling, or aging for 12–48 h. Interestingly, aging improves rather than degrades ductility. R-Mo changes from a yield strength of 1271 ± 13 MPa and an elongation to fracture of 19 ± 2% in the recrystallized state to 1257 ± 7 MPa and 24 ± 0.5% after aging (Fig. 1, right). R-Al changes from 1186 ± 4 MPa and 26 ± 2% to 1162 ± 2 MPa and 32 ± 0.95%, respectively. Thus, aging increases elongation, and the Al-containing alloy provides the strongest ductility benefit.

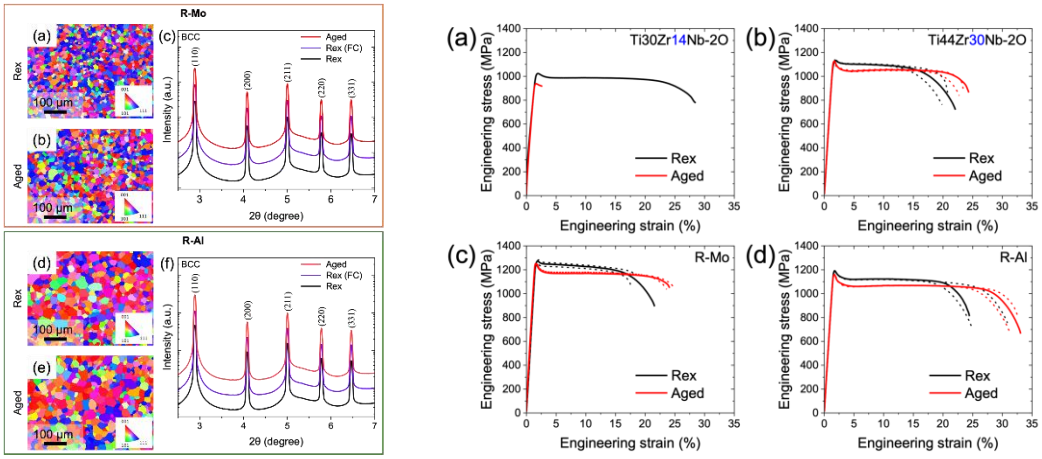

Figure 1. Phase and mechanical stability of Ti44Zr30Nb–2X–2O (X = Mo, Al; Nb = balance). Left: EBSD maps and synchrotron diffraction patterns in the recrystallized and aged states. Right: engineering stress-strain curves showing aging-enhanced elongation without a major loss of yield strength.

A suite of characterization methods, including surface slip-trace analysis, electron channeling contrast imaging (ECCI), synchrotron peak-broadening analysis, atom-probe tomograph (APT), and stress relaxation tests, was used to investigate the origin of the aging-enhanced ductility.

1. Surface slip traces were statistically classified in ~200 grains spanning different orientations for each condition after 15% deformation (Fig. 2, left). Aging increases the fraction of grains exhibiting wavy slip and multiple-slip intersections containing wavy slip. The spatial extent of multiple slip activity increases in the order of R-Mo-Rex < R-Mo-Aged < R-Al-Rex < R-Al-Aged.

2. ECCI of 40–45 grains per condition reveals the dislocation structures connecting the planar bands (Fig. 2, right). These structures include branched second-generation slip bands, mixed straight-wavy bands, multiple-slip intersections, and heterogeneously distributed but well-aligned

coplanar short dislocation segments in the inter-band regions. The inter-band segments are most prevalent in R-Al, particularly after aging.

3. To clarify the microscopic deformation behavior, the dominant straight traces were analyzed. In oxygen-free Ti44Zr30Nb, the trace plane generally follows the maximum shear stress plane, consistent with frequent nanoscale cross-slip that appears macroscopically straight in TiZrNbTaHf CCAs [3]. In the oxygen-containing alloys, by contrast, the dominant straight traces deviate from the maximum shear stress plane and exhibit substantially greater scatter. These traces are therefore interpreted as genuinely planar bands formed through obstacle depinning and glide-plane softening rather than as the macroscopic average of frequent cross-slip.

4. Synchrotron peak-broadening data analyzed using the modified Williamson–Hall method indicate that the stored dislocation population is edge-dominated under every condition. This result is consistent with edge dislocations accumulating within planar bands because they cannot cross-slip, while a smaller mobile screw-dislocation population mediates obstacle-triggered cross-slip and three-dimensional propagation.

5. APT results were interpreted because oxygen field evaporation produces both atomic O and molecular ZrO ions. In the recrystallized states, the cluster-count and cluster-size distributions obtained from both channels are statistically consistent with randomized datasets. After aging, the atomic-O channel develops nonrandom spatial correlations in both alloys, whereas the ZrO channel remains random. This divergence does not establish the presence of discrete ZrO clusters; instead, it indicates that aging modifies the local oxygen coordination or field-evaporation environment.

6. Stress-relaxation measurements provide a complementary deformation-sensitive length scale. The apparent effective obstacle spacing increases from 1.37 to 1.43 nm for R-Mo and from 1.50 to 1.65 nm for R-Al after aging, compared with an approximately 1.0 nm random-O spacing. This systematic trend is consistent with a redistribution of the rate-controlling atomic-scale OOCs below the practical resolution of the APT cluster analysis.

Taken together, these results support the following working mechanism. OOCs and edge-dominated plasticity initially promote planar glide. Locally pinned screw dislocations due to OOCs then cross-slip out of saturated bands, creating inter-band segments and second-generation bands. Interactions among the planar bands, inter-band plasticity, and newly activated slip systems progressively refine the deformation structure, increase dislocation intersections and storage, and sustain work hardening. The Al-containing alloy exhibits the strongest response, consistent with an Al-sensitive modification of Ti/Zr-rich local ordering and/or BCC–α phase stability. These two contributions cannot yet be separated and are therefore presented as a compositional hypothesis rather than as a direct measurement.

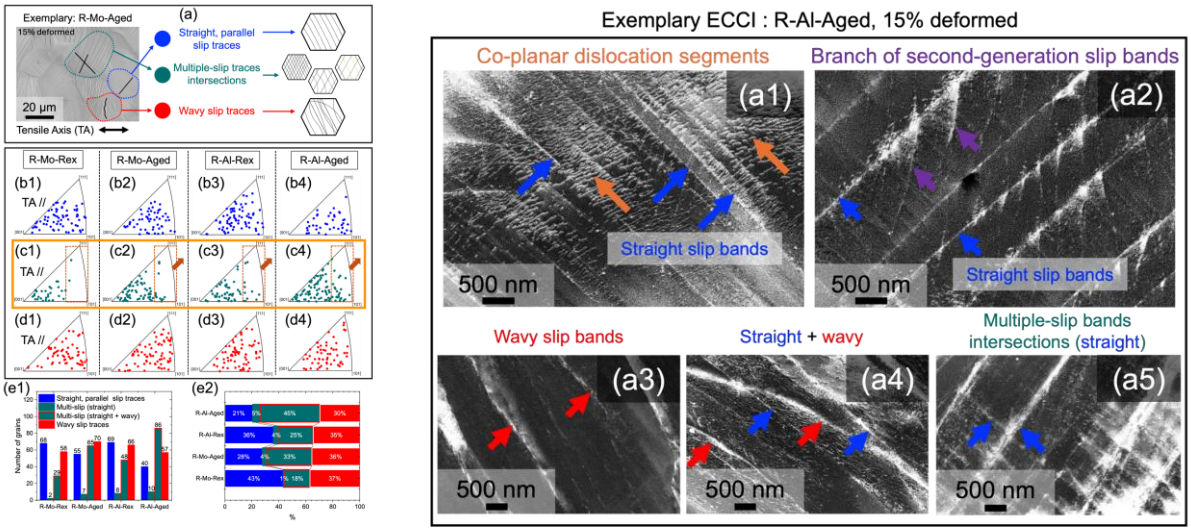

Figure 2. Multigrain slip-trace statistics (left) and representative ECCI observations from R-Al-Aged (right). Aging and Al broaden wavy/multiple-slip activity; ECCI reveals coplanar inter-band segments, second-generation bands, and mixed straight-wavy deformation structures.

Future Plans

In the long term, we aim to establish minor-element-induced short-range ordering (X-SRO) as a general strategy for stabilizing interstitial complexes in CCAs. We will test whether these complexes remain difficult to shear after irradiation and thereby activate PMDP. The initial focus will remain on TiZrNb-X-O (X=Al, Mo, or other elements) alloys, followed by extension to low-SFE FCC CCAs, including FeCoNiSi and CoCrNiW.

1. The four TiZrNb-X-O states—Al- and Mo-containing alloys in the recrystallized and aged conditions—will be irradiated to 1–10 dpa at intermediate temperatures. Nanoindentation and pile-up analysis will quantify depth-dependent hardening and strain localization, while ECCI and TEM will measure channel spacing, inter-channel dislocation activity, and irradiation defects. APT and synchrotron grazing incidence diffraction will probe oxygen redistribution and phase instability. We will test whether the aged Al alloy retains its planar-wavy slip coupling and multiple-slip activity, thereby suppressing channel-dominated localization and enabling PMDP after irradiation.

2. Separating the chemical and phase-stability effects of Al. To distinguish whether Al promotes oxygen-complex formation through Ti/Zr-centered local ordering or by changing the BCC–α/ω thermodynamic landscape, Al-, Mo-, and reference alloys will be aged near 500 °C for multiple durations. Synchrotron SAXS will track the kinetics and length scale of nanoscale compositional fluctuations or precipitation. Stress-relaxation measurements and APT will provide complementary obstacle-spacing and oxygen-correlation information. Accelerated ω/α formation correlated with mechanical changes would indicate a dominant phase-stability contribution.

3. Extending X-(Ti, Zr) SRO engineering within TiZrNb-X-O alloys. Candidate X elements will be selected based on asymmetric mixing enthalpies with Ti and Zr relative to Nb, their influence

on local oxygen coordination, and their ability to preserve the BCC matrix. Thermodynamic and atomistic screening will distinguish X-induced hcp stabilization from X-induced Ti/Zr-rich chemical environments or SRO.

4. Extension to low-SFE FCC CCAs (extended goal). The concept will also be tested in low- or potentially negative-SFE FCC alloys, initially FeCoNiSi and CoCrNiW. Because these alloys may deform through stacking faults, twinning, or phase transformation PMDP may develop through an intersecting fault/twin network that distributes strain beyond the initially activated irradiation channels. Ion irradiation, nanoindentation, ECCI, and TEM will determine whether deformation remains confined to cleared channels or expands through secondary faulting and slip transfer.

References

1. M. D. McMurtrey, B. Cui, I. Robertson, D. Farkas, and G. S. Was, "Mechanism of dislocation channel-induced irradiation assisted stress corrosion crack initiation in austenitic stainless steel," Current Opinion in Solid State and Materials Science 19, 305-314 (2015).
2. M. Jiao, Z. Lei, Y. Wu, J. Du, X.-Y. Zhou, W. Li, X. Yuan, X. Liu, X. Zhu, S. Wang, H. Zhu, P. Cao, X. Liu, X. Zhang, H. Wang, S. Jiang, and Z. Lu, "Manipulating the ordered oxygen complexes to achieve high strength and ductility in medium-entropy alloys," Nature Communications 14, 806 (2023).
3. Q. He, S. Yoshida, S. Okajo, M. Tanaka, and N. Tsuji, "Characteristic dislocation slip behavior in polycrystalline HfNbTiZr refractory medium entropy alloy," Journal of Materials Science & Technology 210, 29–39 (2025).

Publications

N/A

Assessing energetic contributions to slip/twinning selection in low symmetry ceramics

Corinne E. Packard, University of Southern California

Garrit J. Tucker, Baylor University

Keywords: twins, ceramics, stress, dislocations, symmetry

Research Scope

Classical metrics fail to fully explain the experimentally observed relative abundance of plasticity carriers in deformable low-symmetry ceramics, which have many non-equivalent twinning modes and slip systems. This knowledge gap is particularly salient in rare earth disilicates and rare earth orthophosphates, where plastic strain accommodation is critical to their functions in barrier coatings and fiber coatings in ceramic matrix composites. Nanomechanical and structural characterization are integrated with computation of deformation mechanism energetics to identify the atomic-scale origin of twin selection, twin stability, and twin energetics in monazite-structured rare earth orthophosphates ($REPO_4$s). Experimental work shows lower average onset requirements and less superelastic energy dissipation in $LaPO_4$, compared with $GdPO_4$ in the same crystal structure, illustrating composition-dependent sensitivities in deformation behavior. Linking experimental results to the atomic-scale origins of plasticity accommodation first requires understanding the energetics of slip/twin selection within a single material. Computational work focusing on differences in twin energetics between twin modes in $LaPO_4$ uses the construction and relaxation of supercell structures for the most observed twinning modes. The energetics and structure of twin boundaries vary greatly, potentially accounting for differences in experimentally observed twin mode abundance. This work provides a first step in identifying how crystal chemistry, involving composition as well as aspects of crystal structure including arrangement and connectivity of subunits in the polyhedral representation of ceramic structure, controls the planar fault pathways for slip and twinning in $REPO_4$s and other low-symmetry ceramics.

Recent Progress

Published data from experimental observation of deformed $LaPO_4$ (both chemically synthesized and naturally occurring) and $GdPO_4$ show multiple active twin modes and suggests that all monazite-structured $REPO_4$s generate a similar set of modes[1], [2] (Table 1), but the connection between crystal chemistry, twin mode activation requirements, and the twin populations that result from deformation is incomplete. We are working to identify how chemistry and structure control twin energetics, and whether those energetics dictate the relative abundance of distinct twin modes and slip systems. When $LaPO_4$ is subjected to spherical nanoindentation, the deformation volume contains (100) twin modes at an anomalously high frequency compared

to other observed twin systems, without a straightforward advantage in any shear or shuffle parameters[1].

Density functional theory (DFT) calculations performed in VASP provide the twin-boundary energetics reported here. Various energy convergence studies with VASP aids in the selection of the final twinned interface structures. This includes sampling various exchange-correlation functions, k-point configurations, and energy cutoffs. Calculation parameters follow prior first-principles studies of the pressure-induced structural changes of rare-earth orthophosphates, including $LaPO_4$. Relaxation of the monoclinic $P2_1/n$ cell supplies the reference structure and bulk energy for all boundary calculations to date, and for future work.

Twin bicrystals follow the mode definitions of Hay and Marshall: reflection of a monazite block across K_1 (or rotation about η_1 for type II modes), then stacking of the 'twinned' and parent blocks into a periodic supercell containing two crystallographically identical boundaries. These supercell blocks are subsequently translated into an initial state close to the energy minimum based on maintaining transformations across the boundary. The $(100)[100]_C$ and $(001)[001]_C$ twins use 4x1x1 unit cell configurations (96 atoms) with two unit cells in each twin variant, resulting in interplanar twin spacing around 13Å. The $(120)[010]_I$ bicrystal required derivation of a (120)-oriented cell referenced in the $P2_1/n$ configuration. This new (120)-oriented cell was found by comparing minimum-lattice points in 3D space and drawing superlattice vectors corresponding to the relevant in-plane minimum distance configurations. Energy difference between the relaxed $P2_1/n$ unit cell and (120) supercell was < 0.05meV/atom. This (120) supercell was stacked according to the same twin-creation procedure in a 1×1×2 configuration (240 atoms). Twin plane boundaries are initially considered along the unit-cell boundaries, and additionally at a half-cell boundary for the $(001)[001]_C$ twin.

Ionic relaxation at fixed cell shape yields the excess twin-plane energy $\gamma = (E_{twin} - NE_{bulk})/2A$, with E_{bulk} the energy of the relaxed unit cell and N the number of unit cells in the twin structure. The final relaxed twin-plane energies span a factor of nearly three across the three twinning modes: 498.9 mJ/m^2 for $(100)[100]_C$, 751.8 mJ/m^2 for $(120)[010]_I$,

Table 1. Experimentally observed twin modes, after Hay and Marshall (2003), showing observed defect abundance does not strictly correlate with shuffle or shear parameter. Computed energies are derived from the present study Systems are fully relaxed, including ionic and structural degrees of freedom. PBEsol exchange-correlation function with an energy cutoff of 520eV is used for all calculations.

Twin Mode $(K_i)[\eta_j]_{type}$	Observed Abundance	λ	Max δ_{La} and δ_{PO4} (nm/10)	ϕ and θ (°)	Computed relaxed twin-plane energies (mJ/m^2)
$(100)[100]_C$	58/70 grains	1	0.4 0.7	39 26	**498.9**
$(001)[001]_C$	5/70 grains	1	0.4 0.7	39 26	**999.3 (half cell) 1404.9 (full cell)**
$(120)[010]_I$	5/70 grains	1	0.7 0.8	85 56	**751.8**
$(12\bar{2})[01\bar{1}]_I$	2/70 grains	2	1.1 1.2	53 23	**(in progress)**
$(100)[2\bar{1}0]_{II}$	2/70 grains	1	0.8 1.1	63 60	**(in progress)**

and 999.3 and 1404.9 mJ/m^2 for the half-cell and full-cell terminations of (001)[001]$_C$, respectively (Table 1). The ordering of these twin energies initially corresponds to the experimentally observed grain activation frequency ranking in spherically indented polycrystalline $LaPO_4$, where (100)[100]$_C$ occupies 58 of 70 deformed grains. However, both the (100)[100]$_C$ and (120)[010]$_I$ twins were observed in 5 of 70 deformed grains, despite a significant difference in twin boundary energy. Overall, calculated twin boundary energies exceed the tens to low hundreds of mJ/m^2 tabulated for metals but fall far below the ≈1900 mJ/m^2 representative of oxide ceramic interfaces, thus explaining their thermodynamic accessibility during room-temperature deformation. Our results reveal a clear energetic advantage of the relaxed twin plane for (100)[100]$_C$ over (001)[001]$_C$, despite similar shear (θ) and shuffle (δ, ϕ) parameters, and over the (120)[010]$_I$. Thus, initial findings demonstrate that while tabulated geometric metrics may fail to explain twin mode abundance, the advanced computational techniques used here provide additional insight. Further investigation into specific deformation mechanics is warranted to better reveal behaviors which more fully encapsulate the twin behavior and resolve discrepancies between twin modes when comparing their energies and experimental observations.

Our analysis of the relaxed twin structures reveals similarities to twin configurations proposed by Hay and Marshall for the (100)[100]$_C$ and (001)[001]$_C$ configurations (Fig. 1). In our (100)[100]$_C$ bicrystal configuration, the mirror falls between cation planes, and the neighboring planes rotate their PO_4 tetrahedra and RE–O polyhedra toward the xenotime configuration (tetragonal symmetry) while the remaining twin structure retains monazite registry. Hay and Marshall proposed a twin configuration with the mirror lying on a cation plane, where that plane is a xenotime structure. The fact that our system maintains a twin mirror between the cation planes indicates an energy barrier between these two potential configurations. For the (001)[001]$_C$ twin, our half-cell based twin structure corresponds to the twin structure Hay and Marshall inferred on crystallographic grounds. The large energy difference of 405 mJ/m^2 between half-cell and full-cell twin construction challenges straightforward boundary transformation pathways. Direct xenotime-like reconstruction is difficult to evaluate for the (120)[010]$_I$ twin as the monazite-xenotime transformation pathway is not directly aligned.

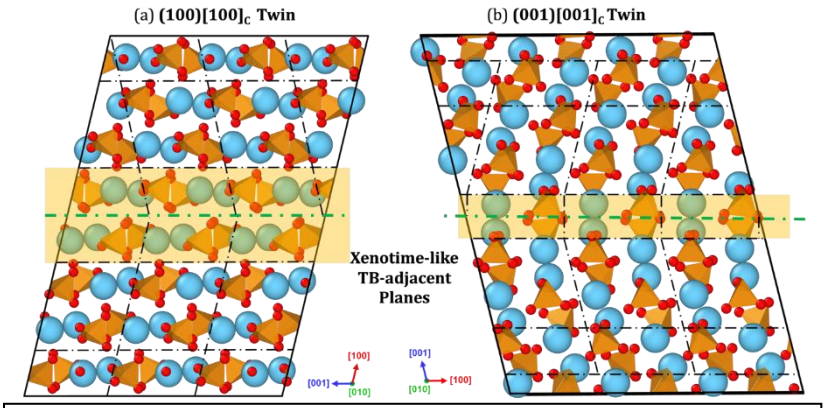

Fig. 1. Relaxed DFT twin bicrystals of monazite LaPO4. (a) (100)[100]$_C$ boundary bicrystal replicated 3x along the TB for visualization, γ = 498.9 mJ/m2. (b) (001)[001]$_C$ half-cell boundary replicated 3x along the TB for visualization, γ = 999.3 mJ/m^2. Shaded regions mark the twin-boundary-adjacent planes that relax toward xenotime-like ordering. Atom coloring: blue - La; orange - PO_4 tetrahedra; red - O. Dashed green line marks the twin plane.

Orientation of the local monazite-xenotime rearrangement relative to the fault plane distinguishes the twinning modes. The (100) and (120) interfaces accommodate the disregistry through in-plane rotation of PO_4 tetrahedra and RE–O polyhedra, whereas (001) exhibits plane-normal rearrangement. This provides initial support that twin selection in monazite therefore links with the direction of polyhedral rotation accessible at the interface rather than the magnitude of shear or shuffle. We are now developing a sequential generalized planar fault energy (GPFE) search that accommodates polyhedral rotation to identify candidate deformation pathways and reveal further distinctions between the deformation associated with the various twin modes.

Future Plans

An interconnected experimental/ computational approach will be employed to efficiently manage the scope of the problem in determining the broader question of the role of pressure and shear in controlling twinning in low-symmetry ceramics (Fig. 2). Computational results will be compared to experimentally observed deformation defect populations, which we will compile from target chemistries and varied stressing conditions. This work supports the development of crystallographic structure-function relationships sophisticated enough to reliably predict the dominant plasticity carriers in low-symmetry ceramics by illuminating how local atomic environments and stress state interact to bias favorable planar fault pathways for slip and twinning.

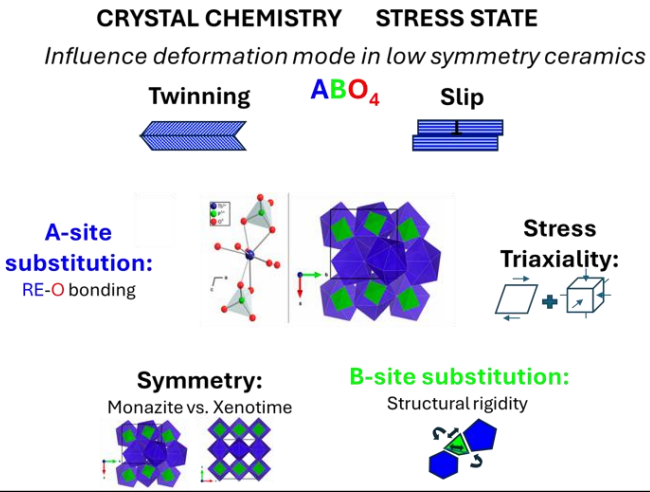

Fig. 2. Proposal Concept- Identifying how twinning and slip deformation modes are fundamentally influenced by crystal chemistry and stress state

References

1. R. S. Hay and D. B. Marshall, *Deformation twinning in monazite*, Acta Materialia **51**, 5235 (2003).
2. R. S. Hay, E. E. Boakye, and P. Mogilevsky, *Transformation plasticity in TbPO4 and (Gd,Dy)PO4 orthophosphates during indentation of polycrystalline specimens*, Journal of the European Ceramic Society **34**, 773 (2014)

Publications

1. H. Q. Afful, C. E. Packard, *Role of Crystal Chemistry in Twinning-based Superelasticity in Rare-Earth Orthophosphate Ceramics*, in review
2. H. Q. Afful, C. E. Packard, *Deriving Functionality from Mechanical Behavior of Rare Earth Orthophosphates*, In S. Miralya & T. Okura (Eds.), Functional Oxoate Ceramics and Glasses: Current Progress and Future Perspectives, submitted

Fundamental Studies of the Mechanical Behavior of Charged Hetero-Interfaces

Nitin P. Padture (PI) and Yue Qi (co-PI), Brown University

Keywords: Fracture, Interfaces, Defects, Electric Field, Charge

Research Scope

Mechanical adhesion of hetero-interfaces, which are ubiquitous in energy-conversion and -storage multi-layer devices, is key to their reliability. However, accumulated charge at those interfaces that can be subjected to external stimuli (electric field, light) during operation, are typically not considered in the measurement and analyses of mechanical adhesion. This represents a critical knowledge gap in interface science. The project is designed to address that gap, with the overarching objective of gaining fundamental understanding of the possible effects of accumulated charge, modulated by electric field or/and light, on the adhesion and fracture behavior of a range of hetero-interfaces. The project sets out to answer the following broad questions towards achieving the above objective. (1) To what extent do accumulated charges at hetero-interfaces modulated by the application of external stimuli (electric field, light), influence the adhesion toughness of those interfaces? (2) How do the characteristics of the charge accumulation affect the hetero-interface fracture behavior? (3) Can these effects be tuned *via* interfacial engineering?

The project focuses on hetero-interfaces between brittle 'soft' and 'hard' semiconductors relevant to halide perovskite solar cells (PSCs), which provides a model platform for this fundamental study. However, the basic experimental and computational tools that are being developed here will be general, with the potential for extending their application in the future to more complex interfaces and operating conditions relevant to other energy devices such as electrochemical batteries and fuel cells. In this study the 'soft' semiconductor is a metal halide perovskite (MHP) and the 'hard' semiconductor is an oxide which serves as electron transport layer (ETL) or hole transport layer (HTL). Thus, the specific objectives are: (a) Understand quantitatively the effects of external stimuli (electric field, light) on the interfacial adhesion and fracture of a range of MHP/ETL and MHP/HTL interfaces. (b) Understand quantitatively the roles played by the nature and distribution of the accumulated charges, modulated by the external stimuli, on the interfacial adhesion and fracture of the above interfaces. (c) Elucidate the possible role of engineered interfaces on the interfacial adhesion and fracture quantitatively.

Recent Progress

Cleavage Fracture of Single-Crystal MHPs

Density-functional theory (DFT) computations of fracture of bulk halide perovskites (MHPs) first performed as this is lacking in the literature. To that end, the surface energies and the fracture energies of two prototypical cubic MHPs, methylammonium lead tribromide ($MAPbBr_3$) and formamidinium lead triiodide ($FAPbI_3$) were computed using DFT for different high-index surfaces: {100}, {110}, and {111}. While the surface energy (G_C) is more sensitive to the chemical

potential of different species, G_C maintains the stoichiometry of the bulk. Generally, the G_C of a bulk crystal is considered to be the sum of the relaxed surface energies of the two mating fracture surfaces. However, here it is argued that the very process of fracture at the crack tip involves unrelaxed surfaces which can have different terminations. Thus, the 'unrelaxed' G_C are the most appropriate representation of the true fracture energy of crystalline materials in general, and MHPs in particular.

Table 1 summarizes the DFT-computed unrelaxed G_C of different cleavage planes and surface terminations in MHPs depicted in Fig. 1. Significant anisotropy in the G_C is observed. This anisotropy is manifested in cleavage-fracture experiments on lab-grown $FAPbI_3$ and $MAPbBr_3$ single-crystals, where cracks, even when forced along {110} planes, turn along the lowest fracture energy {100} planes (Fig. 2). Additionally, the average {100} fracture energy of $MAPbBr_3$ is experimentally measured to be ~0.3 $J{\cdot}m^{-2}$, which compares with the DFT-computed 0.31 $J{\cdot}m^{-2}$ (relaxed) and 0.47 $J{\cdot}m^{-2}$ (unrelaxed) values. A paper describing these calculations and experiments was published recently in *Acta Materialia*.

Table 1. DFT-calculated anisotropic fracture energies of MHPs.

MHP	Cleavage Plane	Mating Surface Terminations	Fracture Energy ($J{\cdot}m^{-2}$)
$FAPbI_3$	(100)	FAI / PbI_2	0.39
	(110)	Stoichiometric	0.54
	(111)	FAI_3 / Pb	1.97
$MAPbBr_3$	(100)	$MABr / PbBr_2$	0.47
	(110)	Br_2 / -Br_2	0.91
	(111)	$MABr_3$ / Pb	1.61

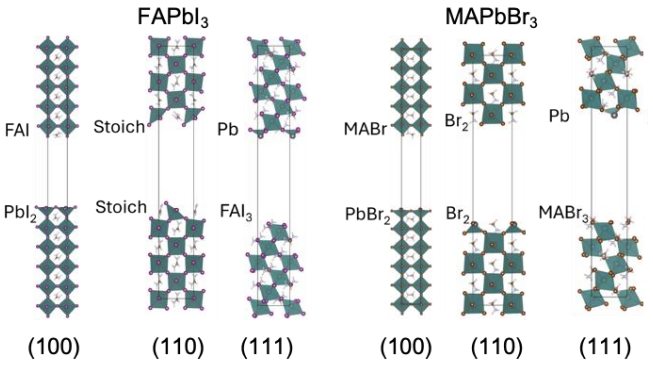

Figure 1. Cleavage of $FAPbI_3$ and $MAPbBr_3$ on different planes and different mating surface terminations corresponding to Table 1.

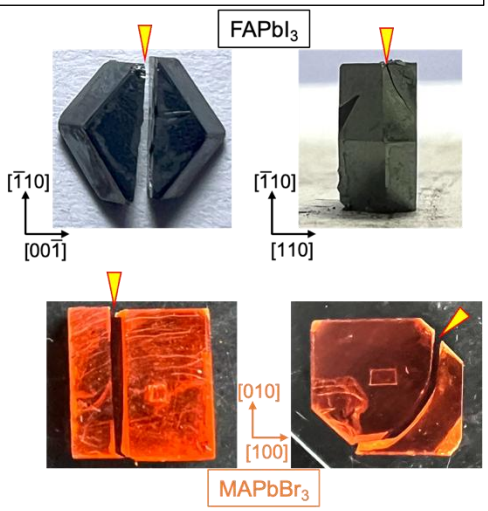

Figure 2. $FAPbI_3$ (top) and $MAPbBr_3$ (bottom) single-crystals cleavage along {100} plane (left), and ones forced to cleave along {110} but the cracks turns along {100} plane (right).

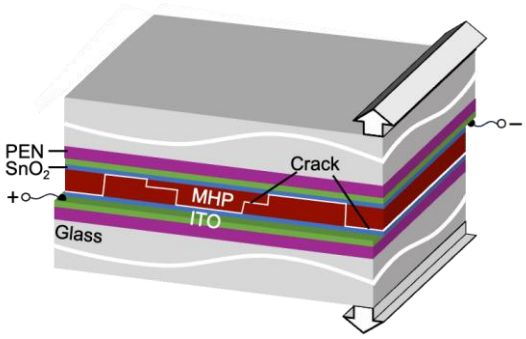

Figure 3. Schematic illustration of specimen used for G_C measurement under applied voltage.

Electric field effects on fracture of hetero-interfaces

As mentioned earlier, accumulated charge at hetero-interfaces, which is also ubiquitous in these devices that are invariably subjected to external stimuli (electric field, light) during operation, are typically not considered in the

measurement and analyses of mechanical adhesion. Here, interfacial toughness (G_C) of interface between a prototypical MHP thin film ($(Cs_{0.03}FA_{0.95}MA_{0.02})Pb(I_{0.95}Br_{0.05})_3$) and a prototypical SnO_2 ETL thin film on glass substrates was measured *in situ* under electric bias (in dark), for the first time. The double-cantilever beam (DCB) symmetric specimen was used (Fig. 3)[1], where there is an offset to access the indium-tin oxide (ITO) transparent-conducting electrodes on either side. The toughness measurements were conducted while under 0, 1.5, or 2.0 V applied bias after soaking for ~1 or ~8 h.

The current-density (J) of the specimens was measured as a function time (t) for applied voltages (V) of 1.0, 1.5, and 2.0 V in dark, and results are presented in Fig. 4. It was found that at applied 1.0 V, J is relatively constant with time, indicating no charge buildup at the interfaces. At applied 1.5 V there was slow change in J with time, which attained steady-state at ~8 h. At 2.0 V, J changed rapidly with time, attaining steady-state in ~ 1 h. The latter two results indicate motion and accumulation of ionic charges at interfaces with applied voltages >1 V, which is typical bias in operating perovskite solar cells.

Fig. 5 shows the *in situ* G_C results under 1.5 V bias (soaked for ~8 h) and 2.0 V bias (soaked for ~1 h), together with the control (0 V). The embrittlement under electrical bias is unmistakable. Furthermore, in the control case (0 V) there is about 50:50 chance of top or bottom MHP/SnO_2 interface fracturing in the symmetric specimens. However, under bias (1.5 or 2.0 V) there is overwhelming tendency for fracture to occur at the top positive MHP/SnO_2 interface (Fig. 6). This clearly indicates that changes are occurring at that interface causing it to become relatively more brittle.

The X-ray photoelectron spectroscopy (XPS) characterization of the MHP side of the fracture surfaces reveals shift of Pb 4f core level to higher binding energy relative to the control, which is indicative of under-coordination of Pb at subjected to 2.0 V bias.

Since MHPs have intrinsic point defects, which can diffuse toward the interface, their accumulation at the charged interface can influence the interfacial bonding and

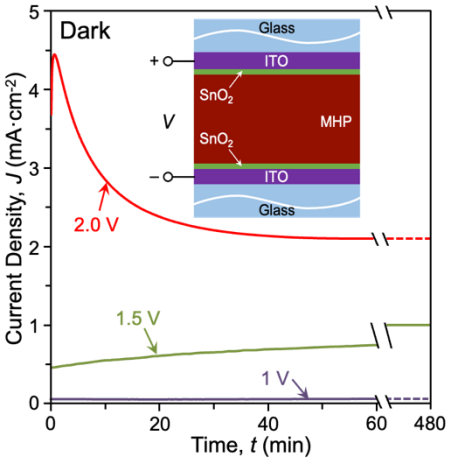

Figure 4. *J-t* responses at 1.0, 1.5, or 2.0 V bias of the symmetric specimens illustrated in the inset.

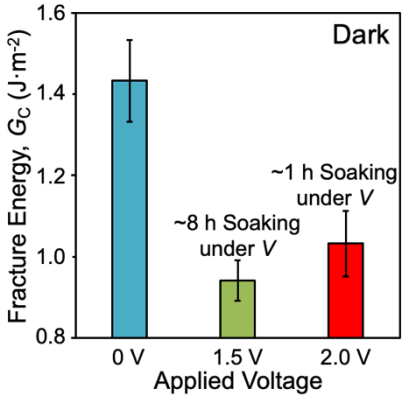

Figure 5. *In situ* G_C measurements under electrical bias.

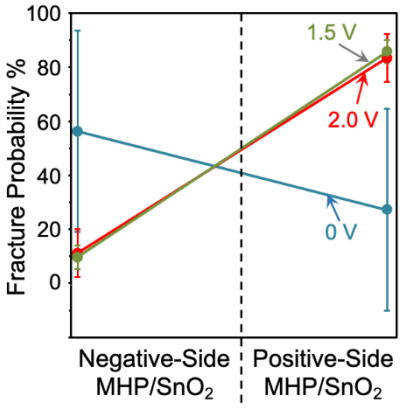

Figure 6. Change in fracture mode under electrical bias.

change the fracture behavior. Thus, to understand charged point defect generation and accumulation at the interface, we performed DFT computations of point-defect energies.

The key DFT results are plotted in Fig. 7, where the equilibrium formation energy as a function of Fermi level is shown. In the bulk of MHP, charge neutrality is maintained (dashed line), it indicates that I-interstitial (I_i) and FA-interstitial (FA_i) are energetically most favorable, followed by Pb-vacancy (V_{Pb}) and I-vacancy (V_I). Considering the self-interactions of the point defects and solving the charge neutrality conditions, the concentrations of these defects are shown in Fig. 8. Furthermore, at the charged interface, the defect formation energy depends on the local electric potential, ϕ, and the charge neutrality of point defects are not maintained in the space charge layer. The accumulation and concentrations of the various point defects under different electric potentials are plotted in Fig. 8, showing the highest concentration of I_i at the positive electrode, which appears to be responsible for the interface embrittlement. It is noteworthy that concentrations of defects in the bulk are generally very low, but when they accumulate on a 2D interface, their interfacial concentration increases dramatically, and can have an outsized effect on the interfacial mechanical properties.

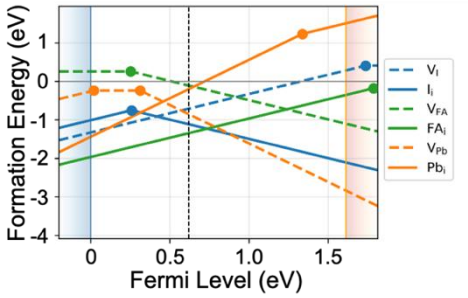

Figure 7. DFT-computed formation energies of point defects in $FAPbI_3$.

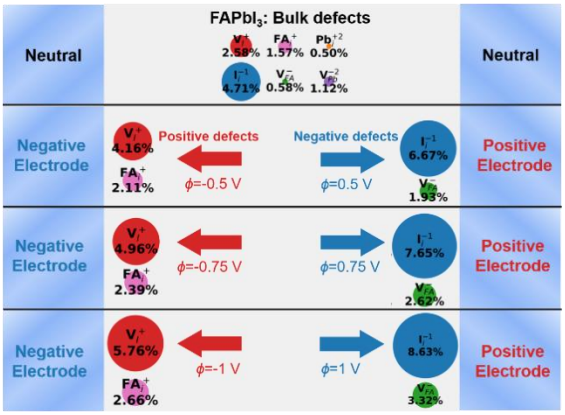

Figure 8. DFT-computed concentrations of various accumulated defects for -ve or +ve bias.

Future Plans

In the remainder of the project three major experiments are planned. First, we plan to perform detailed characterization of the interfaces using scanning transmission electron microscopy (STEM) to observe interfacial morphology changes, and energy dispersive spectroscopy (EDS) to measure the composition profiles in the MHP film. Second, we plan to perform Kelvin probe force microscopy (KPFM) measurements of the interfaces to quantify the potentials under electrical bias. Third, we plan to perform the G_C measurements only under light illumination (without bias) to evaluate any effects. Also, we will characterize the interfaces to understand any effects. If time permits, we plan to perform preliminary experiments to evaluate any effects on G_C and fracture mode due to combined light and applied bias.

Regarding computational modeling, only isolated point defects are considered so far. Paired defects, defects trapping electrons or holes, will be considered in the next step to understand

the evolution of point defects under accumulation. Also, the interface fracture requires a simulation size beyond the current DFT limit. We will train machine learning potentials (MPL) for interface models and calculate the impact of defect concentration on fracture energy.

References

1. Z. Dai, S.K. Yadavalli, M. Chen, A. Abbaspourtamijani, Y. Qi, and N.P. Padture, *Science*, 372, 618-22 (2021).

Publications

1. A. Ranka, M. Layek, S. Kochiyama, C. López-Pernia, A.M. Chandler, C.A. Kocoj, E. Magliano, A. Di Carlo, F. Brunetti, P. Guo, S. Suresh, D.C. Paine, H. Kesari, and N.P. Padture, "Cracking in Polymer Substrates for Flexible Device and its Mitigation," *npj Flexible Electronics*, **9**, 92 (2025). DOI: 10.1038/s41528-025-00470-z
2. V. Arzumanyan, M.C. Doyle, A. Ranka, N.P. Padture, and Y. Qi, "Anisotropic Fracture of Metal-Halide Perovskites," *Acta Materialia*, **318**, 122617 (2026). DOI: 10.1016/j.actamat.2026.122617

Determining rate-controlling, grain-boundary-mediated mechanisms in nanocrystalline and ultrafine grained metallic films

Olivier Pierron, Josh Kacher and Ting Zhu, Georgia Tech

Keywords: In situ TEM, activation volume, grain-boundary stability, dislocation nucleation, diffusion-assisted plasticity

Research Scope

The central goal of this project is to identify the grain-boundary (GB)-mediated unit processes that control plastic-flow kinetics in ultrafine-grained and nanocrystalline metallic films. Our approach combines quantitative microelectromechanical-system (MEMS)-based in situ transmission electron microscopy (TEM), transient activation-parameter measurements, 4D-STEM orientation mapping, and transition-state-theory-based atomistic modeling. This integration is essential because activation volume is a sensitive kinetic fingerprint, but several candidate processes—including GB dislocation nucleation, disconnection-mediated sliding and migration, and diffusion-assisted interfacial rearrangements—can all produce values in the few-to-tens of b^3 range [1-3]. Directly measuring activation parameters while observing the evolving microstructure provides the mechanistic discrimination that is not available from stress-strain data or postmortem microscopy alone.

Our recent work tests a central hypothesis: the rate-limiting mechanism is selected not by grain size alone, but by the structural and kinetic stability of the GB network. We varied GB stability through deposition route and mild thermal exposure in nanocrystalline Ni, and through solute stabilization in Pt and $Pt_{90}Au_{10}$. These comparisons reveal two reproducible kinetic regimes. Stable grain structures exhibit larger activation volumes and dislocation-controlled plasticity, whereas unstable structures undergo stress-assisted coarsening and exhibit much smaller activation volumes associated with diffusion-assisted boundary motion. The results establish GB stability as a kinetic variable that governs which localized process controls plastic flow.

Recent Progress

Freestanding dog-bone specimens, nominally 75-100 nm thick, were tested in a 300 kV TEM using our calibrated MEMS tensile platform. Physical activation volumes were obtained from repeated stress-relaxation transients. Three Ni films were prepared by electron-beam evaporation, room-temperature sputtering without substrate preheat, and sputtering with the substrate preheated to 100 °C. Their mean grain sizes were closely matched at 9.7, 10.1, and 11.4 nm, respectively, thereby separating GB-state effects from grain-size effects. Sputtered Pt and $Pt_{90}Au_{10}$ provided a complementary comparison in which Au solute kinetically stabilized the boundary network.

Atomic-resolution observations show that the deposition routes produced markedly different defect states despite the nearly identical Ni grain sizes. The evaporated film was comparatively free of lattice dislocations, whereas the room-temperature sputtered film contained the highest dislocation content and frequent GB-associated lattice-fringe offsets and dislocation-like interfacial defects. The sputtered (preheat) film retained some intragranular dislocations but did not exhibit the same population of interfacial defect structures (Fig. 1). These observations are consistent with lower-energy deposition and mild thermal exposure promoting defect annihilation and boundary relaxation, while energetic sputtering stores excess defects and free volume in a nonequilibrium GB network [4].

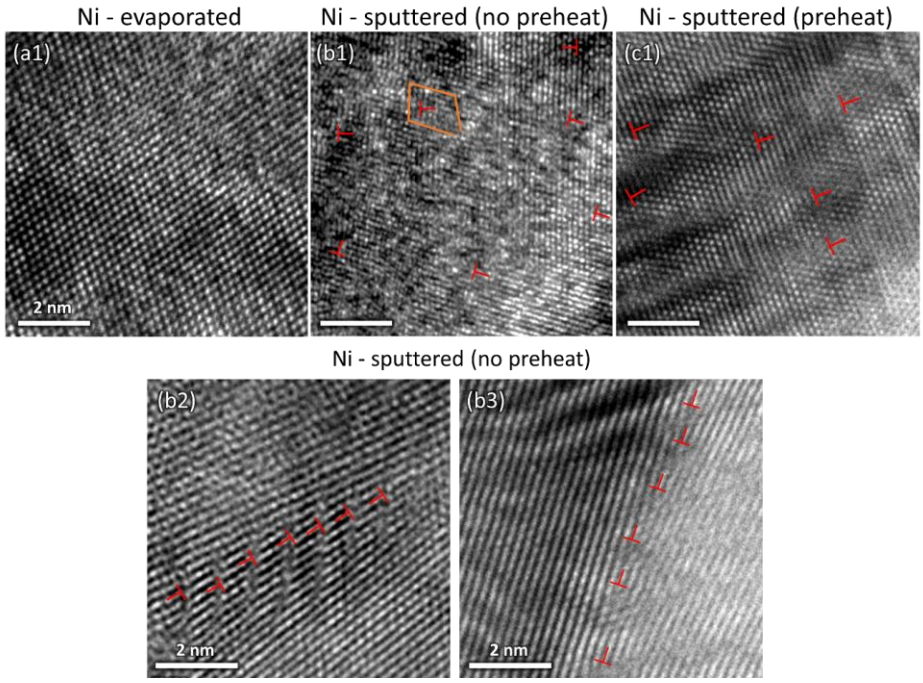

Figure 1. Atomic-scale lattice defects in the three Ni films. Representative HRTEM images show grain interiors in evaporated Ni (a1), sputtered (no preheat) Ni (b1), and sputtered (preheat) Ni (c1). GB regions in the sputtered (no preheat) film (b2,b3) contain interfacial defect structures marked by red symbols.

The mechanical response separates according to the same stability ranking. Evaporated and sputtered (preheat) Ni both yielded at approximately 1.4 GPa, while the defect-rich sputtered (no preheat) film yielded at approximately 0.9 GPa (Fig. 2a). $Pt_{90}Au_{10}$ reached a yield strength of approximately 1.8 GPa and sustained strain hardening over roughly 10% plastic strain, whereas pure Pt yielded near 1.4 GPa and necked after only a few percent strain (Fig. 2b). Rate-dependent tests on evaporated Ni further revealed two regimes: the strain-rate sensitivity decreased from $m = 0.157$ at 10^{-6}-10^{-4} s^{-1} to $m = 0.069$ at 10^{-3}-10^{-1} s^{-1} (Fig. 2c,d). This transition indicates that the relative accessibility of GB-mediated and displacive processes changes with the available deformation time.

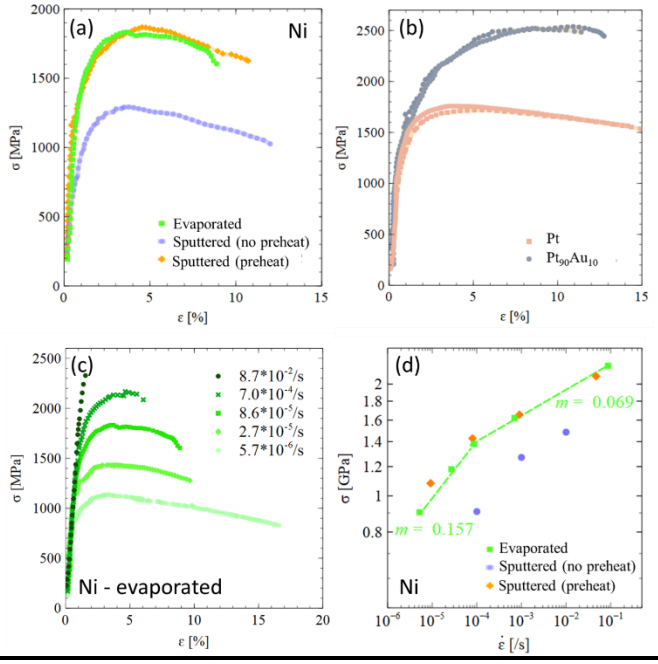

Figure 2. Mechanical response of the Ni and Pt-based films. (a) Engineering stress-strain curves for evaporated, sputtered (no preheat), and sputtered (preheat) Ni. (b) Curves for Pt and $Pt_{90}Au_{10}$. (c) Strain-rate-dependent response of evaporated Ni. (d) Flow stress versus strain rate for the three Ni conditions

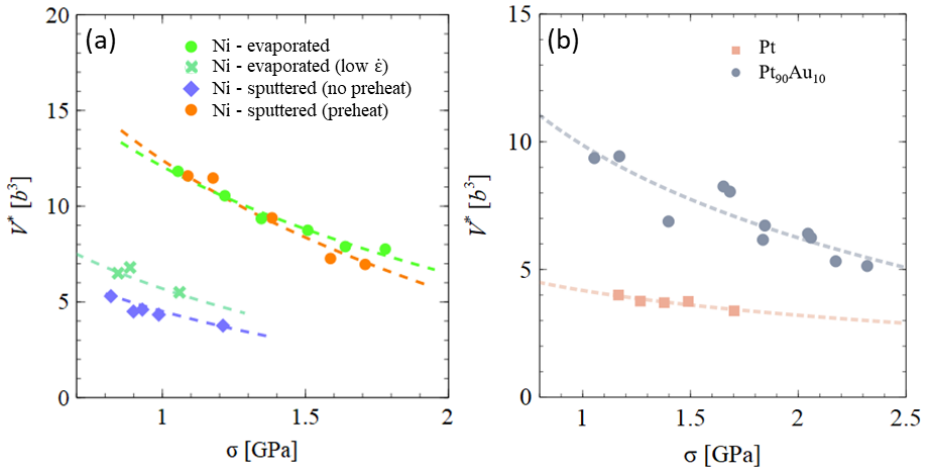

Figure 3. Activation volume, V*, as a function of applied stress for (a) the three Ni deposition conditions, including evaporated Ni at a low strain rate of 10^{-5} s^{-1} (all other measurements performed at 10^{-4} s^{-1}), and (b) Pt and $Pt_{90}Au_{10}$. The data separate into a larger-V* stable-grain branch and a smaller-V* grain-coarsening branch

The transient measurements provide the clearest separation of the two regimes. At comparable stresses, stable evaporated and sputtered (preheat) Ni exhibited V* ≈ 7-12b^3, whereas sputtered (no preheat) Ni remained near 4-5b^3. Likewise, solute-stabilized $Pt_{90}Au_{10}$ exhibited V* ≈ 6-10b^3, while pure Pt remained near 3-4b^3 (Fig. 3). When the applied strain rate is decreased from

approximately 10^{-4} to 10^{-5} s^{-1}, the measured V* for evaporated Ni is shifted downward to roughly 5-7b^3, showing that even a comparatively stable boundary network can enter the coarsening regime when sufficient time is available for diffusion-assisted processes.

In situ TEM observations and atomistic calculations identify the unit processes underlying these branches. In the stable-grain regime, stress-assisted GB migration was suppressed and plasticity was carried primarily by dislocation activity. High-resolution observations of sputtered (preheat) Ni directly captured the nucleation of a new dislocation segment from a GB. The measured Ni activation volumes of approximately 7-12b^3 agree quantitatively with free-end nudged elastic band calculations for GB dislocation nucleation: a representative asymmetric boundary gives $V^* \approx 7b^3$ at a laboratory-rate energy barrier, while idealized symmetric tilt boundaries provide an upper estimate near $20b^3$ [3]. The $Pt_{90}Au_{10}$ values lie much closer to the expected dislocation-nucleation range after accounting for elastic-modulus differences.

In the unstable-grain regime, pronounced stress-assisted coarsening accompanied deformation in sputtered (no preheat) Ni and pure Pt. Importantly, the small V* values persisted even after the grains had coarsened enough to support extensive dislocation nucleation and glide. Thus, the most visible carrier of plastic strain was not necessarily the rate-limiting event. Values as low as 3-5b^3 instead point to a highly localized, diffusion-assisted interfacial step. Nonequilibrium GBs contain excess free volume, interfacial dislocations, and long-range strain fields that enhance short-circuit diffusion. Their migration can proceed through disconnections carrying both step and Burgers-vector character; climb-assisted disconnection motion requires point-defect transport and naturally produces small activation volumes [5]. The combined observations show that GB stability controls the competition between this diffusion-assisted pathway and displacive GB dislocation nucleation. Grain size sets the geometrical weighting of interfaces, but the GB state determines whether those interfaces remain kinetically active.

Future Plans

We will extend this stability framework to thermally and mechanically processed Ni, Pt, Au, $Pt_{90}Au_{10}$ in order to decouple grain size from processing history. Preliminary results show that annealing generally produces grain growth and shifts V* toward larger values, consistent with a reduced contribution from GB-controlled processes [6]. In Ni, increasing the average grain size from approximately 10 to 140 nm lowers the strain-rate sensitivity and increases the activation volume. However, matched-grain-size Pt provides a counterexample to a grain-size-only description: annealing at 500 °C and mechanical prestraining produce nearly identical mean grain sizes of approximately 45, yet the mechanically coarsened state retains substantially smaller activation volumes. On the characterization side, we will continue to develop diffraction mapping-based techniques to extract quantitative metrics on the grain boundary defect states. These measurements will be directly correlated to the observed GB migration behavior and indirectly to the measured V* values. We will use this data to determine how grain boundary stability and grain size jointly select the rate-controlling process.

References

[1] I.A. Ovid'ko, R.Z. Valiev, Y.T. Zhu, Review on superior strength and enhanced ductility of metallic nanomaterials, Progress in Materials Science 94 (2018) 462-540.
[2] Y.M. Wang, A.V. Hamza, E. Ma, Temperature-dependent strain rate sensitivity and activation volume of nanocrystalline Acta Materialia 54 (2006) 2715-2726
[3] Y. Zhang, K. Ding, S. Stangebye, D. Chen, J. Kacher, O. Pierron, T. Zhu, Atomistic modeling of surface and grain boundary dislocation nucleation in FCC metals, Acta Materialia 237 (2022) 118155.
[4] C.A. Schuh, K. Lu, Stability of nanocrystalline metals: The role of grain-boundary chemistry and structure, MRS Bulletin 46(3) (2021) 225-235.
[5] J. Han, S.L. Thomas, D.J. Srolovitz, Grain-boundary kinetics: A unified approach, Progress in Materials Science 98 (2018) 386-476.
[6] H. Conrad, Grain size dependence of the plastic deformation kinetics in Cu, Materials Science and Engineering a-Structural Materials Properties Microstructure and Processing 341(1-2) (2003) 216-228.

Publications from past two years

1. S. Stangebye, K. Ding, Y. Yang, T. Zhu, O. Pierron, J. Kacher, *Grain size effects on stress-assisted grain boundary migration in polycrystalline Au thin films under tension*, Acta Materialia 297 (2025) 121330.
2. L. Daza-Llanos, S. Stangebye, E.J. Lang, K. Hattar, O. Pierron, J. Kacher, *Influence of irradiation damage on stress-assisted grain growth in ultrafine-grained Au thin films using in situ transmission electron microscopy mechanical testing*, Materials Science and Engineering A 947 (2025) 149256.
3. Y. Yang, K. Ding, X. Liu, T. Zhu, J. Kacher, O. Pierron, *In situ TEM measurement of strain-rate-dependent activation volume of ultrafine-grained Au films*, Acta Materialia 306 (2026) 121868.
4. Y. Yang, K. Ding, T. Zhu, J. Kacher, O. Pierron, *The role of grain size distribution on the anomalous yielding of ultrafine-grained Au thin films*, Scripta Materialia 275 (2026) 117178.
5. Y. Yang, Y. Liu, T. Zhu, O. Pierron, J. Kacher, *Decoupling the effects of temperature and stress on grain growth in nanocrystalline Ni films*, Acta Materialia 313 (2026) 122305.
6. Y. Yang, K. Ding, K.R. Dorman, B.L. Boyce, T. Zhu, J. Kacher, O. Pierron, *Grain boundary stability dictates the rate-limiting deformation process in nanocrystalline metals*, Acta Materialia (accepted).
7. Y. Yang, O. Pierron, J. Kacher, D. Rowenhorst, *NLSTEM: Non-local denoising for enhanced 4D-STEM pattern indexing*, submitted to Microscopy and Microanalysis.
8. Y. Yang, K. Ding, T. Zhu, O. Pierron, J. Kacher, *Direct observation of grain-size-dependent sequential yielding in heterogeneous ultrafine-grained Au*, manuscript in preparation.

Closing the Loop: AI-Accelerated Interstitial Engineering of Complex Concentrated Alloys

Stephanie Ribet[1], Andrew Minor[1], Brandon Bocklund[2], Aurelien Perron[2], Mingwei Zhang[3]

[1]Lawrence Berkeley National Laboratory; [2]Lawrence Livermore National Laboratory; [3]University of California, Davis

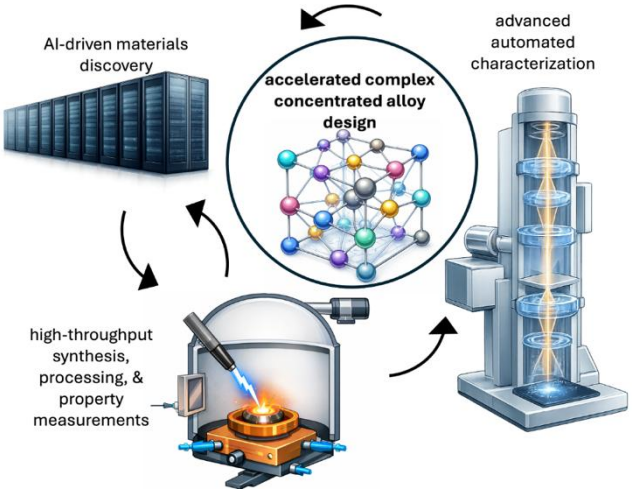

Overview of AI-enabled workflow: We will predict (LLNL), synthesize (UC Davis), and characterize (LBNL) novel CCAs, feeding experimental results back to the model to improve predictions.

Advanced technologies like clean energy systems, aircraft, and nuclear reactors need metals that can withstand extreme heat and stress without becoming brittle or failing. Complex concentrated alloys (CCAs), particularly body-centered cubic refractory systems, offer a promising pathway, with recent work showing that incorporating oxygen in a controlled manner can dramatically enhance both strength and ductility. However, the underlying design rules remain poorly understood, and conventional materials discovery approaches are too slow to explore the vast compositional and processing space. This project proposes a closed-loop, artificial intelligence (AI)-accelerated framework to design, synthesize, and characterize oxygen-containing CCAs, specifically in systems containing niobium, zirconium, titanium, and other high-melting-point elements. The effort integrates high-throughput computational screening, rapid experimental synthesis, and advanced electron microscopy into an end-to-end workflow. Lawrence Livermore National Laboratory's AI-enabled Materials Acceleration Platform (MAP) will evaluate millions of candidate compositions to identify promising regions of composition–processing space. These predictions guide high-throughput synthesis at UC Davis, where multi-cavity arc melting enables rapid fabrication followed by mechanical screening. At Lawrence Berkeley National Laboratory, state-of-the-art scanning transmission electron microscopy probes oxygen clustering and defects across multiple length scales, providing mechanistic understanding of alloy performance. Experimental results feed back into the computational models, forming an adaptive, self-improving discovery loop. Over nine months, the project will demonstrate accelerated optimization of alloy strength and ductility and quantify AI advantage through reduced experimental iteration cycles, expanded compositional search space, and improved predictive accuracy.

Damage-Tolerance in Structural Materials

Robert O. Ritchie, Mark Asta and Andrew M. Minor

Lawrence Berkeley National Laboratory

Keywords: High-entropy alloys, Deformation, Fracture, Toughness, *fcc vs. bcc* alloys

Research Scope

Achieving strength and toughness is vital for structural materials; unfortunately, these properties are often mutually exclusive. Using an approach that combines multiscale mechanical testing and characterization with theoretical and machine-learning-informed computational methods, we are examining strategies to solve this "conflict" in advanced metallic alloys by focusing on the interplay between the individual mechanisms that contribute to strength and toughness, that of plasticity and crack-tip shielding, noting that these phenomena may originate at wildly different structural length-scales. Our central objective is to seek a fundamental understanding, at atomistic to near-macroscopic length-scales, of the scientific origins of damage-tolerance in multiple-element (largely single-phase) metallic alloys. Our focus is on medium- and high-entropy alloys (M/HEAs), which can display excellent mechanical properties due to a novel combination of mechanisms arising from their disordered structures. We found that the face-centered cubic (*fcc*) CrCoNi-based M/HEAs exhibit the highest fracture toughness on record. Their strength, ductility, and toughness arise from a synergistic sequence of deformation mechanisms (slip, stacking-fault formation, nano-twinning, and phase transformation, catalyzed, we believe, by local chemical ordering) that promotes prolonged strain hardening. The damage tolerance of these alloys is further enhanced at cryogenic temperatures and ultrahigh strain rates. In contrast, the body-centered cubic (*bcc*) refractory high-entropy alloys (RHEAs) are characterized by high strength at ultrahigh temperatures. Although they perform well in compression, we have shown that in tension they are invariably plagued by severe brittleness, with very high ductile-brittle transition temperatures (DBTTs), often far above 1000°C, *e.g.*, NbTaMoW. However, replacing group VI with group IV elements promotes plasticity. RHEAs such as NbTaTiHf display remarkable toughness over a wide temperature range from 77K to 1200°C, with minimal evidence of strain hardening. Damage tolerance arises from a different, now competitive, sequence of plasticity mechanisms, including kink banding. Testing at 20K revealed no change in strength or toughness compared to 77K, with no ductile-brittle transition, which we associate with a change in the sequence of plasticity mechanisms. Although these group IV+VI RHEAs show no apparent DBTTs, they still lack the ultrahigh strength of the typical RHEAs. If this can be solved, these materials represent a true promise of a superior class of alloys for high-temperature extreme environments.

Recent Progress

Following our studies on the damage tolerance of *fcc* HEAs, where we found that the CrCoNi-based alloys displayed a record K_{Ic} fracture toughness exceeding 450 MPa√m,[1] we have been examining the corresponding damage-tolerant properties of *bcc* RHEAs over a range of temperatures. Our initial studies on NbTaTiZrAl and the well-known NbTaMoW alloy confirmed their ultrahigh strength and reasonable ductility, but only in compression; in tension, these properties were over an order of magnitude lower, with excessively high DBTTs and K_{Ic} < 10 MPa√m.[2] To avoid the extremely brittle nature of these alloys, we focused on NbTaTiHf where the two group VI elements were replaced by group IV. This shifts the Fermi Energy out of the pseudogap in the d-electron density of states, decreasing the unstable stacking fault energy and effectively reducing resistance to dislocation glide.[3] Unlike most *bcc* alloys, this single-phase RHEA displayed remarkable tensile ductility and toughness over a wide temperature range from 20K to 1200°C (K_{Ic} > 253 MPa√m at room temperature),[4] with no apparent DBTT and no change in strength or toughness (K_{Ic} ~90 - 100 MPa√m) between 77 and 20 K (**Fig. 1**)[5] Akin to the toughness of the *fcc* HEAs, which we attributed to a regimented sequence of deformation mechanisms of slip, stacking-fault formation, nanotwinning and phase transformation that prolonged strain hardening, the high toughness of the *bcc* NbTaTiHf could also be similarly related to a series of multiple deformation mechanisms – dislocation slip, twinning, phase transformations and the unusual formation of kink bands - but now in a competitive sequence which hardly affects strain hardening.[2] Unlike NbTaTiW, NbTaTiHf is exceptionally resistant to fracture, but unlike the *fcc* alloys, the material is tough in the absence of strain hardening in tension. It shows no apparent DBTT because, at cryogenic temperatures, twin formation and an omega-phase

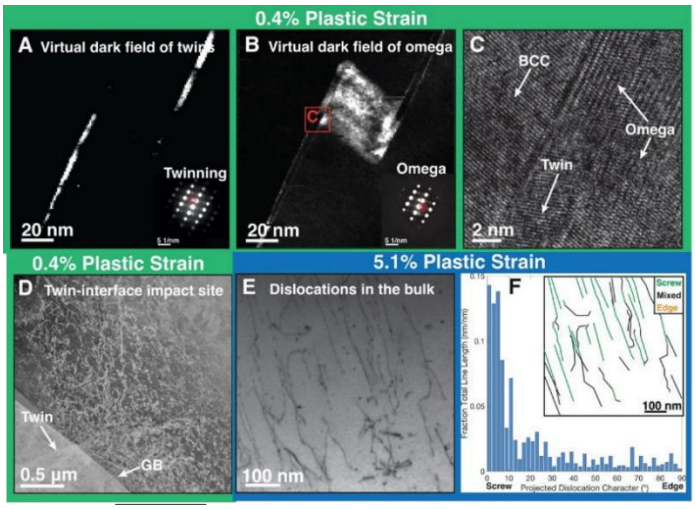

Fig. 1 Virtual dark-field images from 4D-STEM scans of two twins in NbTaTiHf with ω collapse occurring between them. Omega is additionally observed in (b) as a transitional twin boundary structure. Once the twins propagate, they impact interfaces such as grain boundaries, as shown in (d), generating a local stress concentration that nucleates mixed dislocations. At higher plastic strains, the dislocations can glide into the grain interiors, as shown in (e). A *g·b* analysis demonstrates they adopt screw character as plotted in (f) and illustrated in the inset.

transformation can nucleate dislocations at interfaces before global dislocation motion, *i.e.*, the deformation-mechanism sequence becomes inverted (which we verified by atomistic simulations). The initial mechanism is temperature-insensitive and controls yielding, thereby preserving abundant plasticity at low temperatures.

We also studied both *fcc* CrCoNi and *bcc* NbTaTiHf under ultrahigh strain rates using laser shock impact conditions, where strain rates are approximately 10 orders of magnitude higher than in quasi-static tests. Both M/HEAs show excellent impact resistance and, depending on the local stress state, a deformation-mechanism sequence similar to that observed at cryogenic temperatures, although amorphous structures can form in the *fcc* alloys at these very high strain rates.

Future Plans

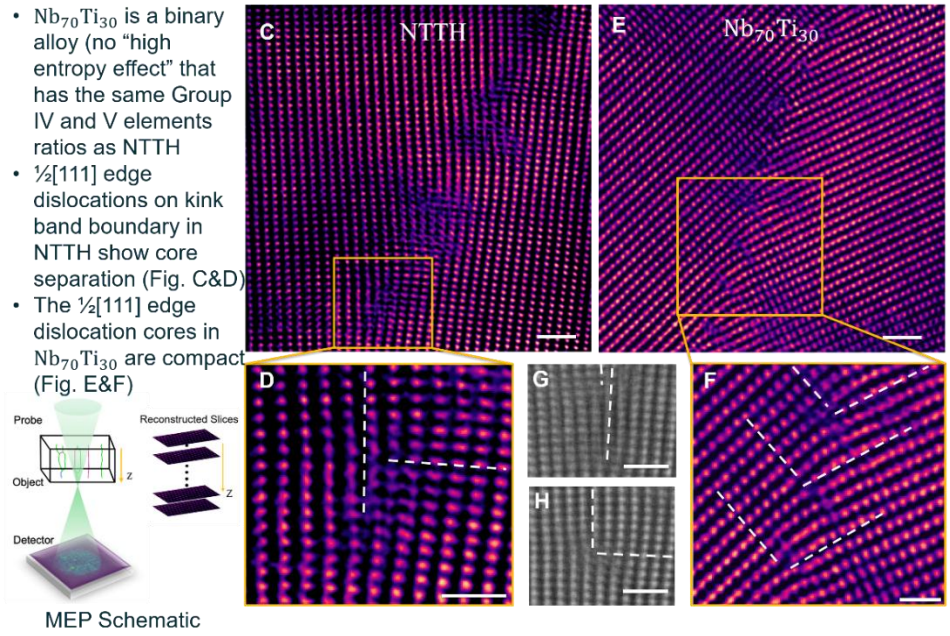

Fig. 2 MEP=Multi-slice electron ptychography shows reconstructed images of kink band boundaries (scale bars are 1 nm) in C NbTaTiNf showing dislocation core separation, that is not seen in E a $Nb_{70}Ti_{30}$ binary alloy.

As there is not that much known about kink formation in these alloys, we are currently examining the nature of the kink structures using advanced transmission electron microscopy techniques, specifically multislice electron ptychography (MEP) and parallel-beam 4D-STEM, which have provided new perspectives on kink-band formation (**Fig. 2**). Dislocations in the kink boundaries are initially of edge character. In the NbTaTiNf RHEA, they are found to display distinct core separations and are curvy in three dimensions, although this appears to be an effect of their multi-element character. Dislocations in a group IV element binary alloy, $Nb_{70}Ti_{30}$, with similar electronic characteristics, remain straight with far fewer jogs and little core separation compared with NbTaTiNf. Atomistic simulations agree with these experimental results; however, the precise role of dislocation core separation in the RHEA is not yet known, although it would presumably affect dislocation motion and possibly increase alloy strength.

The other major issue we will study is that adding Group IV elements to these RHEAs, despite solving the tensile ductility problem, tends to decrease strength somewhat compared to traditional but highly brittle RHEAs such as NbTaMoW. A conventional way to increase strength in single-phase refractory alloys has been to add interstitial or substitutional elements, which are known to work but often at the expense of ductility.

To guide our approach, we have developed machine-learning (AI/ML) atomistic potentials for these alloys and are initially performing Monte Carlo simulations of interstitial oxygen additions to alloys such as NbTaTiNf, as early studies[8] have suggested that this could increase both strength and ductility. Increases in ductility may be related to increased strain hardening, but local chemical order again may play a pertinent role here as Group IV elements tend to cluster with other elements. This leads to atomistic clustering of the O interstitials, with a direct relationship with the degree of local order, and thus to enhanced strength due to dislocation pinning. Naturally, oxygen may lead to other problems which may not be beneficial, and so that we intend to examine this by experiment and characterization.

With respect to the *bcc* RHEAs, which currently display ultrahigh strength at very high temperatures but are highly compromised by negligible tensile ductility, we believe that we have a solution for the ductility (or DBTT) issue but still need to fully explore the strength issue. If successful, we believe this could be a *game changer* for the development of a superior class of refractory metallic materials for applications in ultrahigh-temperature extreme environments. Nevertheless, our overall plan remains a focus on developing capabilities to model, characterize, and advance fundamental understanding of the origins of the unique properties of compositionally and structurally complex "high-entropy" materials.

References

1. D. Liu, Q. Yu, S. Kabra, M. Jiang, P. Forna-Kreutzer, R. Zhang, M. Payne, F. Walsh, B. Gludovatz, M. Asta, A. M. Minor, E. P. George, R. O. Ritchie, *Exceptional fracture toughness of CrCoNi-based medium- and high-entropy alloys at 20 kelvin*, Science, **378** (6623), 978 (2022).
2. P. Kumar, X. Gou, D. H. Cook, M. I. Payne, N. J. Morrison, W. Wang, M. Zhang, M. Asta, A. M. Minor, R. Cao, Yi Li, R. O. Ritchie, *Degradation of the mechanical properties of NbMoTaW refractory high-entropy alloy in tension*, Acta Materialia, **279**, 120279 (2024).
3. P. P. P. O. Borges, R. O. Ritchie, M. Asta, *Electronic descriptors for dislocation deformation behavior and intrinsic ductility in bcc high-entropy alloys*, Science Advances **10** (38), eadp7670 (2024).
4. D. H. Cook, P. Kumar, M. I. Payne, C. H. Belcher, P.P.P.O. Borges, W. Q. Wang, F. Walsh, Z. Li, A. Devaraj, M. Zhang, M. Asta, A. M. Minor, E. J. Lavernia, D. Apelian, R. O. Ritchie, *Kink bands promote exceptional fracture resistance in a NbTaTiHf refractory medium-entropy alloy*, Science, **384** (6692), 178 (2024),
5. D. H. Cook, X. Chen, M. O'Leary, S. Rao, W. Wang, C. H. Belcher, M. Payne, P.P.P.O. Borges, T. L. Lee, A. Devaraj, M. Asta, E. J. Lavernia, D. Apelian, A. M. Minor, D. Liu, P. Kumar, R. O. Ritchie, *Competing mechanisms ductilize bcc binary and medium-entropy alloys at 20 K*, Nature, in press (2026).
6. W. Wang, A. A. Abu-Odeh, D. H. Cook, R. O. Ritchie, M. Asta, S. Rao, "A theoretical study of solid solution strengthening in the refractory medium-entropy alloy, $Nb_{45}Ta_{25}Ti_{15}Hf_{15}$", Materials & Design, **261**, 115368 (2026).
7. P. P. P. O. Borges, R. O. Ritchie, M. Asta, *Effects of interstitial oxygen on ω transformations and twin formation in bcc NbTaTiHf high-entropy alloy from First-Principles*", Computational Materials Science, **266**, 114569 (2026).
8. Z.F. Lei, X. Liu, Y. Wu, H. Wang, *et al*., "*Enhanced strength and ductility in a high-entropy alloy via ordered oxygen complexes*", Nature, **563**, 546–550 (2018).

Publications

1. P. Kumar, S. J. Kim, Q. Yu, J. Ell, M. Zhang. Y. Yang, J. Young Kim, H.-K. Park, A.M. Minor, E. S. Park, R.O. Ritchie, "*Compressive vs. tensile yield and fracture toughness behavior of a body-centered cubic refractory high-entropy superalloy $Al_{0.5}Nb_{1.25}Ta_{1.25}TiZr$ at temperatures from ambient to 1200*℃", Acta Materialia, **245**, 118620 (2023).

2. F. Walsh, A. Abu-Odeh, M. Asta, "Reconsidering short-range order in 3D complex concentrated alloys," MRS Bulletin **48**, 753-761 (2023).

3. P. P. P. O. Borges, R. O. Ritchie, M. Asta, *"Electronic descriptors for dislocation deformation behavior and intrinsic ductility in bcc high-entropy alloys"*, Science Advances **10** (38), eadp7670 (2024).

4. P. Kumar, S. Huang, D. H. Cook, K. Chen, U. Ramamurty, X. Tan, R. O. Ritchie, *"A strong fracture-resistant high-entropy alloy with nano-bridged honeycomb microstructure intrinsically toughened by 3D-printing"*, Nature Communications **15** (1), 841 (2024).

5. P. P. P. O. Borges, R. O. Ritchie, M. Asta, *"Chemical trends favoring interstitial cluster formation in bcc high-entropy alloys from first-principles calculations"*, Acta Materialia **294**, 121091 (2025).

6. P. Kumar, D. H. Cook, W. Wang, M. Payne, P. P. P. O. Borges, A. M. Minor, M. Asta, R. O. Ritchie, *"Fracture behavior of high-entropy alloys: Resistance to fracture from strain hardening and softening"*, Matter **8** (4), 102042 (2025).

7. P. Kumar, X. Gou, D. H. Cook, S. I. Rao, W. Wang, M. Asta, R. O. Ritchie, M. Zhang, *"Rationalization of the tensile creep behavior of the $Nb_{45}Ta_{25}Ti_{15}Hf_{15}$ bcc refractory complex concentrated alloy using Rao-Suzuki screw dislocation glide model"*, Scripta Materialia 2**65**, 116752 (2025).

8. P. P. P. O. Borges, R. O. Ritchie, M. Asta, *"Tunable energy landscape of screw dislocation cores by compositional fluctuations in bcc high-entropy alloys from first-principles calculations"*, Physical Review Materials **9** (9), 093602 (2025).

9 W. Wang, P. Kumar, D. H. Cook, F. Walsh, B. Zhang, P.P.P.O. Borges, D. Farkas, R. O. Ritchie, M. Asta, *"Ductility Mechanisms in Complex Concentrated Refractory Alloys from Atomistic Fracture Simulations",* npj Computational Materials **11**, 330 (2025).

10. W. Wang, A. A. Abu-Odeh, D. H. Cook, R. O. Ritchie, M. Asta, S. Rao, *"A Theoretical Study of Solid Solution Strengthening in the Refractory Medium Entropy Alloy, Nb45Ta25Ti15Hf15"*, Materials & Design*,* **261**, 115368 (2026).

11. P. P. P. O. Borges, R. O. Ritchie, M. Asta, "*Chemical Complexity and Local Order Suppress Cottrell Atmosphere Formation in BCC NbTaTiHfZr High-Entropy Allo*y", Acta Materialia, **308**, 122024 (2026).

12. S. I. Rao, W. Wang, D. H. Cook, P. Kumar, M. Asta, R. O. Ritchie, "*A Simple Rice-Ashby Ductile-Brittle Transition Temperature (DBTT) Model Based on Dislocation Mobility for Body-Centered Cubic Complex Concentrated Alloys*", Materials & Design, **265**, 115835 (2026),

14. W. Wang, D. H. Cook, X. Chen, P. Kumar, A. M. Minor, S. I. Rao, M. Asta, R. O. Ritchie, D. Farkas, *"Extended Rice–Thomson Analysis and Atomistic Simulations Revealing Grain Boundary Effects on Fracture in NbMoTaW and Nb45Ta25Ti15Hf15 Refractory Complex Concentrated Alloys",* Proceedings of the National Academy of Sciences (PNAS), **123** (15), e2536219123 (2026).

15 P. P. P. O. Borges, R. O. Ritchie, M. Asta, "*Effects of Interstitial Oxygen on ω Transformations and Twin Formation in bcc NbTaTiHf High-Entropy Alloy from First-Principles*", Computational Materials Science, **266**, 114569 (2026).

16. D. H. Cook, X. Chen, M. O'Leary, S. Rao, W. Wang, C. H. Belcher, M. Payne, P.P.P.O. Borges, T. L. Lee, A. Devaraj, M. Asta, E. J. Lavernia, D. Apelian, A. M. Minor, D. Liu, P. Kumar, R. O. Ritchie, "*Competing mechanisms ductilize bcc binary and medium-entropy alloys at 20 K*", Nature, in press (2026).

Structural Short-Range Order and the Damage Tolerance of Amorphous Grain Boundary Complexions

Timothy J. Rupert - Johns Hopkins University

Keywords: complexions, grain boundaries, nanocrystalline, interfacial engineering

Research Scope

Grain boundaries often act as failure nucleation sites during plastic deformation. This research aims to understand how amorphous grain boundary complexions can be used to toughen these critical weak points, and then subsequently engineer these complexions to further improve damage tolerance. Our primary focus is on mechanical damage due to dislocation-based plasticity, which is relevant for a wide range of high-strength engineering alloys. The effect of complexion thickness on damage tolerance was studied, followed by the investigation of structural short-range order (SSRO) as a key descriptor of internal structure of amorphous grain boundary complexions.

Recent Progress

The description of our progress here is organized based on our efforts to test two core mechanistic hypotheses: (1) Thicker amorphous complexions will be more damage tolerant. (2) SSRO patterning will influence resistance to damage nucleation and growth. Within each of these areas, we sought to uncover new structure-property relationships while also identifying pathways for the engineering of amorphous complexion structure for improved performance.

Thickness of Amorphous Complexions

Complexion thickness was varied in nanocrystalline Cu-Zr samples by annealing at a temperature where amorphous complexions form and then creating a quenching/cooling gradient by placement on a heat sink, with subsequent samples taken from either near the contact location (fast-quenched) or far away (slow-quenched). The fast-quenched region exhibited thicker complexions (t_{mean} = 3.24 nm) while the region that was slow-quenched had significantly thinner complexions (t_{mean} = 2 nm). Mechanical behavior was measured with microcompression experiments, with a large number ($N > 50$) of annular milled pillars used to rapidly study larger deformations to identify failure modes and then perfect lathe milled pillars were used to study early stages of plasticity. The sample with thinner complexions was more likely to experience non-uniform plastic deformation in the form of localized plastic flow or shear banding. In contrast, the sample with thicker complexions displayed more homogeneous plasticity and higher damage tolerance. **Figure 1** shows a set of representative annular pillars from each sample set, showing that plastic localization is reduced as complexion thickness increases. Specifically, the sample with thinner complexions experienced localized deformation 74% of the time compared to the sample with thicker complexions that experienced localized deformation only 36% of the time. Three decades of strain rates were probed, with no significant effect observed, suggesting that these behaviors are tied only to the boundary state. Perfect lathed pillars were also tested from these sample sets, with

the degree of plastic asymmetry used to quantify the localization of plasticity. Early deformation stages probed in lathed pillars showed that the sample with thinner complexions had an average plastic asymmetry that was more than 2× larger than the thicker complexion sample. Our earlier computational/theoretical work suggested that this is related to the ability to dissipate the incoming plastic strain as a dislocation is absorbed, with more dislocations absorbed before crack nucleation.

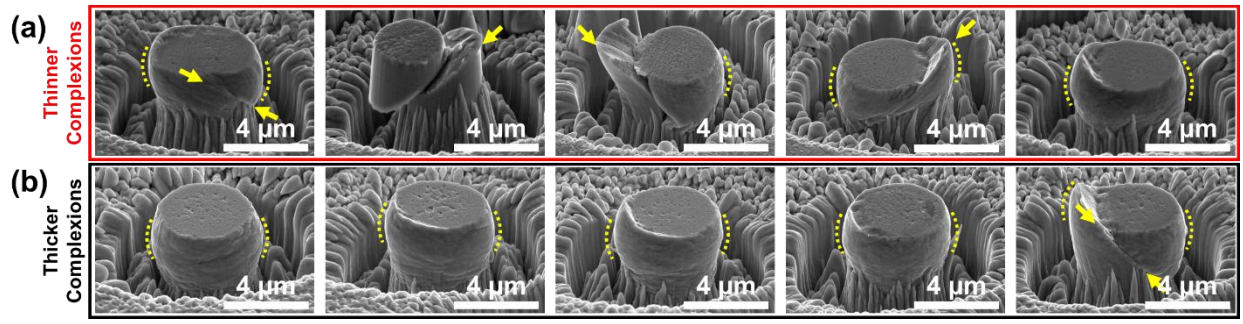

Figure 1. Heavily deformed annular-milled pillars with (a) thinner and (b) thicker complexions. Yellow arrows highlight where localized plastic deformation occurred in the form of shear banding and yellow dashed lines outline the barreling associated with stable plastic deformation.

Binary Al-rich nanocrystalline alloys with different mixing enthalpies, segregation enthalpies, and atomic size mismatches were studied to understand how alloy selection influences complexion formation. Samples were either quenched or slow cooled after hot pressing to give two extreme cooling rates. We found that Al-Y formed the most stable and thick complexions, followed by Al-Ni, and then Al-Mg. Our results confirmed that more rapid cooling gives thicker complexions and were interpreted in terms of the time-temperature-transformation (TTT) diagram shown in **Figure 2(a)**, where one would like to avoid transitioning back to the ordered boundary states preferred at low temperatures. A collaboration was initiated with Dan Gianola at UCSB to study additional alloys at more controlled cooling rates and under multiple heating/cooling cycles with ultrafast nanocalorimetry. **Figure 2(b)** shows a series of such experiments, where sharp exothermic peaks during cooling signal an ordering transition at the grain boundary while broad humps mean the interfaces have retained their amorphous structure. We were able to identify key signatures of both premelting and ordering transitions, find critical cooling rates for different alloys, and show that amorphous complexions can be recovered through a series of 1000 annealing runs where they went from ordered-to-disordered each time.

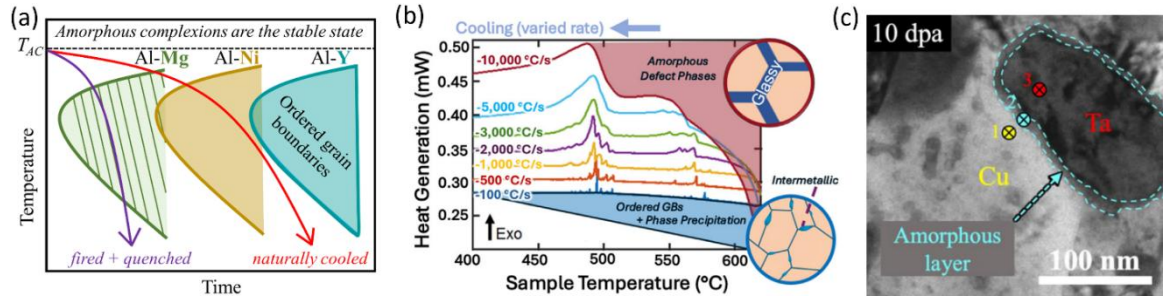

Figure 2. Amorphous complexion transitions can be induced due to variations in (a) composition, (b) thermal history, or (c) irradiation damage.

Other driving forces for grain boundary amorphization were also probed, such as ion irradiation in collaboration with Janelle Wharry at UIUC. **Figure 2(c)** shows an example of amorphization at an interphase boundary in Cu-Ta that was driven by irradiation. Interestingly, this alloy cannot achieve amorphous complexions from a thermal treatment pathway, demonstrating that new driving forces can induce unexpected complexion transitions. Finally, we investigated mechanical behavior at elevated temperatures using in situ micropillar compression experiments. These experiments suggested that boundary amorphization may occur at lower temperatures (~150-200 °C) than previously thought. This is an example of using a direct behavior (plasticity mode) to identify the transition temperature, which may allow for more accurate measurements.

Structural Short-Range Order (SSRO) of Amorphous Complexions

The dissipation of plastic strain and the onset of grain boundary failure was found to be very sensitive to SSRO. Both overall SSRO levels and the asymmetry of SSRO at opposite amorphous-crystalline transition regions (ACTRs) are hypothesized to be critical. Recently we have been using multi-element doping to tune SSRO and SSRO asymmetry in a controlled manner. **Figure 3(a)** shows local transmission electron microscopy (TEM) measurements of complexion composition in Cu-Zr and Cu-Zr-Nb, where Zr content is highest in the complexion interior while Nb content is highest in the ACTRs. This chemical partitioning is critical, as it opens the door for the tunable engineering of SSRO within complexions. However, while we could show that SSRO was different in the complexion interior and the ACTR with 4D-STEM, we could not quantify the SSRO levels due to difficulties with overlapping grains and curved grain boundaries. Therefore, we had to perform complementary modeling, which also required the development of a new machine-learned interatomic potential (ML-IAP) capable of simulating the Cu-Zr-Nb system. **Figure 3(b)** shows important configurations from the ternary compositional and structural space that were used to fit the potential, as well as Monte Carlo/molecular dynamics simulations of bicrystal samples. In this case, an increased level of overall disorder and increased ACTR asymmetry was observed when moving from the binary to the ternary alloy.

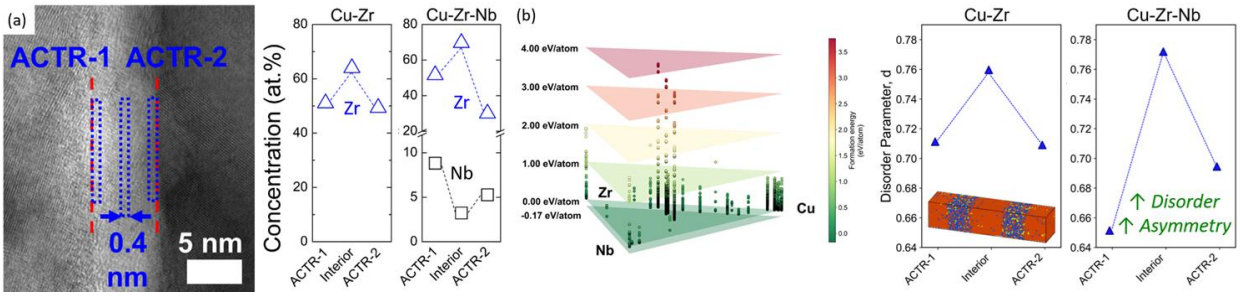

Figure 3. (a) TEM investigation of amorphous complexions in nanocrystalline Cu-rich alloys shows that dopant partitioning occurs to different regions of the complexion. (b) Complementary simulations using a newly developed ML-IAP suggest that this partitioning can change overall disorder level and asymmetry between ACTRs.

To study SSRO experimentally, we have developed new 2D planar complexion specimens to enable the study of internal complexion structure by providing alignment of the features of interest with the electron beam for detailed characterization. The starting microstructure is two nanocrystalline layers, with a doped region in between whose composition can be directly

controlled during sputtering, with a Cu-Zr example shown in **Figure 4(a)**. Following deposition, high temperature heat treatments evolve the material from the as-deposited configuration to a local equilibrium state containing an interface along a planar orientation in the middle of the sample that is confined by larger grains on either side, creating a model row of bicrystal grain boundaries where complexions can form. A 2D planar sample that was annealed and quenched is shown in **Figure 4(b)**, where one can see an example of an ordered grain boundary (top right) as well as an amorphous complexion with thickness of 2.5 nm (bottom right). This demonstrates the full relaxation of the sample, where the different grain boundary crystallography is responsible for the different complexion types here.

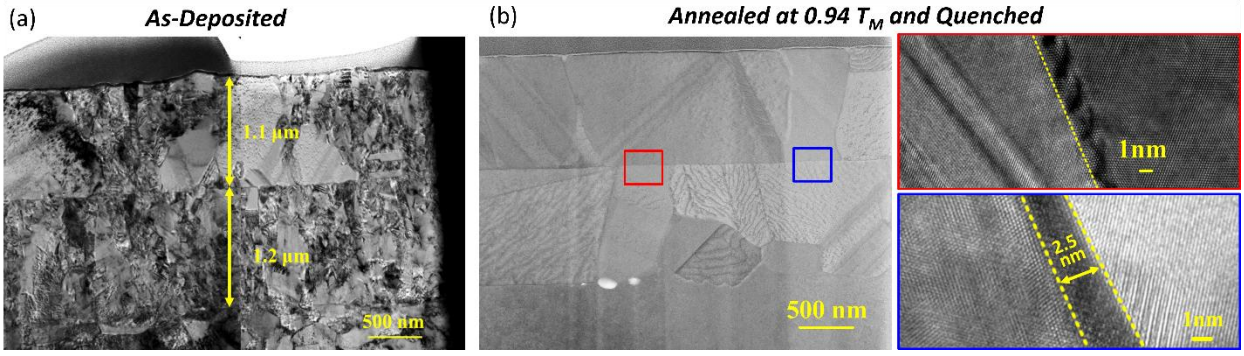

Figure 4. (a) An as-deposited 2D planar sample in Cu-Zr showing two layers of nanocrystalline grains. (b) High temperature relaxation followed by quenching allows for equilibration of the 2D sample. The Cu layers coarsen until they contain relatively large grains while the interface relaxes into the preferred complexion state. Both ordered and amorphous complexions are found, demonstrating that local equilibrium is reached.

Finally, while nanobeam diffraction patterns provide structure signatures, there was no way to extract a quantitative measure of SSRO. Therefore, we built a machine learning (ML)-based analysis tool that can obtain SSRO metrics from these diffraction patterns. A ResNet-18 model was trained on simulated diffraction patterns taken from different locations within simulated metallic glasses and amorphous grain boundary complexions in Cu-Zr, with the model low errors and high transferability when being tested on published experimental patterns. This opens the door for experimental characterization of SSRO in the upcoming period.

Future Plans

The ML-IAP has been extended so that Cu-Zr, Cu-Zr-Nb, Cu-Zr-Hf, and Cu-Zr-Ti can all be simulated, allowing us to investigate how dopant selection and concentration influences SSRO patterning and subsequent damage tolerance during dislocation absorption tests. These same simulations can also be used to improve the ML analysis tool for nanobeam diffraction patterns, allowing us to quantify SSRO experimentally. All four alloys are being created in 2D planar sample form and annealed/quenched using a new conductive heating rig which allows for huge variations in heating and cooling rates. We will work to characterize SSRO distributions in all four alloy systems using 4D-STEM, followed by bending experiments to quantify the overall resistance to mechanical damage.

Publications (August 2024 - August 2026)

PUBLISHED:

1. E.C. Hessong, T. Lei, B. Fields, R.P. Thiraux, B.L. Boyce, T.J. Rupert. *Amorphous complexion-aided sintering enables scalable processing of bulk nanocrystalline Cu-Zr with high strength and compressive plasticity*, Materialia, **43**, 102510 (2025).
2. T. Lei, E.C. Hessong, B. Fields, R.P. Thiraux, D.S. Gianola, T.J. Rupert. *Bulk nanocrystalline Al-Mg-Y alloys with amorphous grain boundary complexions display high strength and compressive plasticity*, Journal of Materials Science, **60**, 18486 (2025).
3. W.S. Cunningham, T. Lei, H.C. Howard, T.J. Rupert, D.S. Gianola. *Kinetics of Amorphous Defect Phases Measured Through Ultrafast Nanocalorimetry*, Acta Materialia, **304**, 121764 (2026).
4. E.C. Hessong, Z. Zhang, T. Lei, M. Xu, T. Aoki, T.J. Rupert. *Modulation of structural short-range order due to chemical patterning in multi-component amorphous interfacial complexions*, Acta Materialia, **310**, 122108 (2026).
5. S. Mondal, P.V. Patki, W. Chen, A. Chatterjee, K.A. Darling, J.R. Trelewicz, T.J. Rupert, J.P. Wharry. *Beyond Ballistic Mixing: New Mechanisms for Irradiation Resilience of Immiscible Interfaces*, Acta Materialia, **314**, 122348 (2026).
6. A. Hunter, V. Agrawal, I.J. Beyerlein, S. Ghosh, C. Oskay, B. Gu, Y. Chen, S.C. Foster, J.W. Wilkerson, X. Sun, T.J. Rupert, C. Chen, A.M. Dongare, D.N. Blaschke, M.P. Echlin, T.M. Pollock, B. Katzer, K. Schulz, Z. Croft, M. Chlupsa, A.J. Shahani, K. Thornton, D.T. Fullwood, E.R. Homer, E.V. White. *Roadmap on Novel Computational Approaches for Bridging Length and Time scales: Addressing Challenges in Modeling Processes, Characterization, and Performance of Metals and Alloys*, Modelling and Simulation in Materials Science and Engineering, In Press (2026).
7. E.C. Hessong, N.M. della Ventura, T. Niu, D.S. Gianola, H. Kim, N. Li, S. Fensin, B.L. Boyce, T.J. Rupert. *Thicker amorphous grain boundary complexions reduce plastic strain localization in nanocrystalline Cu-Zr*, Scripta Materialia, **283**, 117437 (2026).
8. J. Wu, T.J. Rupert. *Extraction of a structural short-range order descriptor from nanobeam electron diffraction patterns using a transfer learning approach*, Computational Materials Science, **272**, 114902 (2026).

SUBMITTED:

1. B. Xing, B. Xie, W. Zou, E. Lang, E. Boltynjuk, H. Chen, M.P. Short, G. Tynan, T.J. Rupert, J.R. Trelewicz, H. Hahn, B.P. Uberuaga, K. Hattar, P. Cao. *Fragmenting Diffusion Pathways Confer Extraordinary Radiation Resistance in Refractory Multicomponent Alloys*, Submitted.

Ion-irradiation-assisted strain relaxation in epitaxial high entropy oxide films

Ritesh Sachan

School of Mechanical and Aerospace Engineering, Oklahoma State University, Stillwater, Oklahoma 74078, United States

Keywords: High entropy oxides, epitaxial film growth, perovskite, machine learning, atomic-resolution electron microscopy

Research Scope

The effects of ion irradiation on ceramics, particularly metal oxides, have been extensively investigated due to their significant impact on the development of radiation-tolerant and new functional materials. However, the constant need to search for new materials that can generate new properties or significantly improve existing ones has motivated a shift in attention from traditional metal oxides towards new candidates. The recent emergence of high-entropy oxides (HEOs), which consist of multiple cations (typically five or more) in an ordered lattice site, has offered one such alternative due to their highly modified physical properties compared to conventional oxides. These HEOs align well with the scope of this research shift, where ion irradiation is expected to either facilitate the order-disorder transformation leading to the formation of metastable phases or demonstrate high radiation tolerance. However, the understanding of ion-irradiation effects in HEOs is highly limited to date and insufficient to draw any scientific trends. While many parallels are drawn between high entropy alloys (HEAs) and HEOs to understand the irradiation response, HEOs demonstrate more complex disorderness at the levels of structural, charge, orbital and spin in comparison to primarily structural disorder in HEAs and thus present the grand challenge demanding more quantitative investigations.

This research scopes to uncover the role of elemental size, charge state, and composition of the constituent elements in advancing the atomic-level understanding of defect formation and phase transformation in HEOs due to nuclear and elastic interactions during ion irradiation. The scientific outcomes of this project will advance the fundamental understanding of the irradiation response of HEOs, particularly in the nuclear energy-loss regime. The study will investigate the role of ionic radii, charge state, and composition via elevated entropy-led multielement mixing in HEOs in relation to defect formation and phase transformation under heavy ion irradiation. To accomplish the goals of this project, we aim to develop a synergistic approach by performing irradiation on HEO thin films, with investigations using data-driven atomic-resolution transmission electron microscopy (TEM). Using the HEO thin film approach, the understanding of radiation response in several possible combinations of material libraries will be accelerated covering a large compositional space. Furthermore, the integration of data-driven TEM investigations at the atomic scale will provide highly quantitative analysis of atomic arrangement, local strain, atomic

defects/vacancies, chemical/electronic disorder, and phase transformation, which can be used as descriptors to measure radiation tolerance in HEOs. Overall, the proposed synergistic plan will build fundamental knowledge, expertise, and infrastructure to accelerate high-impact discoveries on the radiation effects in high-entropy ceramics.

Research Progress

1. Swift heavy ion track morphology in Sr-Based High Entropy Perovskites

To understand the irradiation effects in HEOs, we studied the atomic rearrangement and phase transformation occurred due to single ion impact of swift heavy ion irradiation in this work [1]. Here, we investigated atomic-scale insights into the irradiation-induced nanoscale phase transformations in the perovskite high-entropy oxide $Sr(Zr_{0.2}Sn_{0.2}Ti_{0.2}Hf_{0.2}Nb_{0.2})O_3$ [$Sr(HE)O_3$] subjected to 774 MeV swift Xe heavy-ion irradiation, where energy deposition is dominated by inelastic ion–lattice interactions. Although swift heavy ions typically generate nanoscale disordered channels, commonly referred to as ion tracks, $Sr(HE)O_3$ exhibits discontinuous and partially recrystallized ion tracks, revealing a distinctly different damage response.

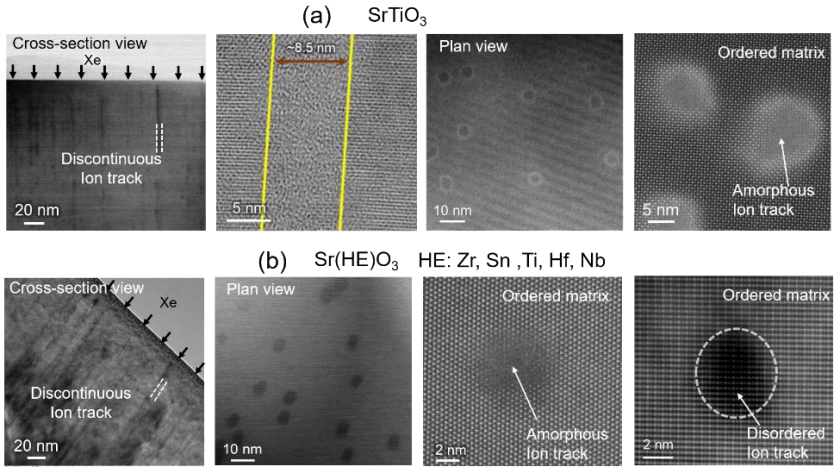

Fig. 1. Cross-sectional and plan-view images of formed ion tracks in (a) $SrTiO_3$ and (b) $Sr(HE)O_3$. Plan-view images of tracks in $SrTiO_3$ show an amorphous core with a disordered (brighter contrast) shell in the ordered matrix. On the contrary, $Sr(HE)O_3$ consists of ion tracks with two different morphologies: (i) completely amorphous and (ii) disordered crystalline ion tracks as shown in (b) (right two images).

Compared with $SrTiO_3$ irradiated under equivalent energy-loss conditions, $Sr(HE)O_3$ develops substantially smaller ion tracks with a markedly different crystalline–amorphous interfacial structure (Fig.1). In particular, lattice distortion at the track–matrix interface in $Sr(HE)O_3$ is confined to approximately 2–3 monolayers, in contrast to the more extended disordered region observed in $SrTiO_3$. In situ atomic-resolution electron microscopy further reveals that the amorphous/disordered regions within $Sr(HE)O_3$ tracks remain highly stable under electron irradiation, whereas the corresponding tracks in $SrTiO_3$ readily recrystallize [2]. This enhanced stability is attributed to the structural and chemical complexity introduced by multiple B-site cations, which restricts defect migration and suppresses templated recrystallization induced by electronic excitation and localized heating. Collectively, these findings demonstrate that high-entropy-induced disorder fundamentally modifies irradiation-damage formation, interfacial structure, and subsequent defect evolution, providing new insights into the design of

compositionally complex oxides for enhanced structural stability under extreme irradiation environments.

2. Ion-irradiation-assisted strain relaxation in epitaxial high entropy oxide films

This work focuses on understanding ion–lattice interactions in single-crystalline $Ba(Zr_{0.2}Sn_{0.2}Ti_{0.2}Hf_{0.2}Nb_{0.2})O_3$ [Ba(HE)O_3] films epitaxially grown on $SrTiO_3$ (001). This heterostructure provides a unique platform for directly comparing the irradiation response of a compositionally complex high-entropy oxide with that of the conventional perovskite $SrTiO_3$. More broadly, ion-irradiation studies of HEO thin films provide an ideal materials platform for elucidating how elemental complexity, cation charge states, composition, and crystal structure govern irradiation-induced defect formation and evolution. Epitaxial thin films introduce an additional dimension through structural and interfacial strain, enabling investigation of the coupling between irradiation-induced defects and pre-existing strain fields and potentially providing pathways toward metastable structural states and modified properties.

Following irradiation with 1 MeV Au^{2+} ions at a fluence of 1.2×10^{13} ions cm^{-2}, X-ray diffraction reveals measurable changes in the lattice parameters while the crystalline epitaxial structure is preserved. Preliminary atomic-scale analysis further indicates reduced structural disorder within the Ba(HE)O_3 film accompanied by increased disorder in the underlying $SrTiO_3$ substrate, suggesting an irradiation-induced redistribution of strain across the heterointerface. Although irradiation produces structural changes in both the film and substrate, Ba(HE)O_3 exhibits significantly lower defect accumulation and, remarkably, signatures of improved crystalline ordering. Atomic-resolution STEM imaging combined with machine-learning-assisted analysis further supports this observation, revealing a reduced spread in the local interatomic spacing of Ba(HE)O_3 after irradiation. In addition, substantial annealing and structural reorganization of defects are observed near the Ba(HE)O_3/$SrTiO_3$ interface.

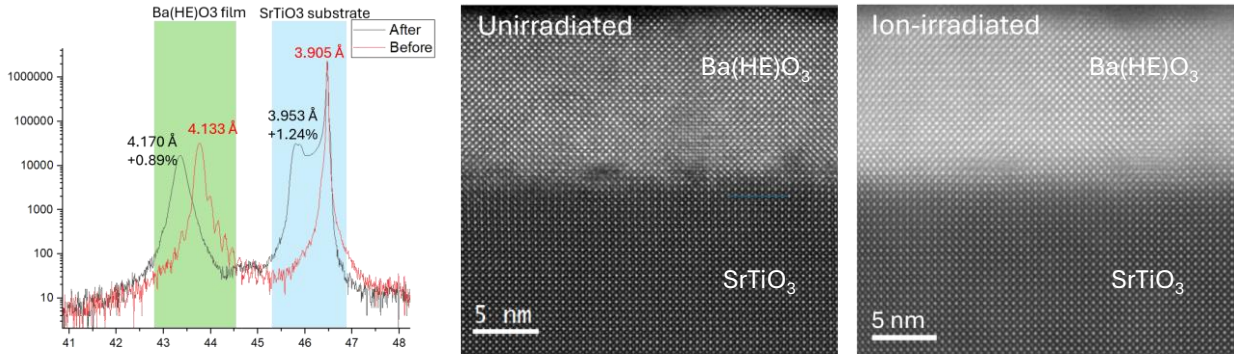

Fig. 2. XRD and HAADF images of unirradiated and irradiated Ba(HE)O_3 film and $SrTiO_3$ substrate.

We attribute this counterintuitive irradiation-assisted structural improvement to the coupled response of the film and substrate. Irradiation-induced disorder in $SrTiO_3$ produces lattice expansion, thereby modifying the lattice mismatch and strain state across the heterointerface, while

highly localized energy deposition within $Ba(HE)O_3$ may promote defect rearrangement and annealing without disrupting its crystalline framework. The chemically and structurally disordered high-entropy lattice may further influence defect mobility and accumulation, enabling a response distinct from that of the conventional $SrTiO_3$ perovskite. Collectively, these results suggest that energetic-ion irradiation can serve not only as a source of radiation damage but also as a nonequilibrium pathway for defect reorganization and strain redistribution in epitaxial high-entropy oxide heterostructures. This behavior opens opportunities to use controlled irradiation as a post-growth approach for manipulating interfacial strain, local structural disorder, and potentially the functional properties of compositionally complex oxide thin films.

Future Plans

In near future, we intend to systematically investigate the following key aspects of ion-irradiated HEOs, with a particular emphasis on perovskite structures:

1. Decouple film and substrate responses: Investigate $Ba(HE)O_3$ films with different thicknesses and epitaxial strain states to determine how irradiation-induced lattice expansion and disorder in the $SrTiO_3$ substrate influence strain redistribution and defect annealing within the HEO film and across the interface.
2. Compare high-entropy and conventional oxides: Perform identical irradiation experiments on HEO films and compositionally simpler perovskite reference systems to isolate the specific contribution of high-entropy chemical and structural disorder to radiation tolerance and defect recovery.
3. Probe the role of high-entropy disorder: Expand the compositional space from similar-to-dissimilar ionic radii and cation charge states, as well as from equiatomic to non-equiatomic compositions, to establish how chemical disorder and local lattice distortion govern irradiation-induced defect formation, migration, and recovery.

References

[1] A.K. Gupta, E. Zarkadoula, B.L. Musico, J.A. Hachtel, M.A. Roldan, V.R. Paduri, C. Harris, R. Subedi, M. Ziatdinov, S. V. Kalinin, C. Trautmann, V. Keppens, J. Liu, Y. Zhang, W.J. Weber, R. Sachan, Unveiling Swift Heavy Ion Track Morphology in Sr-Based High-Entropy Perovskites, ACS Nano 20 (2026) 6632–6643.
[2] A.K. Gupta, E. Zarkadoula, M. Ziatdinov, S. V. Kalinin, V.R. Paduri, J.A. Hachtel, Y. Zhang, C. Trautmann, W.J. Weber, R. Sachan, Nanoscale core-shell structure and recrystallization of swift heavy ion tracks in SrTiO3, Nanoscale 16 (2024) 14366–14377.

Publications

1. A.K. Gupta, E. Zarkadoula, B.L. Musico, J.A. Hachtel, M.A. Roldan, V.R. Paduri, C. Harris, R. Subedi, M. Ziatdinov, S. V. Kalinin, C. Trautmann, V. Keppens, J. Liu, Y. Zhang, W.J. Weber, R. Sachan, Unveiling Swift Heavy Ion Track Morphology in Sr-Based High-Entropy Perovskites, ACS Nano 20 (2026) 6632–6643.

Interplay of plasticity events, fracture, and local microstructure on 3D growth of small fatigue cracks

Michael D. Sangid, University of California, Berkeley

Keywords: Microstructurally small fatigue cracks, Fatigue, Microstructure, X-ray diffraction, Fracture

Research Scope

For microstructurally small fatigue cracks (MSFC), the length of the crack is comparable to the microstructural feature size, and the rate of crack progression is highly variable due to the crack's interaction with microstructural features and their complex micromechanical fields. Despite its importance to application, in which most components spend a significant portion of their life in the MSFC regime, there are no widely accepted models to capture this behavior due to a lack of understanding of the fundamental physics. Previous experimental observations have been limited to 2D observations of cracks (not accounting for the tortuous nature of the crack) or make incorrect assumptions of the stress state in the grains surrounding the crack tip. The predominant theories for MSFC describe the process as shear driven, confined to well-defined crystallographic slip systems, and the interaction with grain boundaries (GBs) is primarily governed by geometric relationships. Yet, recent 3D experiments have shown a significant and non-negligible portion of MSFC crack growth occurs on high index crystallographic planes that are unlikely to facilitate crystallographic slip, and crystallographic geometric relationships alone do not accurately predict the direction of crack growth. Based on advances in point-focus high energy x-ray diffraction microscopy (pf-HEDM) and micro-computed X-ray tomography (CT), during in situ loading, which are enabled by the recent upgrade to the Advanced Photon Source at Argonne National Lab, we can identify a 3D sub-granular map of the stress state (full tensor representation, to examine various stress metrics as well as stress gradients), crystallographic grain morphologies, intragranular orientations, as well as the crack topology, growth direction, and growth rates. The availability of these datasets provides a disruptive shift in our ability to uncover new scientific understanding of MSFC, both in terms of mechanisms and rates.

Experiments involve cyclic loading of Ni201 polycrystalline samples, performing CT to map the crack at distinct cycle counts at frequent cycle intervals, and conducting pf-HEDM around the crack tip periodically. The crack plane and growth direction will be correlated with the well-defined crystallographic planes and slip directions of the encompassing microstructure to determine the likelihood of slip-mediated mechanisms for crack advancement. Additionally, we will investigate the application of fracture mechanics approaches to the breakdown of slip mediated MSFC growth theories. Specifically, we will examine local MSFC progression and their effect on the surrounding segments of the crack, whether the dissimilar local directions and rates for various crack segments create an irregular crack front that promotes local fracture events to

connect these segments. The constraints around crack segments will be explored to determine if the transition between plasticity-dominated and fracture-dominated crack growth, as well as crack deflections within a grain or at a GB, are related to the acceleration or deceleration of the crack growth rate.

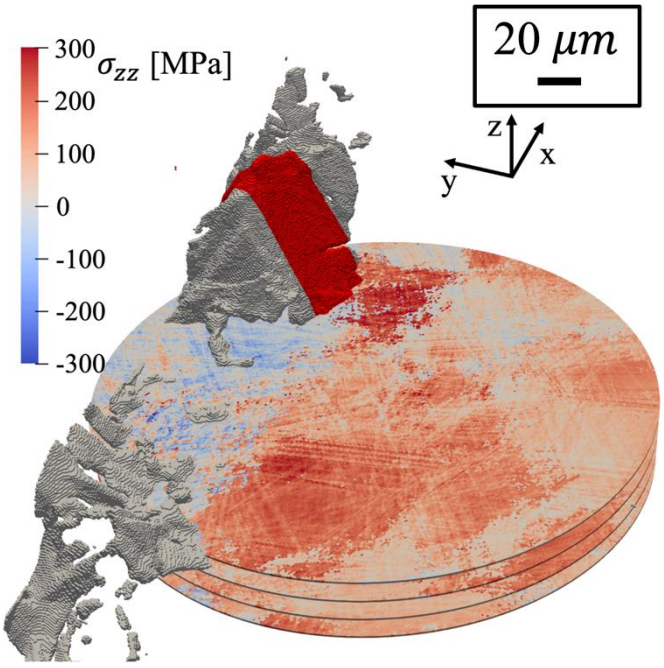

Fig. 1. 3D MSFC shown with stress field aligned the loading direction about a given 2D slice identified via pf-HEDM.

Using novel pf-HEDM characterization combined with CT data during in situ loading, we will uncover the 3D nature of the crack, underlying microstructure, and stress fields ahead of the crack tip, at unprecedented length-scale. We will be in a position to understand the mechanisms that drive MSFC, specifically the interconnectivity between crystallographic slip and fracture events. With this improved understanding, we are positioned to create new insights and new theories into the mechanisms that drive MSFC growth, including directions, deflection, branching, interactions with GBs, and most importantly the rate effects governing each of these events. Elucidating this MSFC behavior will have direct and significant impact on life determination of structural alloys that can either last longer or safely be exposed to higher temperatures, the potential exists for advances in energy efficiency, including gas turbine engines and nuclear applications. With these structure-property relationships, future components can be designed to exhibit longer lifetimes while not overdesigning to ensure reliability and energy efficiency.

Recent Progress

This program is just about to kick-off. Of note, from recent progress, initial reconstructions and registration of CT and pf-HEDM results are shown, in Fig. 1, from a recent beamtime.

Future Plans

The initial work will focus on correlations of the stress fields associated with distance away from the crack tip as well microstructure effects (in terms of grain orientation, grain interactions, and slip localization near grain boundaries) informed through comparison of pf-HEDM results to crystal plasticity modeling activities.

Crack-Tip Mechanisms Driving Environmental Degradation

D.K. Schreiber, A. Devaraj, K. Kruska, K.M. Rosso, M.L. Sushko, C. Wang

Keywords: corrosion, fracture, diffusion, grain boundaries, microscopy

Research Scope

Environmental degradation and associated stress corrosion cracking (SCC) are persistent materials science challenges that affect energy systems that operate in high-temperature, hostile environments. Research has revealed many processes that underpin material degradation, including elemental selectivity for reactions, interface-dominated transport kinetics, and vacancy-driven acceleration of mass transport. Despite these advances, a comprehensive understanding of the atomic-scale crack-tip mechanisms that underpin environmental degradation remains elusive. For example, contradictory behaviors have been observed for degradation in gaseous and aqueous environments under nominally identical oxidizing potentials, and SCC responses can diverge significantly from the kinetics of visible degradation processes that precede mechanical cracking. It is, therefore, the long-term vision of this program to both elucidate the mechanistic processes occurring at the atomic scale and build definitive connections to meso-to-macroscale cracking of materials under high-temperature, corrosive conditions. In this project, we focus on the roles of different corrosive media under similar electrochemical potentials, evolving alloy microstructures, and targeted alloy additions to affect these behaviors. To do so, we integrate a suite of in situ and ex situ microscopy techniques, multiscale mechanistic modeling, and macroscale mechanical testing under controlled environments to produce a comprehensive picture of the roles that environment, hydrogen insertion, applied stress, alloying additions, surfaces, interfaces, and microstructural defects have in the resulting behaviors. Through these studies we seek to advance our fundamental understanding of the atomic-scale crack tip processes driving micro-to-macroscale environmental degradation and SCC in current and future energy systems.

Recent Progress

Our current research has focused on understanding SCC behavior in aqueous and gaseous environments at moderately high-temperatures (~300-600 °C) where atomic transport and reactions are primarily limited to surfaces, near-surface interfaces, and grain boundaries (GBs). Using Ni-Cr as a primary model alloy system, we systematically alter the electrochemical potential of the corroding medium to favor the selective oxidation of Cr over Ni, which closely mimics the hydrogenated water environment of light water reactors, to understand how the selective oxidation process alters the local alloy GB structure and chemistry to promote SCC. Advanced characterization methods, including operando transmission electron microscopy (TEM) and

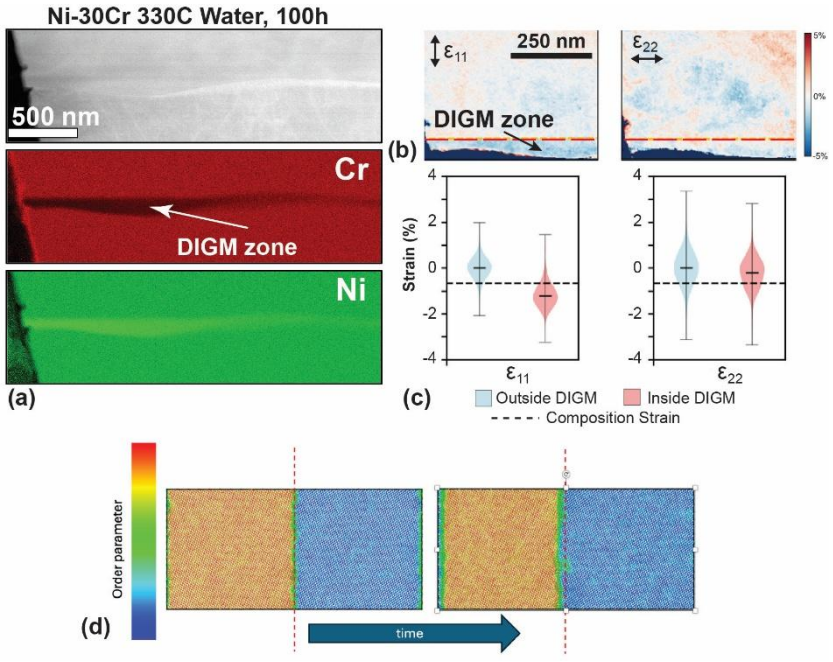

Fig. 1 – 4D STEM and MD reveal how DIGM alters local alloy structure during selective oxidation. (a) STEM-HAADF and STEM-EDS reveal local composition changes associated with selective depletion of Cr during surface corrosion and associated DIGM. (b-c) Corresponding 4D STEM strain measurements show anisotropic strain exceeding that of local composition measurements. (d) Complementary MD simulations of synthetically driven GB migration are further revealing how vacancies and solute species alter migration and local structural rearrangements during corrosion. [1]

isotope-sensitive atom probe tomography (APT), in combination with atomistic simulations (molecular dynamics [MD] and density functional theory [DFT]), are used to probe these local processes and reveal how alloy degradation leads to macroscale SCC responses.

New experimental and modeling capabilities are probing how selective oxidation and correlated diffusion induced grain boundary migration (DIGM) alter the local structure of GBs. Figure 1a presents a typical observation from a Ni-30Cr exposed to 330 °C hydrogenated water for 100 h. Selective oxidation leads to a Cr-rich surface oxide and concomitant Cr-depletion and DIGM in the alloy beneath, increasing its susceptibility to further corrosion and SCC. In Fig. 1b-c, 4D STEM measures local lattice strain within the compositionally altered DIGM zone. Consistent with work by Yang et al. on molten salt corrosion [2], we find strain exceeding that predicted from the composition changes resulting from Cr leaching into the oxide. However, our observations also reveal a surprising anisotropy in the local strain, with a greater compressive stress perpendicular to the direction of GB migration. To understand this behavior and its origins, we are pursuing MD simulations of GB migration under synthetic driving forces (Fig. 1d) that selectively include or exclude excess vacancies that emulate those generated by the selective oxidation at the alloy surface. Initial results have shown strong linkages between alloy solute composition, GB character, and the resulting migration behavior, suggesting the observed strain anisotropy is one part of a complex landscape of GB structural changes that have yet to be fully unveiled.

To unravel the effect of applied stress on these oxidation and corrosion processes, we have also used gaseous Rhines pack exposure cells with 4 point bend sample geometries [3]. In this scheme, illustrated in Figure 2, a single specimen can simultaneously test the effects of tensile and

compressive stress on selective oxidation, GB diffusion, and GB migration. A Ni/NiO buffer powder mixture is used to control the oxidation potential to be similar to that of the hydrogenated water used in Figure 1, while also removing complexities of aqueous dissolution during corrosion. These Rhines pack studies have shown that the applied stress state (up to 19% surface strain) has a limited impact on the resulting oxidation behavior of Ni-5Cr GBs. As shown by TEM micrographs in Fig. 2, similar oxide morphologies formed on the Ni-5Cr sample after 72 h exposure to the Rhines pack environment at 420 °C in both stress conditions: a thin protective surface oxide forms directly above the grain boundary with corresponding Cr depletion and DIGM in the underlying alloy GB. The primary difference observed from the applied stress was statistical in nature, with a higher percentage of GBs forming protective capping oxides under either tension or compression than in the unstressed condition. The greatest Cr depletion in the underlying GB was observed under compressive stress, suggesting that compression effectively promotes the outward diffusion of Cr to form the surface oxide layer. Ongoing studies are further looking into the effect of applied stress by using two-stage $^{16}O/^{18}O$ Rhines pack exposures to understand where oxidation is proceeding after initial formation of these protective oxide layers.

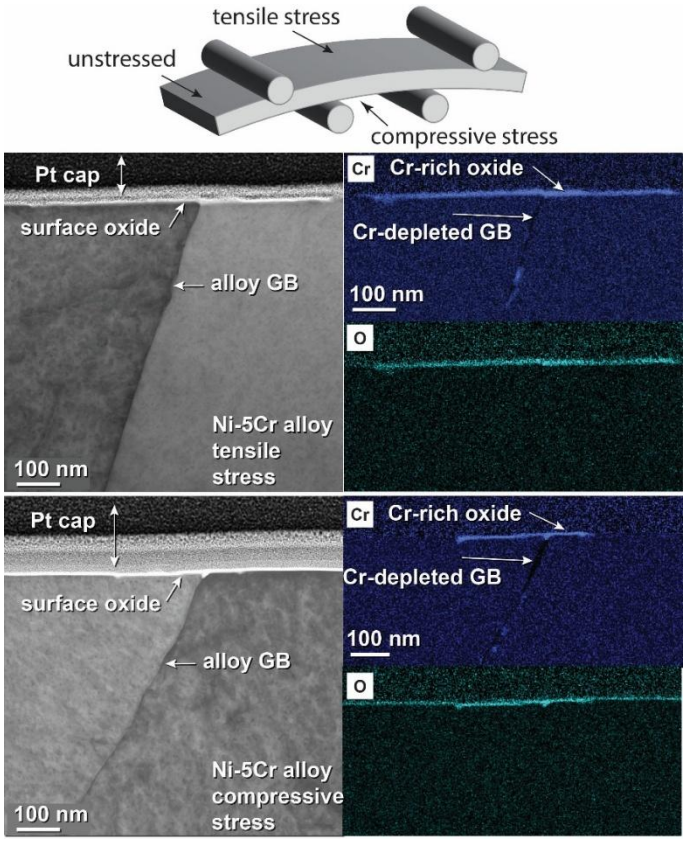

Fig. 2 – Tensile and compressive stress from 19% surface strain in a 4-point bend sample geometry promote surface passivation of Ni-5Cr in a 420 °C Rhines pack. Analytical TEM reveals GB Cr depletion and surface oxide passivation in both stress states, while unstressed regions of the sample showed a higher percentage of GBs without passivation, showing that applied stress universally promoted Cr diffusion and surface passivation. [3]

We have also recently completed long-term SCC testing for a series of Ni-xCr alloys (x = 5 – 30 at.%) using both compact tension (CT) and 4 point bend sample geometries in high temperature hydrogenated water. Subsequently, we commenced conversion of one autoclave system (Figure 3) to perform similar long-term SCC testing in high-pressure steam. Although the Rhines pack experiments described in Figure 2 have been useful in establishing fundamental aspects of selective oxidation, the new high-pressure steam SCC system affords new opportunities to directly probe how aqueous dissolution (present in water but largely absent from steam) impacts

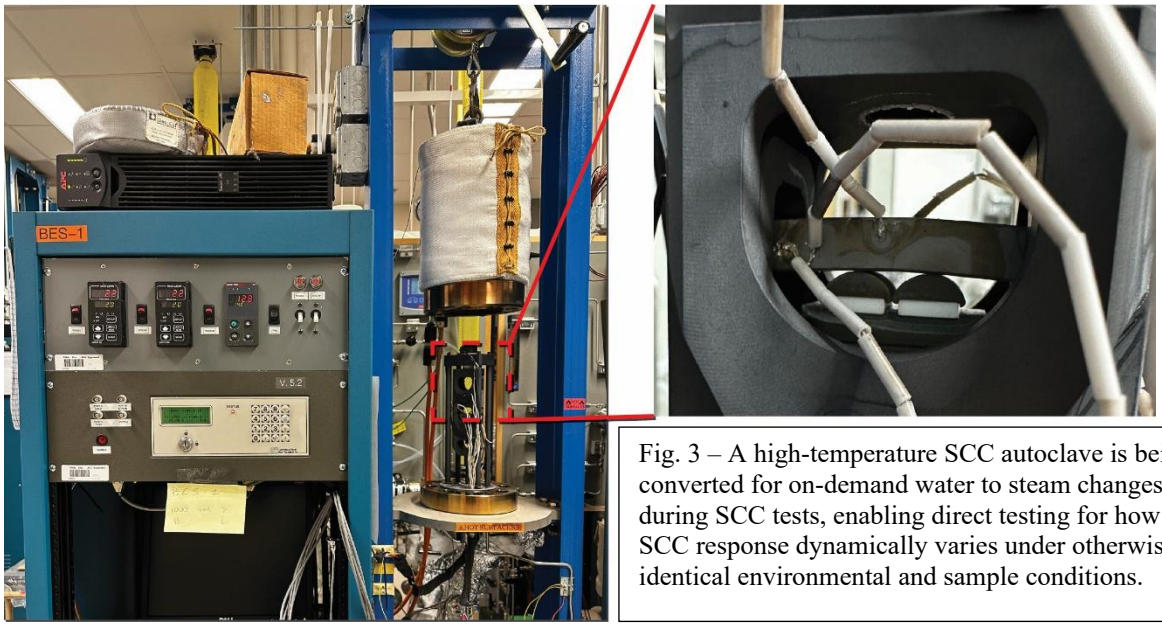

Fig. 3 – A high-temperature SCC autoclave is being converted for on-demand water to steam changes during SCC tests, enabling direct testing for how SCC response dynamically varies under otherwise identical environmental and sample conditions.

quantitative SCC behavior. With this new capability, we will dynamically switch back and forth between steam and water at a given temperature and oxygen activity to directly probe macroscale changes in SCC response and, when paired with ex situ microscopy, how these differences link with atomic-to-mesoscale in grain boundary corrosion at crack tips.

Future Plans

Our focus continues to be on understanding how atomistic features of selective oxidation, interfacial diffusion, and local structural and composition changes associated with high-temperature corrosion and applied stress lead to macroscale SCC behavior. Several capabilities highlighted above, in addition to cryogenic workflows for H mapping by APT [4] and in situ mechanical testing with electron microscopy, will continue to be developed and employed across a variety of environments to understand how stress couples with selective oxidation to drive SCC. New two-stage oxidation experiments with $^{16}O/^{18}O$ isotopic tracers will identify how dilute alloying addition (e.g., Al and Mn) alter the transport behavior along oxide GBs and oxide/metal interfaces. In parallel, our modeling efforts will continue to develop MD and higher-scale simulations, informed by experimental observations, to understand how vacancy generation and injection impacts diffusion and grain boundary migration, especially in proximity to the nanoscale high-stress regions surrounding crack tips.

References

1. E.M. Kershkovitz, K. Krusa, P.G.N. Noles, K. Walter, E. Marquis, C. Wang, and D.K. Schreiber, *Utilizing 4D-STEM to Characterize Diffusion-Induced Grain Boundary Migration in Ni-Cr Alloys,* npj Material Degradation (*2026 – in press*).
2. C. McRobie, M.J. Olszta, J.C. Hartmann, K. Kruska, Z. Zhu, Z. Zhai, B. Gwalani, D.K. Schreiber, and E.J. Kautz, *Elucidating the impact of stress states on local surface passivation in Ni-5Cr using the Rhines pack method*, Corrosion Science (*2026 - in press*)
3. Y. Yang, W. Zhou, S. Yin, S.Y. Wang, Q. Yu, M.J. Olszta, Y.-Q. Zhang, S.E. Zeltmann, M. Li, M. Jin, D.K. Schreiber, J. Ciston, M.C. Scott, J.R. Scully, R.O. Ritchie, M. Asta, J. Li, M.P. Short, and A.M. Minor, *One dimensional wormhole corrosion in metals*, Nature Communications 14, 988 (2023).
4. V.B. Vukkum, Z. Li, J.R. Grimm, S. Mukhopadhyay, T. Liu, V. Shutthanandan, and A. Devaraj, *Insights from quasi-in situ cryogenic-transfer atom probe tomography for analyzing hydrogen diffusion in metallic alloys*, npj Materials Degradation 9, 85 (2025).

Publications

1. E.M. Kershkovitz, K. Krusa, P.G.N. Noles, K. Walter, E. Marquis, C. Wang, and D.K. Schreiber, *Utilizing 4D-STEM to Characterize Diffusion-Induced Grain Boundary Migration in Ni-Cr Alloys,* npj Material Degradation (*2026 – in press*).
2. C. McRobie, M.J. Olszta, J.C. Hartmann, K. Kruska, Z. Zhu, Z. Zhai, B. Gwalani, D.K. Schreiber, and E.J. Kautz, *Elucidating the impact of stress states on local surface passivation in Ni-5Cr using the Rhines pack method*, Corrosion Science (*2026 - in press*)
3. E.A. Marquis, A. Devaraj, R.G. Forbes, I. Ghamarian, M. Kühbach, J.-B. Maillet, B. Mazumder, F. Meisenkothen, J. Qi, D. Schreiber, P. Styman, F. Vupillot, and W. Windl, *Frontiers of Atom Probe Tomography Physics, Data Processing, and Analysis*, Microscopy and Microanalysis **32**, ozag070 (2026).
4. E.J. Kautz, K.H. Yano, J.C. Hartmann, A.Y. Gerard, S.D. Taylor, J.R. Scully, and D.K. Schreiber, *Strategies for Preparing and Analyzing Thin Passive Films With Atom Probe Tomography*, Microscopy and Microanalysis **31** ozaf023 (2025).
5. K. Kruska, D.W. Saxey, T. Terachi, T. Yamada, D.K. Schreiber, and S. Lozano-Perez, *Deformation band corrosion as a result of applied stress and cold-work in 304 stainless steel in simulated pressurized water reactor primary water conditions*, Journal of Nuclear Materials **607,** 155686 (2025).
6. B.W. Caplins, A.N. Chiaramonti, J.M. Garcia, L. Miaja-Avila, K.H. Yano, D.K. Schreiber, and J.H. Bunton, *On the instrument-dependent appearance of ion dissociation events in atom probe tomography mass spectra*, Ultramicroscopy **267**, 114061 (2024).

Low-Pressure, Extreme Strain-Rate Mechanics from Microparticle Impact

Christopher A. Schuh, Department of Materials Science and Engineering, Northwestern University, Evanston IL

Keywords: extreme strain-rate mechanics; laser-induced particle impact testing (LIPIT); dynamic strength and hardness; phonon drag; deformation mechanism maps

Research Scope

Conventional high-rate mechanical tests are often limited in their accessible strain rates, capped to avoid a shock-dominated loading regime. Optically driven microparticle impact experiments can access strain rates above 10^6 s^{-1} without necessarily entering the strong-shock regime [1, 2]. Laser-induced particle impact testing (LIPIT) is one such method, which has been used in recent years as a dynamic indentation platform in which particle impact and rebound trajectories, crater volumes, temperature, composition, and impactor geometry can all be controlled well enough to extract quantitative strength and hardness [3, 4] (an example of our hardness measurements is shown in Fig. 1). LIPIT has provided a coherent experimental and mechanistic foundation for studying plasticity at extreme strain rates. In particular, the mechanistic transition between the low and high strain rate regimes shown in Fig. 1 has become addressable in new ways in the past few years. Our work aims to map this transition, with a focus on the shift from thermally activated dislocation motion (at low rates) to drag-controlled, ballistic dislocation transport (at high rates), and furthermore to identify the composition and temperature limits of these regimes.

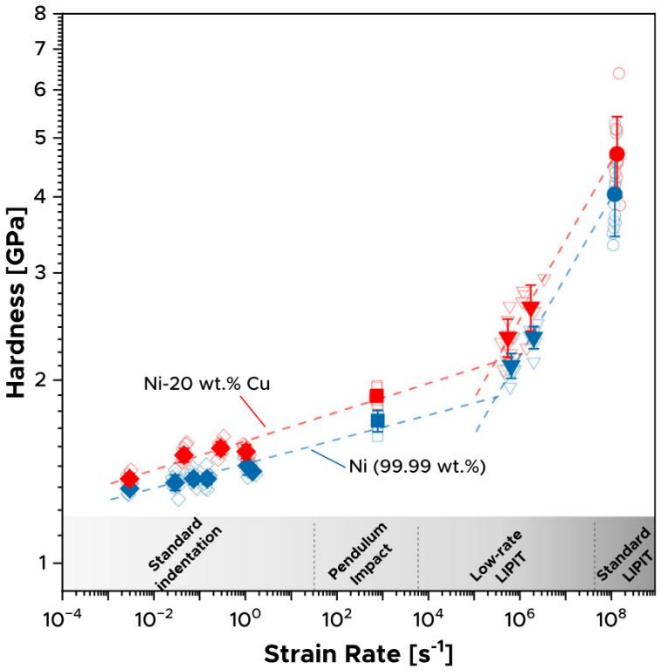

Figure 1. Self-consistent hardness measurements across eleven decades of strain rate in Ni and Ni-20 wt.% Cu, combining conventional indentation, pendulum indentation, low-rate LIPIT, and standard LIPIT [P2].

Recent Progress

A central challenge in high-rate mechanics is that strength data are usually stitched together from different instruments, stress states, operators, sampled volumes, and material batches. We have addressed this problem by measuring microindentation hardness from 10^{-3} to 10^8 s^{-1} using a common hardness definition and the same material surface [P2], as shown in Fig. 1. The key experimental advance is the design of diamond impactors for low-rate LIPIT: sharp or

microfabricated diamond projectiles provide a small contact area combined with a large trailing mass, allowing controlled indentation at velocities on the order of 1–20 m s^{-1} while retaining micrometer-scale indentation depths. This fills the long-standing gap between conventional impact indentation and standard alumina-particle LIPIT. In Ni and Ni-20 wt.% Cu, the resulting data show a modest strain-rate sensitivity below about 10^4 s^{-1}, followed by a sharper upturn above about 10^5 s^{-1}. The high-rate data support a transition to viscous, dislocation-phonon drag-dominated plasticity and permit a direct estimate of a macroscopic viscosity and drag coefficient for nickel.

The physical meaning of this upturn is developed most directly in Ref. [P1]. Here, we have demonstrated that pure metals can strengthen when heated at extreme strain rates, a reversal of the usual low-rate temperature dependence. Using alumina microparticles impacting pure Cu, Au, and Ti, that work shows that the dynamic strength and hardness of pure metals increase with temperature at strain rates above 10^6 s^{-1}, as shown in Fig. 2. For copper, the dynamic yield strength increases from 280 MPa at 20 °C to 364 MPa at 177 °C, while crater volumes decrease and rebound velocities increase at higher temperature. The effect is counterintuitive because the thermal and athermal components of strength decrease with temperature under conventional conditions. At extreme strain rates, however, dislocation motion reaches a ballistic-like transport regime in which phonon drag becomes dominant. Since dislocation-phonon interactions intensify with temperature, the drag term can overtake the conventional softening terms and produce net thermal hardening.

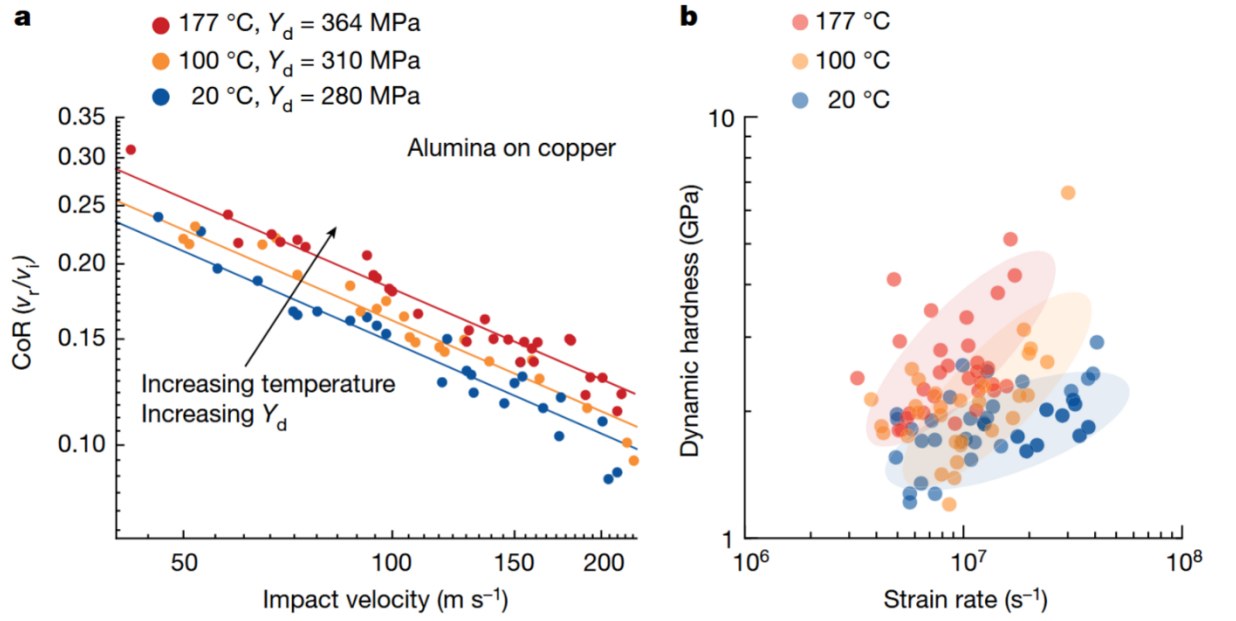

Figure 2. Pure-metal thermal hardening at extreme strain rate: copper strength and hardness increase with temperature, and a summed strength model captures the role of dislocation drag [P1].

We have also expanded our investigation to examine how robust this phonon-drag-dominated regime is when pure metals are alloyed [P3]. At extreme strain rates, Ni samples of decreasing purity show a systematic transition from hotter-is-stronger to hotter-is-softer behavior, as shown in Fig. 3. High-purity Ni exhibits higher dynamic yield strength and hardness at elevated temperature, but lower-purity Ni exhibits the opposite trend. This crossover is observed both in coefficient-of-restitution fits and in dynamic hardness distributions. A mechanistic strength model explains the result by adding a solute-strengthening term to the thermal, athermal, and drag terms. Solutes introduce dislocation pinning interactions that are thermally activated; as solute content rises, that term becomes strong enough to overcome the positive temperature dependence of phonon drag. For Ni, the crossover between the two regimes occurs at an interstitial concentration of about 0.3%. The same qualitative transition is also observed in Ti and Au alloy families, indicating that composition can be used to tune the temperature dependence of strength under extreme conditions.

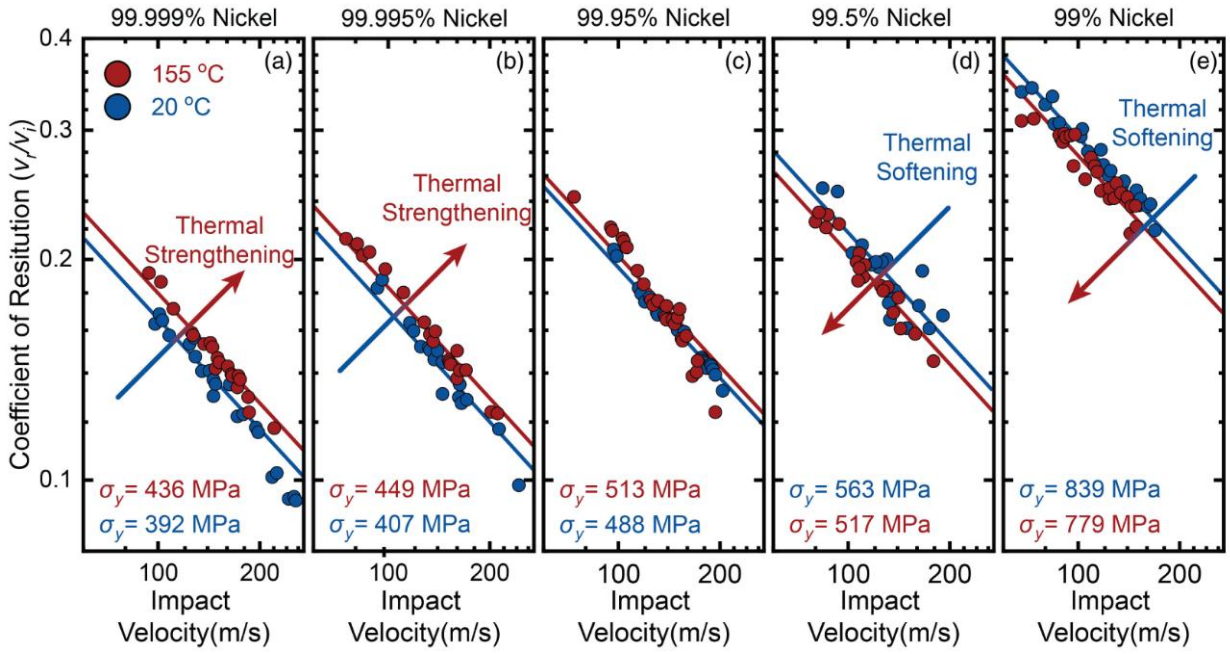

Figure 3. Dynamic yield trends in Ni of decreasing purity show a transition from ballistic phonon-drag control to solute-pinning control, with a crossover near 0.3% interstitial content [P3].

Furthermore, we have identified a second boundary on the phonon-drag regime: even in a pure or model system, hotter-is-stronger behavior cannot continue indefinitely as homologous temperature approaches the melting point [P4]. Tin is used as a low-melting-temperature model material at strain rates above 10^6 s^{-1} and homologous temperatures above $0.80T_m$. At lower impact velocities, tin behaves as expected for a drag-controlled solid, with the effective dynamic strength increasing from 220 to 292 MPa as temperature rises from 20 to 150 °C. At higher velocities, however, the coefficient-of-restitution data deviate from the plastic-impact scaling and the dynamic hardness

trend reverses. The transition occurs when adiabatic heating during impact produces melting; once liquid forms, material ejection enlarges the measured crater volume and lowers the apparent hardness. The velocity for the onset of melting decreases strongly with increasing temperature, from about 310 m s^{-1} at 20 °C to about 75 m s^{-1} at 150 °C. The result maps an upper-temperature and upper-strain-rate bound on the phonon-drag-dominated regime, as shown in Fig. 4.

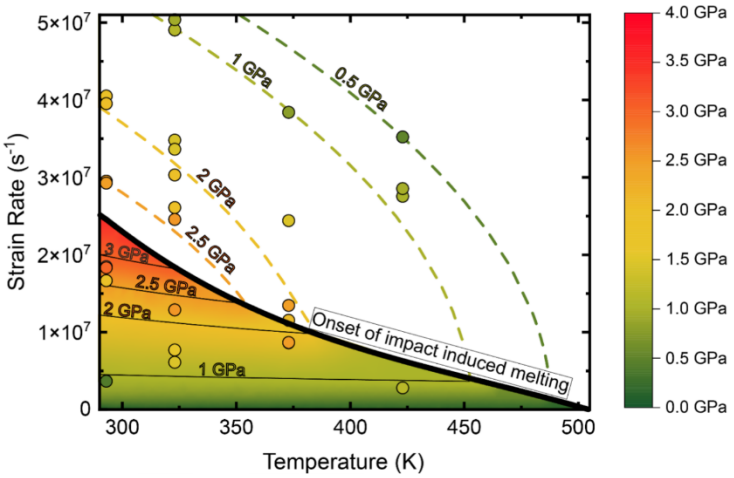

Figure 4. Temperature-strain-rate deformation map for tin showing the boundary between phonon-drag thermal hardening and adiabatic-melting thermal softening [P4].

Future Plans

These new results are moving the field from qualitative recognition of unusual high-rate behavior to predictive design of metals and alloys for erosion, impact, high-speed manufacturing, cold spray, and other dynamic service environments. Moving forward, we are interested in exploring other intrinsic (alloy composition and structure) and extrinsic (fields, conditions) parameters that affect the dislocation drag mechanism, and other manners in which it manifests unexpected behavior. For example, the Tabor factor relating strength to hardness needs some analysis in the unusual conditions of dislocation drag domination. Additionally, dislocation drag can be dominated by either phonons (which is the case for all of the work reviewed here), or electrons (which is a frontier case for high strain rate experiments). We will be exploring other materials and conditions to understand the limits of the phonon-limited regime, and seeking regimes where electron transport limits strength. Finally, most of our work has focused on relatively pure metals, and transitioning our studies to systems with microstructure (i.e., chemical order, phases, etc.) is plausible now that we have a firmer understanding of the single-phase, dilute cases.

References

1. M. Hassani, D. Veysset, K. A. Nelson, and C. A. Schuh, *Material hardness at strain rates beyond 10^6 s^{-1} via high velocity microparticle impact indentation*, Scripta Materialia 177, 198-202 (2020).
2. T. J. Lucas, A. M. Saunders, and C. A. Schuh, *Microstructure effects on high velocity microparticle impacts of copper*, Acta Materialia 280, 120329 (2024).
3. Y. Sun, D. Veysset, K. A. Nelson, and C. A. Schuh, *The transition from rebound to bonding in high-velocity metallic microparticle impacts: jetting-associated power-law divergence*, Journal of Applied Mechanics 87(9), 091002 (2020).
4. L. Borasi, S. E. Kooi, and C. A. Schuh, *Crossing from thermally activated to drag-controlled plasticity in mild steel as strain rate increases*, Acta Materialia 310, 122120 (2026).

Publications

P1. I. Dowding and C. A. Schuh, *Metals strengthen with increasing temperature at extreme strain rates*, Nature 630, 91–95 (2024).

P2. L. Borasi and C. A. Schuh, *Self-consistent hardness measurements spanning eleven decades of strain rate on a single material surface*, Nature Communications 16, 6148 (2025).

P3. I. Dowding and C. A. Schuh, *At Extreme Strain Rates, Pure Metals Thermally Harden while Alloys Thermally Soften*, Physical Review Letters 136, 076101 (2026).

P4. I. Dowding and C. A. Schuh, *The breakdown of ballistic "hotter-is-stronger" deformation as the melting point is approached*, Applied Physics Letters 129, 000000 (2026), proof copy.

Towards High-Throughput Computation of Phase-and Defect Diagrams

Christopher A. Schuh, Department of Materials Science and Engineering, Northwestern University, Evanston IL

Keywords: grain boundary structure; grain boundary segregation; alloy thermodynamics; materials design

Research Scope

Defect engineering plays a critical role in our ability to design for specific material properties. In polycrystalline materials in particular, control of the grain boundary (GB) chemistry and structure via GB alloying, or segregation, enables targeted selection of a vast range of properties, both negative – such as intergranular embrittlement, which one may seek to mitigate via the segregation of elements which strengthen GBs – and positive – such as the stabilization of nanocrystalline alloys against grain growth, and the myriad of enhanced functional and mechanical properties they possess.

In recent years, the push to rigorously model and design for grain boundary segregation has led to the revitalization and broader adoption of the so-called "spectral model" of GB segregation [1, P1], first introduced in the 1970s, and recently made tractable due to modern machine learning and data science approaches [2]. Prior DOE-funded work of the PI greatly advanced the spectral model into a quantitative framework, which has enabled the predictive design of GB segregation in polycrystalline systems (an example of which is shown for Al-Au in Fig. 1) [3,4], as well as a broader effort to experimentally measure spectral behavior [5, P2]. The spectral model for binary alloys is now sufficiently sophisticated as a design tool that the production of phase-and-defect diagrams, which map defect behavior in a manner similar to traditional bulk phases diagrams, is now possible. Here, we review the recent advancements of the spectral model and provide a brief discussion of the physics and methods which need to be developed for future extensions to more complex cases, such as multicomponent alloys and ordered systems.

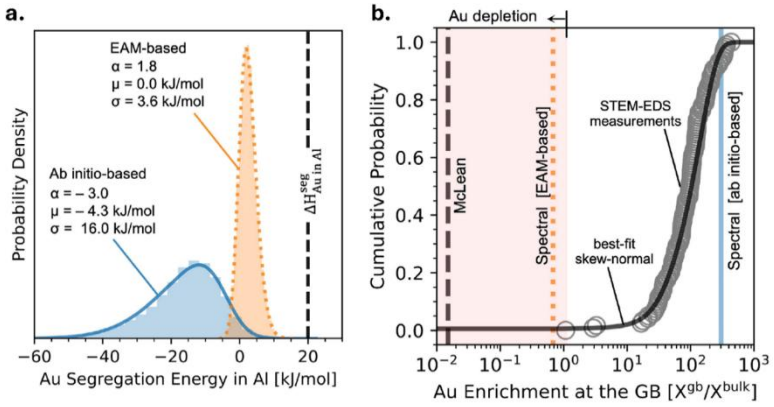

Figure 1. (a) Segregation enthalpy spectra for Al-Au from various sources, with quantum-accurate calculations shown in blue. (b) Predicted GB enrichment compared against STEM-EDS, with only the quantum-accurate spectrum providing an accurate result [3].

Recent Progress

The spectral model for GB segregation has been rapidly developed and expanded upon over the past seven years during the previous DOE-funded work of the PI. For a detailed and thorough review of the history of the model and its usage, we refer the reader to our recently published overview article in Ref. [P1]. Most of the recent advancements in this area have been focused on applying machine learning and data science tools to rapidly populate atlases of thermodynamic information that can be used for screening and design, including segregation enthalpies, excess entropies, and solute interactions [P3]. These methods typically involve the use of numerical descriptors to encapsule the local atomic environments (LAEs) of atomic sites in polycrystalline GBs, which can then be used to construct a mapping between the local structure and corresponding energetics.

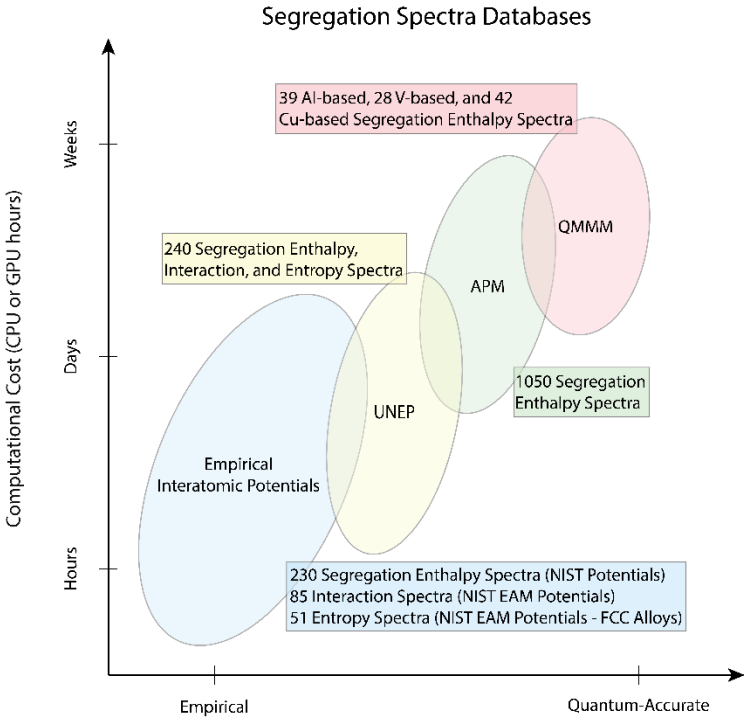

Figure 2. Summary of spectral thermodynamic databases for grain boundary segregation, including from quantum accurate QM-MM, near-quantum accurate APM, a high-efficiency universal potential, UNEP, and traditional empirical interatomic potentials [P1].

A summary of the spectral databases produced to date is shown in Fig. 2. The most recent of these placed an emphasis on the use of hybrid multiscale methods, which apply quantum or near-quantum accurate methods in the local environment surrounding the atomic sites of interest. For instance, we have recently used the quantum-mechanical/molecular-mechanical (QM-MM) framework, which treats the local region with density functional theory methods, to populate a periodic table of segregation enthalpy spectra for Cu-based alloys [P4], alongside our previously published Al and V-based databases. Similarly, we have recently introduced the augmented potential method (APM), which uses a high-fidelity machine learning potential for local calculations, to produce segregation enthalpy spectra for over 1000 binary alloys [P5].

Alongside the development of atlases of spectral data, we have sought to expand upon the use cases of the spectral model via the incorporation of additional physics. In the prior DOE-funded work of the PI, these included the consideration of grain sizes effects, interstitial segregation, solute interactions and entropy. In our most recent work, we have expanded the spectral model to consider embrittlement [P6], and have produced an atlas of spectral embrittlement measurements for cubic systems [P7], and we have incorporated means of modeling the overlap between finite grain size effects and interstitial alloys [P8].

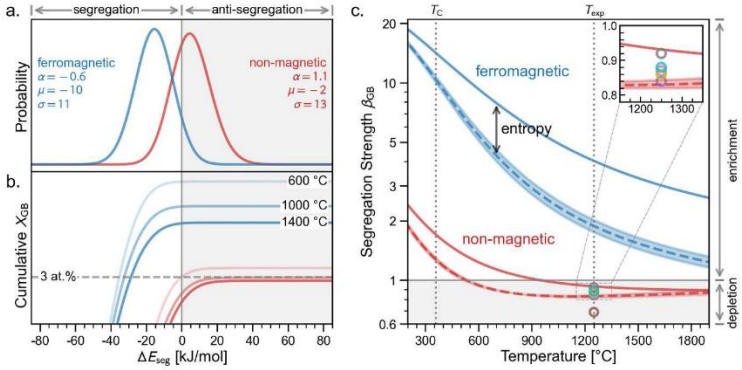

Figure 3. The effect of magnetic on Ni-Re. (a) Segregation energy spectra under ferromagnetic and non-magnetic conditions. (b) Cumulative GB enrichment at various temperatures. (c) Predicted enrichment under ferromagnetic and non-magnetic conditions, with experimental evidence for comparison [P8].

In our most recent extension to the spectral model, we have considered the effects of magnetism [P9]. In all of the above examples, the atomistic methods assume the 0 K behavior of the material – in the case of a magnetic solvent such as Ni, this assumption implies ferromagnetic behavior. However, the spectral measurements made under these assumptions for Ni-Re, which predict favorable segregation, are contradicted by experimental evidence of anti-segregation. This discrepancy is resolved when the high temperature processing and paramagnetic conditions of Ni-Re during segregation are taken into consideration and incorporated into the QM-MM workflow, as shown in Fig. 3.

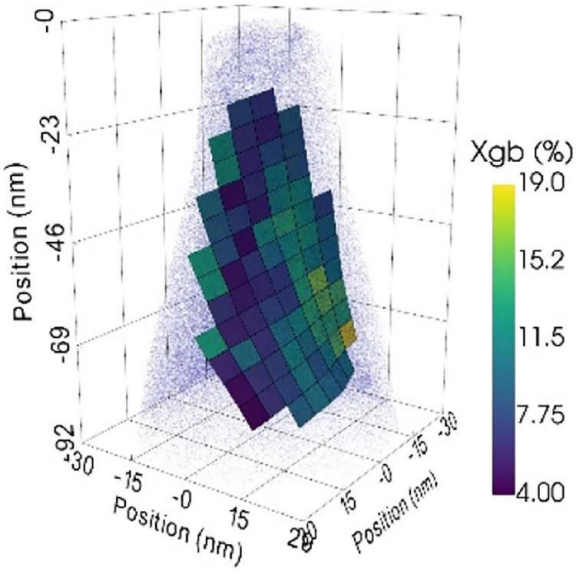

Figure 4. 3D APT reconstruction of a GB from an example metallic binary alloy, with local solute concentrations overlaid onto the GB surface [P2].

Furthermore, a consistently open area of research in the development of the spectral model is the development of techniques used to extract spectral quantities from experiment. Traditionally, this was done using average enrichment quantities with bulk techniques such as Auger electron spectroscopy (AES), or for specifics GBs using transmission electron microscopy (TEM) or atom probe tomography (APT). In the pursuit of more accurately mapping experimental results to spectral forms, we have recently developed an APT approach to extract local compositions along

the GBs at various resolutions [P2], an example of which is shown for a binary alloy in Fig. 4. While site-specific resolutions, like those assumed by the spectral model, are not yet accessible to experiments, this provides an important first step towards a true 1:1 mapping between the theory and practical experimental design.

Future Plans

The above advancements have focused on binary alloys, and the spectral model has become a robust predictive tool in that space, with the capability of producing phase-and-defect diagrams and enabling the accurate design of segregated alloys. However, most practical alloys contain multiple alloying components, and often involve complex ordered phases which have not yet been treated under the spectral model. The prediction of GB segregation in multicomponent systems must therefore consider the spectral segregation of every solute, alongside their complex interactions. Similarly, ordered systems must consider segregation across a complex system of sublattices, which again necessitates the consideration of multiple spectra concurrently. Our future work will therefore seek to address these needs by stepping back to develop the fundamental physical models necessary to accurately capture these phenomena, so they can be incorporated into a spectral workflow with the same rigor that had been achieved for binary alloys.

References

1. M. Wagih, and C.A. Schuh, *Spectrum of Grain Boundary Segregation Energies in a Polycrystal*, Acta Mater. **181**, 228-237 (2019).
2. M. Wagih, P.M. Larsen, and C.A. Schuh, *Learning Grain Boundary Segregation Energy Spectra in Polycrystals*, Nat. Commun. **11**, 6376 (2020).
3. M. Wagih, Y. Naunheim, T. Lei, and C.A. Schuh, *Grain Boundary Segregation Predicted by Quantum-accurate Spectra but not by Classical Models*, Acta Mater. **266**, 119674 (2024).
4. M. Wagih, Y. Naunheim, T. Lei, and C.A. Schuh, *Designing for Cooperative Grain Boundary Segregation in Multicomponent Alloys*, PNAS **122**, e2511930122 (2025).
5. X. Chen, W. Goncalves, Y. Hu, Y. Gao, P Harrison, G. Dehm, B. Gault, W. Ludwig, E. Rauch, X. Zhou, and D. Raabe, *Secondary Grain Boundary Dislocations Alter Segregation Energy Spectra*, Nat. Commun. **16**, 8422 (2025).

Publications

P1. T.P. Matson, N. Tuchinda, and C.A. Schuh, *Overview: The Spectral Model of Grain Boundary Segregation*, Acta Mater. **313**, 122109 (2026).
P2. J. Mack and C. A. Schuh, *Identifying and Measuring Local Enrichment Within Grain Boundaries by Atom Probe Tomography*, Microsc. Microanal. **32**, ozag053.073 (2026).
P3. N. Tuchinda, and C.A. Schuh, *Grain Boundary Segregation Spectra from a Generalized Machine-learning Potential*, Scr. Mater. **264**, 116682 (2025).
P4. C. Li, and C.A. Schuh, *Multiscale Computations of Grain Boundary Solute Segregation Spectra in Cu Polycrystals*, Materialia **44**, 102603 (2025)
P5. N. Tuchinda, C. Li, and C.A. Schuh, *The Augmented Potential Method: Multiscale Modeling Toward a Spectral Defect Genome*, Scr. Mater. **271**, 116969 (2026).
P6. N. Tuchinda, G.B. Olson, and C.A. Schuh, *Grain Boundary Segregation and Embrittlement of Aluminum Binary Alloys from First Principles*, Acta Mater. **293**, 121058 (2025).

P7. N. Tuchinda, G.B. Olson, and C.A. Schuh, *A Grain Boundary Embrittlement Genome for Substitutional Cubic Alloys*, Appl. Phys. Lett. **126**, 171602 (2025).
P8. N. Tuchinda, M. Wagih, and C.A. Schuh, *Interstitial Solute Segregation at Triple Junctions: Implications for Nanomaterials and a Case Study of Hydrogen in Palladium*, Phys. Rev. Mater. **9**, 056002 (2025).
P9. C. Li, S.B. Kadambi, B. Kombaiah, N. Tuchinda, and C.A. Schuh, *Why does Re Anti-segregate from the Grain Boundaries in Ni?*, Research Square, preprint (2026).

Toughening mechanisms in ceramic nanocomposites

Principal Investigators: Brian W. Sheldon, Brown University; Jun Lou, Rice University

Co-Investigator: Nitin P. Padture, Brown University

Keywords: fracture, nanomaterials, small-scale testing, multiscale modeling

Research Scope

The brittleness of ceramic materials prevents their use in applications that could exploit their unique properties, such as high hardness, high strength, corrosion resistance, light-weight, etc. One of the most effective ways to improve their poor fracture resistance is by creating ceramic matrix composites (CMCs) based on long fiber reinforcements. The promise of extending this approach to create tougher nanoscale ceramics via nanotube and nanoplatelet reinforcements is supported by prior research, in spite of the conventional understanding that moving to smaller length scales in advanced ceramics typically leads to stronger but less tough materials. Determining whether these conventional scaling ideas are fully applicable to nanoceramic composites is a primary motivation for the research described in this project.

The overall goal of our work is to evaluate and understand the ways in which the inherently smaller microstructural length scales in ceramic nanocomposites will impact toughening mechanisms. The key objectives of these efforts are:

- Evaluate the failure and toughening mechanisms that occur in ceramic matrices reinforced with different nanoreinforcements. A major focus is on the use of in situ mechanical testing methods that make it possible to investigate phenomena over a broad range of length scales. The interpretations of these measurements are closely integrated with related multiscale modeling and analysis.
- Quantitatively evaluate the toughening contributions from phenomena that occur in 2-D reinforcements. This includes inelastic deformation mechanisms in reduced graphene oxide (*r*-GO), increased fracture resistance in *h*-BN sheets (compared to graphene-related sheets), and strength-limited interfacial debonding at small-scales (compared to the classical energy-limited debonding that occurs at larger length scales).
- Determine how the toughening mechanisms that operate in 2-D reinforced materials differ from those that operate in other composites (i.e., at larger length scales, with fiberous reinforcements, etc).
- Make detailed comparisons between *r*-GO and *h*-BN reinforced composites with the full range of platforms that are being employed in this work (i.e., nanocomposites produced by spark plasma sintering (SPS), nanosheet pull-out tests, deformation and fracture of single nanosheets).

Recent Progress

The research conducted in this program demonstrates that fracture in ceramic nanocomposites differs substantially from the characteristic behaviors that occur in brittle matrix composites with larger reinforcements (e.g., continuous fibers, etc). Recent experiments at Brown have largely focused on investigations of 2-D *h*-BN (hexagonal boron nitride) reinforcements in ceramic matrices (primarily silicon nitride produced by spark plasma sintering). Two central features of this work are: (1) direct measurements of crack growth resistance curves (R-Curves) using the indirect compliance method, and (2) in situ observations of stable crack propagation inside a scanning-electron microscope (SEM).

Stable crack propagation in h-BN nanosheet (BNNS) reinforced Si3N4 was carefully monitored with *in situ* SEM. These observations show the interaction of the crack with the nanofillers and demonstrate that the mechanisms that dictate toughening in this material differ from behaviors in fiber-reinforced ceramics. In these materials, the outer layers of the BNNS are strongly bonded to the matrix, and two main shear-based deformation mechanisms are observed in the BNNS: shear pullout and interlayer sliding between BNNS layers. The crack opening displacements that were monitored in situ were quantitatively modeled with a shear model for crack bridging behavior. The results show that the bridging length and the interfacial shear stress are critical phenomena that dictate the effective bridging tractions.

To quantitatively investigate the fracture process in these materials, we are continuing to employ and improve new methods that have been developed in our DOE-BES-funded research. This includes microcantilever and micropillar measurements (at both Brown and Rice). These methods require FIB milling, which limits the number of specimens that can be tested, and here we have developed machine learning methods that improve our ability to quantitatively analyze results from these tests. We recently conducted a parallel study on several different materials with both of these methods. With unreinforced (i.e., monolithic) SiC, the pillar splitting and microcantilever beam measurements are in good agreement. However, with CNT reinforced composites, the pillar splitting measurements give a fracture toughness which is significantly below the values obtained with microcantilevers. Our initial hypothesis is that the difference between these methods is due to the smaller cracks that are inherently being tested with the micropillars.

Building on our efforts in identifying monolayer hBN as the most fracture-resistant 2D material and discovering the unique toughening mechanism owing to the asymmetrical lattice structures, experiments at Rice further revealed an anomalous mechanical interlayer coupling that involves interlayer-friction toughening and edge-reconstruction embrittlement during the fracture of multilayer *h*-BN. Both asynchronous and synchronous fracture modes and their flaw-size dependence are identified. Edge reconstruction in the synchronous fracture mode can eliminate a lattice asymmetry-induced toughening mechanism in monolayer *h*-BN, leading to embrittlement of the multilayer *h*-BN, while the asynchronous fracture mode results in greater fracture resistance. These findings provide important insights into the interfacial behaviors of multilayer (most likely

case under practical conditions) hBN nanosheet-reinforced ceramic nanocomposites. Going beyond r-GO and hBN, we also discovered a new potential 2D reinforcement candidate, monolayer amorphous carbon (MAC). By incorporating both amorphous and nanocrystalline phases, MAC significantly enhances energy absorption during fracture propagation, as evidenced by crack blunting, deflecting, and bridging. Our results indicate a sevenfold increase in the energy release rate compared to monolayer graphene, along with improved deformation strain and crack stability.

In another effort, we demonstrated the synthesis of an hBN/Covalent organic framework (COF) nanocomposite and highlighted how neutron radiation exposure can enhance its mechanical performance, making it a promising candidate for polymer coatings in radiative environments. Our other relevant efforts include the development of a semi-quantitative high-strain rate nanomechanical tensile testing method capable of measuring dynamic mechanical properties of 1D and 2D nanomaterials, and the integration of in-situ nanomechanical testing with the Transmission Kikuchi Diffraction methods to study nanolaminate composites.

Future Plans

More extensive comparisons will be made between *r*-GO and *h*-BN, based on nanocomposites with the same reinforcement volume fraction and the same matrix phase, using the experimental methods at Brown and Rice that are outlined above. Based on our work to date, we anticipate that the *h*-BN reinforced materials will exhibit notable differences when compared with *r*-GO based composites. The direct interpretation of the experiments with both nanocomposites and individual reinforcements will require detailed modeling. This effort is designed to overcome the limitations of previous models, which are based almost exclusively on extending models of toughening by embedded fibers. Our experiments to data have demonstrated that toughening mechanisms associated with 2-D nanomaterials differ from these descriptions, and new modeling will be based on these observations.

Publications

- Xing Liu, Christos E. Athanasiou, Cristina López-Pernía, Ting Zhu, Nitin P. Padture, Brian W. Sheldon, and Huajian Gao, "Tailoring the toughening effects in two-dimensional nanomaterial-reinforced ceramic matrix composites", *Journal of Applied Mechanics* **91**, 011003 (2024). https://doi.org/10.1115/1.4063029
- Zhigong Song, Boyu Zhang, Yingchao Yang, Guanhui Gao, Daiming Tang, Qiyi Fang, Youtian Zhang, Bongki Shin, Doug Steinbach, Qing Ai, Xuan Zhao, Yimo Han, Nitin P. Padture, Brian W. Sheldon, Takashi Taniguchi, Kenji Watanabe, Huajian Gao, and Jun Lou "Fracture of Van der Waals Materials: Flaw-size Induced Mechanical Interlayer Coupling and Edge-Reconstruction Embrittlement", *Nature Materials*, **24**, 1554–1560 (2025). https://doi.org/10.1038/s41563-025-02194-x.
- B. Shin, B. Ni, C. Toh, D. Steinbach, Z. Yang, L. Sassi, Q. Ai, K. Niu, J. Lin, K. Suenaga, Y. Han, M.J. Buehler, B. Ozyilmaz and J. Lou, "Intrinsic Toughening in Monolayer Amorphous Carbon Nanocomposites", *Matter*, Vol. 8 (4), 102000 (2025). https://doi.org/10.1016/j.matt.2025.102000.
- D. Steinbach, B. Zhang, F. Arifurrahman, R. Xin, B. Shin, Y. Camacho, N. Balaji, M. RW Brake, M. Tang, Q. Li, and J. Lou, "A Semi-quantitative Nanomechanical Tensile Testing Method at High Strain Rates",

Materials Today Communications, Vol. 42, 111503 (2025). https://doi.org/10.1016/j.mtcomm.2025.111503

- D. Steinbach, Yifan Zhu, J.C. Philipps, W. Tu, X. Liu, X. Tian, T. Xie, Y. Yan, J. Gahl, J. Brockman, and J. Lou, "Neutron-Radiation-Induced Strengthening and Toughening of Hexagonal Boron Nitride Nanosheet/Covalent Organic Framework Composites for Polymer Coatings in Radiative Environments", *ACS Applied Nano Materials*, Vol. 8(19), 10160-10167 (2025). https://doi.org/10.1021/acsanm.5c02174
- T. Vermeij, A. Sharma, D. Steinbach, J. Lou, J. Michler, and X. Maeder, "In Situ Transmission Kikuchi Diffraction Tensile Testing", *Scripta Materialia*, Vol. 261, 116608 (2025). https://doi.org/10.1016/j.scriptamat.2025.116608
- B. Zhang, W. Tu, X. Liu, D. Steinbach, Y. Zhu, C. Lin, Q. Ai, T. Zhai, J. Zhang, G. Gao, N. Padture, B. Sheldon, and J. Lou, "3D Printed Strong and Tough h-BN-Reinforced Silica Nanocomposites", *ACS Applied Materials*, submitted (2026).
- D. Steinbach, X. Liu, B. Zhang, A. Mijailovic, C. Athanasiou, C. Ramirez, I. Szlufarska, N. Padture, B. Sheldon, J. Lou, "Microstructural Inhomogeneity Complicates Small-Scale Fracture Toughness", *Advanced Engineering Materials*, submitted (2026).
- C. López-Pernía, A. Mijailovic, X. Liu, J. Lou, N.P. Padture, and B.W. Sheldon, "Direct *in situ* observation of interlayer shear-based pull outs as crack bridging mechanisms in nanocomposites of silicon nitride with boron nitride nanoplatelets", *Scripta Materialia*, submitted (2025).
- B. Zhang, X. Liu, D. Steinbach, W. Tu, Q. Ai, T. Taniguchi, K Watanabe, N. Padture, B. Sheldon, J. Lou, "Interface Engineering Enabled Toughening of h-BN/PDC Nanocomposites", in preparation.

Micromechanics of Migrating Interfaces

Ryan Sills

Department of Materials Science and Engineering, Rutgers University

Keywords: grain boundary, phase boundary, disconnection, dislocation, migration

Research Scope

In the last decade, it has become widely accepted that the primary mechanism of interface migration is formation and migration of disconnections—interfacial line defects characterized by a Burgers vector and a step height. Despite this progress, numerous recent experimental observations have brought into question basic tenets of the theory of interface migration [1]. This discrepancy between experimental observations and theory results from a lack of knowledge about how disconnections form and what controls their migration rate; the focus of this project is to fill these knowledge gaps through molecular dynamics (MD) simulations of grain and phase boundaries. Capabilities developed previously under this project, including tools for predicting line defect structures and identifying interfacial line defects in MD simulations, uniquely enable the research methods. The hypothesis guiding the work is that interactions with dislocations—both in the bulk and within the interface—govern the formation and migration rates of disconnections. The project is comprised of three research tasks aimed at (1) predicting and classifying line defect structures for a variety of interfaces, (2) identifying disconnection formation mechanisms and quantifying formation rates, and (3) understanding how dislocations affect formation and migration of disconnections.

Recent Progress

The project is focused on both grain and phase boundaries: while the latter are more complex in that many possible orientation relationships are possible (e.g., Σ orientations), the former have the added complexity of misfit strain between the crystals. Research under this project has provided insights into both boundary types. The interfacial line defect analysis (ILDA) tool previously developed under the project [2] has provided unprecedented insights into line defect structures and dynamics with face-centered cubic (FCC), body-centered cubic (BCC), and hexagonal close-packed (HCP) crystals. In our studies of martensitic phase transformations, we have revealed novel transformation mechanisms and also explored evolution of interfacial defect structures during misfit relaxation.

Fig. 1 shows α'-martensite (BCC phase) formation at a slip band intersection in Fe-Ni-Cr stainless steel. It has long been hypothesized that these transformations occur via slip transmission. On the contrary, our simulations reveal that no such transmission occurs. Instead, disconnection loops nucleate and expand within the secondary slip band, a process which we reveal in detail using ILDA (see Fig. 1). Fig. 2 shows the evolution of interfacial line defect structures within an FCC-BCC phase boundary in pure Fe. Dislocation loops are inserted in the bulk, which then multiply and impinge on the interface (Fig. 2(a)). The results show that the formed defect structure only partially relieves the misfit stresses between the crystals (Fig. 2(b)). Furthermore, we show that the gross Burgers vector content in the interface significantly exceeds the net content (Fig. 2(c)), meaning that many of the interfacial line defects do not contribute to relaxation of the misfit stresses. This is contrary to prevailing theories that predict idealized defect structures.

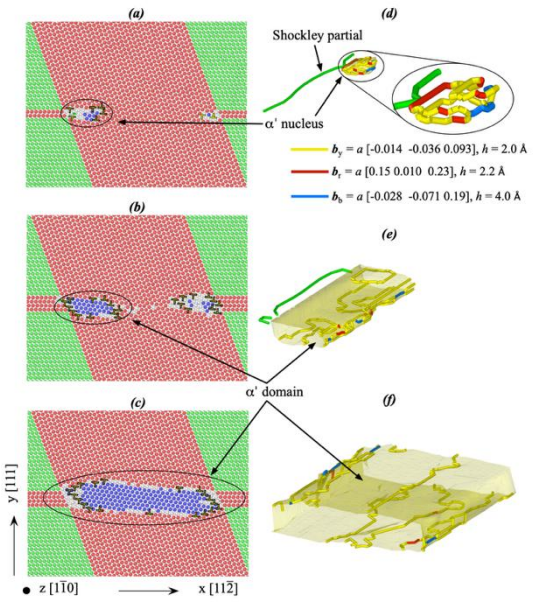

Fig. 1: Formation of a'-martensite at twin-twin slip band intersection in Fe-Ni-Cr stainless steel, line defects revealed by ILDA.

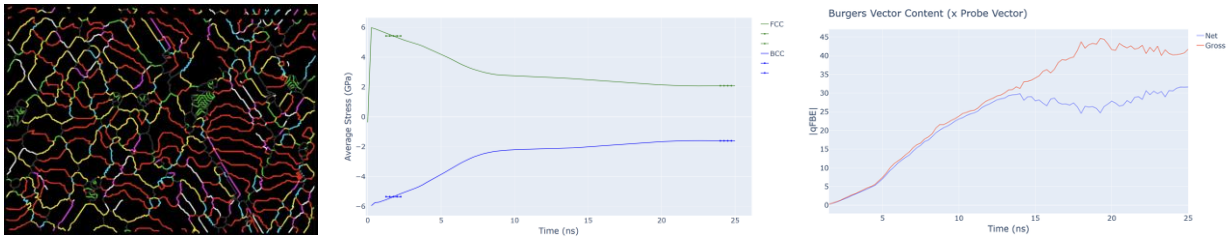

(a) (b) (c)

Fig. 2: (a) Line defect structure identified by ILDA in an FCC-BCC interface. (b) Relaxation of stress in the crystals as the structure forms. (c) Net and gross Burgers vector content in the interface, showing a large excess line defect content.

The α'-martensite simulation above revealed something deeply fundamental: a new state of interfacial coherency and an associated new class of interfacial line defects. Specifically, this interface was found to exhibit some atom pairs (one from each crystal) which were close to being coincident, but still separated from each other. In such interfaces, the energy is lowered by removing one atom from each pair and then displacing the remaining atom to a position between the two lattice sites. This non-affine operation is exactly equivalent to inserting a disconnection dipole or loop into the interface. In contrast to traditional disconnections, however, these defects lead to an additional (non-affine) coincidence site between the crystals; for this reason, we term

these defects as *discohesions* and we term interfaces containing discohesions as *e-coherent* (short for enhanced-coherent) [3]. Fig. 3 demonstrates e-coherency in the BCC-HCP martensitic interface. Fig. 3(a) shows the ground state of the interface along with a comparison to a high-resolution transmission electron microscopy (HR-TEM) image of a real martensitic interface in 304L stainless steel (from collaborators Douglas Medlin and Alejandro Hinojos at Sandia National Laboratories). Fig. 3(b) shows interface migration via two different disconnections with Burgers vectors $\mathbf{b}_1$ and $\mathbf{b}_2$, which give rise to different discohesion Burgers vectors $\mathbf{b}_{coh1}$ and $\mathbf{b}_{coh2}$. Figs. 3(c) and (d) show MD simulations of interface migration and associated line defects; parallel green lines denote the discohesion arrays in the e-coherent interface.

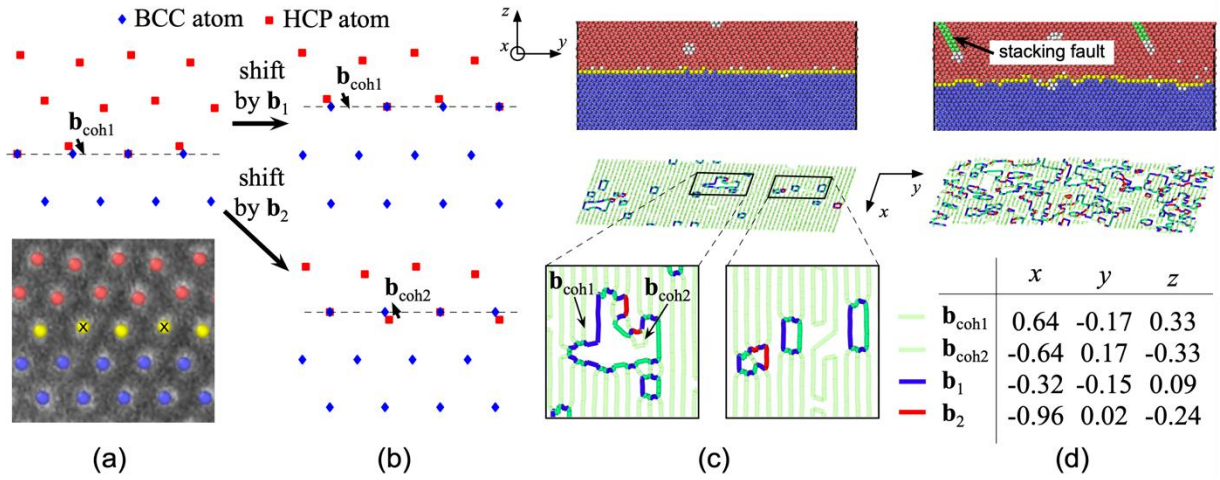

	x	y	z
$\mathbf{b}_{coh1}$	0.64	-0.17	0.33
$\mathbf{b}_{coh2}$	-0.64	0.17	-0.33
$\mathbf{b}_1$	-0.32	-0.15	0.09
$\mathbf{b}_2$	-0.96	0.02	-0.24

Fig. 3: Structure and behavior of an e-coherent BCC-HCP phase boundary. (a) Traditional coherent atomic structure (top) and e-coherent structure with comparison to HR-TEM (bottom). (b) Migration of the interface via two different disconnections. (c-d) Simulation snapshots showing interface migration and line defects revealed by ILDA. Green lines are discohesion arrays which make the interface e-coherent. Burgers vectors in the table are in Å.

We have also studied grain boundary (GB) structures to determine whether they can exhibit e-coherency. Specifically, we have successfully analyzed using ILDA 6,819 of the 7,304 minimized FCC GB structures obtained via Homer et al. [4]. We find that out of these GBs, only 127 contain no interfacial line defects with the remaining 6,692 containing discohesions, making them e-coherent. Fig. 4 compares the populations of GBs which are coherent (defect-free) with those that are e-coherent. Fig. 4(b) shows that while lower Σ-number GBs are more likely to be coherent, many "low" Σ-number GBs are e-coherent.

Fig. 4 compares the populations of GBs which are coherent (defect-free) with those that are e-coherent. Fig. 4(b) shows that while lower Σ-number GBs are more likely to be coherent, many "low" Σ-number GBs are e-coherent. Fig. 4(c) shows the probability distribution of GB width for the two populations; coherent GBs have lower GB width on average, but the distributions exhibit significant overla p. These results demonstrate that e-coherency is a common feature of crystalline interfaces and that e-coherent GBs exhibit different trends and behaviors on average.

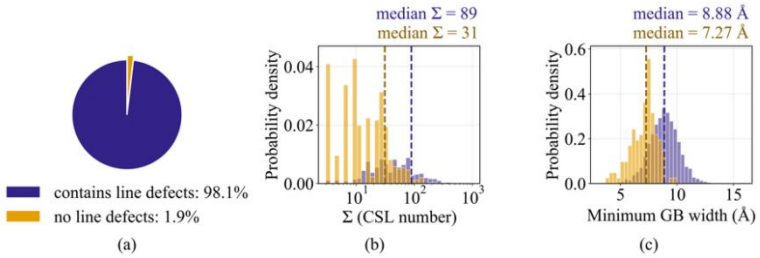

Fig. 4: Comparison of coherent (defect-free) and e-coherent (containing discohesions) GBs from Homer et al. database [4]. (a) Fraction of GBs containing defects. (b) Probability distribution of Σ-number and (c) GB width for the two populations.

Finally, we have performed a detailed examination of GB migration with the well-studied Σ5(210)[001] FCC symmetric-tilt GB (a coherent GB containing no discohesions). Through our analysis, we observed several previously unobserved phenomena, shown in the snapshot sequence of Fig. 5 [5]. Firstly, we observe a significant amount of line defect "flickering" whereby small loops rapidly nucleate and annihilate. Such flickering gave rise to the second phenomena: formation of pure steps, which formed in large densities. Pure steps were often associated with previously unobserved *mixed-step complexes* where disconnections of different step heights intersect. Finally, one disconnection mode was observed to migrate via a dissociation-reassociation mechanism we termed *dissociation-mediated glide*. To our knowledge, this study represents the first deep dive into line-defect-based GB migration mechanisms.

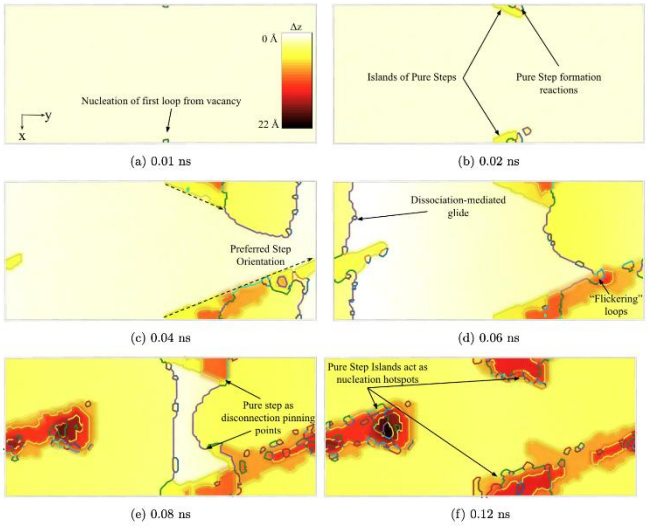

Fig. 5: Simulations snapshot sequence of migration in the S5(210)[001] FCC symmetric-tilt GB, showing (a) nucleation of a disconnection loop at a pre-seeded vacancy, (b-c) formation of pure-step islands, (d) migration of a disconnection via dissociation-mediated glide, (e) annihilation of the disconnection, and (f) deepening of pure-step islands. GB color denotes migration distance.

Future Plans

We will build on the existing findings by considering the influence of bulk dislocations and applied stress on migration mechanisms. Dislocation loops will be inserted into crystals and shear stresses will be applied—in conjunction with synthetic driving forces—to elucidate how migration mechanisms change under different driving

forces and line defect states. These findings will build towards the comprehensive understanding of interfacial migration micromechanisms which is the overall thrust of the project.

References

1. A. Bhattacharya, Y.-F. Shen, C. M. Hefferan, S. F. Li, J. Lind, R. M. Suter, C. E. Kill III, and G. S. Rohrer, *Grain boundary velocity and curvature are not correlated in Ni polycrystals*, Science **374**, 189-193 (2021).
2. N. Deka, A. Stukowski, and R. B. Sills, *Automated extraction of interfacial dislocations and disconnections from atomistic data*, Acta Materialia, **256**, 119096 (2023).
3. R. B. Sills, A. Hinojos, T. J. Murray, S. H. Cooley, D. B. Robinson, X. W. Zhou, and D. L. Medlin, *E-coherent crystalline interfaces: coherency enhanced by discohesion arrays*, Physical Review Materials, In-Press.
4. E. R. Homer, G. L. W. Hart, C. B. Owens, D. M. Hensley, J. C. Spendlove, and L. H. Serafin, *Examination of computed aluminum grain boundary structures and energies that span the 5D space of crystallographic character*, Acta Materialia **234**, 118006 (2022).
5. I. Lalani and R. B. Sills, *Complexity of disconnection dynamics during grain boundary migration*, npj Computational Materials, In-Press.

Publications

1. D. B. Gordon and R. B. Sills, Self-consistent solution of the Frank-Bilby equation for interfaces containing disconnections, J. Mech. Phys. Sol. **193**, 105845 (2024).
2. R. B. Sills, A. Hinojos, T. J. Murray, S. H. Cooley, D. B. Robinson, X. W. Zhou, and D. L. Medlin, *E-coherent crystalline interfaces: coherency enhanced by discohesion arrays*, Physical Review Materials, In-Press.
3. I. Lalani and R. B. Sills, *Complexity of disconnection dynamics during grain boundary migration*, npj Computational Materials, In-Press.

Origins of elastomeric nanocomposite reinforcement: internal volume and stress competitions between coexisting hard and soft solids

David S. Simmons, University of South Florida

Keywords: Elastomers, Nanocomposites, Molecular Dynamics Simulations, Toughness

Research Scope

Prior work in this effort produced a unifying understanding of how nanoparticles reinforce elastomers at low to medium deformation. Results found that the nanoparticles and elastomer compete over how the volume of the system changes under deformation (caused by a mismatch in their "Poisson's Ratio"). This leads the volume of the composite to increase under deformation. Elastomers strongly prefer to keep a constant volume, so that they resist this change strongly, with a contribution from their bulk modulus – a contribution to stiffness that is much higher than their usprual resistance to elongation. Ongoing work seeks to understand the mechanisms ultimately accounting for fatigue and failure of these elastomeric nanocomposites, and to encompass phenomena (such as glassy bridges, tie chains, and adsorption effects) that are proposed to link nanoparticles together and to connect nanoparticles to the polymer matrix.

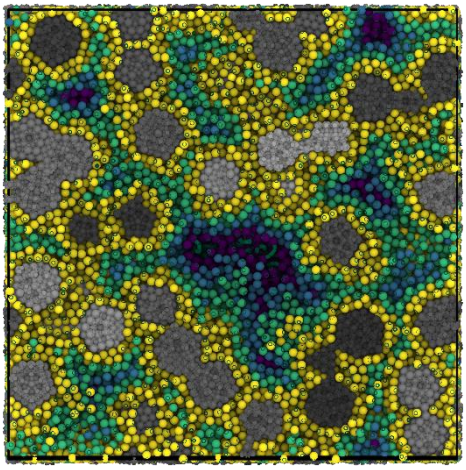

Rendering of a simulated elastomeric nanocomposite in which polymer segments are colored by distance from the nearest particle.

Recent Progress

Here we report on simulations pointing to a unified understanding of nanoparticle-driven elastomer reinforcement, integrating and reconciling both direct contact and glassy bridge effects. These results indicate that nanoparticles enhance elastomers' mechanical response by drawing on the polymer's incompressibility to enhance its resistance to deformation. Specifically, a competition between the particle and elastomer networks over the volume of the composite under deformation compels the nearly incompressible elastomer matrix to increase in volume under deformation, inducing a large contribution from the polymer's bull modulus. We find that the addition of glassy bridges between particles primarily serves to augment this effect, but not to introduce a new elongational cohesive mechanism to the rubbery restoring stress. This mechanism accounts for high levels of reinforcement typical of experimental nanocomposites. We also find that it explains an anomalous feature of elastomeric nanocomposites – an inversion of the temperature dependence of their modulus relative to neat elastomers.

Finally, we discuss how this mechanism continues to evolve and dominate response at high strains, playing a central role in dissipation, cavitation, and ultimate failure. We specifically report on simulations resolving the longstanding question of why introduction of nanoparticles tends to favor cavitation and failure at lower strains than in neat elastomers, despite also producing mechanical reinforcement. Finally, we report on new results beginning to question of how covalent grafting of polymer chains to nanoparticles modulates mechanical response, cavitation, and failure.

Future Plans

Future work aims to understand how flocculation (structural evolution) of nanoparticles prior to deformation modulates the onset of cavitation and failure in elastomeric nanocomposites. By probing both initial dispersion state and the effects of polymer/particle linkage on particle structural evolution and jamming state during deformation, this research will provide insight into how the mechanisms of reinforcement and failure can be rationally modulated. Finally, these simulations will be extended to consider multi-cycle deformation and fatigue processes essential to controlling the lifetime of mechanical elastomeric elements.

Publications

1. Kawak, P., Bhapkar, H. & Simmons, D. S. *Central Role of Filler–Polymer Interplay in Nonlinear Reinforcement of Elastomeric Nanocomposites*. Macromolecules **57**, 9466–9475 (2024).
2. Kawak, P., Bhapkar, H. & Simmons, D. S. *Origin of Heating-Induced Softening and Enthalpic Reinforcement in Elastomeric Nanocomposites*. ACS Macro Lett. **14**, 1867–1873 (2025).
3. Kawak, P., Bhapkar, H. & Simmons, D. S. *Glassy interphases reinforce elastomeric nanocomposites by enhancing percolation-driven volume expansion under strain*. Proceedings of the National Academy of Sciences **123**, e2528108123 (2026).
4. Kawak, P., Drayer, W. F. & Simmons, D. S. *AMDAT: An Open-Source Molecular Dynamics Analysis Toolkit for Supercooled Liquids, Glass-Forming Materials*, and Complex Fluids. Preprint at https://doi.org/10.48550/arXiv.2602.05865, (2026).

Closed-loop, Feedback-driven Design of Metastable Alloys with Predictable Strength-toughness via a Scalable, Agentic Multimodal Diffraction-Chemistry Framework

University of Florida: Douglas Spearot (PI), Ravit Silverstein, Yijia Gu
University of California Santa Barbara: Daniel Gianola, Arda Genc
Thermo-Fisher Scientific: Austin Wade

The next generation of energy, aerospace, nuclear, and manufacturing applications will require structural materials to perform successfully in extreme environments. A promising class of metallic materials for these applications are body-centered cubic (BCC) refractory alloys and multi-principal element alloys (MPEAs). These metals have exceptionally high melting points and perform well during dynamic thermal cycling and under large mechanical loading. It is known that the behavior of BCC refractory alloys and MPEAs is governed by atomic and nanoscale chemistry and lattice distortions; however, resolving and understanding coupled structure–chemistry–deformation relationships at the sub-nanometer scale remains a key barrier to predicting performance and developing next-generation alloy design spaces.

This project develops an artificial intelligence (AI)-driven, closed-loop analysis framework that integrates multimodal diffraction data, co-registered local chemical information, and physics-informed crystallographic phase transformation models. Leveraging advanced characterization techniques such as 4D-STEM and X-ray energy-dispersive spectroscopy (XEDS), this agentic framework enables automated, high-throughput extraction of physically meaningful information from high-dimensional diffraction and compositional datasets. AI-driven feature detection, unsupervised multimodal learning, and physics-informed microstructure modeling are also included to understand structural and chemical states and their evolutions in BCC refractory alloys and MPEAs. This approach enables real-time interpretation of evolving microstructures during *in situ* experiments.

Phase I will establish the AI-enabled analysis pipeline and demonstrate its capability on representative BCC refractory alloys and MPEAs. The project aims to achieve greater than 100x acceleration in data interpretation, reducing analysis time of atomic and nanoscale structural and chemical data from weeks to minutes. Thus, the AI-enabled analysis pipeline will allow real-time detection of local strain evolution, phase transformations and structure–chemistry relationships during *in situ* experiments. These capabilities will support the navigation of alloy design space, with targets of greater than 25% improvement in mechanical performance and a 50% reduction in the breadth of the experimental search space. By drastically reducing development timelines, this project supports the rapid development and deployment of metallic materials with improved strength, toughness, and reliability. The framework will be designed for scalability and future deployment at DOE user facilities, enabling broader access to advanced data analysis tools.

Radiation Effects in High-Entropy Carbides

Izabela Szlufarska

Keywords: High-entropy carbides, defects, diffusion, radiation

Research Scope

The overarching goal of this project is to establish the fundamental physical mechanisms that control radiation-damage resistance in high-entropy carbides and to lay the scientific foundation for the rational design of radiation-tolerant ceramics for nuclear reactor environments.

This overall research is guided by the following hypotheses: (1) Cation size mismatch in HECs strongly influences point-defect migration, defect clustering, and radiation-induced segregation (RIS), through mechanisms that are unique to HECs. (2) Chemical short-range order (CSRO) can either accelerate or impede defect diffusion, depending on the chemical mismatch between diffusing species and the composition of CSRO. (3) Carbon off-stoichiometry significantly alters defect populations, recombination kinetics, and long-term radiation response. (4) CSRO modifies defect production mechanisms by altering threshold displacement energies, cascade morphology, and in-cascade recombination. (5) Reduced thermal conductivity in HECs plays an important role in enhancing radiation tolerance by affecting cascade cooling and defect survival.

Recent Progress

1. Chemical short-range order (CSRO) in HECs

We discovered the presence of chemical short-range order (CSRO) in high-entropy carbides (HECs) and demonstrated that it can significantly influence radiation-induced swelling.

Using hybrid molecular dynamics/Monte Carlo (MD/MC) simulations with machine-learning interatomic potentials developed in this project, we predicted and quantified CSRO in $(Ti_{0.25}V_{0.25}Zr_{0.25}Nb_{0.25})C$ (HEC-Zr) and $(Ti_{0.25}V_{0.25}Mo_{0.25}Nb_{0.25})C$ (HEC-Mo), with predictions subsequently validated using atomic-resolution Z-contrast STEM and 4D-STEM (Fig. 1). Both HECs exhibited a strong tendency for V-V clustering, with important implications for defect diffusion. We further identified two approaches for controlling CSRO: substitution of specific metal cations and thermal treatment. By annealing HEC-Mo, we varied the degree of CSRO without changing composition, allowing us to isolate its effect on radiation response and demonstrate that increased CSRO suppresses radiation-induced swelling. Our results indicate that this behavior arises from the influence of CSRO on defect diffusion and with a negligible influence from defect production, while comparisons between HEC-Mo and HEC-Zr also reveal a strong coupling between CSRO and composition. Ongoing work is aimed at resolving these mechanisms

and establishing how composition and CSRO can be jointly controlled to improve radiation resistance in HECs.

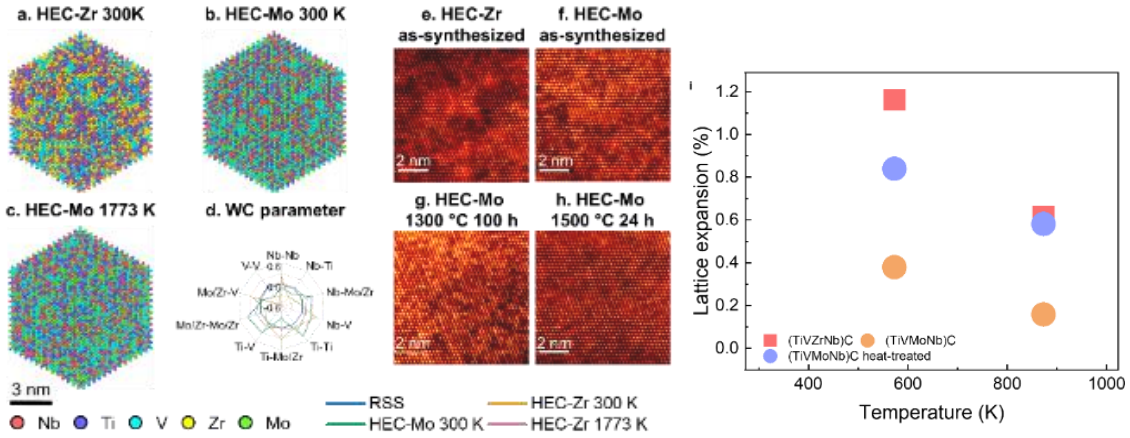

Figure 1 Simulation (a-d) and experimental evidence (e-h) of CSRO in HECs and lattice expansion of HECs after irradiation (i). **Nature Communications 2026**

2. Impact of the complex energy landscape on defect diffusion in HECs

We have discovered that defect recovery processes on the cation sublattice in HECs are dominated by the smallest metal cation. Additionally, we have demonstrated that CSRO in HECs can accelerate diffusion, in contrast to what has been often found in HEAs.

In HEAs defect diffusivity is slowed down compared to pure metals or alloys with fewer components due to HEA's complex energy landscape that arises from lattice distortion caused by mismatch between atomic species. Additionally, it had been found that CSRO in HEAs slows down the diffusion even further because of additional roughening of the potential energy landscape for defects. We hypothesized that the effect of the atomic size mismatch in HECs would be similar, i.e., it would roughen the energy landscape, and the resulting lattice strain would control diffusion. We were able to confirm that the atomic size mismatch between cations in HECs does play an important role in diffusion, but the mechanism is distinct from that in HEAs. Specifically, we observed that diffusion on the metal sublattice is dominated by the smallest cations and that larger species are simply unstable as interstitials and unable to diffuse. This phenomenon was found both in HEC-Mo and HEC-Zr. In both HECs, V interstitials were found to be the dominating species diffusing on the simulation time scales up to the temperatures of 2600K. In the same simulations, interstitials of other cations were found to kick out V from lattice sites and assume lattice site positions. Vacancy diffusion on a cation sublattice was found to be slow with the average migration barriers on the order of 3.9-5.3 eV. To confirm that atomic size plays a critical role in interstitial diffusion, we also simulated HEC where V was replaced with Ta (Ta is comparable in size to Nb, Mo, and Zr). In this case, diffusion became dominated by Ti, which is the smallest of the metal

elements in HECs, confirming that the smallest metal mediates cation diffusion and is expected to control radiation-damage recovery.

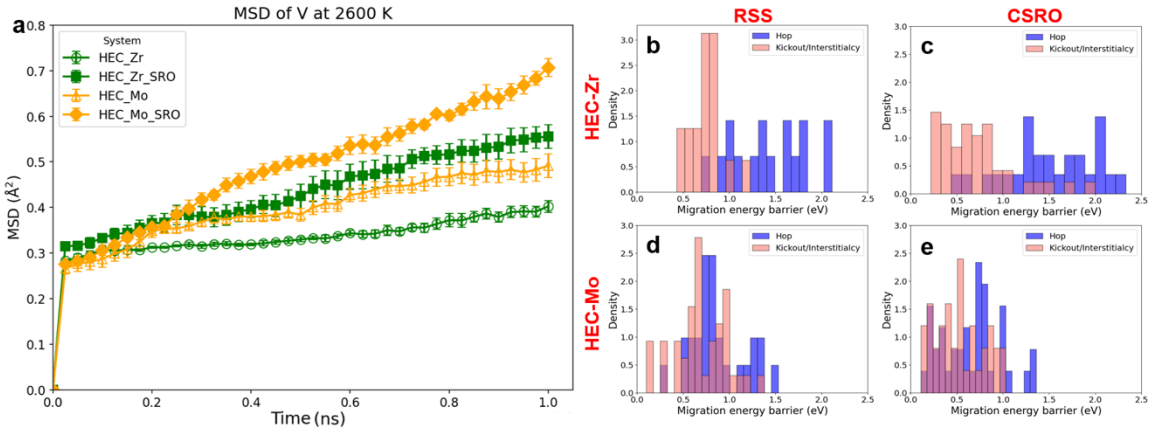

Figure 2 (a) Mean-square-displacement of V interstitial in HEC-Mo and HEC-Zr with and without CSRO. (b-e) Distributions of migration energy barriers for V via interstitialcy and hop mechanisms in the different samples, showing that interstitialcy mechanism has lower energy barriers. ***npj Comp. Materials (2026)***

We have also discovered, that in contrast to HEAs, CSRO in HECs can *accelerate* diffusion (Fig. 2). The reason for CSRO accelerating diffusion in HECs is that CSROs in our samples are rich in V, which enables V diffusion via interstitialcy (V interstitial kicks out another V from its lattice site). Vanadium interstitialcy migration energies are generally lower than energy barriers for the hopping mechanism of V interstitials (Fig. 2 b-e), which means that in HECs without random arrangements of atoms (no CSRO), V spends more time diffusing via the slower hopping mechanism.

3. Radiation-induced segregation (RIS) in covalent ceramics

We established that grain boundaries (GBs) in covalent ceramics can be inherently off-stoichiometric, even in materials with a strong thermodynamic driving force to form line compounds, and demonstrated that irradiation can further modify GB chemistry through radiation-induced segregation (RIS). In earlier studies funded by this project we have found RIS in binary ceramics, such as SiC and TiB_2 and demonstrated that RIS in ceramics is tightly coupled to the complex energy landscape for defect evolution in these materials. Although the changes in chemistry due to RIS occur within a narrow (~1nm wide) region center at GBs, we have shown RIS to have important implications on corrosion Most recently, we extended these studies to the high-entropy carbide $(Ti_{0.25}V_{0.25}Mo_{0.25}Nb_{0.25})C$ (HEC-Mo), where simulations and experiments revealed intrinsic Mo depletion at GBs and irradiation-induced V enrichment accompanied by slight Ti depletion (Fig. 3). These trends are consistent with preferential V diffusion, the relatively low displacement threshold of Ti, and limited bulk Ti diffusion. Together, these results

demonstrate that RIS is prevalent across covalent ceramics but can arise through fundamentally different atomic-scale mechanisms, pointing to the defect-energy landscape, and its coupling to chemistry, bonding, and CSRO, as a key factor governing irradiation-driven changes in GB composition and properties.

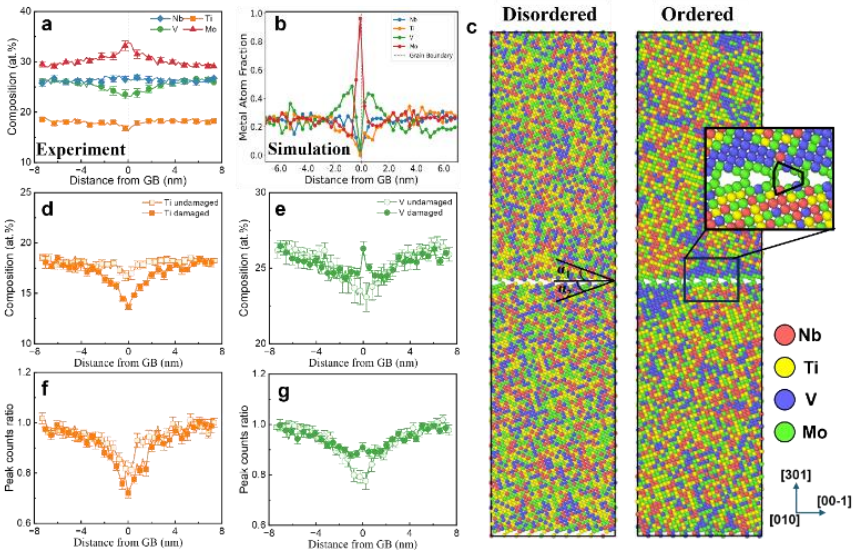

Figure 3 Local composition near the GBs before irradiation in (a) experiments and (b) simulations. Radiation-induced changes in composition near a GB in experimental samples (d,f) and simulations (e.g.). **npj Comp.** ***Materials (2026)***

Future Plans

Future plans include: understanding how the chemistry of CSRO couples to the chemistry of diffusing species to accelerate or slow down diffusion using experiments and molecular simulations based on machine-learning potentials; understanding the role of chemical complexity in primary damage production and investigating the hypothesis that thermal conductivity plays a key role in determining cascade efficiencies; understanding the role of C sub-lattice and its stoichiometry in defect diffusion; and understanding the impact of radiation damage in HECs on mechanical properties as our preliminary studies indicate that radiation can increase both strength and toughness of these materials.

Publications

1. MW Qureshi, S. Wei, A. Annamareddy, J. Chen, J. Mao, H. Zhang, and I. Szlufarska, *Chemical short-range order accelerates defect diffusion in high-entropy carbides*, npj Computational Materials **1456** (2026).
2. S Wei, MW Qureshi, J Wei, L Liu, X Hu, J Xi, S Attarian, R Su, H Zhang, E. Willing, X Wang, K Sridharan, PM Voyles, JH Perepezko, and I. Szlufarska, *Short-range order in high-entropy carbides*, Nature Communications **17**, 2362 (2026)
3. L He, S Wei, X Hu, W Zhang, L Shi, H Zhou, I. Szlufarska, R Su, and H. Zhang, *Critical role of Co/O impurities in suppressing deuterium diffusion and supersaturated layers in tungsten*, Acta Materiala **299**, 121457 (2025)
4. MW Qureshi, S Wei, L Liu, S Paul, JY Kim, C Zhang, X Wang, JH Perepezko, D Morgan, and I. Szlufarska, *Predictive screening of phase stability in high-entropy carbides*, Materials Advances **6**, 5286 (2025)
5. Xi, J., Zhang, H., Su, R., Wei, S., Hu, X., Queylat, B., Kim, T., Couet, A. & Szlufarska, I. *Coupling of radiation and grain boundary corrosion in SiC*. npj Materials Degradation **8**, 16- (2024)
6. Wei, S., Qureshi, M. W., Xi, J., Kim, J. Y., Wang, X., Wei, J., Su, R., Liu, L., Nachlas, W. O., Perepezko, J. H., Zhang, H., and Szlufarska, I. *Radiation induced segregation in titanium diboride*. Acta Materialia **267**, 119739 (2024).
7. Quillin, K., Sasidhar, K. N., Qureshi, M. W., Yeom, H., Szlufarska, I. & Sridharan, K. *Unusual nanoscale amorphization of metallic chromium interfacing with SiC under high energy irradiation*. Acta Materialia **278**, 120236 (2024).
8. He, L., Zhang, W., Wei, S., Hu, X., Zhang, G., Su, R., Shi, L., Zhang, H. & Szlufarska, I. *Real-Time Analysis of Dynamic Deuterium Retention in Plasma-facing Materials Using a Novel Dual Ion Beam System*. Submitted (2025).

Mapping the Damage Evolution Hierarchy in Compositionally Complex Alloys

Mitra L. Taheri (Johns Hopkins), Michael L. Falk (Johns Hopkins), and Jaime Marian (UCLA)

Keywords: Multi-Principal Element Alloys, Irradiation, Short-Range Order, Self-interstitials

Research Scope

This work aims to understand how irradiation damage evolves in multi-principal element alloys (MPEAs) as compared to traditional dilute alloys. MPEAs are promising for next-generation nuclear systems. Unlike dilute alloys, where the main mechanism for controlling defect behavior is solute–defect binding, MPEAs exhibit complex, spatially varying chemical environments that fundamentally alter defect energetics, migration, and recombination. This multi-PI effort will articulate and test a hierarchical framework linking local lattice characteristics to emergent irradiation behavior. This will be achieved by examining how atomic-scale features—such as strain fields and chemical short-range order—affect point-defect recombination, early-stage defect clustering, and the subsequent formation of extended defect networks. This multiscale perspective provides a mechanistic basis for understanding how complexity propagates upward to influence macroscopic radiation tolerance. Three hypotheses guide the work: (1) defect concentration controls the transition from rafted dislocation structures to entangled loop networks, (2) defect gradients and vibrational properties define thresholds for defect migration and stability, and (3) grain boundary structures evolve in response to changes in the surrounding defect and chemical landscape. To address our hypotheses, we will leverage our toolset of multiscale modeling, experiment, and machine learning tools, to pave a pathway to predictive design and optimization of modern energy concepts.

In our current program, we seek to resolve the following unknowns in defect evolution and microstates in MPEAs:

1. What is the role of MPEA stoichiometry in microstate motif development, independent of defect bias in the matrix?
2. How does the heterogenous defect-evolution landscape depend on order-driven phenomena at the cascade stage, defect migration energies, or reverse bias from strongly metastable GBs in MPEAs?
3. How does the near-GB dislocation network mediate the phenomena in (1) and (2) and does the network evolve independently of the matrix and GB regions?

Recent Progress

Recent progress has centered on addressing Hypothesis 1, investigating hierarchical defect network evolution under irradiation in dilute alloys and MPEAs. The team combined displacement-cascade and defect-accumulation modeling, a coupled rate-theory/kinetic Monte Carlo (KMC) framework, in situ and post-mortem electron microscopy, atom probe tomography (APT) and machine-learning-enabled tracking of GB microstates to directly compare defect

network evolution in the equiatomic MPEA MoNbTaW against its pure and dilute Mo-5Ta counterparts.

Cascade-Driven Defect Production and Loop Character in MoNbTaW. Atomistic displacement cascade simulations were performed in the MoNbTaW MPEA, showing defect production scales with PKA energy across all systems, with Frenkel Pair (FP) counts in the MPEA just below pure W. However, FP counts alone do not capture defect character: at PKA energies ≥50 keV, small loops form initially as SIA clusters, followed by both SIA and vacancy loops that increase in size and number. Most loops are 1/2<111>, with occasional <100> loops forming at higher energies.

Frenkel-Pair Accumulation Simulations Reveal Dose-Rate Dependent Defect Lifetimes. To probe post-cascade dynamics and extended defect formation, FP accumulation molecular dynamics simulations were conducted for Mo-5Ta and MoNbTaW, progressively introducing FPs into equilibrated cells at three insertion rates to mimic continuous irradiation. Lower FP dose rates yield longer defect lifetimes **(Figure 1a)**. At high dose rate, SIAs are more likely to interact with nearby sinks (vacancies and dislocations) are rapidly absorbed by loops before recombining, leading to extended vacancy lifetimes and excess vacancy populations that exacerbate damage **(Figure 1b)**. In the dilute alloy, recombination rates are consistently faster, resulting in lower vacancy counts. Since cascade simulations show similar initial FP production across systems, differences in extended defect formation arise from defect migration barriers. Interestingly, the FP models suggest a selective stability of Mo SIAs in MoNbTaW as seen by their long lifetimes under low dose rate. This leads to Mo clustering due to irradiation, which was confirmed experimentally by atom probe tomography after ex-situ Kr^{2+} ion irradiation.

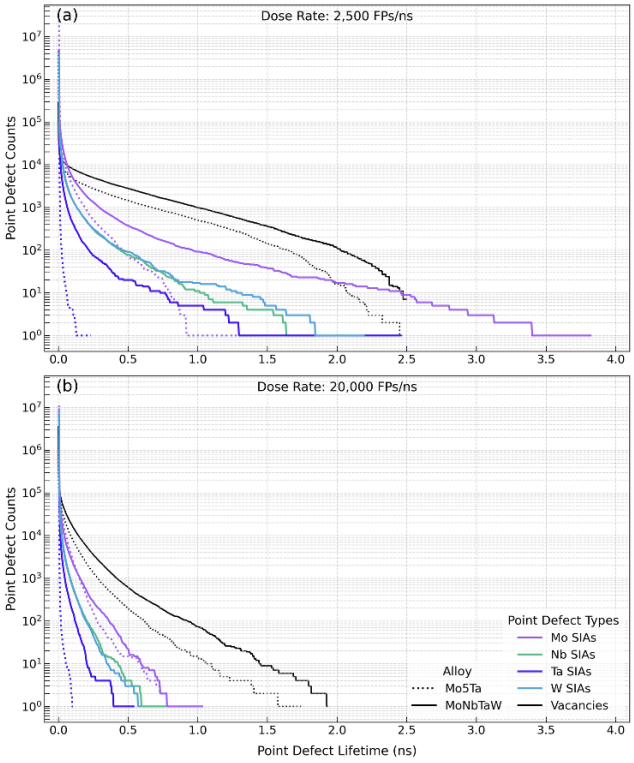

Figure 1. Point defect survivability during Frenkel pair insertion. (a) Low dose rate (2,500 FPs/ns) models show strong stabilization of Mo as interstitial atoms and enhanced vacancy recombination in the dilute alloy. (b) Both interstitial and vacancy survival times decrease substantially given high dose rates (20,000 FPs/ns).

Self-Interstitial Energetics and Dumbbell Stability Govern the SRO Landscape in MPEAs. Frenkel-pair accumulation simulations reveal a selective stability of Mo self-interstitial atoms (SIAs) in MoNbTaW. The equilibrium order for MoNbTaW, shown in **Figure 2a,** predicts

repulsion of Mo-Mo pairs. However, during FP creation, **Figure 2b** shows strong Mo-Mo ordering due to highly stable Mo-Mo dumbbells, which our previous work has predicted as the lowest energy dumbbell chemistry for this alloy [1]. The interstitial landscape in MPEAS during Frenkel pair production is governed by low-energy self-interstitial atoms, which directly influences the evolution of chemical order. This contrasts with dilute alloys where point defect recombination is primarily controlled by solute–vacancy binding energies. This distinction opens a pathway for control of SRO in MPEAs based purely on SIA energetics [2].

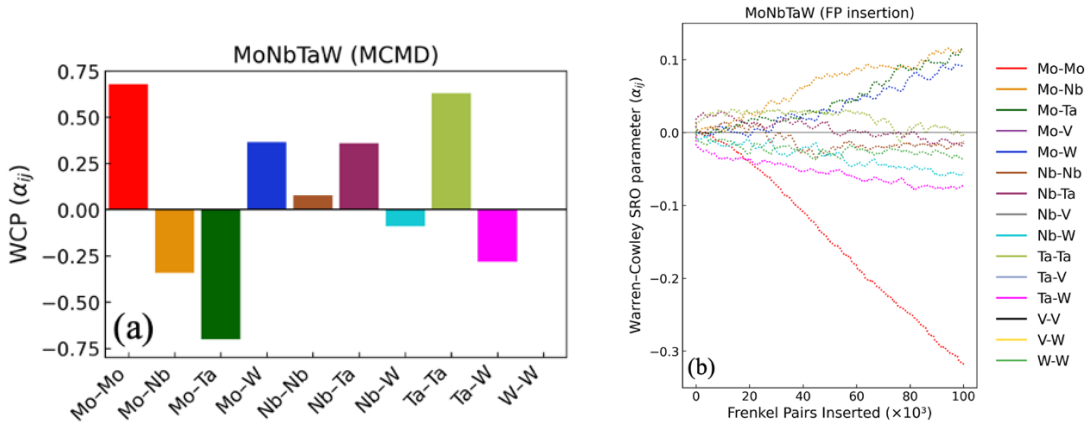

Figure 2. Warren-Cowley parameter predictions for MoNbTaW. All calculations were performed at 300 C. (a) Equilibrium order predicted using hybrid Monte-Carlo Molecular Dynamics simulations. (b) Order evolution observed during Frenkel pair creation simulations.

Role of Chemical Complexity in Defect Evolution Mechanisms. In situ TEM during 1 MeV Kr^{2+} ion irradiation, followed by post-mortem ABF-STEM were performed to provide dynamic observation of defect evolution morphology in MoNbTaW and the dilute Mo-5Ta. In Mo-5Ta, 1/2<111> loops align along <110> directions, forming rafted networks. In contrast, MoNbTaW exhibits more random loop distributions that evolve into entangled chains pinned at high-stress regions. MoNbTaW shows greater heterogeneity in loop size and spatial distribution, along with faster defect density accumulation. Post-mortem high-resolution ABF-STEM in **Figure 3** confirms strong <111> loop rafting in Mo-5Ta and mixed-character entanglement in MoNbTaW. These results indicate that transformation from 1/2<111> to <100> dislocations occurs more readily in MPEAs, where numerous small loops nucleate rather than fewer large loops dominating [3].

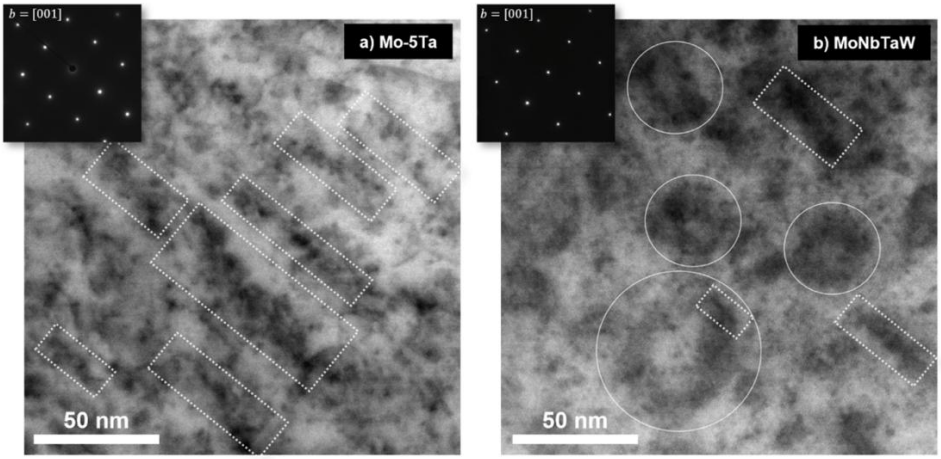

Figure 3. On-zone ABF-STEM comparison of dislocation morphologies in Mo-5Ta and MoNbTaW. a) Loop rafts of <111> loop types and black spots are in Mo-5Ta outlined by dashed rectangles follow [011] crystallographic direction. While morphology in (b) MoNbTaW is more complex. Some striated features in [011] comparable to loop raft morphologies in Mo-5Ta are outlined with dashed rectangles, while large, indistinct circular loops, possibly indicating in-plane <001> loop-types are marked by solid circle overlays. Inset images show [001] zone axis diffraction condition.

Coupled Rate-Theory and Kinetic Monte Carlo Modeling Quantifies Defect Kinetics. A coupled rate-theory/KMC framework quantifies SIA and vacancy kinetics in MoNbTaW, treating SIA migration as a Markov process on a chemically disordered energy landscape. Loop concentration increases then saturates while vacancy concentration and loop size continue to grow, with both SIA and vacancy concentrations exceeding dilute-alloy values. Recombination follows Arrhenius kinetics with an effective barrier of 4.889 eV — above typical migration energies due to the added cost of spatial encounter — and scales with system volume as $\Gamma \propto V^n$ ($n \approx -2.0$ to -2.5), providing a predictive scaling law consistent with independent KMC estimates of interstitial survival rates.

Compositional Complexity Shapes the Microstate Landscape Near Grain Boundaries. Complementary work has shown that increasing alloy chemical complexity broadens the population of structural motifs accessible to a grain boundary under irradiation, with more microstates becoming available as both irradiation dose and solute content increase [4]. What remains open is how this GB-level microstate variability, and its coupling to the adjoining denuded zone, is shaped by the matrix-level defect and dumbbell behavior identified.

Future Plans

A priority is to directly test the link between chemistry and structure suggested by these results. We will extend our approach to determine whether the entangled dislocation networks that emerge during the raft-to-network transition are themselves chemically enriched in Mo. In parallel, we are extending this framework to a new vanadium-containing refractory alloy system, testing whether V-V dumbbells exhibit analogous stability and segregation behavior to that observed in the Mo-Mo dumbbells; confirming this would establish the raft-to-network transition mechanism as a

generalizable design principle across group-V and group-VI interstitial chemistries rather than a Mo-specific effect.

More broadly, we intend to frame our future work around the full radiation-response ecosystem to establish a framework for how microstate-level behavior propagates through the near-GB region to shape point defect concentration, recombination, and raft stability in the surrounding matrix. *Pursuits will address the following overarching questions:*

1. Do the defect networks observed near the GB originate from complexity within the surrounding matrix or reflect saturation and motif character intrinsic to the GB?
2. Will any single region of this ecosystem behave in a distinct way in CCAs or will increasing chemical complexity compound the same behavior across all three regions?
3. Are the governing mechanisms in each region fundamentally altered by chemical complexity, or do the same post-cascade mechanisms persist across dilute and highly concentrated alloys?

References

1. Zhou, X., Barnett, A., Mang, E. H., Falk, M. L., Taheri, M. L., & Marian, J. *Self-interstitial atom properties in Nb–Mo–Ta–W alloys*. Computational Materials Science, *234*, 112765. (2024).
2. A.K. Barnett, Zhou, X., Mang, E.H., Marian, J., Falk, M.L, Taheri, M.L., "Radiation Induced Ordering in Multi-principal Element Alloys: Not All Interstitials are Created Equal," Acta Materialia, in edit 2026
3. Mang, E.H., Barnett, A.K., Rose, M.N., Chen, W-Y, Habaruk, E., Baldo, P, J. Marian, M.L. Falk, M.L. Taheri, "Influence of Chemical Complexity on Radiation Damage Evolution in Refractory Alloys," Submitted 2026
4. Barnett, Annie K.; Marian, Jaime; Taheri, Mitra L.; Falk, Michael L., "Chemical complexity enhances grain boundary absorption efficiency through expansion of microstate phase space", Physical Review Materials, Volume 9, 083604, Published, 2025, DOI: 10.1103/qnmb-nd7k.

Publications

1. Barnett, Annie K.; Marian, Jaime; Taheri, Mitra L.; Falk, Michael L., "Chemical complexity enhances grain boundary absorption efficiency through expansion of microstate phase space", Physical Review Materials, Volume 9, 083604, Published, 2025, DOI: 10.1103/qnmb-nd7k.
2. El-Atwani, Osman; Barnett, Annie K.; Martinez, Enrique; Han, Jian; Leff, Asher C., et al., "Grain boundary metastability controls irradiation resistance in nanocrystalline metals", Materials & Design, Volume 260, 115038, Published, 2025, DOI: 10.1016/j.matdes.2025.115038.
3. Foley, Daniel L.; Mang, Emily H.; Wang, Yongqiang; Spearot, Douglas E.; Taheri, Mitra L., "Low frequency band pass Fourier filtering for irradiation damage analysis in the transmission electron microscope", Micron, Volume 196-197, 103864, Published 2025, DOI: 10.1016/j.micron.2025.103864.
4. Mang, Emily Hopkins; Barnett, Annie K.; He, Sicong; Nathaniel, James E.; Jacobs, Ryan, et al., "Metastable grain boundary sink behavior revealed through deep-learning image analysis", Journal of Nuclear Materials, Volume 622, 156369, Published, 2026, DOI: 10.1016/j.jnucmat.2025.156369.
5. Zhou, Xinran; Wang, Xinyao; Barnett, Annie; Mang, Emily H.; Falk, Michael L., et al., "Primary defect production from molecular dynamics simulations of high-energy displacement cascades in NbMoTaW alloys", Physical Review Materials, Volume 10, 023601, Published, 2026, DOI: 10.1103/ngh9-3zkn.
6. Mang, Emily H.; Wang, Yongqiang; Taheri, Mitra L., "Surface stability of Mo-based compositionally complex alloys and evidence of radiation-induced dynamic recrystallization", Materials Letters, Volume 397, 138862, Published, 2025, DOI: 10.1016/j.matlet.2025.138862.
7. Yu, J., Barnett, A.K., Zhou, X., Falk, M.L., Taheri, M.L., Marian, J., "Point-defect role reversal controls irradiation tolerance in refractory complex alloys", Physical Review Letters, Submitted July 2026

8. A.K. Barnett, Zhou, X., Mang, E.H., Marian, J., Falk, M.L, Taheri, M.L., “Radiation Induced Ordering in Multi-principal Element Alloys: Not All Interstitials are Created Equal,” Acta Materialia, in edit 2026
9. Mang, E.H., Barnett, A.K., Rose, M.N., Chen, W-Y, Habaruk, E., Baldo, P, J. Marian, M.L. Falk, M.L. Taheri, “Influence of Chemical Complexity on Radiation Damage Evolution in Refractory Alloys,” Submitted 2026
10. Barnett, A.K., Foley, D.L, Falk, M.L., and Taheri, M.L, “Signatures of CoCrNi short range order and its Toplogy,” Submitted 2026

Mechanisms of Irradiation-Induced Grain Subdivision

Michael Tonks, Assel Aitkaliyeva, and Simon Phillpot (University of Florida)

Keywords: Recrystallization, Radiation Damage, In Situ Ion Irradiation, Molecular Dynamics

Research Scope

In irradiation-induced grain subdivision (IIGS), metals and ceramics form nanocrystalline grains under irradiation [1,2]. There is debate on whether IIGS results from subgrain formation that forms low angle grain boundaries (LAGBs) or from recrystallization that forms high angle grain boundaries (HAGBs). Recent experimental results by co-PI Aitkaliyeva and others [3,4] have revealed that subgrains with LAGBs that form during IIGS transition to form HAGBs. This process is similar to continuous dynamic recrystallization (CDRX) [5] and therefore comparing the two processes will provide critical insights into the fundamental mechanisms of both IIGS and CDRX. In this project, we are identifying the mechanisms driving IIGS and comparing them to CDRX mechanisms to better understand both phenomena. The project is built on three hypotheses:

(1) **The governing mechanisms for IIGS are the same as for CDRX, except that dislocations are produced by irradiation rather than deformation.** This hypothesis is tested using in-situ ion irradiation of aluminum (Al), atomistic simulations of dislocation formation from radiation damage in Al, and mesoscale modeling to interpret the observed behavior.
(2) **An additional source of stress is required to drive the motion of dislocations produced by irradiation to transform LAGBs to HAGBs.** This hypothesis is tested with in-situ ion irradiations of Al samples loaded in compression, as well as atomistic simulations with and without applied load and mesoscale modeling that represents grain rotation due to deformation.
(3) **The IIGS mechanisms are the same in metals and ceramics since the dislocations are generated due to radiation damage and do not require significant ductility.** We test this hypothesis by completing in-situ ion irradiation, atomistic simulation, and mesoscale modeling of yttria-stabilized zirconia (YSZ) and comparing the behavior with that shown in Al.

We are testing these hypotheses using a combination of ion irradiation experiments, atomistic simulation, and mesoscale modeling. We are utilizing various characterization techniques during ex-situ and in-situ irradiations to investigate the mechanisms governing IIGS and CDRX, define how radiation damage results in dislocation networks, detail formation of LAGBs from dislocation networks, and observe the transition of LAGBs to HAGBs. We are quantifying formation of LAGBs from dislocation networks to produce subgrains during IIGS and comparing it with the subgrain production observed in CDRX. The atomistic simulations are using molecular dynamics (MD) with established empirical potentials to capture the material behavior. The mesoscale simulations will include dislocation formation, subgrain formation, and subgrain rotation.

Recent Progress

Experimental Progress:

To test Hypotheses 1 and 3, in situ ion irradiation was used to observe the evolution of dislocation structures in Al. Irradiations were performed to damage levels of up to 0.3 dpa (displacements per atom). At low damage levels (0-0.03 dpa), minimal dislocation motion was observed, indicating that irradiation-induced defect production had not yet produced substantial dislocation rearrangement. As the damage level increased to 0.08 dpa, dislocation loop annihilation and alignment became progressively more active. The development of organized dislocation structures with increasing damage is consistent with dynamic recovery (DRV), in which dislocations continuously rearrange, annihilate, and align to reduce the microstructure's stored energy. This behavior provides direct evidence that irradiation promotes the recovery processes expected to precede grain subdivision.

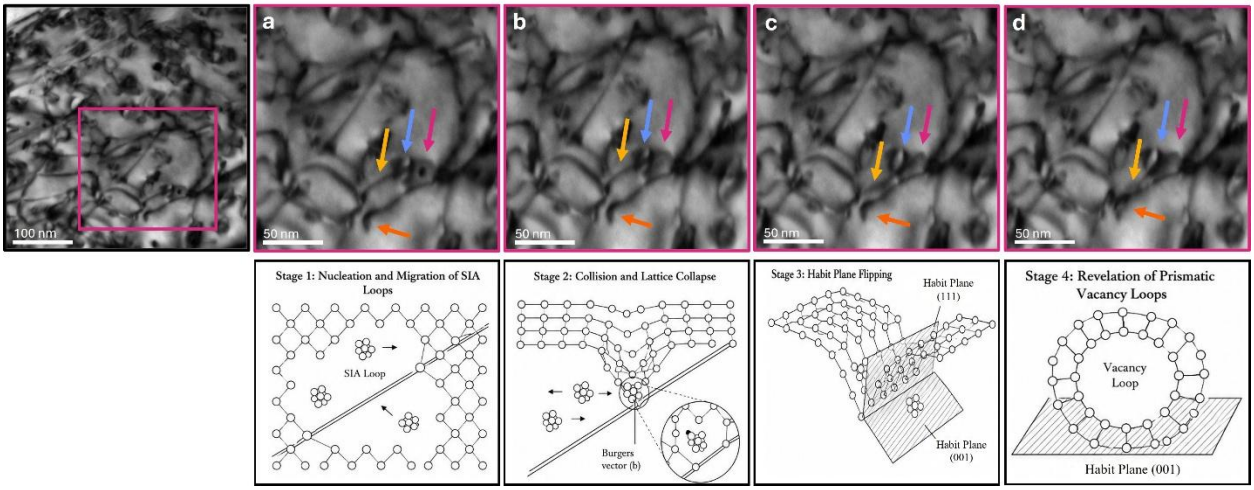

Figure 1: Interaction between a Shockley partial dislocation and a Frank dislocation loop. The pink box shows an enlargement of the cellular dislocation structure to highlight the unfaulting mechanism. Frames (a)-(d) are taken at 2 consecutive frames per second. Figure 1a shows a nucleated Shockley partial form within the Frank loop, indicated by the pink arrow. Figure 1b shows the partial sweep left across the loop and interacting with the Frank loop, removing its stacking fault. Figure 1c shows the Frank loop collapsing because of the stacking fault being removed, and displacing the upper dislocation line downward, indicated by the yellow arrow, while simultaneously revealing an edge vacancy loop, indicated by the blue arrow. Figure 1d shows that as the collapse continues, the lower line becomes unstable, and the upper line sweeps beneath it, revealing an additional edge vacancy loop at the tail of the lower line. The two dislocation lines subsequently reconnect to form a perfect, glissile loop that can migrate and ultimately annihilate at the free surface. The schematics illustrate the proposed reaction sequence and the associated reorientation of edge loops within the imaging plane.

A dislocation-loop unfaulting was observed throughout the irradiation and became particularly apparent as the damage level approached 0.3 dpa. Unfaulting converts a sessile, faulted loop, most commonly a Frank-type loop, into a glissile perfect dislocation loop through the removal of its stacking fault. In our case, unfaulting occurred through the interaction between a Shockley partial and a Frank loop, as shown in Figure 1, which allowed incorporation of sessile irradiation-induced loops into the mobile dislocation population, thereby contributing to the

evolving dislocation network. The resulting dislocation migration and rearrangement contributed to the formation of a cellular dislocation structure, with the initial cell wall developing at approximately 0.06 dpa. Following its formation, dislocations were repeatedly generated, annihilated, and aligned within the cell wall throughout the remainder of the irradiation, resulting in continued refinement and definition of the cellular structure. This behavior is akin to DRV and represents the early stages of polygonization, in which dislocations rearrange into LAGBs. The observed unfaulting reaction and subsequent dislocation rearrangement provide a mechanistic link between irradiation-induced defect reactions, cellular structure formation, and the development of microstructural precursors to grain subdivision via CDRX. The edge loops revealed during the reaction are assumed to remain Frank-type throughout the remainder of the irradiation because their sessile character prevents significant glide.

Together, the observed unfaulting and DRV mechanisms provide experimental evidence for the proposed IIGS sequence. Although grain subdivision has not yet been directly captured, the development of organized dislocation walls, continued dislocation rearrangement, and irradiation-driven loop reactions demonstrates that the microstructure is progressing toward the conditions required for subdivision. In particular, the results support the hypothesis that irradiation-induced dislocation structures initially form LAGBs through polygonization and that continued dislocation accumulation and rearrangement can increase boundary misorientation toward HAGBs. These observations establish the dislocation-reaction and recovery mechanisms that precede grain subdivision and provide a mechanistic foundation for interpreting subsequent experiments.

Modeling Progress:

We have also tested Hypothesis 1 with MD simulations. A 5 keV displacement cascade in Al produced ~45 stable Frenkel pairs, which was used to calibrate our accelerated molecular dynamics framework, the Iterative Kinetic Approach (IKA) [P1] (see Fig. 2(a)).

Comparison with conventional cascade-overlap simulations shows that IKA reproduces key irradiation-induced mechanisms, including defect clustering, dislocation-loop formation and interactions, and SFT formation. Its computational efficiency enables simulations to reach substantially higher damage levels, revealing continued defect accumulation and loop reorganization at only ~2.2% of the computational cost of conventional cascade simulations.

We used IKA to investigate irradiation-induced damage mechanisms in Al up to 0.175 dpa and compare them with CDRX. We observe progressive defect accumulation and identify mechanisms of dislocation nucleation, interaction, and absorption, revealing three regimes: recombination-driven annihilation, defect accumulation, and sink-controlled absorption [P2], as shown in Fig. 2(b). Frank partials nucleate first, even at low damage, while at higher damage their dissociation into Shockley and stair-rod partials accelerates, ultimately promoting SFT nucleation and growth. The coupled evolution of interstitial and vacancy loops and SFTs increases irradiation hardening at 300 K, exhibiting similarities to deformation-driven damage (see Fig. 2(c)).

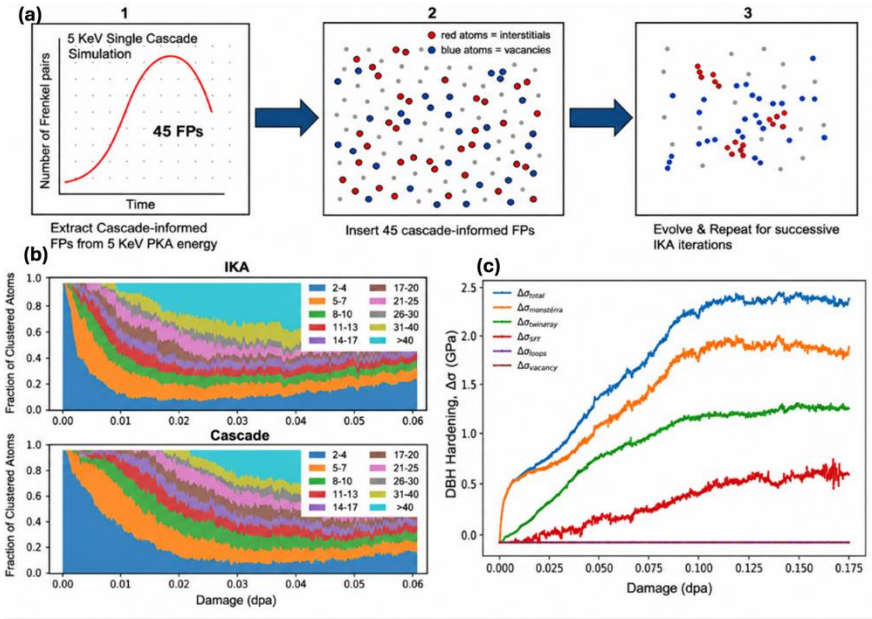

Figure 2: Irradiation induced damage evolution in Al. (a) Schematic of the iterative IKA workflow: 1) getting a cascade-informed number of FPs; 2) seeding it into the domain; 3) evolving for 35 ps and thereafter. (b) Comparing interstitial cluster size distribution from IKA and CA at different size ranges [P1], (c) Irradiation induced hardening contribution from five different obstacles, $\Delta\sigma_{\text{monsterra}}$, $\Delta\sigma_{\text{twinarray}}$, $\Delta\sigma_{SFT}$, $\Delta\sigma_{\text{loops}}$, $\Delta\sigma_{\text{vacancy}}$.

To compare these results with restructuring mechanisms observed in nuclear fuels, we examine whether temperature in metals may play a role analogous to irradiation-driven processes in fuels. Post-irradiation annealing of Al from 300–800 K reveals three distinct regimes: defect reorganization and dislocation-network growth at 300–500 K, a transition near 600 K, and recovery-dominated evolution at 700–800 K, with vacancy mobility governing the transition between these regimes

Finally, using the results from the MD and the experiments, we are now building a cluster dynamics (CD) rate theory model to predict the process of radiation defects growing into dislocation loops and then dislocation networks and estimate threshold for Grain Subdivision. This part of the work is currently ongoing.

Future Plans

We are continuing this work to test Hypotheses 2 and 3. For Hypothesis 2, we are seeking to determine if applied stress is necessary to transition from LAGB to HAGBs. This will be

achieved by applying stress in addition to irradiation in the in situ experiments and by applying load in MD simulations. This additional work will be performed at Sandia National Laboratory's Ion Beam Laboratory through a recently awarded Nuclear Science User Facilities Rapid Turnaround Experiment and Center for Integrated Nanotechnologies User Proposal, "Identifying the Roles of Irradiation and Stress in Dislocation-Mediated Grain Subdivision" (#26-5666) and "Understanding the Mechanisms behind Irradiation-Induced Grain Subdivision" (2026A0222). For Hypothesis 3, we will carry out similar experimental and modeling work with YSZ, focusing on identifying differences in the IGGS mechanisms between metals and ceramics.

References

[1] V.V. Rondinella, T. Wiss, Mater. Today 13 (2010) 24–32.
[2] L.M. Wang, S.X. Wang, R.C. Ewing, A. Meldrum, R.C. Birtcher, P. Newcomer Provencio, W.J. Weber, H. Matzke, Mater. Sci. Eng. A 286 (2000) 72–80.
[3] C.A. Smith, S. Biswas, B.D. Miller, B. Kombaiah, D. Frazer, D.D. Keiser, A. Aitkaliyeva, J. Nucl. Mater. 563 (2022) 153617.
[4] T.J. Gerczak, C.M. Parish, P.D. Edmondson, C.A. Baldwin, K.A. Terrani, J. Nucl. Mater. 509 (2018) 245–259.
[5] H.K. Zhang, H. Xiao, X.W. Fang, Q. Zhang, R.E. Logé, K. Huang, Mater. Des. 193 (2020) 108873.

Publications

[P1] A. S. Issaka, S. Wicks, V. Yadav, A. Aitkaliyeva, M. R. Tonks, S. R. Phillpot, Cascade-informed accelerated simulation of complex defect structures in irradiated aluminum using iterative kinetic approach, **Materials Letters**, Volume 414, 140572, 2026.
[P2] A. S. Issaka, S. Wicks, V. Yadav, A. Aitkaliyeva, M. R. Tonks, S. R. Phillpot, Mechanisms of Microstructural Evolution and Degradation in Aluminum under High Damage Irradiation, **npj Materials Degradation** (Accepted), 2026.
[P3] A. S. Issaka, S. Wicks, V. Yadav, A. Aitkaliyeva, M. R. Tonks, S. R. Phillpot, Temperature-Dependent Defect Evolution and Mechanical Recovery During Post-Irradiation Annealing of Aluminum, (Under Preparation).

Irradiation Defect Formation and Evolution in Doped Metallic Interfaces

Jason R. Trelewicz, Stony Brook University; Andrea M. Hodge, University of Southern California

Keywords: helium implantation, radiation defects, amorphous-crystalline interfaces, nanometallic multilayers, amorphous complexions

Research Scope

The scope of this research project is focused on addressing knowledge gaps related to the scientific questions: (i) how are the mechanisms of bubble formation and evolution at interfaces affected by the presence of a dopant species introduced to stabilize the interfacial network, and (ii) how are these mechanisms connected to interfacial structure, particularly in interfaces containing enhanced disorder relative to the crystalline matrix? The overarching hypothesis is that, at doped metallic interfaces, changes in the local energy landscape arising from chemical contributions of the solute species and associated structural transitions dictate gas bubble nucleation, which in turn delays the critical concentration for bubble coalescence and grain boundary decohesion. To test this hypothesis, nanometallic multilayers (NMMs) composed of crystalline-amorphous Fe/Fe–38 at.% W layers were synthesized with Fe–W layer thicknesses of 5, 10, and 20 nm while maintaining a constant 20-nm crystalline Fe layer thickness. The scope of this highlight includes *in situ* TEM heating experiments to investigate the mechanisms governing thickness-dependent thermal transitions, followed by He implantation experiments to map the effects of layer thickness on microstructural stability in the presence of He-induced defects. Multimodal characterization workflows combining transmission electron microscopy (TEM) with TEM-informed synchrotron X-ray scattering and diffraction experiments were employed for microstructural and phase analyses. Collectively, these experiments test the hypothesis that increasing the amorphous interlayer thickness enhances thermal stability and irradiation tolerance by (i) suppressing interdiffusion, intermetallic precipitation, devitrification, and layer breakdown and (ii) promoting He accommodation and redistribution, thereby suppressing cluster and cavity growth.

Recent Progress

In-situ TEM heating experiments were performed on the Fe/Fe–38 at.% W NMMs containing 5 nm (20-5 NMM) and 20 nm (20-20 NMM) amorphous Fe-W layers to probe the effect of thickness on stability. Both configurations retained their amorphous layers up to 500 °C; however, substantial differences in the NMM architecture began to emerge upon exposing the samples to higher temperatures as highlighted in **Figure 1**.

In the 20-5 NMM, redistribution of W across the interfaces was detected following heating to 500 °C, preceding the first directly observed intermetallic precipitation event at 668 °C. Continued precipitation and growth progressively consumed the amorphous Fe-W layers, and complete crystallization was apparent at approximately 737 °C. In contrast, the 20-20 NMM exhibited minimal interlayer diffusion following heating to 500 °C and retained its multilayer morphology and amorphous Fe-W phase up to 750 °C. Initial precipitation was delayed until approximately 815 °C, followed by progressive crystallization during heating to 850 °C. An extended isothermal hold at 850 °C was required to drive further degradation of the remaining multilayer structure. These observations support the first component of our hypothesis: increasing amorphous interlayer thickness substantially suppresses interdiffusion, delays intermetallic precipitation by approximately 150 °C, and increases resistance to complete layer breakdown.

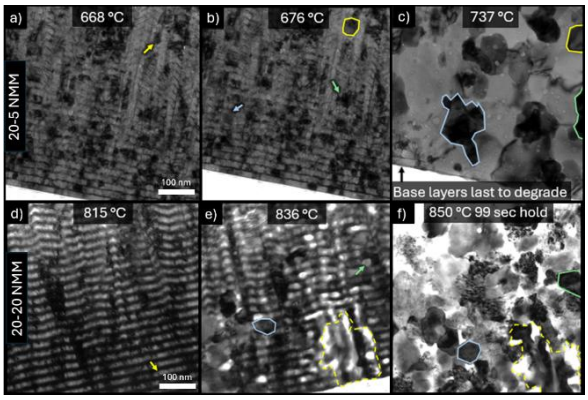

Figure 1: *In-situ* BF-TEM of the (a-c) 20-5 and (d-f) 20-20 NMMs. Arrows mark intermetallic precipitation and outlines track precipitate growth.

The consequences of this thickness-dependent thermal stability were subsequently investigated under He implantation. The 20-5, 20-10, and 20-20 NMMs were implanted with 200 keV He^+ ions at 250 and 500 °C to three fluences of 1 x 10^{15}, 1 x 10^{16}, and 1 x 10^{17} He^+ ions/cm^2, with the two temperatures selected to probe defect evolution below and above the approximate He-V mobility transition [1]. XRD measurements across the complete implantation matrix revealed a strong dependence of phase stability on amorphous interlayer thickness (**Figure 2**). The 20-5 NMM progressively lost the broad amorphous Fe-W contribution with increasing temperature and fluence, accompanied by the emergence of crystalline Fe-W intermetallic reflections. The 20-10 NMM exhibited intermediate behavior, with partial retention of the amorphous phase and increasing crystallization at elevated temperature and fluence. In contrast, the amorphous contribution remained evident in the 20-20 NMM throughout the

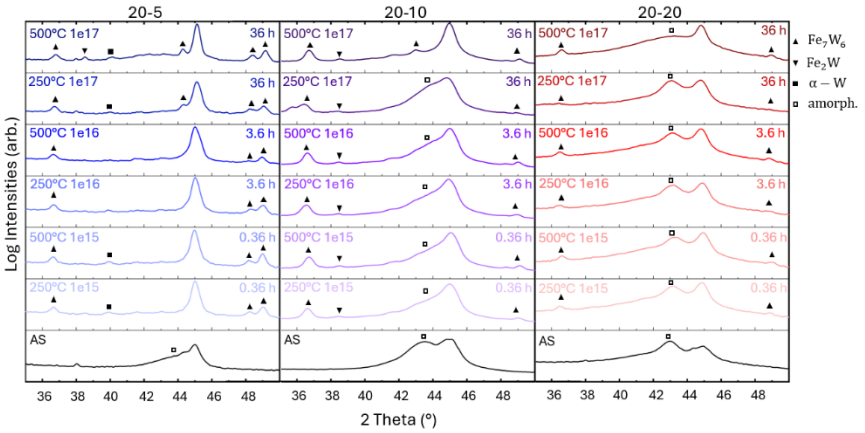

Figure 2: XRD patterns of the 20-5, 20-10, and 20-20 Fe/Fe-W NMMs following He^+ implantation as a function of temperature and fluence. Symbols identify crystalline, intermetallic, and amorphous phases.

implantation matrix, including the most extreme condition of 36 h at 500 °C to 1 x 10^{17} He^+ ions/cm^2. These results demonstrate that the thickness-dependent stability identified during *in-situ* heating persists under the combined thermal and irradiation environment.

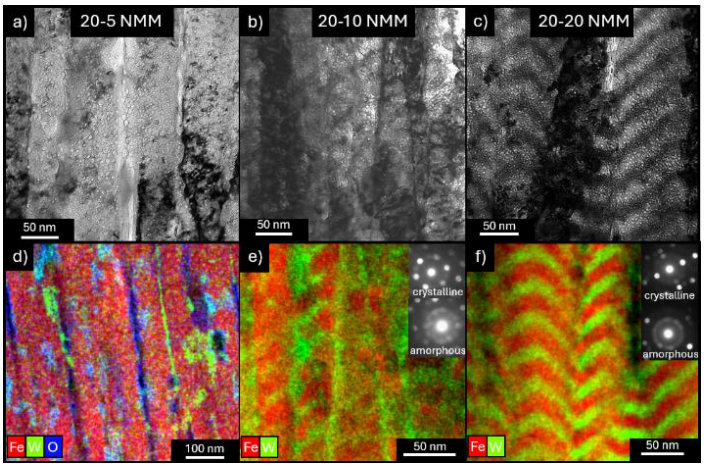

Figure 3: Post-implantation BF-TEM and EDS maps of the (a, d) 20-5, (b, e) 20-10, and (c, f) 20-20 NMMs following 1 x 10^{17} He^+ ions/cm^2 at 500 °C. NBED confirms retained amorphous Fe-W in the 20-10 and 20-20 NMMs.

Direct S/TEM characterization following implantation to 1 x 10^{17} He^+ ions/cm^2 at 500 °C confirmed the architecture-dependent structural evolution identified by XRD in **Figure 3**. The 20-5 NMM exhibited extensive Fe-W intermixing and complete loss of the original multilayer architecture, with oxygen enrichment originating from the Corning Eagle glass substrate detected by EDS. No residual amorphous Fe-W regions were identified in the amorphous-phase NBED analysis. The 20-10 NMM retained portions of the layered structure but exhibited substantial intermixing and crystallization, whereas the 20-20 NMM maintained well-defined Fe/Fe-W chemical modulation with NBED confirming the retention of crystalline Fe and amorphous Fe-W layers. Notably, He cavities are visible within the crystalline regions of each implanted architecture, with substantial differences in their size and distribution accompanying the observed differences in structural stability. These defect populations are quantified in **Figure 4**.

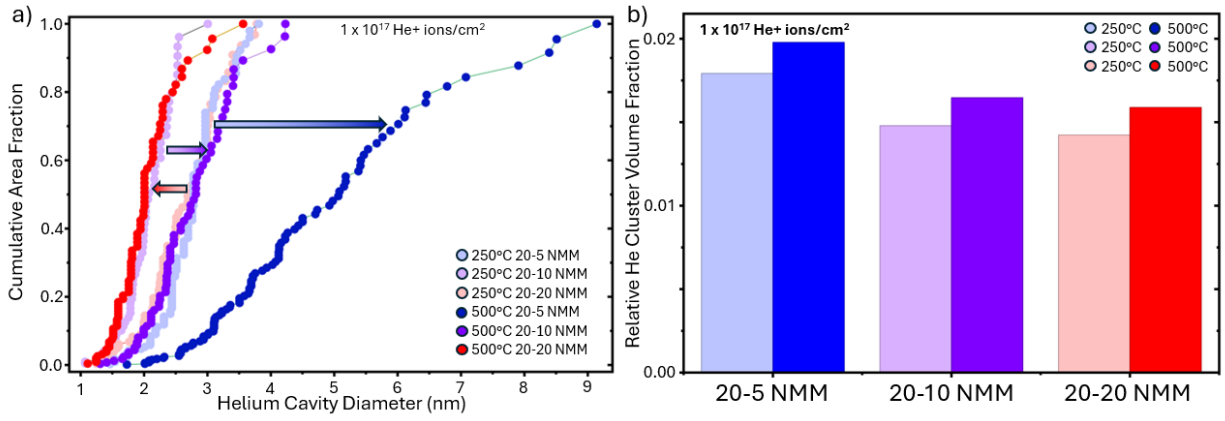

Figure 4: (a) TEM-resolved He cavity size distributions and (b) relative sub-nanometer He-cluster volume fractions following implantation to 1 x 10^{17} He^+ ions/cm^2 from the WAXS analysis.

At 500 °C, the structurally degraded 20-5 NMM developed a broad, bimodal distribution of substantially larger cavities, while the partially stable 20-10 NMM exhibited a modest increase in cavity size relative to 250 °C. In contrast, the structurally stable 20-20 NMM exhibited a marked

reversal in cavity growth, with cavities decreasing in diameter at 500 °C from 250 °C. Guinier analysis of wide-angle X-ray scattering (WAXS) data, a methodology developed in our previous study [2], further revealed decreasing relative volume fractions of sub-nanometer He clusters with increasing amorphous interlayer thickness. Combined with the biased distribution of cavities within crystalline Fe layers (**Figure 3)**, these results indicate that above the He-V mobility regime, transport toward stable amorphous interfaces suppresses He accumulation and cavity growth. Consequently, irradiation tolerance is governed by the coupled effects of interface stability and defect mobility rather than interface density alone.

Future Plans

Ongoing work will extend defect characterization of the irradiated NMMs using small-angle X-ray scattering (SAXS) to quantify He cavity size distributions and volume fractions and correlate these measurements with TEM-derived cavity populations shown in **Figure 4a**. This analysis will provide complementary statistical characterization of He defect distributions across the implanted volume and further quantify the relationship between amorphous interface stability and He defect evolution. More broadly, the interface-design principles established in the Fe/Fe-W NMMs will be extended from engineered planar interfaces to amorphous GB complexions. Current work investigates the thermodynamic and chemical factors governing complexion formation and stability in Fe based alloys, including competition between segregation, amorphization, and intermetallic formation, with the goal of establishing materials-selection rules for stabilizing amorphous interfacial structures (**Figure 5**) for future irradiation studies.

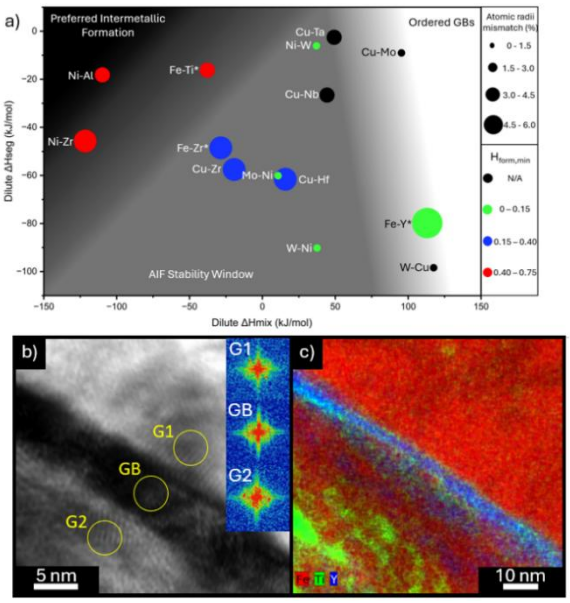

Figure 5: (a) Amorphous complexion materials selection framework for Fe-based alloys based on experimental observations from this work and published literature. (b,c) Representative Fe-Ti-Y amorphous GB complexion.

References

[1] V.A. Borodin, P.V. Vladimirov. *Kinetic Properties of Small He–Vacancy Clusters in Iron*, Journal of Nuclear Materials 386-388 (2009) 106–108.

[2] C. Killeen, Y. Zhang, W.S. Cunningham, D.J. Sprouster, D. Olds, S. Chodankar, J.R. Trelewicz. *Microstructurally Informed Synchrotron X-Ray Analysis Revealing Helium Defect Transitions in Ultrafine Grained Tungsten*, Journal of Nuclear Materials 616 (2025).

Publications

[1] K. Russell, K. Jagadish, J.R. Trelewicz, A. M. Hodge, *Revisiting Grain Boundary Segregation and Precipitation in Nanocrystalline Metallic Alloys*, Scripta Materailia, 271, 117023, 2026

[2] C. Killeen, K. Russell, A.M. Hodge, J.R. Trelewicz, *Diffusion-mediated Amorphous Interface Stability in Fe/Fe-W Crystalline-Amorphous Nanomultilayers*. In preparation (2026)

[3] C. Killeen, K. Russell, A.M. Hodge, D.J. Sprouster, S. Chadankar, J.R. Trelewicz. *Interface-Thickness-Dependent Helium Defect Evolution in Fe-W Nanomultilayers*. In preparation (2026)

Disorder & Diffusion in Complex Oxides: Towards Prediction & Control

Blas Pedro Uberuaga, Caitlin Kohnert, Cortney Kreller, Brianna Musico, Yongqiang Wang, Arjen van Veelen

Los Alamos National Laboratory

Keywords: complex oxides, radiation damage, transport, disordering, defect kinetics, phase transformation

Research Scope

The central hypothesis of this project is that irradiation induces structural changes in complex oxides that impact their functionality and that, concurrently, those changes in functionality modify the material's response to irradiation. There are multiple aspects to the changes we are considering. Our past work has focused extensively on how irradiation changes the cation ordering in oxides such as pyrochlore ($A_2B_2O_7$) and spinel (AB_2O4) and how cation disorder then changes ionic conductivity. Mass transport and chemical disorder are still central themes of this project, but we now also consider other types of radiation-induced structural changes, including the formation of metastable phases, and other types of functionality such as changes in the electronic structure of the oxide. In the current phase of the project we are focused on lanthanide sesquioxides – Ln_2O_3 and $LnLn'O_3$ – which are a fascinating family of compounds as the functionality and metastability of phases (Figure 1) is very sensitive to the Ln chemistry while the groundstate structure is much less so [1], providing an excellent compositional space to examine the structure-chemistry-property relationship of these materials.

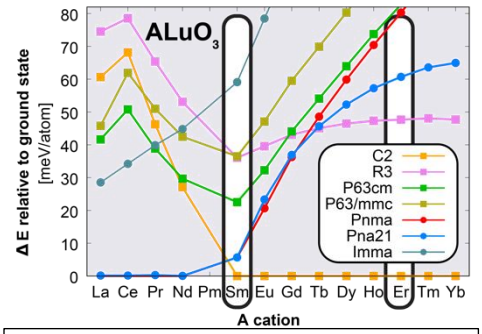

Figure 1. Our DFT calculations of the metastability of phases in $ALuO_3$ compounds. Despite both $SmLuO_3$ and $ErLuO_3$ exhibiting the same bixbyite groundstate, the metastability of other phases is very different.

Recent Progress

Theoretically, we have considered fundamental aspects of transport in chemically complex materials. In these materials, transport is not described by a single atomic event but rather a collection of many events. It becomes challenging to both quantify the individual contributions of each mechanism to diffusion and to thus determine how to control the rates of each of those mechanisms. Using the variational principle of diffusion [2] and the theory of kinosons [3], we have derived how some events, typically events that are quite rare, have outsized contributions to transport. These "superkinetic" kinosons are the events that really contribute to transport, as the fast events lead to correlation traps that don't lead to long-range diffusion. We have used these ideas to quantify how transport in bixbyite-structure $LnLn'O_3$ compounds depends on chemistry.

More recently, we have derived a statistical mechanics view of diffusion in complex systems in which the non-Arrhenius behavior of diffusion (the temperature dependence of the activation energy) can be cast as a sum of three terms [4]: the fluctuations in the energies of the individual states, the fluctuations in the energies of the transition states, and the fluctuations in the derivatives of the so-called relaxation vectors, which describe how much correlation a given event has. This allows us to directly relate the energy landscape of a material as a function of chemical order to the transport characteristic of that order.

Computationally, we have determined how the functional properties – explicitly the bandgap – of Ln bearing oxides depends on the chemistry and phase of the compound. This is motivated by work in which we had seen that the bandgap of Bi_2O_3 changes as its structure changes during irradiation. Our calculations reveal that the bandgap in pyrochlores is very sensitive to chemical order, a result validated by experiment (Figure 2), and thus the electronic structure, which can be probed locally using electron energy loss spectroscopy (EELS), can be used as a proxy for disorder. These calculations also reveal that the bandgap of LnLn'O_3 compounds will be very sensitive to the phases induced by irradiation.

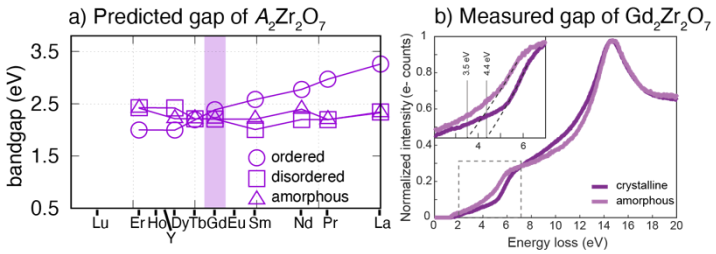

Figure 2. Both (a) density functional theory and (b) electron loss function measurements reveal that the bandgap of lanthanide-bearing pyrochlores changes as the material's structure changes, as might be induced by irradiation.

In collaboration with Pratik Dholabhai at Rochester Institute of Technology, we have been examining the structure of heterointerfaces formed in bixbyite-structured compounds (A_2O_3) [5]. The bixbyite structure is related to fluorite (BO_2) but is characterized by structural oxygen vacancies to balance charge. These vacancies lead to especially complex interfacial structures. As opposed to fluorite heterointerfaces where the structure of the interface is described by misfit dislocations, in bixbyites those dislocations (which still exist) are overwhelmed by the presence of the structural vacancies, leading to a much rougher energy landscape.

Experimentally, we have irradiated different LnLn'O_3 compounds to test the hypothesis that the radiation response can be related to the energetics of metastable phases. Our initial results are highlighted in Figure 3, showing how, as a function of dose, a secondary phase grows in for $SmLuO_3$ but not for $ErLuO_3$. This response directly connects to the energetics presented in Figure

1 in which $SmLuO_3$ exhibits low-lying metastable phases while $ErLuO_3$ does not. Our calculations suggest that $SmLuO_3$ has much greater chemical flexibility than $ErLuO_3$, and that is directly reflected in the response of the two compounds to irradiation. Not only does this provide an accessible metric for identifying radiation-resistant materials but generalizes previous concepts relating tendencies in cation disordering to amorphization resistance, providing greater fundamental insight into the factors that dictate phase evolution under irradiation.

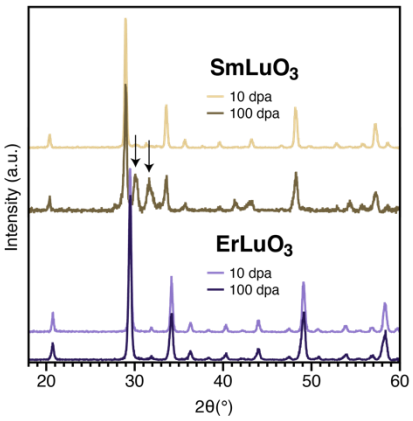

Figure 3. X-ray diffraction reveals that, while $ErLuO_3$ exhibits no structural changes to doses of 100 dpa, $SmLuO_3$ sees the growth of a second phase as indicated by the arrows.

Future Plans

Our future work follows from the results we have obtained over the last two years. First, we will examine how the chemistry of $LnLn'O_3$ compounds impacts their overall radiation response with the goal of quantifying the local structural changes accompanying the larger-scale changes in phase structure. In addition to understanding how the Ln chemistry impacts that response, we will consider aliovalent dopants which further modify the defect chemistry of the compound. The hypothesis is that these defects – typically oxygen vacancies – will modify the radiation response as they provide new kinetic pathways for defect evolution. Using local probes of atomic and electronic structure like EELS and EXAFS, we will identify local chemical and structural motifs that describe the evolution of these materials that can be directly calculated with DFT to provide enhanced insight into the chemical and structural drivers that govern response.

Second, we will directly examine how the complex interfacial structures associated with bixbyite-structured compounds impact defect thermokinetics to influence radiation damage evolution. To do this, we will synthesize composites of bixbyite and fluorite such that in one sample we have all of the relevant interfaces: fluorite/fluorite, fluorite/bixbyite, and bixbyite/bixbyite. After irradiation, we will assess how the damage differs based on the nature of the interface, considering factors such as intermixing, radiation-induced phase transformations, and damage/bubble denuded zones. These experiments will be interpreted by molecular dynamics simulations that determine how the differences in structure impact defect thermokinetics.

Finally, we will expand on our consideration of electronic effects in these materials and how irradiation modifies their electronic structure. Here we will focus on the metastable phases induced in $LnLn'O_3$ compounds under irradiation with the goal of identifying changes in electronic structure predicted by our DFT calculations. As the electronic structure changes, so does the propensity for different types of charged defects, which will have further impact on the overall evolution of the material. By identifying how the electronic structure changes, we will provide a

greater understanding of how the defect chemistry and thus overall long-term response of the material changes as it is irradiated.

References

1. V. Kocevski, J. A. Valdez, B. K. Derby, Y. Q. Wang, G. Pilania, and B. P. Uberuaga, *Predicting and accessing metastable phases*, Materials Advances **4**, 1101 (2023).
2. D. R. Trinkle, *Variational principle for mass transport*, Physical Review Letters **121**, 235901 (2018).
3. S. Chattopadhyay and D. R. Trinkle, *Contributions to diffusion in complex materials quantified with machine learning*, Physical Review Letters **132**, 186301 (2024).
4. S. Chattopadhyay and B. P. Uberuaga, *Statistical Mechanics of Thermal Diffusion in Rough Energy Landscapes*, arXiv preprint arXiv:2607.22742 (2026).
5. A. More, B. P. Uberuaga, and P. P. Dholabhai, *Influence of intrinsic oxygen vacancies on interface structure and functionality in fluorite and bixbyite heterostructures*, under review.

Publications

1. S. Chattopadhyay and B. P. Uberuaga, *Larger than uncorrelated vacancy diffusion contributions in chemically disordered crystalline materials*, Scripta Materialia **270**, 116928 (2026).
2. B. K. Downing, S. M. Hnatko III, T. DeForest, E. L. Brosha, J. Valdez, R. Bloom, J. P. Smith, B. P. Uberuaga, and B. L. Musico, *Synthesis of inter-lanthanide sesquioxides $LnLn'O_3$ by polymeric steric entrapment*, Journal of the American Ceramic Society **108**, e70024 (2025).
3. W. Ebmeyer, P. Hatton, B. P. Uberuaga, and P. P. Dholabhai, *Influence of misfit dislocations on ionic conductivity at oxide interfaces*, Journal of Materials Chemistry A **12**, 21252 (2024).
4. E. R. Kennedy, J. A. Valdez, Y. Q. Wang, S. M. Ribet, K. E. Sickafus, C. R. Kreller, B. Pedro Uberuaga, and B. K. Derby, *Insights into defect kinetics, mass transport, and electronic structure from spectrum effects in ion-irradiated Bi_2O_3*, Journal of Materials Chemistry A **12**, 31445 (2024).
5. Y. Lu, B. P. Uberuaga, and S. Choudhury, *Machine learning guided prediction of solute segregation at coherent and semi-coherent metal/oxide interfaces*, Computational Materials Science **264**, 114480 (2026).
6. N. J. Madden, M. T. Janish, J. A. Valdez, B. P. Uberuaga, and J. A. Krogstad, *Radiation Tolerance of Nanoporous Gadolinium Titanate*, Journal of the American Ceramic Society **109**, e70731 (2026).
7. K. E. Sickafus and B. P. Uberuaga, *Lattice Relaxations in Bixbyite-Structured Rare-Earth Sesquioxides*, Crystal Research and Technology **61**, e70116 (2026).
8. L. Sotelo Martin, A. Campos-Quiros, M. Watanabe, J. K. Mason, P. C. M. Fossati, B. P. Uberuaga, and R. H. R. Castro, *Grain boundary energy control in zinc aluminate nanoceramics*, Journal of the American Ceramic Society **108**, e20383 (2025).
9. B. P. Uberuaga, V. Kocevski, A. A. Talapatra, B. K. Derby, and E. R. Kennedy, *Relationship between atomic and electronic structure in Ln-bearing oxides*, Physical Review Materials **9**, 103603 (2025).
10. B. P. Uberuaga and S. Chattopadhyay, *The impact of chemistry on anion migration in bixbyite-structured lanthanide oxides*, Solid State Ionics **444**, 117264 (2026).

Understanding the Competition between Plastic Flow and Fracture in BCC Transition Metals

Christopher R. Weinberger, Colorado State University
Gregory B. Thompson, University of Alabama

Keywords: Brittle-to-Ductile Transition, Fracture, Dislocations

Research Scope: The ductility and formability of body-centered-cubic (BCC) metals can vary significantly, with the origins for such differences being rather elusive. For example, molybdenum and tungsten are quite limited in their ductility and formability while niobium and tantalum easily deform. For those with limited formability, engineering solutions, such as thermomechanical processing and alloying, are primarily used to improve these properties. In this program we will test the hypothesis that extrinsic point defects, *i.e.*, impurities, are more influential to the ductility of certain BCC metals than others. Through an integrated experimental and modeling approach, we will understand the origins of embrittlement regarding extrinsic impurities, both the impurity types and their concentration. The experiments will examine the change in material properties with respect to impurity level, including dislocation mobility and intrinsic fracture behavior, that will be used in a semi-analytic coupled plasticity-fracture model of the brittle-to-ductile transition temperature (BDTT). This model will enable us to fundamentally determine if and how impurities influence these BCC metals' mechanical properties.

Recent Progress: The differences in the brittle-to-ductile transition (BDT) in the BCC transition metals is attributed to either being limited by dislocation mobility, in which dislocation shielding of the crack tip dominates toughening, or by dislocation nucleation. Recent work on refractory HEAs [1] has suggested that the competition between fracture and plastic flow, equivalently the competition between plasticity and fracture, can be understood through dislocation nucleation at the crack tip using the Rice-Thompson criteria [2]. However, this metric cannot predict a BDT, it only predicts a temperature independent brittle or ductile response. To see if this can be responsible for the BDT observed in BCC transition metals and compare against mobility/shielding models of the BDTT, we expanded the Rice-Thompson criteria to be a thermally activation dislocation nucleation model.

This model is based on the idea that dislocations nucleation from the crack tip and move away fast enough that they do not shield the crack tip. If they do not, the model reverts to a dislocation mobility and shielding model, which we have explored already in this program. In this new model, the fracture resistance of the material can be written as the fracture resistance due to the surface energy (energy required to separate two planes) and effects due to crack tip blunting – which is a function of the number of dislocations nucleated from the crack tip: $\mathrm{K_R} = \mathrm{K_G} + \mathrm{K_B} = \mathrm{K_G} + \xi N_{\mathrm{dis}}^{\mathrm{p}}$. The thermally activated nature of the process arises by assuming that dislocation nucleation is a thermally activated process: $N_{\mathrm{dis}} = \int n_0 \exp\left(-\frac{\Delta G^*}{k_B T}\right) dt$. Now, to model experimental

measurements of the BDTT, we apply a constant loading rate: $K_{\mathrm{app}} = \dot{K}t$ and note that the BDT occurs when K_{app} osculates $\mathrm{K_R}$ as shown in Figure 1(a).

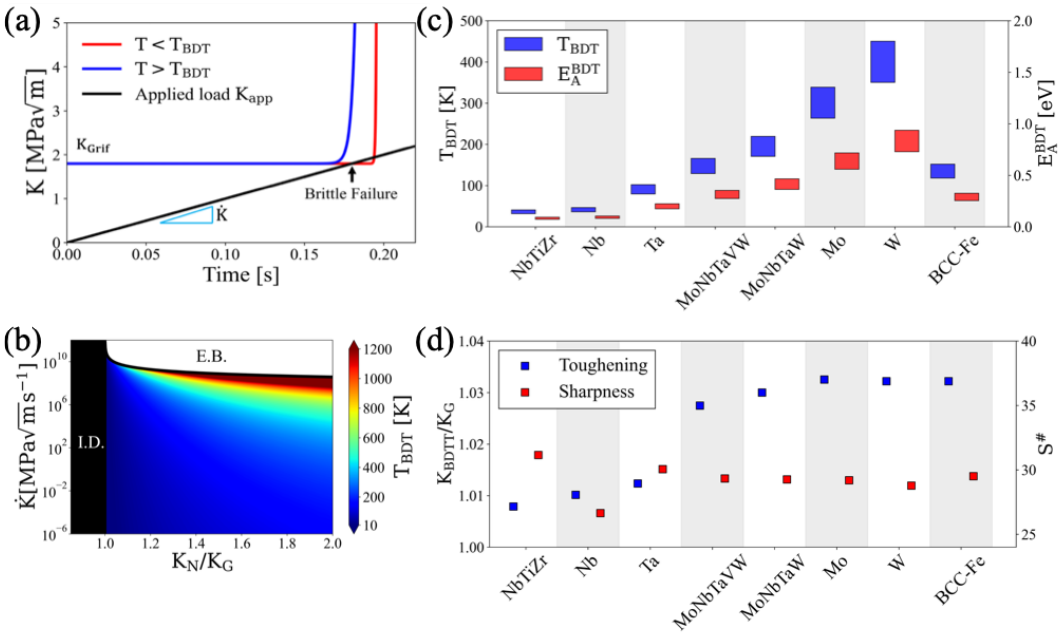

Figure 1: (a) The plot of the applied stress intensity factor and the resistance as a function of time. The blue line indicates ductility behavior while the red line shows brittle behavior relative to a fixed loading rate. (b) A plot of the brittle-to-ductile transition as a function of material parameters predicted by the nucleation model. (c) The activation energy and BDTT range and (d) the toughening and sharpness as predicted from the nucleation model.

To understand the model predictions, we found that there is a semi-analytical solution through perturbation analysis that allows us to full analyze the BDTT, activation energy, and toughening from simply model parameters. The BDTT predicted from this model is shown in Figure 1(b), illustrating that it recovers the intrinsic BDT predicted by Rice and Thompson [2], has a brittle-to-ductile transition temperature, and interesting shows that there are some loading rates at which the material is always brittle.

To compare and contrast different observed toughening behavior up to the BDTT, the idea of soft and sharp transitions has been introduced. Soft transitions show gradual material toughening up to the BDTT, while sharp transitions show little toughening up to the BDTT. To quantify this, we introduced a sharpness measure of the BDT as: $S^{\#} = \frac{\mathrm{T_{BDT}}\Delta K}{\int_{\mathrm{T_{min}}}^{\mathrm{T_{BDT}}}(K_{\mathrm{IC}} - K_{\mathrm{min}})dT}$. Thus, for sharp transitions, $S^{\#}$ is a large number and for soft transitions, $S^{\#}$ is a small number. We have found that experimental measurements of the sharpness of the transition for BCC metals are of order 5-15, which is soft, while silicon is 46, or sharp. Our previous mobility models have a sharpness of around 3, and this new nucleation model around 30. Thus, our work clearly demonstrates that mobility based toughening models are soft while dislocation nucleation models are sharp.

To understand how well the dislocation nucleation model represents real BCC metals, we applied to all the pure metals and select HEAs that were not intrinsically ductile from [1]. We used the

BDTT range from tungsten to fit our unknown enthalpy for nucleation and scaled appropriately to the rest of the materials to produce BDTT ranges, activation energies, toughening, and sharpness values which are shown in Figure 1(c)-(d). These results demonstrate that the toughening predicted is too low and the sharpness is too high; suggesting that shielding is needed, and that dislocation mobility is likely critical to understanding key features of the BDT.

To complement the model, the experimental program has developed means to provide fracture toughness testing of single crystal tungsten using micro-cantilevers with this data then compared to modeling predictions enabling further modeling refinement and/or new modeling direction. Using these micro-mechanical samples, systematic and spatially controlled incorporation of impurities at the notch can then be undertaken to assess the BDTT changes. To ensure a reproducible and repeatable means of mechanical testing, we have performed a series of test to examine both the microcantilever size as well as notch type on the measured fracture toughness. While bulk testing has established ASTM standards, micro-scale mechanical testing lacks these guidelines resulting in a range of reported behaviors, including specimen size dependent toughness [3]. Nevertheless, the advantage of microscale testing is a reduced volume of material (cost) as well as ready accessibility to single crystals enabling both specific cleavage planes to be tested and mitigating grain boundary effects on mechanical responses. Here, we report the effect of sample size and notch geometry on the fracture toughness for 5x5x10um, 10x10x20um, and 20x20x40um cantilevers with either an *inverted-U notch* (where the depth of the notch is deeper on the edges from over-focus ion beam (FIB) milling), a *straight notch* (where the depth of the cut is invariant across the cross-section and formed by making beams larger than initially targeted whereupon the over-FIB sections are removed), and, finally, a *bridge notch* [4] (where the straight notch is cut in the interior portion of the beam but the milling is ceased near both ends leaving the material intact). These different notches are shown in Figure 2(a). Figure 2(c) and (d) are the histograms of the toughnesses.

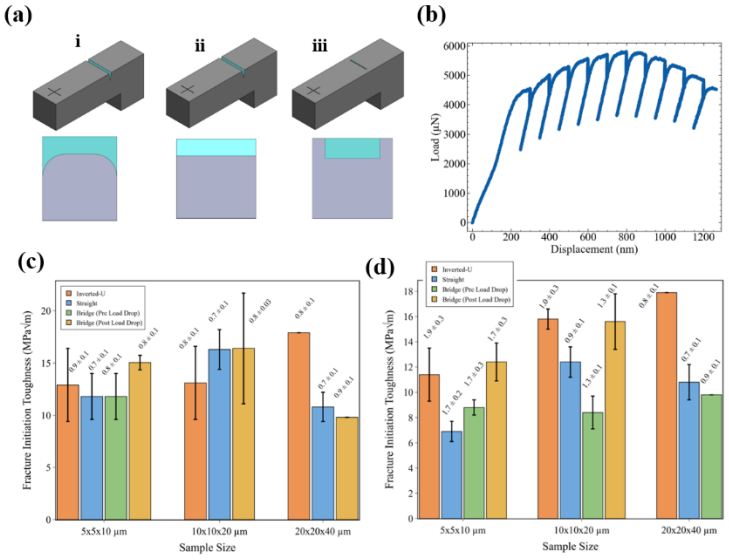

Figure 2: (a) Schematics of the various notch profiles for i: inverted-U, ii-straight notch, iii-bridge notch, with notch profiles under each beam where turquois is the removed material and grey the retained material. (b) Representative load-unload vs. cantilever displacement response of a tested cantilever beam (c) Histogram of fracture initiation toughness at 0.8±0.1 MPa√m. (d) Histogram of fracture initiation toughness at constant displacement rate of 100 nm/s with the corresponding loading rate placed over the varied size beams in the chart.

By using the same loading rate, Figure 2(c), direct comparisons across the different sized beams can be made. Interestingly, for the

majority of beam sizes and notch types, the toughness are statistically equivalent. Furthermore, these values are approximately 2x higher than the bulk tungsten fracture toughness, which is reported to be ≈ 6-8 MPa√m. The higher toughness here suggests that the beam sizes have plasticity contributions within the confined volume being tested, even though it has been suggested that cross-sections equal to or greater than 10x10 um should be sufficient to mitigate these issues [3]. Upon changing from a constant load rate to a constant displacement rate, which translates to a higher loading rate for the smaller sized beams, Figure 2(d), we note that both the straight notch and bridge notch beams, at the 5x5x10 um size, have values now aligned with the bulk response. Furthermore, the straight notch can retain this value even at the larger sized beams for the loading rates indicated in the histogram. This indicates a notch shape dependence, which is linked to the loading rate of the test, where loading rates > ≈1.2 MPa√m/s appear sufficient to have toughness values on par with bulk values. Using this information, we have established the workflow for testing our beams to mimic bulk scale outcomes. Currently, we use the straight notch, at the different sizes and the appropriate loading rate, to examine the BDTT where the temperature step sizes are refined to quantify the sharpness of the transition to compare to the model.

Future Plans: Based on our previous work, we have learned that dislocation mobility and how it is influenced by impurities is a key feature that must be investigated to understand the BDT. We have concluded this because previous work has shown that impurities do not influence fracture toughness substantially to embrittle BCC metals and that dislocation nucleation is likely not a controlling factor. Thus, it is critical to investigate how impurities, such as oxygen, affect dislocation mobility.

We plan on investigating how impurity atoms, such as oxygen, bind to dislocation cores and alter dislocation mobility. Theoretically, we will do this by computing interaction energies between the impurities and screw dislocations using density functional theory. We will then implement these binding energies into a dislocation dynamics simulations that allows for the dislocation to interact with both the impurity and the Peierls potential to evaluate the overall impact of impurities on the overall dislocation mobility. These mobility results will be implemented into our models of the BDT to determine the materials response to such impurities. This will be done targeting tungsten and niobium as representatives from the group VB and VIB transition metals.

These modeling outcomes will be supported by a series of experiments where impurities will be incorporated into the notch region through ion implantation of either oxygen and/or nitrogen using a plasma FIB. TEM and atom probe characterization of the spatial location and concentration of these impurities will be undertaken with cross-correlative efforts to address how these impunity solutes partition to dislocations that emanate from the tip [5]. Under various processed conditions, supported by the outcomes described above, the postulated shifts in the BDTT as well as sharpness of the transition will be measured as a function of impurities and fed to the model. Finally, by using single crystals for testing, the program will assess the preferred cleavage plane(s) for tungsten, where {001} is reported experimentally but atomistic simulations indicate the {011} having the lowest surface energy.

References

1. E. Mak, B. Yin, and W.A. Curtin, *A ductility criterion for bcc high entropy alloys*, . Mech. Phys. Solids, **152**, 104389 (2021).
2. J.R. Rice and B. Thompson, *Ductile versus brittle behaviour of crystals*, Philosophical Magazine, **29**, 73-97 (1974).
3. J. Ast, M. Göken, K. Durst, *Size-dependent fracture toughness of tungsten*, Acta Materialia **138** 198–211 (2017).
4. A.K. Saxena, S. Brinckmann, B. Völker, G. Dehm, C. Kirchlechner, *Experimental conditions affecting the measured fracture toughness at the microscale: Notch geometry and crack extension measurement*, Materials & Design 191 108582 (2020).
5. X. Zhou, J. R. Mianroodi, A. Kwiatkowski da Silva, T. Koenig, G. B. Thompson,
P. Shanthraj, D. Ponge, B. Gault, B. Svendsen, D. Raabe *The hidden structure dependence of the chemical life of dislocations*, *Sci. Adv.* **7** eabf0563 (2021).

Publications

1. M. T. Islam, C. R. Weinberger, and G. B. Thompson, *Rapid microcantilever preparation for conditional fracture toughness evaluation*, Journal of Materials Research and Technology **30**, 5444-5454 (2024).
2. H. K. Brumblay, G. B. Thompson, and C. R. Weinberger, *Insights into the soft brittle-to-ductile transition from discrete dislocation dynamics*, Computational Materials Science, **247,** 113503 (2025).
3. S. Hossain, H. K. Brumblay, G. B. Thompson, and C. R. Weinberger, *The role of surface energy and plasticity in determining the fracture toughness of tantalum and tungsten, International Journal of Refractory Metals and Hard Materials*, **131**, 107222 (2025).
4. H. K. Brumblay, G. B. Thompson, and C. R. Weinberger, *Modeling the Role of Thermally Activated Dislocation Nucleation and Crack-Tip Blunting on the Brittle-to-Ductile Transition*, Submitted (2026).
5. S. Hossain, X. Tang, B. Gludovatz, G. B. Thompson, and C. R. Weinberger, *Influence of the statistics of grain boundary toughness on the competition between intergranular and transgranular fracture in tungsten*, Submitted (2026).

Understanding Mechanisms of Irradiation-Induced Crystallization

Janelle P. Wharry, University of Illinois

Keywords: Ion Irradiation, Metallic Glass, Crystallization, Phase Transformations

Research Scope

The objective of this project is to understand irradiation-induced crystallization (IIC), an athermal disorder/order transformation, in amorphous metals. Many advanced materials which offer exceptional radiation tolerance rely on high-energy amorphous or metastable phases, which are susceptible to IIC. IIC is generally understood to be a thermodynamic energy minimization process. That is, the transfer of energy from the irradiating particle to the target material stimulates atoms to a higher-energy, higher-mobility state, from where they can relax into a lower-energy crystalline phase [1]. However, crystals formed by IIC are often themselves high-energy (or high-temperature) metastable polymorphs, inaccessible through thermal annealing alone, which undermines energy minimization theories. Numerous atomic micromechanisms have been proposed to explain IIC, including irradiation-assisted short range ordering (SRO), free volume dilatation, formation of free volume and anti-free volume defects, radiation-enhanced diffusivity, and localized annealing within irradiation thermal spikes. But none of these micromechanisms is able to alone explain the stabilization of high-energy metastable crystals. Instead, transformations involving metastable phases are kinetically, rather than thermodynamically, controlled, with systems tending toward minimizing the nucleation barrier rather than minimizing energy [2,3].

Our overarching hypothesis is that IIC is a kinetic, enthalpy-controlled phenomenon that cannot be explained through simple thermodynamic or energy-minimization criteria. Hence, IIC is favorable when the differential enthalpy change is negative, $dH = dU + pdV + Vdp < 0$. We will resolve this hypothesis through three scientific questions:

(1) How does the starting amorphous short-range ordering (SRO), and its proximity to interplanar spacing of a low-energy crystalline phase, affect the IIC pathway?
(2) How do electronic and nuclear energy losses affect atomic scale micromechanisms, and consequently alter the pathway, of IIC transformations?
(3) How does the amorphous–crystalline interface stabilize the crystalline phases?

Recent Progress

Amorphous-crystalline transformations depend on amorphous phase topology and the resultant crystal structure. Because atoms must be displaced a critical distance, the transformation is more enthalpically favorable for $dV << 0$. However, materials that most readily undergo IIC tend to have amorphous SRO ~ the interplanar spacing of the resultant crystals, as we have observed in our preliminary work on ZrO_2 and TiO_2, ***Figure 1***. Amorphous ZrO_2 experiences more extensive and more rapid IIC than TiO_2, which may be due to the amorphous ZrO_2 SRO being almost exactly aligned with interplanar spacing in low-energy crystalline ZrO_2 polymorphs. By contrast, amorphous TiO_2 SRO is poorly aligned with the interplanar spacing of low-energy crystalline TiO_2 polymorphs. These results suggest dV may actually be small.

If dV is small, the enthalpy inequality can only be fulfilled if either dU or Vdp is more negative than the other is positive. The mode by which irradiating particles transfer their kinetic energy influences Vdp. Nuclear energy losses generate extensive ballistic cascades that produce point defects and high-pressure shockwaves, forcing $Vdp > 0$. Meanwhile, electronic energy losses generate recoils and atomic vibrations, implying $Vdp \sim 0$. While dU will almost always be negative for amorphous-crystalline transformations, its magnitude will depend on the energy loss mode. If Vdp is small due to electronic energy losses, dU can also be relatively small, suggesting that the resultant crystal could contain more high-energy defects, stress, strain, and/or sharp high-energy interfaces. But if Vdp is non-negligible due to ballistic damage, the enthalpy inequality requires dU to be reasonably large, suggesting a low-energy progressive amorphous-crystalline interface must form.

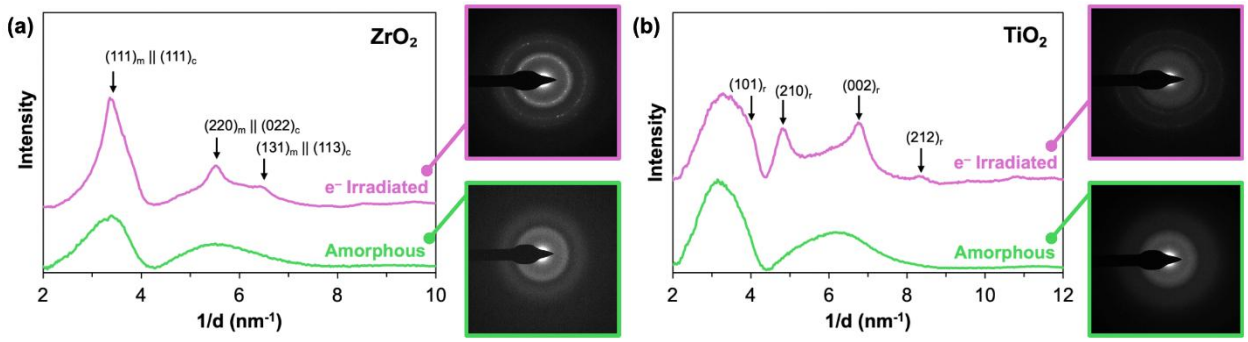

Figure 1 – Radially integrated SAED intensity for initial amorphous and electron irradiated (a) ZrO_2 and (b) TiO_2; diffraction planes for monoclinic "m" and cubic "c" ZrO_2 and rutile "r" TiO_2 are arrowed.

Future Plans

Work will focus on two model binary intermetallic systems, Mg-Ni and Hf-Al, because of their large glass-forming composition range during co-sputtering synthesis [4]. Additionally, Mg-Ni and Hf-Al represent bounding conditions to evaluate the proximity between amorphous SRO and crystalline interatomic spacing, with the alloys exhibiting two and seven equilibrium intermetallic line compounds, respectively, over their glass-forming composition range. The

research approach will primarily couple transmission electron microscopy (TEM) *in situ* irradiations with molecular dynamics (MD)-based materials forensics built on two-dimensional polyhedral template matching (2D-PTM), to obtain a kinetic understanding of the phase transformations. The nature of in situ irradiation enables continuous tracking of the temporal (i.e., dose) evolution of IIC by continuously collecting atomic-resolution scanning TEM (STEM) images. We will intentionally vary the starting amorphous SRO to address our first science question, and vary the electronic and nuclear energy losses to address our second science question. Complementary MD simulations built from 2D-PTM reconstructions of STEM images will inform atomic movements during IIC. This emerging technique is particularly well-suited for studying phase transformations in STEM. First, the technique reconstructs atomic positions throughout the transformation using the obtained STEM images. These reconstructions feed-in to MD simulations, which then extrapolate atomic movements between timesteps (i.e., STEM images). Finally, we will utilize four-dimensional STEM (4D-STEM) and geometric phase analysis coupled with 2D-PTM-informed MD to evaluate the stress, strain, and structure of the amorphous-crystalline interface.

The scientific outcome of this project will be a fundamental understanding of IIC mechanisms in metallic systems. In future renewals, we envisage that we can leverage these findings to understand IIC mechanisms in non-metallic systems, which have additional considerations for charge balance and bond breaking and reformation; eventually, we envision this work will allow us to develop a unifying theory for IIC and irradiation-induced amorphization, the seemingly opposite phenomenon. More broadly, this work is societally relevant because of the keen interest in nanocrystalline grain boundaries, amorphous complexions, and multi-principal element alloys for their exceptional radiation tolerance in irradiation-facing energy applications – but all of these structures and materials rely on high-energy amorphous or metastable phases, which are susceptible to IIC.

References

[1] W. Qin, J.A. Szpunar, and Y. Umakoshi, *Electron or ion irradiation-induced phase-change mechanism between amorphous and crystalline state*, Acta Materialia 59 (2011) 2221-2228.

[2] P. Banerjee and B. Bagchi, *Effects of metastable phases on surface tension, nucleation, and the disappearance of polymorphs*, Journal of Chemical Physics 149 (2018) 214704.

[3] A.P. Solomon, E.C. O'Quinn, J. Liu, I.M. Gussev, X. Guo, J. Neuefeind, C. Trautmann, R.C. Ewing, G. Baldinozzi, and M.K. Lang, *Atomic-scale structure of ZrO_2: Formation of metastable polymorphs*, Science Advances 11 (2025) 5943.

[4] S. Huang, S.A. Kube, N.S. Johnson, S. Sohn, A. Mehta, and J. Schroers, *Glass formation during combinatorial sputtering in binary alloys*, Acta Materialia 296 (2025) 121240.

Publications

In progress.

Integration of High-Throughput Experiments and Physics-Informed Machine Learning to Understand Irradiation-Induced Swelling in Metallic Glass

Yang Yang, Department of Engineering Science and Mechanics, The Pennsylvania State University, University Park, PA 16802, USA

Keywords: metallic glass; irradiation damage; swelling; 4D-STEM; atomistic modeling

Research Scope

Metallic glasses are densely packed solids that lack the long-range periodic order of crystalline materials. Their structurally disordered states can exhibit high strength [1], high fracture toughness [2], and unusual responses to irradiation [3]. In some metallic glasses, irradiation produces changes in strength or ductility rather than the progressive embrittlement [4]. Irradiation-induced swelling has also been observed, and in some systems the swelling approaches a saturation state with increasing dose [5]. These observations suggest that amorphous structures may accommodate radiation damage through mechanisms fundamentally different from the production, migration, and clustering of lattice defects in crystals.

Despite this potential for radiation tolerance, the structural mechanisms underlying irradiation-induced swelling in metallic glasses remain insufficiently validated experimentally, despite several proposed theoretical models. A central objective of this project is therefore to directly test these proposed mechanisms and determine which irradiation-induced structural changes are responsible for swelling and the possible initiation of void-like damage. We specifically seek to establish experimentally measurable signatures of changes in local atomic packing, non-affine structural rearrangements, and open volume, and to determine how these quantities evolve with irradiation.

This project integrates atomistic modeling, electron-scattering simulations, high-throughput four-dimensional scanning transmission electron microscopy (4D-STEM), positron annihilation spectroscopy (PAS), and physics-informed data analysis. The central strategy is to establish a common structural representation that can be generated from atomistic models, measured experimentally through nanobeam electron diffraction, and evaluated against an independent measurement sensitive to irradiation-induced open volume. This approach seeks reproducible structural signatures that evolve under irradiation and correlate with volumetric response. Atomistic simulations provide candidate irradiation-modified configurations that can be compared with 4D-STEM measurements. PAS provides complementary information on open-volume evolution. Data-driven analysis constrained by electron-scattering physics and expected structural trends will then be used to identify physically interpretable connections among these measurements. The resulting framework is intended to clarify why damage accumulation may slow or saturate in some metallic glasses and to establish scientific principles for designing radiation-resilient amorphous materials.

Recent Progress

During the initial project period, we established the specimens and measurement framework needed to distinguish irradiation-induced structural evolution from the intrinsic heterogeneity of metallic glass. This required electron-transparent samples with controlled thickness, a nanodiffraction method sensitive to subtle structural changes, and a defined perturbation for validating the diffraction response.

Uniform metallic-glass films were produced by sputter deposition. Their controlled thickness avoids the large gradients that complicate quantitative nanodiffraction in conventionally prepared specimens and provides a consistent amorphous starting state for comparison among as-prepared, mechanically deformed, thermally modified, and irradiated conditions.

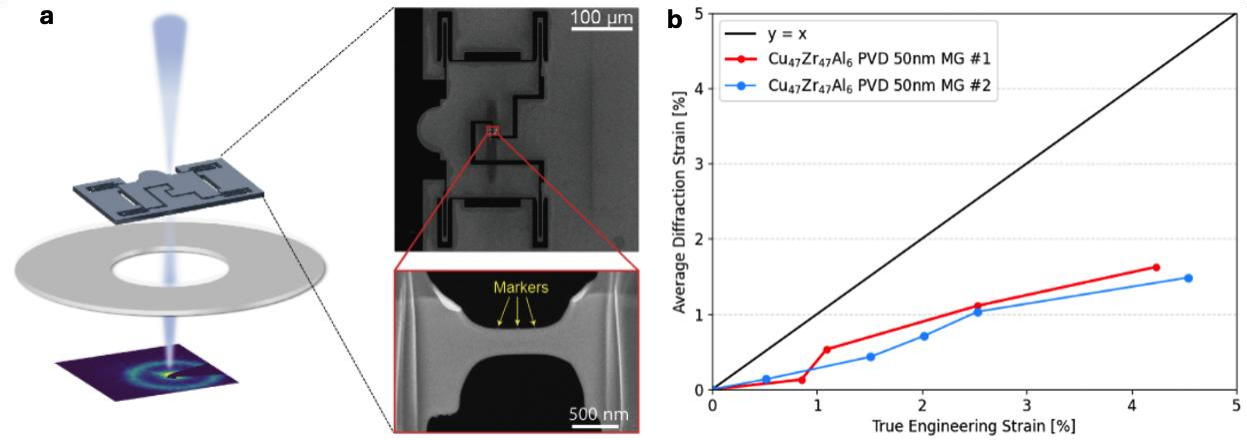

Figure 1. a. Schematic of the in situ STEM nanomechanical testing setup. A push-to-pull MEMS device is used to apply uniaxial tensile loading to a dogbone-shaped metallic-glass specimen. Fiducial markers enable direct measurement of specimen-scale deformation. b. Comparison of the strain measured from the diffraction and fiducial markers (engineering strain) during in situ mechanical deformation.

To test the sensitivity of 4D-STEM, we first applied a controlled mechanical perturbation. Metallic-glass specimens were tensile-loaded in situ while a nanobeam diffraction pattern was recorded at every probe position (Fig. 1a). Spatial variations in the broad amorphous diffraction rings provide information about local atomic correlations, packing, and structural distortion, enabling a statistically robust map of structural evolution.

Deformation was quantified independently at two scales. Specimen-scale strain was measured from fiducial-marker displacement, whereas diffraction-derived strain was inferred from changes in the ellipticity of the amorphous diffraction ring. The fiducial-marker strain consistently exceeded the diffraction-derived strain (Fig. 1b), indicating that the two measurements capture different components of deformation.

Diffraction-ring distortion is expected to reflect primarily the affine deformation of local atomic correlations, whereas fiducial displacement captures the total deformation accumulated over a larger region. The difference between these two measurements may therefore contain contributions from non-affine structural rearrangements associated with excess or free volume. Although further experiments and atomistic calculations are needed to establish the underlying mechanism, we hypothesize that this discrepancy may serve as a signature of "vacancy-like" defects in metallic glasses. Such defects are particularly relevant to irradiation, which can alter local atomic packing and open volume without producing discrete defects that are readily visible by conventional TEM.

These results therefore show that specimen-scale deformation cannot necessarily be inferred from a single diffraction-based strain measurement. More importantly, the difference between macroscopic and diffraction-derived strain may provide a measurable probe of structural processes that are not captured by a purely affine deformation description.

In parallel, we initiated a collaboration with Prof. Qi An's group at Iowa State University to test this hypothesis through atomistic modeling. Simulations will examine how different amorphous environments respond to mechanical loading and irradiation, with particular emphasis on the relationship among free volume, non-affine deformation, and diffraction response. Simulated atomic configurations will also be converted into nanobeam diffraction patterns for direct comparison with experiment.

Together, these efforts establish the key elements for the irradiation study: a controlled metallic-glass specimen platform, an in situ 4D-STEM method, a quantitative benchmark linking macroscopic and diffraction-derived deformation, and an experiment–modeling framework for identifying irradiation-induced changes in amorphous structure.

Future Plans

The next project period will extend the established measurement framework to controlled ion-irradiated metallic-glass specimens. Electron-transparent samples exposed to different doses of ion irradiation will be characterized using 4D-STEM, nano-mechanical testings and complementary STEM methods. PAS measurements will provide an independent assessment of irradiation-induced open-volume evolution. Correlating the PAS response with the statistical distribution of local diffraction signatures will test whether particular amorphous structural states are associated with swelling or with the approach toward a saturated response.

The experimental and computational activities will be integrated through a bidirectional workflow. Experimental observations will guide the selection of structural questions and model configurations, while simulated structures will provide physically motivated signatures to search

for in the experimental datasets. Physics-informed analysis will emphasize interpretable diffraction characteristics, spatial correlations, uncertainty, and consistency across independently prepared specimens rather than relying solely on classification accuracy. The resulting measurements will connect local structural evolution, open-volume response, and macroscopic swelling and will provide a mechanistic basis for comparing the irradiation tolerance of different amorphous structures.

References

[1] C. Schuh, T. Hufnagel, and U. Ramamurty, Mechanical behavior of amorphous alloys, Acta Mater. **55**, 4067 (2007).

[2] M. D. Demetriou, M. E. Launey, G. Garrett, J. P. Schramm, D. C. Hofmann, W. L. Johnson, and R. O. Ritchie, A damage-tolerant glass, Nat. Mater. **10**, 123 (2011).

[3] J. D. Schuler, C. M. Grigorian, C. M. Barr, B. L. Boyce, K. Hattar, and T. J. Rupert, Amorphous intergranular films mitigate radiation damage in nanocrystalline Cu-Zr, Acta Mater. **186**, 341 (2020).

[4] Y. Xie, X. Huang, A. Raj, X. Li, R. Dhall, M. Balooch, A. Minor, J. Schroers, and P. Hosemann, Strengthening of Zr-based metallic glass at low dose helium ion irradiation, J. Nucl. Mater. **592**, 154943 (2024).

[5] R. Gerling and R. Wagner, Density of neutron irradiated and annealed amorphous Fe40Ni40B20, Scr. Metall. **16**, 963 (1982).

Publications Resulting from Work Supported by the DOE Grant over the Previous Two Years

This project started in August 2025. One manuscript is under preparation at the moment.

1. Z. Zhang, K. Luo, Y. Zhu, Q. An, and Y. Yang, Probing Free-Volume Evolution in Metallic Glasses, to be submitted.

Understanding Elevated-Temperature Plasticity in Refractory Complex Concentrated Alloys

Mingwei Zhang, Department of Materials Science and Engineering, University of California, Davis

Keywords: refractory complex concentrated alloys, high entropy alloys, deformation mechanisms, strength, creep

Research Scope

The overarching goal of this research is to fundamentally understand the novel deformation mechanisms that control the high temperature-yield strength of refractory complex concentrated alloys (RCCAs). The most important objective of the research is to experimentally address the hypothesis that **the high-temperature yield strength in RCCAs is controlled by a competition among screw dislocation motion, edge dislocation motion, and the diffusion of the primary constituent atoms** in a quantitative manner. Specifically, it is hypothesized that **lattice distortion in RCCAs can lead to a mechanistic transition from screw- to edge-dislocation-controlled strength at elevated temperatures, thereby enhancing elevated-temperature mechanical properties.** The research combines experimental work in advanced processing, high-temperature testing, and advanced characterization to provide a critical scientific foundation for the development of next generation RCCAs.

The project studies high-temperature plasticity in bulk annealed, homogenized, coarse-grained, and nominally single-phase BCC RCCAs with room temperature tensile ductility. This limits the material system selected in this study to be NbTaTi-based RCCAs. We note that although ductility is explored in this study via the tensile tests and creep tests described below, a detailed study of mechanisms that control tensile or creep ductility, damage tolerance, and fracture in RCCAs is beyond the scope of the current project.

Recent Progress

Over the past two years, we have systematically tested the central hypothesis of this project in the pseudobinary $(NbTaTi)_{1-x}V_x$ system (x = 0, 0.08, 0.16, 0.25), fabricated with matched grain size and interstitial impurity content to isolate the intrinsic effect of V-induced lattice distortion. Elevated-temperature tensile testing (**Fig. 1**) revealed a systematic enhancement of yield strength and a broadening of the intermediate-temperature strength plateau with increasing V content: NbTaTiV exhibits

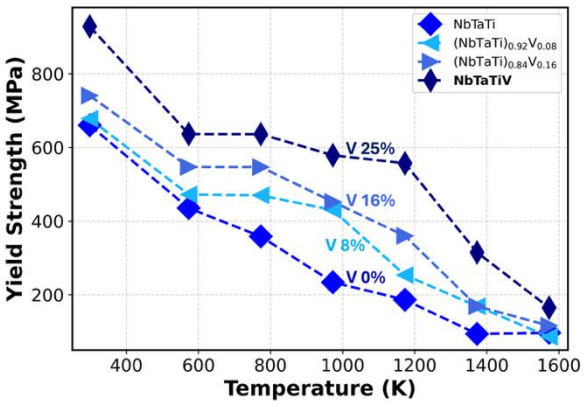

Fig. 1 Temperature-dependent 0.2% offset yield strength of the $(NbTaTi)_{1-x}V_x$ series. Strength and plateau breadth increase systematically with V content.

~3× higher yield strength than NbTaTi from 973-1373 K and ~2× higher strength at 1573 K.

To directly probe the dislocation character responsible for this enhanced strength retention, dedicated in-situ neutron diffraction was performed on NbTaTiV during heating and tension at 1173 K using a modified Williamson-Hall analysis, complemented by STEM diffraction contrast imaging (DCI-STEM) with g·b and 3D stereographic trace analysis. **Fig. 2** and **Fig. 3** show the results from DCI-STEM stereographic analysis for NbTaTi and NbTaTiV. In NbTaTi, long, straight dislocations are present with their sense factors and the Burgers vectors deviating by <7 º

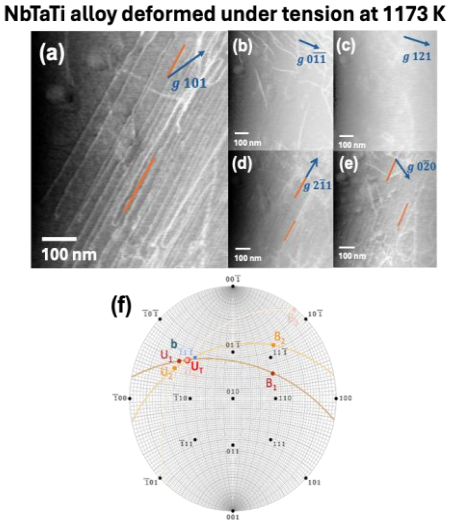

Fig. 2 DCI-STEM images of dislocations in the NbTaTi alloy deformed under tension at 1173 K and interrupted at below 2% strain along (a) the [101] two-beam condition near the [1$\bar{1}$1] zone axis; (b, c) shows that the contrast of these dislocations disappear (d, e) provides two additional images under the [2$\bar{1}$1] two-beam condition near the [1$\bar{1}$1] zone axis and under the [0$\bar{2}$0] two-beam condition near the [$\bar{1}$01] zone axis where these long and straight dislocations are visible; and (f) gives the stereographic projection of all the relevant beam directions B_i, the trace projections U_i, the actual dislocation line direction U_T, and the Burgers vector b, where the character of these dislocations is definitively determined to be screw-dominated..

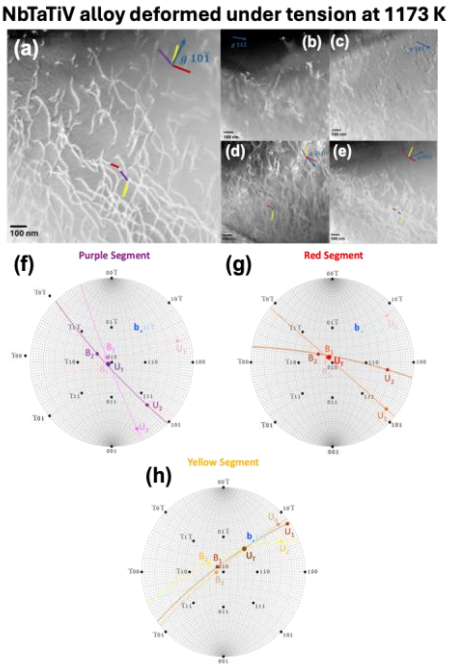

Fig. 3 DCI-STEM images of dislocations observed in the NbTaTiV alloy deformed under tension at 1173 K and interrupted at below 2% strain along (a) the [10$\bar{1}$] two-beam condition near the [010] zone axis; (b, c) shows that the contrast of these dislocations disappear; (d, e) provides two additional images under the [211] two-beam condition near the [$\bar{1}$3$\bar{1}$] zone axis and under the [002] two-beam condition near the [010] zone axis. Representative line directions are marked with purple, red, and yellow segments; and (f-h) gives the stereographic projection of all the relevant beam directions B_i, the trace projections U_i, the actual dislocation line direction U_T, and the Burgers vector b for the purple, red, and yellow segments, respectively. The characters of these curvy dislocations are largely mixed.

in 3D, showing dominant screw characters. However, in NbTaTiV, the dislocations are curvy and largely mixed in character. In the neutron analysis, peak broadening profiles with pure screw and pure edge characters are fitted with the experimental data. The goodness of fit (R^2) of the screw- and edge-dislocation models to the neutron peak-broadening data (**Fig. 4**)

shows that the dominant dislocation character controlling yield transitions from screw-dominated to edge-dominated with increasing V concentrations. This is the first direct experimental evidence linking V-induced lattice distortion to a mechanistic transition in the dislocation character controlling yield strength, and it explains why NbTaTiV retains higher yield strength than the single-crystal Ni-

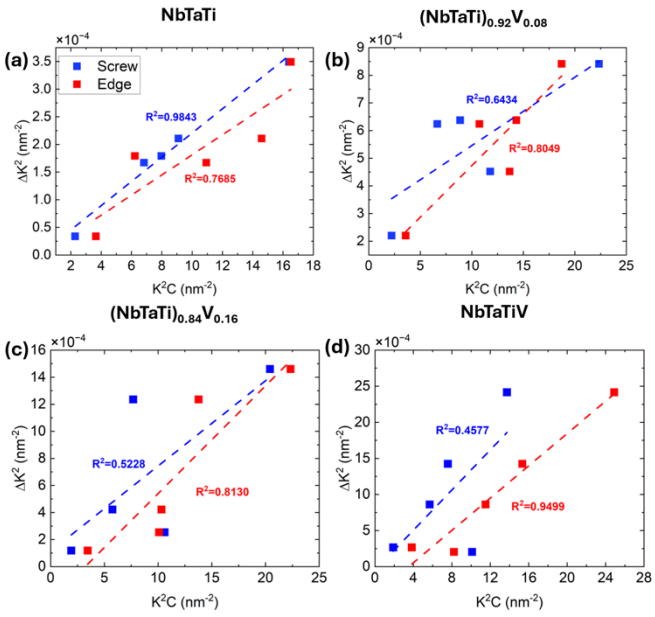

Fig. 4 Modified Williamson-Hall plot from in-situ neutron scattering experiments for (a) V0, (b) V8, (c) V16, and (d) V25 deformed at 1173 K using dislocation contrast factors for screw <1,1,1> type dislocations and edge <1,1,1>{1,1,0} type dislocations.

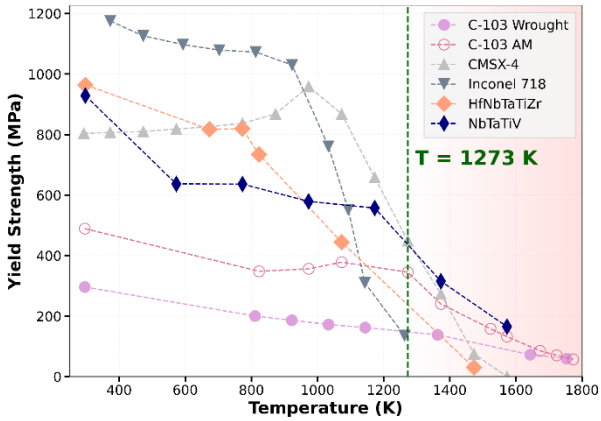

Fig. 5 Temperature-dependent yield strength of NbTaTiV in comparison with the ductile HfNbTaTiZr RCCA (Senkov alloy), a popular commercial Nb-based alloy C-103 (both wrought and additively manufactured), as well as two popular γ/ γ' Ni-based superalloys, Inconel 718 and CMSX-4.

based superalloy CMSX-4 beyond 1273 K, whereas NbTaTiHf-based RCCAs, in which Hf produces weaker edge competition against screw, do not show the same desired properties (**Fig. 5**).

To extend this mechanistic understanding beyond yielding, we measured the tensile creep behavior of NbTaTi and NbTaTiV in high vacuum at 1173 K (**Fig. 6**). NbTaTiV shows slightly higher creep resistance than NbTaTi, consistent with edge-dislocation glide control persisting into the creep regime. Stress exponents near 3 for both alloys indicate thermally activated, viscous glide-controlled creep, and the corresponding activation energies (367 kJ/mol for NbTaTi, 305 kJ/mol for NbTaTiV) agree well with rule-of-mixtures estimates of vacancy diffusion in the constituent elements (322 and 319 kJ/mol, respectively). However, both alloys were also found to develop Ti- and N-rich secondary phases during creep that grow with time and, rather than embrittling the alloys, measurably slow the creep rate. This points to an opportunity for deliberate secondary-phase design. Despite its superior yield strength and creep resistance among ductile RCCAs,

NbTaTiV's creep resistance remains orders of magnitude below that of CMSX-4 under engineering-relevant stresses, underscoring that single-phase solid-solution strengthening alone is insufficient for long-duration, low-stress applications.

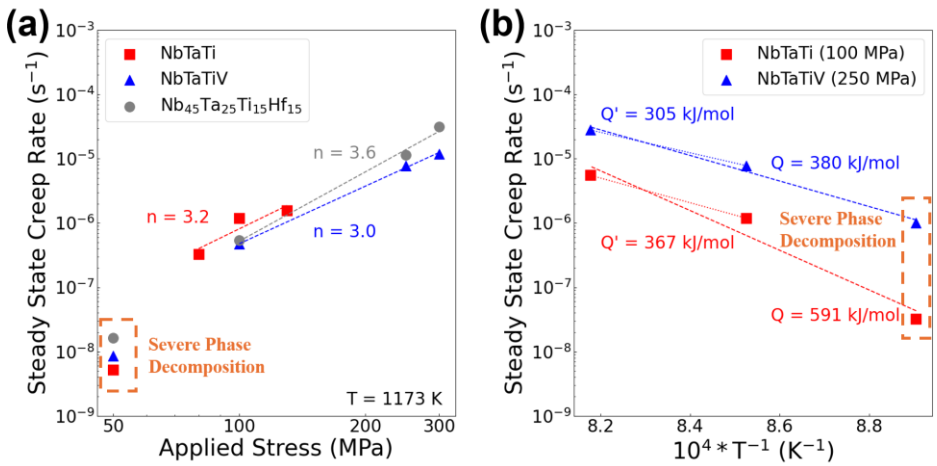

Fig. 6 (a) Steady-state creep rate vs. applied stress at 1173 K and (b) Arrhenius plot for NbTaTi and NbTaTiV, showing stress exponents near 3 and activation energies consistent with vacancy diffusion.

Future Plans

Having established that V-induced lattice distortion drives a temperature- and composition-dependent screw-to-edge dislocation transition that controls yield strength, we will extend this framework to thoroughly understand the yield strength plateau behavior for NbTaTiV at intermediate temperatures. It is envisioned that the glide of edge dislocation alone cannot fully rationalize the plateau behavior, since the edge dislocation-concentrated solid solution interaction is also thermally activated. Additional strengthening mechanisms, such as cross-core diffusion [1] or superjog formation [2] that can contribute to an athermal plateau, must be present. These mechanisms rely on abnormally high vacancy concentrations to reproduce experimental yield strengths, which is plausible given the large local fluctuations in vacancy formation energies arising from the rugged potential energy landscape of RCCAs.

We will directly determine the equilibrium vacancy concentration in NbTaTiV and NbTaTi alloys using the Simmons-Balluffi method ($\Delta L/L - \Delta a/a$), combining dilatometry and in-situ heating with X-ray diffraction. Motivated by the creep activation energies obtained this period, these measurements will directly test whether the equilibrium vacancy concentration in RCCAs deviates from simulation estimates. The measured values will be compared with those of pure Nb, our benchmarking material, to examine whether RCCAs exhibit fundamentally different vacancy energetics relative to pure metals. To probe vacancy behavior local to line defects, we will also attempt spatially resolved measurements, such as 4D-STEM scans in regions of high edge-dislocation density versus dislocation-free regions, to determine whether vacancies are locally enriched near dislocations. These results will be compared against an independent measure of

vacancy concentration, positron annihilation spectroscopy, to provide a holistic understanding of this scientific question.

References

[1]A. Ghafarollahi, Strengthening mechanisms in dilute and random solid solution high-entropy bcc alloys, EPFL (2022).
[2]S. He, X. Zhou, D. Mordehai, J. Marian, Thermal super-jogs control the high-temperature strength plateau in Nb-Mo-Ta-W alloys, Acta Mater. 244 (2023) 118539. https://doi.org/10.1016/j.actamat.2022.118539.

Publications

[1] S.I. Rao, W. Wang, M. Asta, R.O. Ritchie, M. Zhang, Rationalization of the tensile creep behavior of the Nb45Ta25Ti15Hf15 bcc refractory complex concentrated alloy using Rao-Suzuki screw dislocation glide model, Scripta Materialia 265 (2025) 116752.
[2] M. Lau, T. Zakia, A. Stratton, A. Ni, M. Zhang. Tensile Creep Properties of NbTaTi and NbTaTiV Refractory Complex Concentrated Alloys, Acta Materialia 308 (2026) 122021.
[3] M. Zhang, U. Glatzel, M. Heilmaier, E.P. George. Creep behavior of high-entropy alloys: A critical review, Intermetallics 192 (2026) 109242.
[4] T. Zakia, A. Nahin, D. Yu, J. Pustelnik, J. Li, M. Kincheloe, L. Amalia, Y. Chen, P.K. Liaw, H. Xu, M. Zhang. Enhanced Elevated-Temperature Strength in Refractory Complex Concentrated Alloys via Temperature-Induced Transition from Screw-to-Edge Dislocation Control. (in revision).
[5] T. Zakia, A. Nahin, D. Yu, J. Pustelnik, J. Li, M. Kincheloe, L. Amalia, Y. Chen, P.K. Liaw, H. Xu, M. Zhang. Mechanistic Transition from Screw to Edge Dislocation Glide Governs Elevated-Temperature Strength in $(NbTaTi)_{1-x}V_x$ Refractory Complex Concentrated Alloys. (in revision).

Author Index

Abdeljawad, Fadi 141
Aitkaliyeva, Assel 239
Allison, J. 16
Andersson, D. 81
Asta, Mark 186
Averback, Robert S. 21
Bellon, Pascal 21
Beyerlein, Irene J. 25, 136
Bocklund, Brandon 185
Boer, Maarten P. 73
Boyce, Brad L. 30
Branicio, Paulo S. 35
Bucsek, Ashley 16, 40, 45
Burke, K. 81
Burns, James T. 48
Capolungo, Laurent 57
Castro, Ricardo H. R. 62
Charpagne, Marie A. 21, 66
Choy, Jennifer T. 68
Chueh, William 102
Cooper, M. 81
Couet, Adrien 68
Dang, Khanh 57
Demkowicz, M. J. 78
Devaraj, A. 202
Dickey, Elizabeth C. 73
Dillon, S. 81
Dingreville, Remi 30
Dongare, Avinash M. 87
El-Awady, J. A. 92
Falk, Michael L. 233
Field, Kevin G. 156
Finkeldei, S. 81
Gavini, V. 16
Genc, Arda 228
Ghazisaeidi, Maryam 97
Gianola, Daniel 228
Gu, Wendy 102
Gu, Yijia 228
Harley, Joel B. 118
Hodge, Andrea M. 244
Holm, E. 16
Homer, Eric R. 104
House, Stephen 30
Jacobs, Tevis D.B. 108
Jin, Miaomiao 113
Johnson, Oliver K. 104
Kacher, Josh 180
Kenesei, Peter 45
Kesler, Michael S. 118
Kohnert, Caitlin 249
Krause, Amanda R. 118
Kreller, Cortney 249
Kruska, K. 202
Lee, Seok-Woo 123
Leonard, Aeriel 127
Li, Lin 131
Lou, Jun 217
Mara, Nathan A. 136
Marian, Jaime 233
Marquis, Emmanuelle 141
Martinez, Enrique 141
Martini, Ashlie 108
Mathaudhu, Suveen 141
McCabe, Rodney 57
Medlin, Doug 30
Miller, M. P. 25
Mills, Michael 97
Minor, Andrew M. 185, 186
Mishin, Yuri 145
Misra, Amit 16, 150
Morgan, Dane 156
Musico, Brianna 249
Neilson, W. 81
Nygren, K. E. 25
O'Connor, Thomas C. 161
Oh, Hyunseok 166
Packard, Corinne E. 171
Padture, Nitin P. 175, 217
Perron, Aurelien 185
Phillpot, Simon 239
Pierron, Olivier 180
Pokharel, Reeju 45
Pollock, T. M. 25
Puchala, B. 16
Qi, L. 16
Qi, Yue 175
Rao, S. I. 92
Ribet, Stephanie 185
Ritchie, Robert O. 186

Rohrer, Gregory S. 73
Rosso, K.M. 202
Rupert, Timothy J. 191
Sachan, Ritesh 196
Sangid, Michael D. 200
Schreiber, D.K. 202
Schuh, Christopher A. 207, 212
Sehitoglu, Huseyin 40
Sheldon, Brian W. 217
Sills, Ryan 221
Silverstein, Ravit 228
Simmons, David S. 226
Spearot, Douglas 228
Sundararaghavan, V. 16
Sushko, M.L. 202
Szlufarska, Izabela 229
Taheri, Mitra L. 233
Thompson, Gregory B. 104, 253
Thornton, K. 16
Tonks, Michael R. 118, 239
Trelewicz, Jason R. 244
Tucker, Garrit J. 171
Uberuaga, Blas P. 81, 249
Van der Ven, A. 16
Veelen, Arjen v. 249
Vo, H. 57
Voyles, Paul M. 156
Wade, Austin 228
Wang, C. 202
Wang, Y. 81
Wang, Yongqiang 249
Weinberger, Christopher R. 253
Wharry, Janelle P. 258
White, J. 81
Xie, K. Y. 78
Yang, Yang 113, 261
Zhang, Mingwei 185, 265
Zhang, Yongfeng 68
Zhu, Ting 180